

**USING ELECTROMAGNETIC METHODS TO MAP AND  
DELINEATE HIGH-GRADE HARZBURGITE PODS WITHIN  
THE NI-CU MINERALISED JACOMYNSPAN  
ULTRAMAFIC SILL, NORTHERN CAPE, SOUTH AFRICA.**

**Mhaka Ushendibaba**



'A Dissertation submitted to the Faculty of Science,  
University of the Witwatersrand, Johannesburg,  
in fulfilment of the requirements for the degree of Master of Science.'

Johannesburg, 2016

## DECLARATION

I declare that this dissertation is my own, unaided work. It is being submitted for the degree of Master of Science in the University of the Witwatersrand, Johannesburg. It has not been submitted before for any degree or examination in any other University.



---

Mhaka Ushendibaba

19<sup>th</sup> day of May 2016

## ABSTRACT

The Jacomynspan Ni-Cu sulphide mineralisation is hosted within a 100m thick steeply dipping tabular, differentiated, sill of mafic to ultramafic composition intruded into country gneissic rocks of the Namaqualand Metamorphic complex. This sill is predominantly composed of tremolite schist (metamorphosed pyroxenite) containing lenticular bodies of harzburgite. The harzburgite generally hosts net-textured mineralisation with up to 50% by volume of the rock. Massive sulphide veins and stringers are occasionally present within the harzburgite. The sulphide minerals are a typical magmatic assemblage of pyrrhotite, chalcopyrite and pentlandite. The sill covers an approximate strike length of about 5km but only a small portion covering 1km x 1km was selected for this study.

Physical property studies carried out on the drill core (magnetic susceptibility and conductivity) indicate that the country gneissic rocks are not conductive and neither are they magnetically susceptible. However, the mineralized sill has elevated values of both magnetic susceptibility and relative conductivity compared to its host making it a suitable target for both magnetic and electromagnetic inversion.

Drilling done so far on the study area has shown that the well-mineralised harzburgite (hosted within the poorly mineralised ultramafic sill) is not a continuous body but occurs in 'pockets'. There is therefore need to use the available geophysical and geological datasets to derive a model of these well mineralised pods. This study is therefore intended to assess the feasibility of using electromagnetic (EM) methods together with other geophysical methods and geology in obtaining a model of the harzburgite pods hosted within the less conductive poorly mineralised ultramafic sill in order to guide further drilling.

Geosoft's VOXI Earth Modelling software was used to model the high resolution airborne magnetic data for this study. Cooper's Mag2dc ([www.wits.ac.za](http://www.wits.ac.za)) and Stettler's Magmodintrap software (personal communication, 2015) was also used during modelling of the magnetic data to compliment the modelling from VOXI. The mineralised ultramafic sill was clearly mapped in both the 3D model representation from Mag2dc modelling and VOXI's 3D unconstrained smooth model inversion for the study area.

Based on the physical properties studies carried out on the study area, EM data (both ground and downhole EM) were modelled using Maxwell software. The poorly mineralised tremolite schist was clearly modelled. In order to better constrain the targets, an assumption was made that at late decay times the currents would be focused in the centre of the large EM plate probably giving an indication of the most conductive part of the intrusion. Smaller 'Resultant EM plates' of dimensions, 300mx300m that coincide with the centre of the large EM plates (with a conductance above 100S) were constructed in

Maxwell software and integrated with the DXF file of the Micromine geology model of the well mineralised harzburgite clearly mapping the well-mineralised harzburgite and showing its possible extensions.

2D inversion modelling was conducted on all audio-frequency magnetotelluric (AMT) data for this study area. The modelling results clearly mapped the mineralised intrusion.



In memory of my beloved mother

Natsai Ushendibaba

1942 - 2013

## **ACKNOWLEDGEMENTS**

I would like to thank the following people and organisations for their input and support:

- African Nickel Ltd for allowing me to use their data and software.
- Prof Edgar Stettler and Dr Michael Jones my supervisors for all the support, advice and valuable input.
- Anglo American Cooperation for providing equipment during field work.
- African Nickel and Anglo American field staff that assisted during the data acquisition.
- Dr Leonie Mare and the Council for Geoscience for allowing me to use their laboratory equipment.
- Mr Stefaans du Plessis, Dr Panga Dzanga and Mr Ntando Nonoise for the valuable input into the project.
- Mr Neville Brown for his assistance in processing AMT data.
- To my wife and our two boys Prince and Prosper, I say thank you for the moral support.

## TABLE OF CONTENTS

DECLARATION.....	ii
ABSTRACT.....	iii
ACKNOWLEDGEMENTS.....	vi
LIST OF FIGURES.....	xii
LIST OF TABLES.....	xx
 <b>CHAPTER 1: INTRODUCTION.....</b>	 <b>1</b>
1.1 Brief discovery history and previous work.....	2
1.2 Geology of the Area .....	3
1.3 Geophysics.....	4
1.3.1 Geophysical Methods.....	4
1.3.2 Geophysical Inversion Modelling .....	4
1.4 Goals of the Dissertation.....	5
1.5 Dissertation Structure.....	6
 <b>CHAPTER 2: METHOD – GROUND AND AIRBORNE MAGNETICS.....</b>	 <b>8</b>
2.1 Introduction.....	8
2.1.1 Basic Concepts .....	8
2.1.2 Magnetism of Rocks and Minerals .....	10
2.1.3 The Geomagnetic field .....	11
2.1.4 Induced and remanent magnetization.....	13
2.1.5 Magnetic Anomalies.....	15
2.1.6 Diurnal Variations and Magnetic storms .....	16
2.2 Aeromagnetic survey .....	17
2.3 Ground Magnetic Survey .....	18
2.3.1 Instruments for Ground Magnetic Survey .....	18
2.3.2 Geometrics G856 Proton Precession Magnetometer .....	18
2.3.3 Ground Magnetic Survey Design .....	19
2.3.4 Quality control .....	19
2.4 Data Processing .....	20
2.4.1 Ground Magnetic Survey Data Processing.....	20
2.4.2 Aeromagnetic Survey Data Processing .....	20
 <b>CHAPTER 3: METHOD – GROUND AND AIRBORNE ELECTROMAGNETICS.....</b>	 <b>21</b>
3.1 Introduction.....	21

3.1.1	Basic Theory of Electromagnetics Surveying .....	21
3.1.2	Depth of penetration of electromagnetic fields.....	23
3.1.3	Time-domain electromagnetic surveying .....	24
3.1.4	Electrical conductivity properties of rocks .....	24
3.2	Airborne EM survey – SPECTREM System .....	25
3.2.1	SPECTREM System Specifications and Geometry .....	26
3.3	Ground EM Surveys .....	27
3.3.1	Instruments for ground EM survey .....	27
3.3.2	The JESSY DEEP LT SQUID .....	27
3.3.3	The 3 Component Fluxgate Magnetometer System .....	28
3.3.4	The SMARTem V Receiver .....	29
3.3.5	Ground EM Survey Design .....	30
3.3.6	Fixed Loop Survey Design .....	31
3.3.7	Moving Loop Survey Design .....	33
3.3.8	Quality Control.....	34
3.4	Data Processing .....	35
3.4.1	Airborne Electromagnetic Data Processing (SPECTREM).....	35
3.4.2	Ground Electromagnetic Survey Data processing .....	36
<b>CHAPTER 4: METHOD – DOWNHOLE ELECTROMAGNETICS (DHEM) .....</b>		<b>38</b>
4.1	Introduction.....	38
4.1.1	Basic theory of DHEM .....	38
4.2	Instruments for DHEM Survey .....	40
4.3	Survey Design .....	40
4.4	Quality control .....	41
4.5	Data processing .....	41
<b>CHAPTER 5: METHOD – AUDIO-FREQUENCY MAGNETOTELLURICS (AMT). .....</b>		<b>43</b>
5.1	Introduction .....	43
5.1.1	Basic theory of AMT .....	43
5.2	Instruments used.....	44
5.2.1	The GDP-32 <sup>II</sup> Receiver.....	45
5.2.2	ANT/6 Magnetic Antenna .....	45
5.3	Survey design.....	46
5.4	Quality Control.....	47
5.5	Data Processing .....	47
<b>CHAPTER 6: GEOPHYSICAL DATA ENHANCEMENT .....</b>		<b>49</b>

6.1	Introduction.....	49
6.2	Linear transformations (filters) .....	49
6.2.1	Fourier transform.....	49
6.2.2	Convolution .....	50
6.3	Upward and downward continuation .....	51
6.4	Reduction to the pole .....	52
6.5	Derivatives.....	52
6.5.1	Vertical Derivatives .....	52
6.5.2	Horizontal Derivatives .....	53
6.5.3	Tilt Angle Derivative .....	53
6.6	Analytic Signal.....	53
<b>CHAPTER 7: GEOPHYSICAL DATASETS.....</b>		<b>54</b>
7.1	Physical Property Measurements Data.....	54
7.1.1	Magnetic Susceptibility and Relative Conductivity .....	54
7.2	Palaeomagnetic Laboratory Measurements .....	55
7.2.1	Magnetic Susceptibility Measurements.....	56
7.2.2	Demagnetisation of rock specimens .....	57
7.2.3	Measurement of NRM .....	58
7.2.4	Calculating the Koenigsberger Ratio .....	62
7.2.5	Summary of the Palaeomagnetic Results .....	62
7.3	Ground Magnetic Survey Data .....	63
7.3.1	Total Magnetic Field Intensity Data.....	64
7.3.2	Upward continuation of ground magnetic data .....	64
7.4	High Resolution Aeromagnetic Survey Data.....	65
7.4.1	Total Magnetic Field Intensity Data.....	65
7.4.2	Analytic Signal of Aeromagnetic data .....	67
7.4.3	Tilt Angle Vertical Derivative of the Aeromagnetic Data .....	68
7.4.4	Magnetic Ternary Image of the aeromagnetic data .....	70
7.4.5	Interpretation of the Aeromagnetic Data .....	72
7.5	Airborne Electromagnetic survey data (SPECTREM) .....	72
7.5.1	The Late-time Constant.....	73
7.5.2	Interpretation of AEM data .....	73
7.5.3	Spectrem Total Magnetic Intensity data.....	75
7.5.4	Radiometric Data (Spectrem).....	76
7.6	Ground EM survey Data.....	77
7.6.1	Moving Loop Time Domain ground EM survey Data .....	77
7.6.2	Fixed Loop Time Domain ground EM survey Data .....	79
7.7	Downhole EM data .....	80

7.8	AMT Data .....	82
7.9	Drillhole Data.....	84
7.9.1	Borehole JMP001.....	86
<b>CHAPTER 8: THEORETICAL ASPECTS OF GEOPHYSICAL MODELLING.....</b>		<b>89</b>
8.1	Preamble .....	89
8.2	Inversion of Magnetic Data .....	91
8.2.1	VOXI Earth Modelling theory.....	92
8.2.2	VOXI's Magnetization Vector Inversion (MVI) Theory .....	94
8.2.3	Iterative Reweighting Inversion Focusing (IRF) .....	96
8.2.4	Mag2dc Software .....	97
8.3	Inversion of Electromagnetic data.....	97
8.4	Inversion of AMT data .....	99
8.4.1	AMT Model Types .....	99
<b>CHAPTER 9: GEOPHYSICAL MODELLING OF THE DATA .....</b>		<b>102</b>
9.1	Modelling Magnetic Data.....	102
9.1.1	The Three-Dimensional Starting Model .....	103
9.1.2	Mag2dc Modelling of the High Resolution Aeromagnetic data .....	104
9.1.3	Calculating the Regional Field and Levelling .....	105
9.1.4	Calculating the Residual Grid .....	106
9.1.5	Modelling of the Final Residual Data .....	107
9.1.6	Creating a 3D Model Representation from Mag2dc Models.....	108
9.2	VOXI Modelling of the Aeromagnetic Data .....	109
9.2.1	VOXI modelling of the study area .....	110
9.2.2	Iterative Reweighting Inversion Constraint (IRI) .....	112
9.2.3	Magnetization Vector Inversion (MVI) .....	113
9.2.4	VOXI Constrained Inversion.....	115
9.3	Modelling of Ground EM data in Maxwell Software .....	116
9.3.1	Waveform Parameters .....	116
9.3.2	Decay Analysis.....	118
9.3.3	Modelling Fixed Loop EM Data – Loop 1 .....	118
9.3.4	Modelling of Moving Loop EM Data .....	123
9.4	Modelling of DHEM Data.....	127
9.5	Modelling of the AMT data .....	130
9.5.1	AMT Model Types .....	131
9.5.2	AMT Resistivity Depth Sections .....	131
9.5.3	3D-model Representation of AMT Models.....	133
9.6	Summary of Geophysical Modelling .....	134

<b>CHAPTER 10: DATA INTEGRATION, INTERPRETATION AND DISCUSSION .....</b>	<b>136</b>
10.1 Micromine Geology Model of the Intrusion .....	136
10.2 Interpretation of the High Resolution Aeromagnetic Data .....	137
10.3 Integrating Magnetic Models with the Geology Model .....	138
10.4 Interpretation of Ground EM Data .....	140
10.5 Integration of Modelled EM Plates with Geology Models .....	141
10.6 Integration of the Modelled DHEM Plates with Geology Models .....	143
10.7 Interpretation of AMT Data .....	145
10.8 Integrating AMT Data with Geology Models .....	147
10.9 Integrating different models .....	149
<b>CHAPTER 11: CONCLUSIONS AND SUGGESTIONS FOR FURTHER WORK .....</b>	<b>150</b>
<b>APPENDIX A .....</b>	<b>152</b>
<b>APPENDIX B .....</b>	<b>153</b>
<b>REFERENCES.....</b>	<b>154</b>

## LIST OF FIGURES

Figure 1.1 - The Jacomynspan Project Locality Map.....	1
Figure 1.2 - Picture of the land within the study area which is generally flat and undisturbed. Short grasses and shrubs are observed and little to no outcrop is present. ....	2
Figure 2.1- The magnetic flux lines surrounding a bar magnet representing the Earth's magnetic field. ....	9
Figure 2.2 - The variation of the inclination of the total magnetic field with latitude based on a simple dipole approximation of the geomagnetic field. (Sharma, 1976).....	12
Figure 2.3 - The geomagnetic elements (Kearey <i>et al.</i> , 2002) .....	12
Figure 2.4 - North-South schematic profile of a magnetic anomaly over a magnetic dyke with a dipolar effect. The dyke is striking E-W and situated in the southern hemisphere (Roux, 1980).....	15
Figure 2.5 - Schematic diurnal variation, showing the vertical component of the magnetic field through a 24 hour period at varying magnetic latitudes (Roux, 1980). ....	16
Figure 2.6 - Schematic magnetic storm, showing the vertical component of the magnetic field. Note the erratic nature of the field and the change in scale as compared to diurnal variation from Figure 2.5 (Coomber, 2008). ....	17
Figure 2.7 - Ground magnetic traverses covering the study area relative to aeromagnetic survey outline. ....	19
Figure 3.1 - General principle of electromagnetic surveying (Kearey <i>et al.</i> , 2002.).....	23
Figure 3.2 - Jessy Deep Low Temperature SQUID magnetometer in orange colour being filled up by liquid helium in order to cool the sensors down to -269 <sup>0</sup> C (Jessy Deep Manual). ....	28
Figure 3.3 - EMIT's 3-component fluxgate magnetometer taking measurements at Jacomynspan project. ....	29
Figure 3.4 - Crystal synchronisation of the SMARTem V receiver and a transmitter controller before the start of field work at Jacomynspan. ....	30
Figure 3.5 - Ground EM traverses for both fixed loop and moving loop methods relative to the outline of the Airborne EM and Aeromagnetic survey. ....	31
Figure 3.6 - EM forward model for the Fixed Loop survey for the Jacomynspan conductive mineralisation scenario, showing the Primary field lines and coupling with the plate for the transmitter loop location in the left, the anticipated EM response for the Z, X, and Y components on the right. ....	32
Figure 3.7 - TDEM fixed loop survey plan over the main target showing the position of the 3 transmitter loops and stations as black dots. ....	33
Figure 3.8 - TDEM moving loop survey plan showing the moving transmitter loop, position of the receiver in red and station positions as black dots covering the main target. ....	34
Figure 3.9 - The moving loop data in Maxwell. The profiles for the measured components X, Y, and Z for Line 5300 are shown in the profile window on the right while the decay curves at station 800 for the three components are shown on the decay curves window on the left. Black is the Z component, blue is the X component and green is the Y component while the vertical yellow line shows the station position. ....	37
Figure 4.1 - Basic principle of DHEM surveying (Dyck and West, 1984). ....	39
Figure 4.2 - Line editor dialog box for Maxwell which can be used to create a configuration file for the survey. ....	42
Figure 5.1 - Zonge GDP 32 <sup>II</sup> Receiver used to acquire AMT at Jacomynspan. ....	45
Figure 5.2 - AMT traverses relative to aeromagnetic survey outline. ....	46
Figure 5.3 - Typical 100m spread for the vector survey carried out at the study area. ....	47
Figure 6.1 - Schematic example of a spatial 3 x 3 smoothing filter kernel. Note the 6 x 4 input grid is reduced to a 4 x 2 filtered grid, after Cooper (2004). ....	51



Figure 7.1 - Strip log of borehole JMP001 showing how the relative conductivity (red trace) and magnetic susceptibility (blue trace) (in $10^{-3}$ SI units) varies for the different rock units. Massive sulphide stringers and net textured sulphides are highly conductive as well as highly magnetically susceptible. ....	55
Figure 7.2 - Prepared specimen of the well mineralised harzburgite for Palaeomagnetic measurements. The white arrow shows the orientation of the specimen going down. ....	56
Figure 7.3 - The AF demagnetiser used for progressively demagnetising samples at CGS by applying alternating fields. ....	58
Figure 7.4 - The JR-6A spinner magnetometer used for measuring NRM at CGS showing the sample position. ....	59
Figure 7.5 – Demagnetization results of the well mineralised harzburgite plotted in Rama6w software. ....	61
Figure 7.6 – a) Surface magnetic charge produced by magnetization of a Single Domain (SD) grain along the long axis of the grain. The arrow indicates the direction of saturation magnetization $j_s$ ; plus and minus signs indicate surface magnetic charges; note that magnetic charges are restricted to the ends of the grain, b) Surface magnetic charge produced by magnetization of an Single Domain (SD) grain perpendicular to the long axis of the grain. The arrow indicates the direction of saturation magnetization $j_s$ ; plus and minus signs indicate surface magnetic charges; note that magnetic charges appear over the entire upper and lower surfaces of the grain. (Butler, 1992). ....	63
Figure 7.7 - Levelled Total Field Magnetic Intensity Image – ground survey .....	64
Figure 7.8 - High resolution Total Magnetic Intensity image ( <i>bottom</i> ) and the ground total magnetic intensity upward continued to 30m above ground ( <i>Top</i> ). ....	65
Figure 7.9 a) - High resolution Total Magnetic Intensity image for the Jacomynspan project. b) - High resolution Total Magnetic Intensity image for Jacomynspan project showing the outline of the ultramafic intrusion and some major breaks. ....	66
Figure 7.10 a) - Analytic signal image of the Total Magnetic Intensity for Jacomynspan project. b)- Analytic signal image showing edges of the magnetic source bodies and major breaks. ....	67
Figure 7.11 a) - The Tilt angle vertical derivative image for Jacomynspan b) - The Tilt angle vertical derivative image for Jacomynspan clearly mapping approximately 5km of highly prospective strike extent for the sulphide mineralisation. ....	69
Figure 7.12 – A plot of the boundaries as determined from the TA with a Fortran algorithm (Stettler, personal communication, 2015). It also depicts the calculated magnetic susceptibility for each body determined in an automated way. ....	70
Figure 7.13 a) - Ternary image of the high resolution aeromagnetic data for Jacomynspan project. b) Ternary image clearly enhancing structures with annotations. ....	71
Figure 7.14 - Xcalibur high resolution aeromagnetic data interpretation on a Tilt angle Derivative image. ....	72
Figure 7.15 - EM Late-time constant image for Jacomynspan project airborne EM data flown by Spectrem Air mapping the outline of the Jacomynspan ultramafic intrusion and other possible sulphide bodies within the area. The linear very obvious anomalous features are mostly due to fences and other anthropogenic structures. ....	73
Figure 7.16 - EM Late time-constant image for Jacomynspan project flown by Spectrem Air clearly mapped the outline of the Jacomynspan ultramafic intrusion, known deposits and prospective sulphide bodies within the area. Cultural features such as fences were also detected and make up the linear conductors indicated by broken lines. ....	74
Figure 7.17 - EM Total Magnetic Intensity image for Jacomynspan project flown by Spectrem Air clearly mapped the outline of the Jacomynspan ultramafic intrusion. Main contacts and structures within the area were also mapped. ....	75

Figure 7.18 - Radiometrics ternary image for Jacomynspan project flown by Spectrem Air. The image is very speckled and indicates mostly reddish hues due to elevated equivalent eK concentrations with the location of the target area. This may signify that the mineralization is due to hydrothermal enrichment. Purple crosscutting structures indicate the drainage pattern.....	76
Figure 7.19 - The moving loop data after importation into Maxwell Software showing the EM response profiles for the three components Z, X, and Y on the right side and surveyed lines on the left for line 5300 (indicated by a yellow cross) of the study area. ....	77
Figure 7.20 - Channel 20 Z-component image of the moving loop mode mapping the conductive intrusion of the study area. ....	79
Figure 7.21 - The fixed loop data (SQUID sensor) after importation into Maxwell Software showing the EM response profiles for the three components Z, X, and Y to the right and the fixed loop and surveyed lines to the left for line 5300 (indicated by a yellow cross) of the study area.....	80
Figure 7.22 - The DHEM data after importation into Maxwell Software showing the EM response profiles for the three components A, U, and V to the right and the borehole trace and fixed loop position to the left for borehole JMP001 located in the study area. ....	81
Figure 7.23 - A purely positive anomaly is obtained from a borehole intersection near the centre of a conductor, a predominantly positive anomaly from an edge intersection, a negative anomaly with positive shoulders from a relatively close miss, and a totally negative anomaly from a very distant target (Crone, 1980).....	81
Figure 7.24 - Time series from each channel on the instrument. Green is the electric field E while blue is magnetic field H. ....	82
Figure 7.25 - The sounding curves of the two components, $T_m (\rho_{xy})$ in dark blue and $T_e (\rho_{yx})$ in light blue. ....	83
Figure 7.26 – Line 4 2D Smooth-Model inversion stung together into sections showing resistivity and phase of the observed data. The successive apparent resistivity sounding curves along a survey line have been converted into a layered (1D) earth estimation of the subsurface and strung together into pseudo-sections constructed from the resistivity and phase for each of the components. ....	84
Figure 7.27 – a) Collar positions of the drilled boreholes on TMI image of the aeromagnetic data, b) Plan of the position of the boreholes drilled within the study area showing the borehole names. ....	85
Figure 7.28 - Cross section of all the drilled boreholes facing north showing the same stratigraphic sequence on all the drilled boreholes. ....	86
Figure 7.29 - Cross section plot facing west of the Jacomynspan ultramafic sill showing well mineralised harzburgite and some of the borehole traces drilled within the study area. ....	86
Figure 7.30 - Drill core for JMP001 between depth of approximately 581m and 586m showing tremolite schist (metamorphosed pyroxenite) which is host to disseminated sulphides. ....	87
Figure 7.31 - JMP001 drill core showing harzburgite with well mineralised net-textured sulphides and a stringer of massive sulphides. ....	88
Figure 8.1 - Comparing the forward and inverse method. A represents the measured anomaly, and $A_0$ the calculated anomaly. Parameters $p_1, p_2, \dots$ are the source attributes (e.g. depth, thickness, density), (Blakely, 1995). ....	90
Figure 8.2 - Tikhonov or Trade-off curve showing how optimization is carried out for the values of $\lambda$ . ....	94
Figure 8.3 - Volume of rock showing that the magnetization is a vector quantity.....	95
Figure 8.4 - An example of Osborne IOCG deposit model with the now known mineralisation shown in black – comparing MVI with Susceptibility inversion. a)	

Geological Setting, b) Susceptibility model, c) MVI Susceptibility (Ellis <i>et al.</i> , 2012).	96
Figure 8.5 - A Geosoft example of Iterative Reweighting Inversion Focusing (IRI) showing the focusing of the model to the actual known deposit compared to the smooth model. a) Earth Model, b) Smooth inversion model, c) Iterative Reweighting Inversion (VOXI training manual).	96
Figure 8.6 - Schematic view of thin conductive plate in a resistive host below a conductive overburden. No plunge angle (Pirttijarvi, 2003).	98
Figure 8.7 - Natural-field electromagnetic response to a two-dimensional, single lateral contact, model (d'Ecreville and Kunetz, 1962).	100
Figure 9.1 - 3D view of the Micromine model (in green) showing the mineralised ultramafic intrusion steeply dipping to the south with the TMI image on top. This model was used as a starting model during the modelling process.	103
Figure 9.2 – The airborne TMI image showing the 19 synthetic lines created for modelling.	104
Figure 9.3 - Mag2dc modelling results for Line 11 showing the mineralised ultramafic sill in red steeply dipping to the south. The green dotted profile above represents the observed magnetic field while the continuous black profile represents the field due to the model. A second shallow magnetic body with very much lower magnetic susceptibility is present down-dip (south) of the dipping sill which is not present in the Micromine 3D 'starter' model. Susceptibilities' are in SI units.	105
Figure 9.4 - a) Regional field data for each line gridded into a single grid which is stripy and needs levelling. b) The levelled Regional field.	106
Figure 9.5 a) The aeromagnetic TMI image. b) The calculated Residual field map after subtracting the Levelled Regional Field from the TMI.	107
Figure 9.6 - Line 11 final model of the residual field showing the ultramafic intrusion steeply dipping to the south.	107
Figure 9.7 - Final 3D susceptibility smooth model representation of the Jacomynspan area.	108
Figure 9.8 – Final 3D model representation of Jacomynspan clipped to the mineralised ultramafic sill of the study area. a) Smooth model showing the mineralised ultramafic sill, b) Smooth model with the colour tool applied to clearly map the mineralised ultramafic sill.	109
Figure 9.9 - A mesh showing the Area of Interest (AOI) and the depth extent of modelling.	110
Figure 9.10 – Unconstrained smooth model inversion results after performing the inversion. The straight black lines in the susceptibility are a result of the created voxels.	111
Figure 9.11 – 3D unconstrained smooth model inversion results of the study area showing the mineralised Jacomynspan ultramafic intrusion.	111
Figure 9.12 - The 0.007SI magnetic susceptibility iso-surface of the ultramafic intrusion.	112
Figure 9.13 - a) Smooth Model Inversion for the study area, b) IRI focus applied to the smooth model. The results are more focused showing the body steeply dipping to the south.	113
Figure 9.14 - Magnetization vector orientation of the Ampl_Magnetization, Eperp_Magnetization and Eproj_Magnetization (VOXI Training manual).	114
Figure 9.15 - Derived scalars of the Magnetisation Vector Inversion for the study area. a) magnetisation vector orientation, b) the recovered amplitude of the magnetization vector, c) the amplitude of the perpendicular "Eperp" to earth field components of the magnetization, and d) the projection of the magnetization "EProj" on to the earth field direction.	114

Figure 9.16 – a) Well mineralized harzburgite model from Micromine, b) well mineralized harzburgite voxel created from geo-surface in geosoft, c) Well mineralized harzburgite model integrated with the voxel in Geosoft. ....	115
Figure 9.17 – Constrained inversion results showing the Micromine modelled well mineralised harzburgite and its possible extension to the west. ....	116
Figure 9.18 - Waveform parameters used during modelling (Maxwell Training Manual, 2013). ....	117
Figure 9.19 - A window in the line editor display view showing the timing mark, base frequency, on-time, off-time and turn off time. The transmitted current waveform is shown in red while the horizontal blue lines represent receiver time gates. ....	117
Figure 9.20 - Decay analysis window showing the Z component fit used to determine the best time channels to model. The Z component decay curve is shown in black(with yellow hue), the X component decay curve is in green while the Y component is in blue. ....	118
Figure 9.21 – a) position of loop 1 relative to the Tilt Angle Derivative image of the high resolution aeromagnetic survey, b) surveyed lines showing the line numbers on Tilt Angle Derivative image. ....	119
Figure 9.22 - Fixed loop data after importation into Maxwell Software. On the left side is the Plan window which shows the surveyed lines and the transmitter loop position (yellow rectangle). On the right, the profiles for the measured EM response are shown for the Z, X and Y components in that order going down for line 1600 which is indicated by a yellow cross. ....	120
Figure 9.23 – Modelling results for Line 1600. The left widow shows the modelled EM plate steeply dipping to the south correlating with the mineralised ultramafic sill. The right window depicts the measured EM response traces in black and the modelled EM response in red for the three components Z, X and Y. ....	121
Figure 9.24 – Modelling results for four of the surveyed lines. ....	122
Figure 9.25 – a) Modelling results for line 1500 showing the large plate in red and the constructed ‘resultant EM Plate’ in blue. The ‘resultant’ EM plate has no effect on the modelling results b) Modelling results for line 1500 showing only the ‘resultant EM plate’ ....	123
Figure 9.26 – a) Surveyed lines of the moving loop mode relative to the Tilt Angle Derivative image of the high resolution aeromagnetic survey, b) modelled lines for this study showing the line numbers on Tilt Angle Derivative image. ....	124
Figure 9.27 - The moving loop data after importation into Maxwell. On the left side is the Plan view which shows the surveyed lines and on the right, the time channel traces for the measured EM response are shown for the Z, X and Y components in that order going down for line 1600 (indicated by a yellow cross). ....	125
Figure 9.28 – Modelling results for Line 1800. The left widow shows the modelled EM plate steeply dipping to the south correlating with the mineralised ultramafic sill. The right window shows the measured EM response profiles in black and the modelled EM response in red for the three components Z, X and Y. ....	126
Figure 9.29 – a) Collar positions of the drilled boreholes showing Transmitter position on TMI image of the aeromagnetic data, b) Plan of the position of the boreholes drilled within the study area showing the borehole names. ....	127
Figure 9.30 - The DHEM data after importation into Maxwell showing the EM response profiles for the three components A, U, and V on the right and the borehole trace and fixed loop position (yellow triangle) on the left for borehole JMP001 located in the study area. ....	128
Figure 9.31 – Modelled EM plates for JMP001 shown on the left. On the right the pane shows the measured EM response traces in black and the modelled EM response in red for the three components A, U and V. ....	129

Figure 9.32 - The constructed 'resultant' centre of plates for JMP001 is shown on the left. The right-hand window shows the measured EM response traces in black and the modelled EM response in red for the three components A, U and V. ....	130
Figure 9.33 – AMT surveyed lines shown on aeromagnetic TDR image. ....	130
Figure 9.34 – 2D Smooth-Model Inversion Sections for line 4 clearly mapping the intrusion, a) 2D Te Smooth-Model, b) 2D Tm Smooth-Model, c) 2D Smooth-Model. ....	132
Figure 9.35 – 3D Smooth-model representation of the 2D a) Tm model, b) Te model, c) 2D vector model. ....	133
Figure 9.36 – 3D iso-surfaces created from the Te voxel model. The iso-surfaces represent 25, 50 ohm-m showing the most conductive part of the intrusion. ....	134
Figure 10.1 - 3D view of the Micromine model (in green) showing the mineralised ultramafic intrusion (tremolite schist) steeply dipping to the south and the drilled boreholes.....	136
Figure 10.2 - 3D view of the Micromine model showing the mineralised ultramafic intrusion (tremolite schist) in green steeply dipping to the south, the well mineralised net-textured harzburgite in orange and the drilled boreholes. ....	137
Figure 10.3 - Xcalibur high resolution aeromagnetic data interpretation on a Tilt angle Derivative image for the study area. ....	137
Figure 10.4 – Final 3D model representation (Magmodintpr) of Jacomynspan clipped to the mineralised ultramafic sill of the study area. a) Smooth model showing the mineralised ultramafic sill, b) Smooth model with the colour tool applied to clearly map the mineralised ultramafic sill. ....	138
Figure 10.5 – Integrating the 3D smooth model inversion results (Magmodintpr) with the Micromine model of the mineralised ultramafic sill (green) there is a direct correlation.....	139
Figure 10.6 – 3D unconstrained VOXI smooth model inversion results of the study area showing the mineralised Jacomynspan ultramafic intrusion with elevated magnetic susceptibility values. ....	139
Figure 10.7 – Integrating the 3D smooth model inversion results with the Micromine model of the mineralised ultramafic sill (orange) there is a direct correlation.....	140
Figure 10.8 – Constrained inversion results showing the possible extension of the well mineralised harzburgite. ....	140
Figure 10.9 – Modelling results for Line 1600 fixed loop mode. The left window shows the modelled EM plate steeply dipping to the south correlating with the mineralised ultramafic sill. The right window show the measured EM response profiles in black and the modelled EM response in red for the three components Z, X and Y. ....	141
Figure 10.10 – The modelled EM plate in red integrated with Micromine geology model of the mineralised ultramafic sill in yellow showing a direct correlation. The right window show the measured EM response profiles in black and the modelled EM response in red for the three components Z, X and Y. ....	141
Figure 10.11 – Modelling results for line 1500 showing the large plate in red and the constructed 'resultant' EM plate in blue. The 'resultant' EM plate has no effect on the modelling results. The right window shows the measured EM response profiles in black and the modelled EM response in red for the three components Z, X and Y. ....	142
Figure 10.12 – Integration in Maxwell the well mineralised harzburgite geology model (green) with the best fitting conductive centre plates that correlate with the harzburgite and shows that more conductive material could be extending to the east. ....	143
Figure 10.13 – Modelling results for borehole JMP002 showing a large steeply dipping EM plate which map the mineralised ultramafic intrusion. The right hand window	

shows the measured EM response profiles in black and the modelled EM response in red for the three components A, U and V.....	143
Figure 10.14 – Modelling results for borehole JMP002 showing the modelled EM plate integrated with the Micromine geology model of the mineralised ultramafic intrusion. The right hand window shows the measured EM response profiles in black and the modelled EM response in red for the three components A, U and V. ....	144
Figure 10.15 - The Micromine geology model of the well mineralised harzburgite in red is integrated with the 'resultant' EM plates with conductivity thickness above 200 S. The right hand window shows the measured EM response profiles in black and the modelled EM response in red for the three components A, U and V. ....	145
Figure 10.16 – 2D Section model for Line 1 clearly maps the ultramafic intrusion shown by the high resolution aeromagnetic data. Top image illustrates the surveyed lines on the magnetic tilt angle derivative map.....	146
Figure 10.17 – 2D models with equal weight to Te and Tm mode for four lines covering the study area clearly map the steeply dipping mineralised ultramafic. Line 4 agrees with an earlier mag model carried out using Mag2dc. ....	147
Figure 10.18 - Smooth-model representation of the 2D a) Tm model, b) Te model, c) 2D vector model.....	148
Figure 10.19 – 3D representation of the 20 ohm-m iso-surfaces created from AMT resistivity data in grey integrated with the Micromine geology model of the tremolite schist in green. ....	148
Figure 10.20 – 3D representation of the 20 ohm-m iso-surface created from AMT resistivity data in grey integrated with the Micromine geology model of the well mineralised harzburgite in orange.....	149
Figure 10.21 – 3D representation of ultramafic sill (green), mineralised harzburgite (orange) AMT shell (grey), EM plates (yellow) and drillhole traces. ....	149

## LIST OF TABLES

<b>Table 2.1</b> – Ni-Cu-Sulphide ore mineral and host rock magnetic susceptibility in SI units x $10^{-3}$ . Adapted from King, 2007.....	11
<b>Table 3.1</b> – Ni-Cu sulphide ore minerals and host rock electrical resistivities (ohm-m). Adapted from King 2007.....	25
<b>Table 3.2</b> - The geometry and specifications used by SPECTREM during the airborne EM survey at Jacomynspan project.....	26
<b>Table 7.1</b> - Bulk susceptibility measurements of core samples for borehole JMP001 in SI units.....	57
<b>Table 7.2</b> – NRM results in A/m for each demagnetising field intensity measured in mT for the four specimens.....	60
<b>Table 7.3</b> – Normalised NRM values for the four specimens.....	60
<b>Table 7.4</b> – Koenigsberger Ratios for the four different specimens.....	64
<b>Table 9.1</b> – Waveform parameters used for fixed loop survey.....	120
<b>Table 9.2</b> – EM plate parameters for all the modelled Loop 1 lines.....	122
<b>Table 9.3</b> – Waveform parameters used for moving loop survey.....	125
<b>Table 9.4</b> – EM plate parameters for the modelled moving loop lines.....	126
<b>Table 9.5</b> – Waveform parameters used for DHEM survey.....	128
<b>Table 9.6</b> – EM plate parameters for modelling results for all the surveyed boreholes..	129

## CHAPTER 1: INTRODUCTION

The Jacomynspan Nickel-Copper (Ni-Cu) occurrence in the Northern Cape Province of South Africa is located 50km east of Kenhardt and 130km south of Upington the commercial centre of the region. It is located within the Namaqua Tectonic Province which is part of the Kibaran-aged (1400 – 950Ma) orogenic event. Following the period of intense Kibaran-aged deformation, the stabilisation of the continental crust in this area resulted in the deposition of younger sediments which partially obscure the older, underlying Namaqua rocks (Boelema, 1994). The mafic to ultramafic intrusive Ni-Cu sulphide bearing sill occurs on the farms Jacomynspan (176) and Hartebeestpan (175), approximately 15km west of Putsonderwater (Figure 1.1). The intrusion straddles both properties and has approximately an equal strike length of 2500m per property (Attridge, 1986).

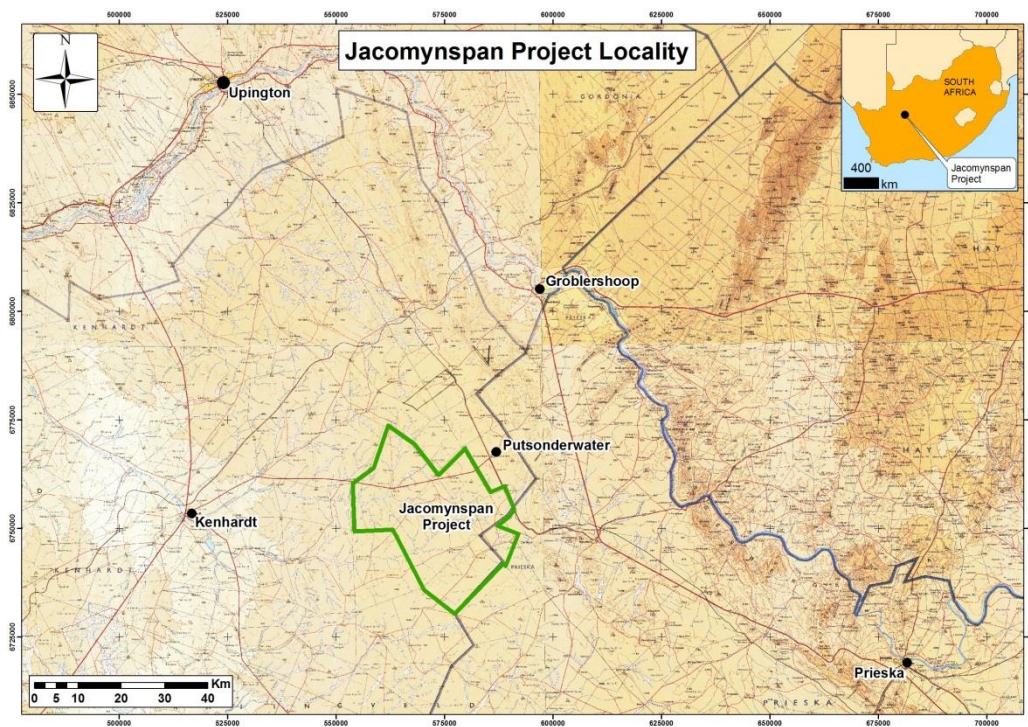


**Figure 1.1** - The Jacomynspan Project Locality Map.

The land that houses the occurrence is generally flat and undisturbed. Short grasses and shrubs occupy the land and little to no outcrop is present (Figure 1.2). This study will only focus on a small portion of the mineralised body located on the farm Jacomynspan that is currently being investigated by African Nickel Ltd.





**Figure 1.2** - Picture of the land within the study area which is generally flat and undisturbed. Short grasses and shrubs are observed and little to no outcrop is present.

Drilling done so far in the study area has shown that the sill is predominantly composed of tremolite schist (metamorphosed pyroxenite) containing lenticular bodies of harzburgite. The harzburgite generally hosts net-textured mineralisation with up to 50% of mineralisation by rock volume. Massive sulphide veins and stringers are occasionally present. The well mineralised harzburgite appears to occur in pods and therefore there is a need to use the acquired geophysical and geological datasets in order to derive a model of these harzburgite pods. In order to determine where such mineralized pods exist, geophysical techniques suited to detect such pods and their sulphide mineralization was applied. Fundamentally, geophysical methods measure a bulk physical parameter (e.g. density, magnetic susceptibility and resistivity) of the rock below surface non-invasively within its measurement cone of detectability, but are ambiguous in determining how rock entities displaying variations in such physical properties are distributed in the larger rock volume. Therefore, in using the different geophysical methods, it is essential that we use both geology and geophysics in integrated models to moderate the ambiguities, and the resulting models will guide further drilling. This study is therefore intended to assess the feasibility of using specifically electromagnetic (EM) methods in combination with the airborne magnetic data set and geology in obtaining a model of the distribution of well mineralised harzburgite pods hosted within the less conductive poorly mineralised ultramafic sill.

### **1.1 Brief discovery history and previous work**

According to Attridge (1986), the deposit was discovered by an airborne electromagnetic survey (INPUT) carried out on behalf of Anglo American Prospecting Services

(Proprietary) Limited over the Prieska – Kenhardt area in mid-1971. The conductive body was detected on a tie line only due to the unfavourable orientation of the flight lines relative to the sill. A subsequent airborne survey, using a McPhar 400 frequency domain electromagnetic system (FDEM), with flight lines at right angles to the strike of the body, clearly defined the zone of conductivity which had a total strike length of about 5000m. A significant magnetic anomaly essentially coincident with the EM conductor was also indicated. Following the initial discovery of the deposit, various ground geophysical survey methods were conducted in the area followed by soil sampling, detailed geochemistry, trenching and diamond drilling.

Anglo American completed a 'First Appraisal' study during 1974 that found that the project was not viable according to the economics and methodologies of the time. Subsequent to that, several other companies undertook more limited prospecting, but still were not successful in moving the project to development (Attridge, 1986). African Nickel Ltd, through an alliance agreement with Anglo American, had access to proprietary information that led to the conclusion that the prospect has potential for economic utilisation. Since a large drill dataset already existed, it was proposed to collect a new set of geophysical data using state-of-the-art electronics and techniques with the aim being to guide drilling and detect the better mineralized parts of the deposit.

## **1.2 Geology of the Area**

The study area is located within the Namaqua-Natal Mobile Belt. The rocks have been subjected to intense tectonic activity and metamorphism (Attridge, 1986). Attridge (1986) described the Ni-Cu mineralisation at Jacomynspan project as being hosted within a steeply dipping tabular, differentiated, sill of mafic to ultramafic composition intruded into country rocks of the Namaqualand Metamorphic complex. These country rocks comprise a sequence of porphyroblastic quartz-feldspar-biotite-garnet gneiss containing minor metadiorite and amphibolite lenses. Attridge (1986) also describes the presence of sillimanite and andalusite in the porphyroblastic gneiss which infers an amphibolite facies grade of regional metamorphism.

The sill has an east-west trending curvilinear surface (according to geophysics since there is no outcrop) expression and dips at  $65^{\circ}$  –  $70^{\circ}$  to the south. It has been intersected by drill holes down to a vertical depth of 900m. It is predominantly composed of poorly mineralised tremolite schist (metamorphosed pyroxenite) containing lenticular bodies of well-mineralised harzburgite with occasional massive sulphide veins and stringers. The sulphide minerals are a typical magmatic assemblage of pyrrhotite, chalcopyrite and pentlandite with pentlandite being the main nickel bearing mineral (Attridge, 1986).

### **1.3 Geophysics**

#### **1.3.1 Geophysical Methods**

The successful application of geophysics depends on contrasting physical properties between the host rock and the target and also the selection of a suitable geophysical technique. It has been stated earlier that the Jacomynspan Ni-Cu sulphide mineralisation is composed mainly of an assemblage of pyrrhotite, pentlandite, and chalcopyrite. These magmatic Ni-Cu sulphide deposits are usually anomalous in most physical properties including electrical conductivity, chargeability, density, magnetic susceptibility, natural radioactivity and acoustic velocity (King, 2007). Whether mapping lithologies or logging drill core or chips during a geological exploration programme, the need to take magnetic susceptibility measurements cannot be over emphasised (Schmidt and Lackie, 2013).

Physical property studies (relative conductivity and magnetic susceptibility) carried out on Jacomynspan drill core by the author indicates that the country gneissic rocks are not conductive and have a relatively low magnetic susceptibility. The well mineralized net-textured harzburgite has elevated values of magnetic susceptibility and relative conductivity compared to the poorly mineralized tremolite schist host rock. Laboratory palaeomagnetic measurements were also carried out at the Council for Geosciences in Pretoria by the author. Bulk susceptibility measurements as well as Natural Remanent Magnetism (NRM) also referred to as 'frozen in' or 'fossil magnetism' were carried out on core specimens because magnetic remanence should always be considered when interpreting magnetic anomalies in mineral exploration.

The three basic platforms for geophysical methods – airborne, ground and borehole were applied at the study area with the author being part of the individual survey teams. These geophysical methods include ground magnetics, airborne magnetics and radiometrics (carried out by Xcalibur Geophysics), airborne electromagnetics (carried out by SPECTREM Air), ground electromagnetics (moving loop and fixed loop using the SQUID sensor), downhole electromagnetics (DHEM), and finally audio-frequency magnetotellurics (AMT) surveys performed in-house by African Nickel-Anglo American staff. All the datasets for these methods were available to the author and have been used for this study.

#### **1.3.2 Geophysical Inversion Modelling**

Inversion modelling is a process used to find the most likely distribution of a physical property that causes a set of physical measurements recorded in a field survey with or without additional constraints. It enables resource explorers to get a better understanding of geophysical measurements into images mapping the subsurface that can be integrated with other surface and subsurface geological observations (Long and Fischer, 2013).

Since the Jacomynspan Ni-Cu sulphide deposit has a coincident magnetic and EM response, Geosoft's VOXI Earth Modelling software was used to model the high resolution airborne magnetic data for this study. VOXI is a Geosoft® geophysical inversion software service that can generate 3D voxel models from airborne or ground gravity and magnetic data using cloud computing (Geosoft, 2013). Cooper's Mag2dc ([www.wits.ac.za](http://www.wits.ac.za)) and E Stettler's Madmodintrap software (personal communication, 2015) was also used during modelling of the magnetic data to compliment the modelling from VOXI.

The dominant physical property for the inductive EM methods used in this study is electrical conductivity which represents the ease of ability of electric charges to move inside matter. As shown by the conductivity measurements taken on borehole JMP001 drill core, there is a very large contrast in conductivity between the well mineralised harzburgite and the host rocks. Since the conductivity of the well mineralised harzburgite is much higher than the surrounding rocks, it produced a strong anomalous EM response. The aim of geophysical interpretation with this dataset is to invert the measured EM data into knowledge about the spatial distribution of conductivity below surface, and to use that information in augmenting the extrapolation of geological information between the different boreholes. ElectroMagnetic Imaging Technology's® (EMIT) Maxwell Electromagnetic software was used in the modelling of all the ground EM data and Downhole Electromagnetics (DHEM) data. It provides fast forward iterative modelling of single and multiple conductors (dipping plates) in free space or with simple flat overburden sheets.

All Audio-frequency Magnetotelluric (AMT) data processing and inversion for this study were carried out using a combination of Zonge® internal software and Geosoft for mapping products. The aim of processing AMT/MT data is to image the subsurface distribution of conductors at depth. This is a multistage process in which Cagniard Resistivity (a frequency-dependent apparent resistivity calculation) and Impedance Phase data are calculated from electric **E**-field and magnetic **H**-field data (Zonge, 2010). The phase difference between the **E** and **H** components of the electromagnetic field is defined as the Impedance Phase. Both Cagniard resistivity and Impedance phase were used in Zonge 1-D and 2-D inversion models to image actual resistivity changes associated with geology (Zonge, 2010).

#### **1.4 Goals of the Dissertation**

Magmatic Ni-Cu sulphide deposits are usually anomalous in most physical properties including electrical conductivity and magnetic susceptibility. In EM prospecting, the properties of Ni-Cu sulphide are essentially the properties of pyrrhotite which is usually

the dominant mineral. This study attempts to take advantage of the physical properties contrast (conductivity and magnetic susceptibility) to delineate and map the high grade harzburgite that appears to occur in pods hosted within a relatively less conductive, poorly mineralised Jacomynspan ultramafic sill using various EM (TDEM and FDEM) and other geophysical and geological datasets.

Geological information was incorporated via the model objective function. The geological model and the associated physical property values were combined to make a reference model  $m_{ref}$ . This model represents our best guess *a priori* model for the true distribution of the physical property distribution. During the inversion process, we attempt to find a model (the most likely distribution of properties) that has an associated EM and magnetic signature that fits the measured data best and is also still close to the reference model  $m_{ref}$ .

Specifically the aims of this work are:

- i) Comparison of the software algorithm known as VOXI, being part of the Geosoft® suite of commercial geophysical software modules, against building a 3D model in the traditional way where the regional field is first determined along a number of profiles. An integrated regional field over a wider area is then constructed, followed by forward modelling of a geologically feasible model along the selected profiles. These models along profiles are then made into a 3D 'starter model', followed by further refinement using a subsequent 3D inversion technique which can include VOXI.
- ii) Determining the physical parameters of the different rock types in the study area.
- iii) Presenting an integrated geological-geophysical subsurface model where due cognisance has been given to all geological and geophysical data sets and the constraints they impose on the model.

## 1.5 Dissertation Structure

Chapter 1 gives an introduction to the dissertation outlining the aims and goals of the intended research project. It gives a brief introduction to the geology of the area as well as the geophysical methods used in the acquisition of the data. Chapters 2 to 5 present and discuss a literature review of all the geophysical methods used to collect field data for this research. A brief description of the instruments used, survey design used for the application of the different techniques of geophysical data collection including quality control, and how the data were processed is covered in these chapters with each chapter dedicated to an individual technique.

Chapter 6 describes the various ways of geophysical data enhancement with the focus mainly on magnetic data. This process makes use of a number of linear and non-linear filtering algorithms that can selectively enhance different anomalies due to one group of geological sources relative to signatures due to other groups of geological sources (World Wide Science, 2014). Emphasis is placed on the principles behind the enhancements and the usefulness of the enhancements in the interpretation of the data.

Chapter 7 discusses the different geophysical and geological data sets used in construction of a final realistic model. These datasets include magnetics (airborne and ground), electromagnetics (TDEM airborne and ground), downhole TDEM, Audio frequency Magnetotellurics (FDEM technique) and borehole geological data from drilling. Palaeomagnetic laboratory procedures carried out on core samples at the Council for Geoscience in Pretoria and are also outlined.

Chapter 8 considers the theory of geophysical inversion modelling while Chapter 9 presents the actual modelling of the geophysical data. Geosoft's VOXI® inversion modelling software as well as Cooper's Mag2dc ([www.wits.ac.za](http://www.wits.ac.za)) and E Stettler's Magmodintrap software (personal communication, 2015) were used in the modelling of the high resolution aeromagnetic data. EMIT's (Electromagnetic Imaging Technology) Maxwell® software was used in the modelling of ground EM data as well as Downhole Electromagnetic data (DHEM). All the Audio-frequency Magnetotelluric (AMT) data processing and inversion for this study were carried out using a combination of Zonge® software and Geosoft® for mapping products.

Chapter 10 considers data integration and interpretation of the modelling results. Finally Chapter 11 concludes the dissertation with a brief summary of the research work and what has been achieved and suggestions for further work.

## CHAPTER 2: METHOD – GROUND AND AIRBORNE MAGNETICS

### 2.1 Introduction

Magnetic methods are integral to modern mineral exploration, usually providing the starting point for explorers. Information regarding structure and lithologies of the subsurface can be obtained by taking measurements of the total magnetic field on surface using a magnetometer (Cooper, 1997). This chapter gives a brief summary of the basic principles of magnetic surveying, and also the basic operation of the Geometrics G856 instrument that was used during the acquisition of ground magnetic data. The specifications of the parameters used for the aeromagnetic survey carried out by Xcalibur Airborne Geophysics will be provided. Survey design and data reduction will be covered later in this chapter.

Both airborne and ground magnetic surveys were carried out over the study area. The ground magnetic survey carried out by the author covered a smaller part focusing mainly on the study area while the airborne survey, because it is much more cost effective and faster, covered a larger region including the study area. The aim of the magnetic survey attempted to map the sub-outcrop of the east-west trending ultramafic rocks over the main target and also to better understand the structure and setting of the intrusion. The fact that the vector magnetic field  $\mathbf{B}$  has an inverse-cubed ( $\mathbf{B} \propto r^{-3}$ ) distance relationship with the source (i.e. for a dipole source), anomalies measured during an aeromagnetic survey have lower amplitude and longer wavelength responses relative to the same anomalies measured with ground surveys, which have larger amplitude, shorter wavelength responses (Coomber, 2008).

#### 2.1.1 Basic Concepts

The Earth's magnetic field can be approximately represented by a bar magnet (Kearey *et al.*, 2002). Within the vicinity of a bar magnet, a magnetic flux is present which is schematically represented by magnetic field lines extending from one end of the magnet to the other (Figure 2.1).

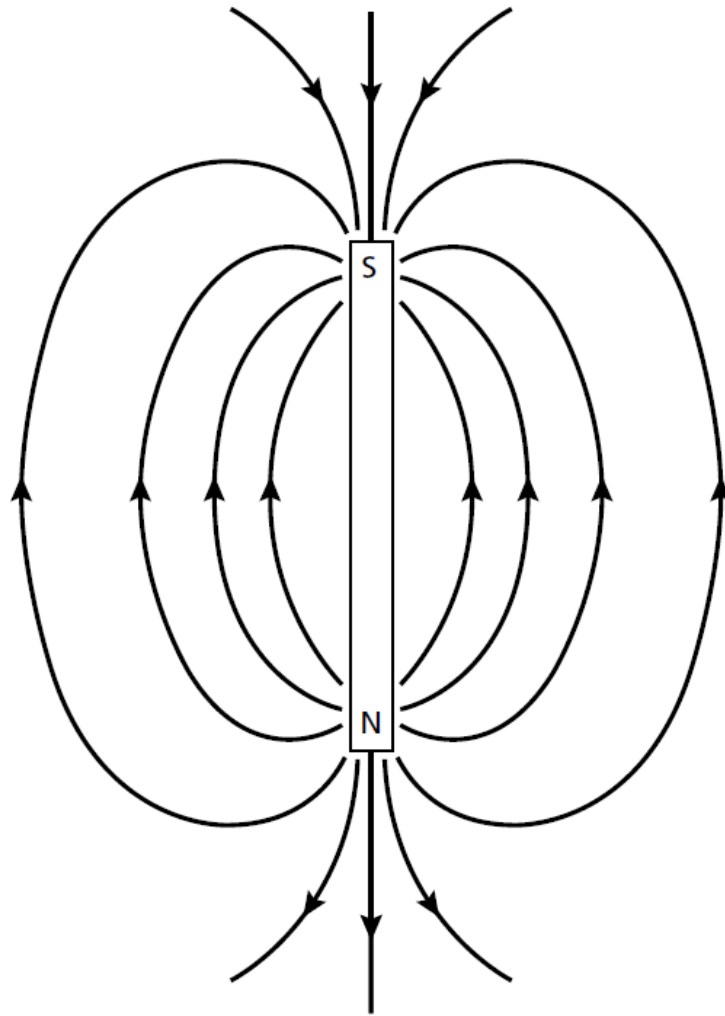


**Figure 2.1-** The magnetic flux lines surrounding a bar magnet representing the Earth's magnetic field.

If we place a material in this magnetic field it may acquire a magnetization in the direction of the bar magnet's magnetic field which commonly is lost when the material is removed from the field. This phenomenon is referred to as induced magnetisation or magnetic polarisation, and results from the alignment of dipoles within paramagnetic material in the direction of the field (Kearey *et al.*, 2002). The induced intensity of magnetisation  $\mathbf{J}_i$  is proportional to the strength of the magnetizing force  $\mathbf{H}$  of the inducing field:

$$\mathbf{J}_i = k\mathbf{H} \quad (2.1)$$

where  $k$  is the magnetic susceptibility of the material which is dimensionless since  $\mathbf{J}_i$  and  $\mathbf{H}$  are both measured in  $\text{Am}^{-1}$ .

Magnetic susceptibility  $k$  is the fundamental rock property defined as the ability of a material to be magnetized (Telford *et al.*, 1990). A rock's magnetic susceptibility is primarily dependent on the amount of ferrimagnetic minerals like magnetite present in the



rock. Virtually all the minerals responsible for the magnetic properties of common rock types are ferrimagnetic (Kearey *et al.*, 2002).

### 2.1.2 Magnetism of Rocks and Minerals

Magnetization of rocks is usually acquired due to polarisation from the Earth's field with a few rare exceptions where the magnetisation results from lightning. This polarisation is usually of induced type and its magnitude and direction are determined entirely by the magnitude and direction of the Earth's field as it is today (Dobrin and Savit, 1988).

According to Kearey *et al.*, (2002), most of the rock-forming minerals exhibit a very low magnetic susceptibility and most rocks' magnetic character is due to the generally small proportion of magnetic minerals they contain. There are only two main geochemical groups which provide such minerals namely the iron-titanium-oxygen and the iron-sulphur groups. The iron-titanium-oxygen group is a solution series of magnetic minerals from magnetite ( $\text{Fe}_3\text{O}_4$ ) to ulvospinel ( $\text{Fe}_2\text{TiO}_4$ ); with the other common iron oxide, haematite ( $\text{Fe}_2\text{O}_3$ ) being antiferromagnetic does not exhibit magnetic properties. The second group, is the iron-sulphur group with pyrrhotite ( $\text{FeS}_{1+x}$ ,  $0 < x < 0.15$ ) whose magnetic susceptibility is dependent upon the actual composition. However, magnetite is by far the most common magnetic material in rocks (Kearey *et al.*, 2002).

Due to their relatively high magnetite content, basic igneous rocks are usually more magnetic than acidic igneous rocks. The proportion of magnetite in igneous rocks depends on the acidity of the rock, decreasing with increasing acidity. Although acid igneous rocks vary in their magnetic behaviour, they are usually less magnetic than basic rocks. Sedimentary rocks are however effectively non-magnetic unless they contain significant amounts of magnetite in the heavy mineral fraction (Kearey *et al.*, 2002).

Ni-Cu sulphide deposits and their usual host mafic and ultramafic rocks are frequently magnetic but not always. The physical properties of Ni-Cu sulphide ores are dominated by pyrrhotite, which is moderately magnetic in its monoclinic form but is essentially non-magnetic in its hexagonal form (such as at Voisey's Bay deposit) (King, 2007). King (2007) compiled a list of the magnetic susceptibilities in SI units for the Ni-Cu sulphide ore minerals and host rocks as shown in Table 2.1. This magnetic variability in pyrrhotite's magnetic properties is important for exploration but it can also be a disadvantage for mineral processing where magnetic separation is sometimes used to separate magnetic pyrrhotite from the non-magnetic economic sulphides pentlandite and chalcopyrite (King, 2007).

**Table 2.1** – Ni-Cu-Sulphide ore mineral and host rock magnetic susceptibility in SI units  $\times 10^{-3}$ . Adapted from King, 2007.

<b>Rock Types</b>	<b>Range</b>	<b>Average</b>	<b>Reference</b>
<b>Sulphides/oxides</b>			
Pyrrhotite	1 - 6000	1500	Telford <i>et al.</i> , 1990
Pyrrhotite (mono)		700	Emerson <i>et al.</i> , 2001
Pyrrhotite (hex)		2	Emerson <i>et al.</i> , 2001
Pentlandite		<1	Emerson <i>et al.</i> , 2001
Chalcopyrite		0.7	Telford <i>et al.</i> , 1990
Magnetite	1200 - 19200	6000	Telford <i>et al.</i> , 1990
<b>Host Rocks</b>			
Felsic Igneous	0 - 80	8	Telford <i>et al.</i> , 1990
Mafic Igneous	0.5 - 97	25	Telford <i>et al.</i> , 1990
Ultramafic rocks (Peridotite)	90 - 200	150	Telford <i>et al.</i> , 1990
Ultramafic rocks (Serpentinite)	Mod - high	Mod - high	

The mafic and ultramafic host rocks are usually but not always magnetic. For example, the host rocks for the Ni-Cu sulphide at Voisey's Bay deposit, non-magnetic troctolites and ultramafic rocks can have variable magnetism depending on the degree of serpentinization (King, 2007). Jacomynspan Ni-Cu sulphide deposit has a coincident magnetic and EM response which means the dominant sulphide pyrrhotite is magnetic. Therefore magnetism is an important aspect of this study.

### 2.1.3 The Geomagnetic field

Magnetic anomalies caused by rocks are localised effects superimposed on the normal magnetic field of the earth which is the geomagnetic field also referred to as the regional field. Therefore knowledge of the behaviour of the geomagnetic field is necessary both in the reduction of the data to a suitable datum and in the interpretation of the resulting anomalies. The geomagnetic field is geometrically more complex when compared to the gravity field of the earth as it exhibits irregular variations in both inclination and magnitude with latitude, longitude and time (Kearey *et al.*, 2002) as shown in Figure 2.2.

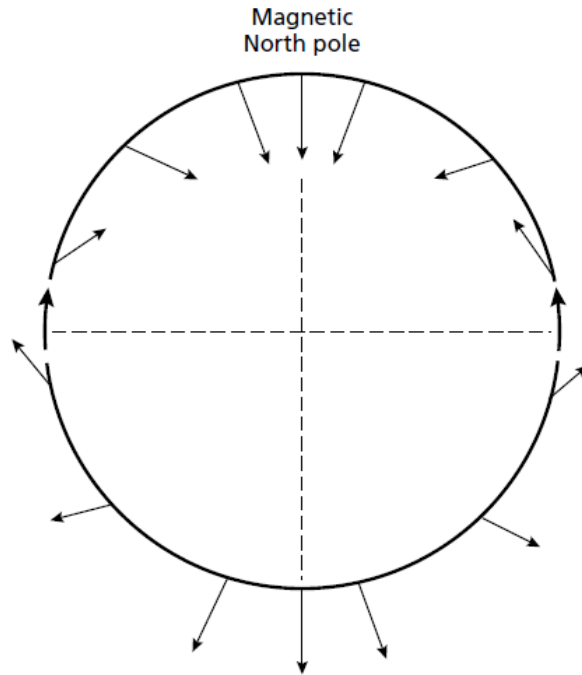


**Figure 2.2** - The variation of the inclination of the total magnetic field with latitude based on a simple dipole approximation of the geomagnetic field. (Sharma, 1976).

If we freely suspend a magnetic needle at any point on the earth's surface it will assume a position in space in the direction of the ambient geomagnetic field. In order to describe the magnetic field vector, we can make use of descriptors known as the geomagnetic elements as shown in Figure 2.3.

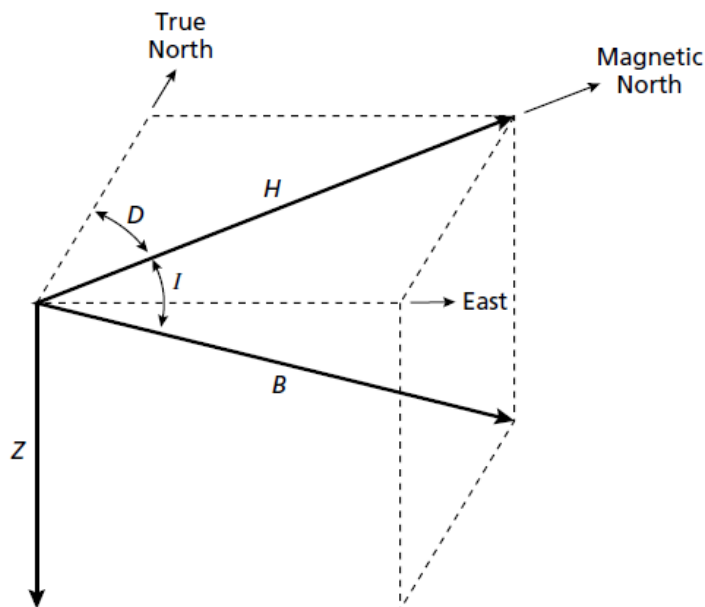


**Figure 2.3** - The geomagnetic elements (Kearey *et al.*, 2002)

The total field vector  $\mathbf{B}$  has a vertical component  $\mathbf{Z}$  and a horizontal component  $\mathbf{H}$  in the direction of the magnetic north. The dip of  $\mathbf{B}$  is the inclination  $I$  of the field and the

horizontal angle between geographic and magnetic north is the declination **D**. **B** varies in strength from about 25 000nT in equatorial regions to about 70 000nT at the poles (Kearey *et al.*, 2002).

The magnetic field in the northern hemisphere generally dips downwards towards the north and becomes vertical at the north magnetic pole. In the southern hemisphere the dip is generally upwards towards the north but by convention is considered negative. The line of zero inclination approximates the geographic equator, and is known as the magnetic equator (Kearey *et al.*, 2002).

According to Kearey *et al.*, (2002), the geomagnetic field cannot result from permanent magnetism in the Earth's deep interior. The required dipolar magnetic moments are far greater than is considered realistic and also the prevailing high temperatures far exceed the Curie temperature (temperature where a material loses its magnetic properties) of any known magnetic material. The cause of the geomagnetic field is attributed to a dynamo action produced by the circulation of charged particles in coupled convective cells within the outer, fluid, part of the Earth's core.

#### 2.1.4 Induced and remanent magnetization

Induced magnetization in rock is a response to the ambient geomagnetic field and is equal to the product of the magnetic susceptibility and the inducing field strength which is essentially along the regional geomagnetic field direction (Austin *et al.*, 2013). According to Dobrin and Savit (1988), the magnetic poles induced in a material by an external field **H** will produce a field of their own, **H'**, which is related to the intensity of magnetization **I** by:

$$H' = 4\pi I \quad (2.2)$$

The total magnetic flux inside the material, as measured in a narrow cavity having an axis perpendicular to the field, is called the magnetic induction **B**. This is the sum of the external and the internal fields and is proportional to the external field strength in moderately magnetic materials, as shown by the relation

$$\begin{aligned} B &= H + H' = H + 4\pi I = H + 4\pi kH \\ &= (1 + 4\pi k)H = \mu H \end{aligned} \quad (2.3)$$

Where **k** is magnetic susceptibility

The proportionality constant  $1+4\pi k$  is referred to as the permeability **μ** and can therefore be written as

$$\mu = \frac{B}{H} = 1 + 4\pi k \quad (2.4)$$

Permeability is a measure of the modification by induction of the force of attraction or repulsion between two magnetic poles and its magnitude depends on the magnetic properties of the medium in which the poles are immersed (Dobrin and Savit, 1988).

Some magnetic rocks display what is referred to as remanent or ‘fossil’ magnetism which is not related to the present Earth’s field but is governed instead by the field that existed when the rock was formed. Remanent magnetisation is a more-or less permanent magnetisation present in the rock, i.e. it is not induced by the earth’s field, but is retained in the rock over geological time spans by fine-grained particles of minerals such as magnetite, pyrrhotite and hematite (Austin *et al.*, 2013). If the rock is igneous, its direction of magnetization will be that of the Earth’s field at some time after it solidified and just before it cooled down through the Curie point. This is referred to as thermo-remanent magnetization. If the rock is sedimentary, any orientation of its magnetic grains during deposition, generally in still water, would have been in alignment with the field that existed when the deposition occurred and is referred to as depositional remanent magnetization (Dobrin and Savit, 1988).

The remanent and induced magnetisation combines in a vector fashion, but the induced field is generally of much greater magnitude. The Koenigsberger ratio (**Q**) is the ratio of the remanent to the induced magnetisation for a particular rock (Cooper, 1997). It is given by:

$$Q = \frac{J}{kH} \quad (2.5)$$

where **J** is the remanent magnetisation in the rock (NRM), **k** is the magnetic susceptibility and **H** is the induced/local magnetisation.

At Jacomynspan, the local geomagnetic field is presently around 26,800nT. In general, the Koenigsberger ratio is used as a measure of stability to indicate a rock's capability of maintaining a stable remanent magnetisation. A low value of the Koenigsberger ratio indicates that minerals have unstable remanent magnetisation and are more susceptible to an external magnetic field (i.e. Induced) (Letts, 2007). Magnetic remanence should always be considered when interpreting magnetic anomalies in mineral exploration. Failing to account for remanence in magnetic modelling and inversion may result in a misinterpretation of the dip of a magnetic body.

### 2.1.5 Magnetic Anomalies

All magnetic anomalies caused by rocks are superimposed on the geomagnetic field in the same way that gravity anomalies are superimposed on the Earth's gravitational field (Kearey *et al.*, 2002). However, the magnetic case is more complex since the geomagnetic field varies both in amplitude and direction whereas the gravitational field is always vertical. The main causes of magnetic anomalies in the Earth's magnetic field are due to dykes, faults and lava flows. These anomalies are usually due to induced or remanent magnetism with the induced field usually being the most dominant. Induced magnetic anomalies are the result of secondary magnetization induced in a ferrous body by the Earth's magnetic field. The shape, dimensions, and amplitude of an induced magnetic anomaly is a function of the orientation, geometry, size, depth, and magnetic susceptibility of the body as well as the intensity and inclination of the Earth's magnetic field in the survey area (Mariita, 2007) as shown in Figure 2.4. While remanent magnetization is an intrinsic property of a geological unit, it is the resultant magnetisation vector that determines the shape and amplitude of the measured magnetic anomaly over the target (Pratt *et al.*, 2012).

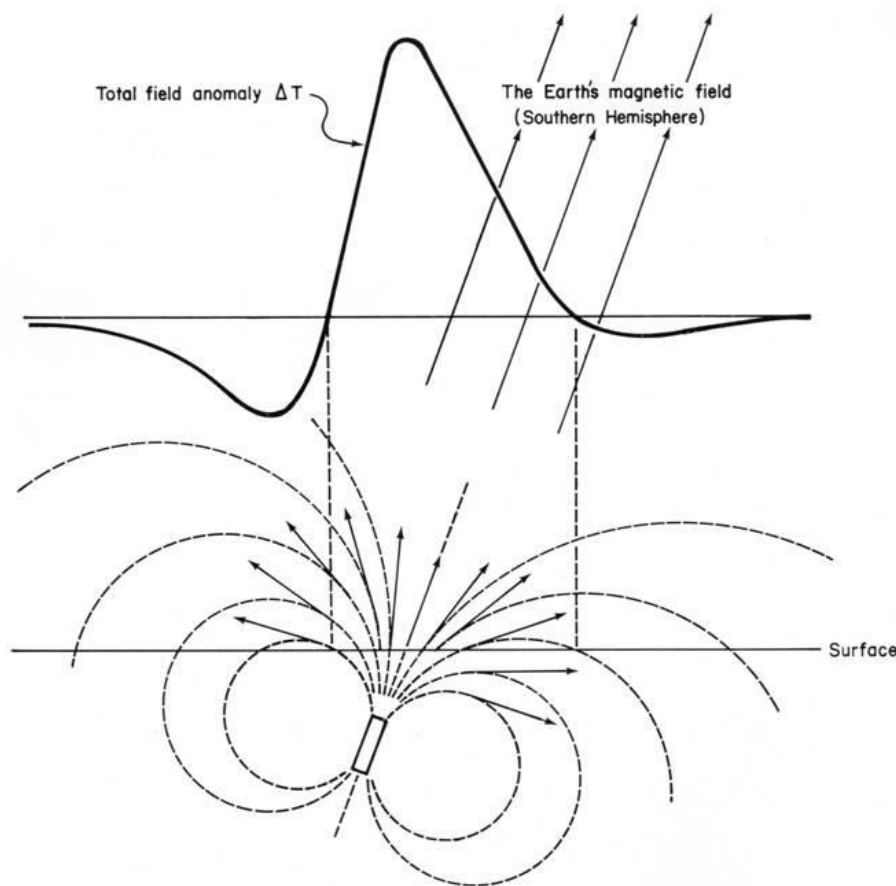


**Figure 2.4** - North-South schematic profile of a magnetic anomaly over a magnetic dyke with a dipolar effect. The dyke is striking E-W and situated in the southern hemisphere (Roux, 1980).

All magnetic anomalies are dipolar i.e. they have a high and low with the magnetic latitude affecting the size and location of the magnetic high and low. In the southern hemisphere the high is located over the northern and north-western perimeter of a magnetic body and the low over the southern and south-eastern perimeter of a normally induced magnetic body. The reason for this is that a commonly used magnetometer just measures the overall intensity of the field at any one point which is referred to as the total field irrespective of the earth's magnetic vector angle at the measurement location. The effect of the vector angle is to change the polarity of the anomaly (size and location of high and low).

#### 2.1.6 Diurnal Variations and Magnetic storms

Magnetic effects of external origin cause the geomagnetic field to vary on a daily basis to produce what is referred to as diurnal variations (Figure 2.5). Under normal conditions i.e. on quiet days, the diurnal variation is smooth and regular and has an amplitude variation of about 10-80 nT over 24 hours, being at a maximum in polar regions. These variations are caused by a magnetic field induced by the flow of charged particles within the ionosphere towards the magnetic poles. These diurnal variations can be easily removed from the acquired data by making use of a base station magnetometer taking readings regularly in an area of low magnetic gradient.

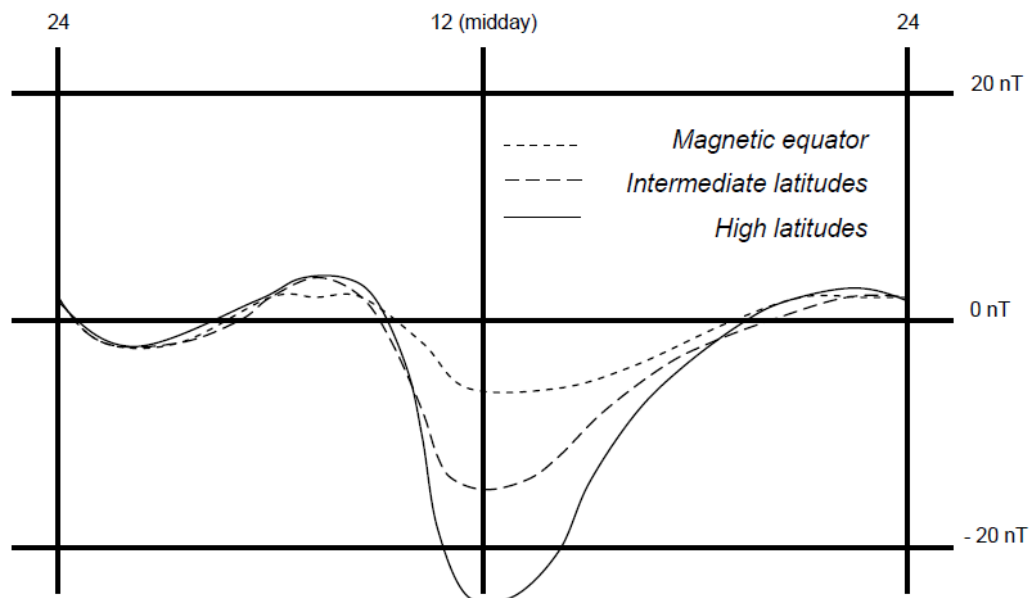


**Figure 2.5** - Schematic diurnal variation, showing the vertical component of the magnetic field through a 24 hour period at varying magnetic latitudes (Roux, 1980).

Magnetic storms on the other hand are caused by solar flares, where increased, irregular amounts of plasma are ejected towards the Earth. This violent interaction with the ionosphere causes irregular variations in the geomagnetic field (Figure 2.6), with

amplitudes of up to 1000 nT (Telford *et al.*, 1990). Magnetic surveys should be suspended during such storms because it is impossible to correct the data collected for the rapid and high-amplitude changes in the magnetic field.

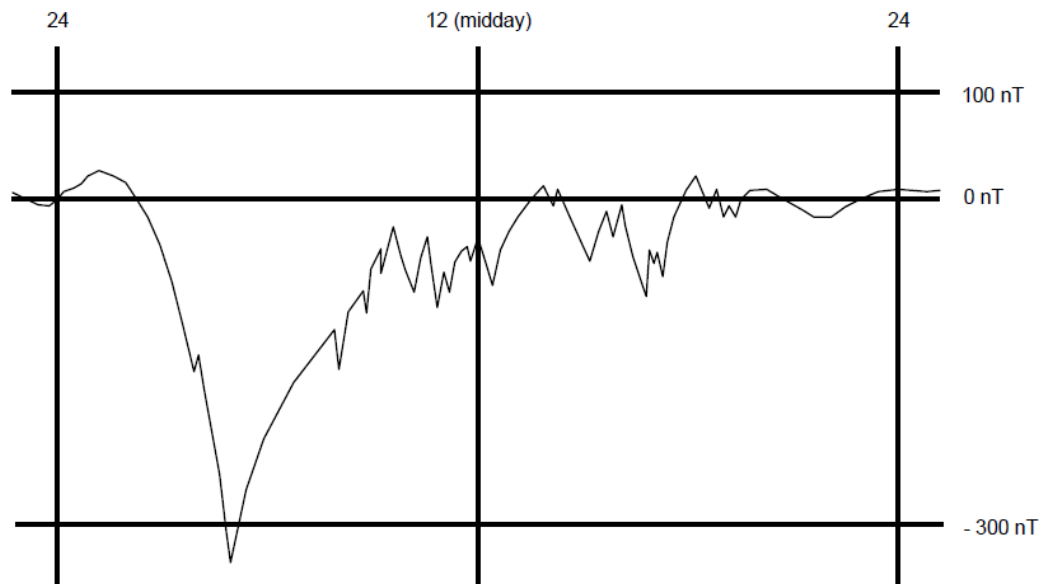


**Figure 2.6** - Schematic magnetic storm, showing the vertical component of the magnetic field. Note the erratic nature of the field and the change in scale as compared to diurnal variation from Figure 2.5 (Coomber, 2008).

## 2.2 Aeromagnetic survey

A high resolution aeromagnetic survey (1496 line-km) was carried out by Xcalibur Airborne Geophysics at Jacomynspan project covering the main target zone during June 2011. The line spacing was 30m flown at a nominal terrain clearance of 30m. The survey area was divided into three blocks flown with different line orientations due to the anticipated strike changes in geology. The purpose of the survey was to attempt to delineate the east-west trending ultramafic rocks over the main target zone and to infer the nature of the structure and setting of the deposit. The specifications for the survey parameters were as follows:

- Aircraft type: Airtractor
- Average aircraft speed: 120km/h
- Survey navigation: AgNav
- Data acquisition: XAGDAS
- Data positioning: Real time differential GPS
- GPS type: 2100LR, 12 channel, Omnistar DGPS
- Magnetometers: 2 x Geometrics G8223A Caesium Vapour
- Magnetometer cycling time: 10Hz resampled at 5Hz
- Compensation: RMS AARC500
- Resolution: 0.001 nT



- Laser/Radar altimeters: Optech/King
- Base station magnetometers: Geometrics G856
- Ground clearance: 30m (hazard dependant)
- Line Spacing: 30m
- Tie Line spacing: 300m
- Sample spacing: 7m

### 2.3 Ground Magnetic Survey

A ground magnetic survey was carried out by the author over the main target zone covering an area approximately 1km x 1km.

#### 2.3.1 Instruments for Ground Magnetic Survey

The ground magnetic survey was carried out using two Geometrics G856 magnetometers with one being used as the roving magnetometer and the other as a base station. A hand held Garmin GPS was used for navigation.

#### 2.3.2 Geometrics G856 Proton Precession Magnetometer

A Geometrics G856 magnetometer is a proton precession magnetometer. According to Telford *et al.*, (1990), the sensor of the proton magnetometer is a container filled with a liquid rich in hydrogen atoms, such as kerosene or water surrounded by a coil. The hydrogen nuclei (protons) act as small dipoles and normally align parallel to the ambient geomagnetic field  $\mathbf{B}_e$ . A current is passed through the coil to generate a magnetic field  $\mathbf{B}_p$  which is 50–100 times larger than the geomagnetic field, and in different direction causing the protons to realign in this new direction. The current to the coil is then switched off so that the polarizing field is rapidly removed. The protons return to their original alignment with  $\mathbf{B}_e$  by precessing, in phase around this direction with a period of about 0.5ms taking some 1-3 s to achieve their original orientation. The frequency  $f$  of this precession is given by

$$f = \frac{\gamma B}{2\pi} \quad (2.6)$$

where  $\gamma$  is the gyromagnetic ratio of the proton, an accurately known constant.

Measurement of  $f$  provides a very accurate measurement of the strength of the total geomagnetic field  $\mathbf{B}$ . The precessing frequency  $f$  is determined by measurement of the alternating voltage induced in the surrounding coil by the precessing protons (Kearey *et al.*, 2002).

### 2.3.3 Ground Magnetic Survey Design

A total of 27 lines measuring 1.15km at 50m line spacing were planned for ground magnetic survey using two Geometrics G856 magnetometers over the main target area (Figure 2.7). One of the magnetometers was used as a rover collecting data at every 10m along the lines and the other was set up to monitor the diurnal variations every 30 seconds in an area of low magnetic field gradient close to the survey area. The grid was established using a Garmin hand held GPS.

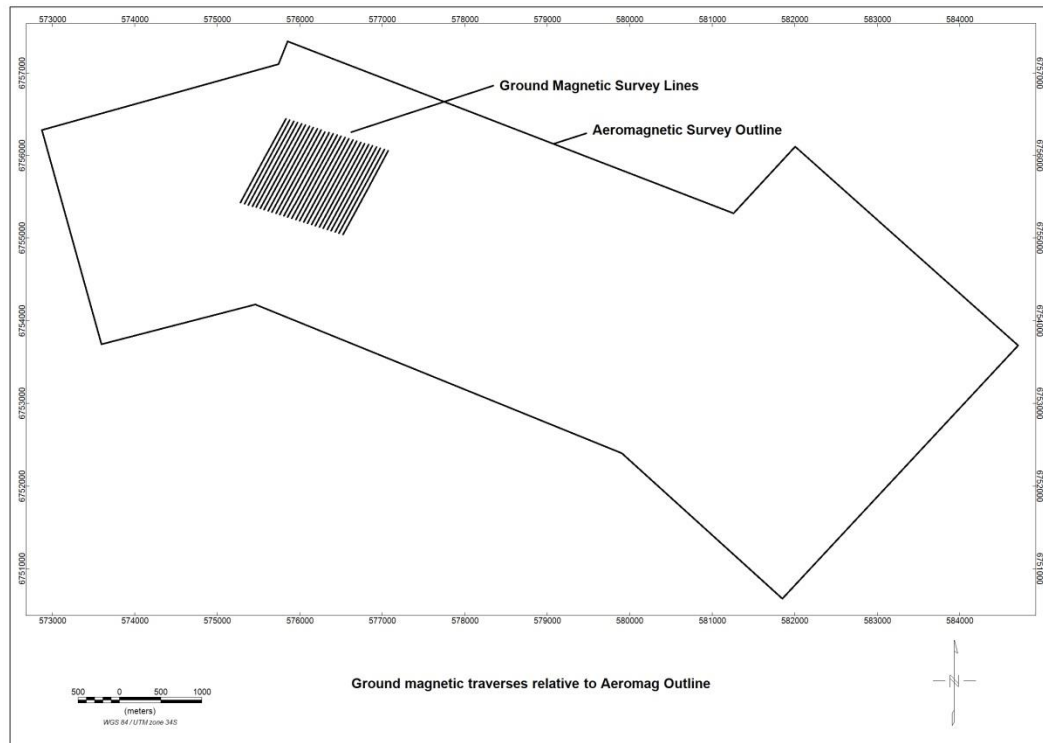


**Figure 2.7** - Ground magnetic traverses covering the study area relative to aeromagnetic survey outline.

### 2.3.4 Quality control

Base station data were checked at the end of each survey day to ensure that the diurnal variation was smooth and within range (i.e. varying between 10 – 80 nT) and that no magnetic storms occurred during the survey. Coordinates of all cultural objects affecting readings like fences and large metal objects were recorded using the hand held GPS (there are no power lines in the area). These readings associated with culture effects were removed from the database by filtering.

## **2.4 Data Processing**

### **2.4.1 Ground Magnetic Survey Data Processing**

Data from both the roving and base station G856 magnetometers were downloaded to a computer using the MagMap2000 software at the end of each survey day. The data were saved as two separate databases indicating the roving data and the base station data. Once the data downloading process was complete, the data were displayed and diurnal corrections could then be applied in MagMap2000 to produce the corrected final dataset. The base station data was analysed to see if the diurnal variations are within range (usually not more than 20nT over 20 minutes) and also whether any magnetic storms occurred. The diurnally corrected readings are allocated the correct coordinates projected as WGS84 South African Grid LO21. The data were then ready for further manipulation using Geosoft Oasis Montaj.

### **2.4.2 Aeromagnetic Survey Data Processing**

The aeromagnetic data were collected and processed by Xcalibur Airborne Geophysics using their in-house software and Geosoft Oasis Montaj. Their infield processing sequence was as follows:

- Downloading and backup of binary data.
- Verification of flight path.
- Verification of compensated magnetic data.
- Verification of altimeter and DGPS data.
- Verification of sample density.
- Verification of Digital Terrain Model (DTM).
- Verification of Diurnal Magnetic Field.

The final dataset was then supplied as a Geosoft database for further manipulation.

## CHAPTER 3: METHOD – GROUND AND AIRBORNE ELECTROMAGNETICS

### 3.1 Introduction

This chapter covers the theory of electromagnetics (EM) as applied to geophysical prospecting. Survey design for ground EM surveys for both moving loop and fixed loop modes will be given. The parameters used by SPECTREM® Air Limited to carry out an airborne EM survey will be provided. The instruments used in the ground EM survey are described as well as the theory behind the operation of the SPECTREM system. Processing of the EM data will be covered towards the end of the chapter.

The Airborne Electromagnetic (AEM) survey carried out by SPECTREM® Air Limited covered the whole license area. These data were useful in delineating the whole Jacomynspan intrusion and also to identify other potential targets within the license area. Ground EM surveys were then carried out in order to try to delineate zones of the better mineralised harzburgite which is highly conductive compared to poorly mineralised tremolite schist. Both loop modes (moving and fixed) were applied at the main target zone.

#### 3.1.1 Basic Theory of Electromagnetics Surveying

According to Pirttijarvi (2003), in EM surveying the two measurable components of EM fields are the electric and magnetic fields, which are functions of spatial position (x,y,z in a rectangular coordinate system) and time t (s), or frequency f (Hz or angular frequency,  $\omega = 2\pi f$ ). Maxwell, (1831) unified electricity and magnetism into an electromagnetic theory describing their behaviour and inter-relationship. The behaviour of the EM fields is traditionally described by equations, which in the time or frequency-domain can be expressed as:

$$\nabla \times \mathbf{H} = \mathbf{J} + \frac{\partial \mathbf{D}}{\partial t} \quad \text{Ampere's Law with Maxwell's term} \quad (3.1)$$

$$\nabla \times \mathbf{E} = -\frac{\partial \mathbf{B}}{\partial t} \quad \text{Faraday's Law} \quad (3.2)$$

$$\nabla \cdot \mathbf{B} = 0 \quad \text{Gauss' Law for magnetic field} \quad (3.3)$$

$$\nabla \cdot \mathbf{D} = \mathbf{q} \quad \text{Gauss's Law for electric field} \quad (3.4)$$

plus the constitutive equations:  $\mathbf{D} = \epsilon_0 \mathbf{E}$ ,  $\mathbf{B} = \mu_0 \mathbf{H}$ , and  $\mathbf{J} = \sigma \mathbf{E}$  (Ohm's law).

where  $\mathbf{E}$  is the intensity vector of the electric field (V/m),  $\mathbf{H}$  is the intensity vector of the magnetic field (A/m),  $\mathbf{D}$  is the electric flux density vector (or electric displacement) ( $\text{C/m}^2$ ),

**B** is the magnetic flux density vector (or magnetic induction) (T), **J** is the electric current density vector ( $A/m^2$ ), and **q** is the density of free charges ( $C/m^3$ ) (Pirttijarvi, 2003).

At low frequencies displacement currents are ignored. The electric conductivity,  $\sigma$  (S/m), is considered as the only variable petro-physical parameter and the electric permittivity (dielectric constant),  $\epsilon$ , and the magnetic susceptibility,  $\mu$ , are assigned free space values ( $\epsilon = \epsilon_0 \sim 80854 \times 10^{-12}$  F/m,  $\mu = \mu_0 = 4\pi \times 10^{-7}$  H/m).

The two mathematical operators, **div** ( $\nabla \cdot$ ) and **curl** ( $\nabla \times$ ), operate on vector fields. The **div**, short for **divergence**, of a vector at a point P is the integral (sum) of the outgoing flux (flow) of the vector in the neighbourhood of P. The **curl**, short for **circulation**, of a vector is the integral of the tangential component of the vector along a defined path (Jones, 2002)

Maxwell's four equations describing the complete classical theory of the interactions between the vector electric (**E**) and magnetic (**H**) fields, were explained by Jones, (2002) as below:

- Equation **3.1** is referred to as Ampere's Law which states that a current flowing produces a magnetic field.
- Equation **3.2** is Faraday's Law of induction which states that an electric field is generated by a time-changing magnetic field.
- Equation **3.3** is Gauss' Law for magnetic fields which states that the net flux of magnetic field lines through a closed surface must be zero, i.e. if you have a bag of magnetic poles, then the lines of magnetic field force leaving the bag must be the same as those entering the bag. This means there cannot be any magnetic monopoles – there must be as many “north” magnetic poles as “south” magnetic poles.
- Equation **3.4** is Gauss' Law for electric fields which states that the electric field is proportional to the net charge, i.e. if you have a bag of electric charges, then the net lines of electric field force leaving the bag is proportional to the net charge inside (positive minus negative charges).

Geophysical EM measurement systems can be divided into frequency (FDEM) or time-domain (TDEM) electromagnetic methods. According to Grant and West (1965), EM surveying methods make use of the response of the subsurface to propagation of electromagnetic fields, which are composed of an alternating electric intensity and magnetizing force. A transmitter generates a time-varying electromagnetic field referred to as the primary field. By induction, this primary field then travels through resistive host rocks and interacts with a conductor (if present) thereby generating eddy currents over the conductor's surface. The eddy currents in turn create a secondary magnetic field

which then travels through the resistive host rock and is measured on surface by the EM receiver (Grant and West, 1965) as shown in Figure 3.1. It is this secondary field response that is interpreted to identify conductors.

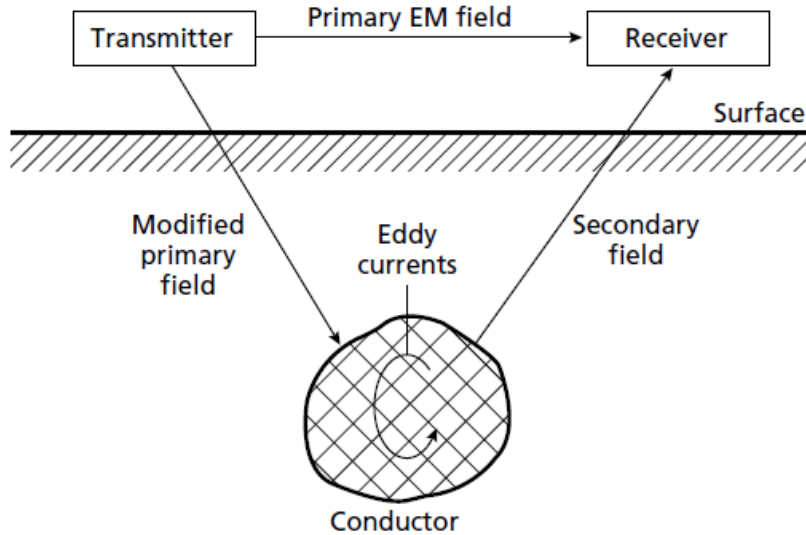


**Figure 3.1** - General principle of electromagnetic surveying (Kearey *et al.*, 2002.)

All anomalous bodies with high electrical conductivity produce strong secondary electromagnetic fields. Some ore bodies contain minerals which are themselves not conductive but may still produce a strong secondary field if sufficient quantities of accessory minerals with a high conductivity are present. This also applies to EM anomalies observed over certain sulphide ores which are due to the presence of conducting pyrrhotite distributed throughout the orebody (Kearey *et al.*, 2002).

### 3.1.2 Depth of penetration of electromagnetic fields

The depth of penetration of EM waves depends mostly upon its frequency and the electrical conductivity of the medium through which they are propagating. For time domain EM, the depth of investigation mainly depends on the length of the recording window (Nabighian, 1979). The measurement of the signal at later times gives information related to larger depths and larger conductivities. EM fields are attenuated during their passage through the ground with the amplitude decreasing exponentially with depth. Depth of penetration is measured by what is referred to as the skin depth which can be defined as the depth at which the amplitude of the field  $A_d$  decreased by a factor  $e^{-1}$  compared to its surface amplitude  $A_0$

$$A_d = A_0 e^{-1} \quad (3.5)$$

$$\text{In this case } d = \frac{503.8}{\sqrt{\sigma f}} \quad (3.6)$$

where  $d$  is depth in meters, the conductivity  $\sigma$  of the ground is in  $\text{Sm}^{-1}$  and the frequency  $f$  of the field is in Hz.

The depth of penetration increases as the frequency of the EM field and the conductivity of the ground decreases (Kearey *et al.*, 2002).

The equivalent diffusion depth of penetration in the time domain can be shown to be:

$$d = \text{sqrt}\left(\frac{2t}{\mu\sigma}\right) \quad (3.7)$$

where  $d$  is diffusion depth in meters,  $t$  is time in seconds,  $\mu$  is magnetic permeability of free space which is  $4\pi \times 10^{-7} \text{H/m}$  and  $\sigma$  is the conductivity of the subsurface in  $\text{S/m}$ .

### 3.1.3 Time-domain electromagnetic surveying

Time-domain ground EM surveys were carried out at Jacomynspan. Time domain EM surveying is sometimes referred to as pulsed or Transient-field EM. This method uses a primary field which is not continuous but consists of a series of pulses separated by periods when it is inactive. According to Faraday's Law, currents are induced in the subsurface by varying magnetic fields, decaying with time and producing secondary magnetic fields that create a measurable voltage in the receiver (Raiche, 1984). In the time domain, the secondary field is induced through a fast changing primary field and measurements take place during the interval when the primary field is absent. However, there are systems such as Spectrem that utilises a 100% duty-cycle waveform where the primary field is always present. In the presence of a subsurface conductor, eddy currents are induced in the conductor and tend to diffuse inwards towards its centre in an effort to maintain the primary field and gradually dissipate by resistive heat loss. For highly conductive bodies, the eddy currents circulate around the boundary of the body and decay slowly. Measuring the rate of decay of the waning eddy currents can provide a means of locating anomalously conducting bodies and estimates for their conductivity (Kearey *et al.*, 2002).

### 3.1.4 Electrical conductivity properties of rocks

EM methods have been successfully used in the discovery and delineation of Ni-Cu sulphide deposits. They are capable of detecting these deposits to depths of several hundred meters based on the extreme contrast in conductivity between the dominant sulphide pyrrhotite and the resistive host rock (Balch, 2007).

As stated earlier, in EM prospecting, the properties of Ni-Cu sulphide are essentially the properties of pyrrhotite which is usually the dominant mineral. King (2007), compiled a list of the contrast between the electrical properties of Ni-Cu sulphide deposits and their host rocks as shown in Table 3.1, and this contrast is of the order of 8-9 orders of magnitude higher than the host rock and makes measurement of electrical conductivity by far the most effective single tool in the identification of semi-massive to massive Ni-Cu sulphides.

**Table 3.1** – Ni-Cu sulphide ore minerals and host rock electrical resistivities (ohm-m). Adapted from King 2007.

Rock Type	Range (ohm-m)	Average (ohm-m)	Reference
<b>Sulphides</b>			
Pyrrhotite	6 – 160x10 <sup>-6</sup>	10 <sup>-5</sup>	Carmichael 1989
Pyrrhotite (Mono)		~3 x 10 <sup>-6</sup>	Emerson <i>et al.</i> , 2001
Pyrrhotite (hex)		~5 x 10 <sup>-6</sup>	Emerson <i>et al.</i> , 2001
Pentlandite	1 – 11 x 10 <sup>-6</sup>	5 x 10 <sup>-6</sup>	Carmichael 1989
Chalcopyrite	1.5 – 90 x 10 <sup>-4</sup>	5 x 10 <sup>-4</sup>	Carmichael 1989
<b>Host Rocks</b>			
Crystalline Host Rocks	10 <sup>3</sup> – 10 <sup>-7</sup>	10 <sup>4</sup>	Telford <i>et al.</i> , 1990
Overburden	1 - 1000		

As explained before, the geophysical responses of massive Ni-Cu sulphides are usually dominated by pyrrhotite which has one of the highest conductivities of any Earth material. Only graphite is of the same order or higher but according to King (2007), it rarely occurs in complete massive crystalline form over large thicknesses i.e. 10's of meter thick. This makes massive to semi-massive pyrrhotite dominated bodies, with or without nickel sulphides fairly unique in conductance (conductivity x thickness).

### 3.2 Airborne EM survey – SPECTREM System

An airborne EM survey was conducted over the Jacomynspan project area by Spectrem Air Ltd on behalf of African Nickel during the period of 22<sup>nd</sup> September to 4<sup>th</sup> October 2012 covering the whole license area at 200m line spacing. The aim of the survey was to map the outline of the Jacomynspan intrusion and also to possibly generate other targets within the area due to the upside potential of the area. SPECTREM is a fixed wing system housed in a BASLER DC3 PLATFORM that simultaneously takes electromagnetic, total field magnetic, radiometric and digital elevation measurements. Both the electromagnetic and magnetic sensors are towed behind the aircraft in "birds" while the radiometric crystals are installed inside the cabin.



### 3.2.1 SPECTREM System Specifications and Geometry

The geometry and system specifications for the Airborne EM survey are listed in Table 3.2.

**Table 3.2** - The geometry and specifications used by SPECTREM during the airborne EM survey at Jacomynspan project

<b>EM system</b>				
Transmitter height above ground	91 m			
Tx – Rx vertical separation	41 m (nominal value)			
Tx – Rx horizontal separation	121 m (nominal value)			
Transmitter coil axis	Vertical			
Receiver coil axes	X : horizontal, parallel to flight direction; Z: vertical			
Current waveform	Square wave (100% duty cycle)			
Base frequencies	25 Hz			
Transmitter loop area	420 m <sup>2</sup>			
RMS current	960 amperes			
RMS dipole moment	400 000 A.m <sup>2</sup>			
Digitising rate @ 25Hz	38 400 Hz / component			
Recording Rate	5 Hz			
Number of windows	9 per component			
Window distribution	Pseudo-binary			
Window Times 25Hz	<b>Window</b>	<b>Window</b>	<b>Window</b>	<b>Window</b>
<b><u>Window Number</u></b>	<b><u>Start (ms)</u></b>	<b><u>End (ms)</u></b>	<b><u>Centre (ms)</u></b>	<b><u>Width (ms)</u></b>
1	0.0260	0.0260	0.0260	0
2	0.0521	0.0781	0.0651	0.0260
3	0.1042	0.1823	0.14325	0.0781
4	0.2083	0.3906	0.29945	0.1823
5	0.4167	0.8073	0.6120	0.3906
6	0.8333	1.6406	1.23695	0.8073
7	1.6667	3.3073	2.4870	1.6406
8	3.3333	6.6406	4.98695	3.3073
9	6.6667	13.3073	9.9870	6.6406
10 (Primary Field)	13.3333	19.9740	16.6536	6.6667
<b>Magnetic system</b>				
Bird height above ground	72 m			
Bird location	19 m below and 41 m behind centre of aircraft			
Sensor	Scintrex CS-2 Sensor with SPECTREM Counter/Sync			
Recording Rate	5 Hz			
Sensitivity	0.01 nT			
Resolution	0.1 nT			

The gamma-ray radiometric sensors consisted of 32l of downward looking and 4l of upward looking NaI crystals sampling at 1 Hz.

### **3.3 Ground EM Surveys**

Ground EM surveys were carried out over the study area in two phases. During the first phase, a fixed loop mode was carried out on two loops. Loop 2 was surveyed using a Fluxgate sensor manufactured by EMIT while Loop 1 was surveyed using a Low Temperature Super Conducting Quantum Interference Device or so-called 'LT SQUID' manufactured by the Institute for Photonic Technology (IPHT), Jena, Germany. During the second phase, the moving loop mode was carried out using the Fluxgate sensor for the first few lines and the LT SQUID for the remainder of the lines. This was due to the non-availability of the LT SQUID in some instances and also the need to compare the two datasets. The surveys were carried out at 100m line spacing and 50m station spacing for both modes.

#### **3.3.1 Instruments for ground EM survey**

This section gives a brief description of the different instruments used for carrying out Ground EM surveys.

#### **3.3.2 The JESSY DEEP LT SQUID**

The IPHT Jessy Deep LT SQUID magnetometer which operates at a very low temperature of  $-269^{\circ}\text{C}$  is a very sensitive instrument which enables Transient Electromagnetic (TEM) measurements to be performed up to very late times. It is made up of a cryostat which is filled with liquid helium in order to cool the SQUID sensors down to their optimum working temperature of 4.2K which is  $-269^{\circ}\text{C}$ . At this low temperature, the sensor becomes superconducting. A control unit provides power to the SQUID electronics, incorporates a cable tester and outputs the voltages of the individual SQUID channels to amplifiers and analogue to digital transcribers after which the signals are stacked and recorded.

There is another type of SQUID (not used during this survey) which is known as the High Temperature SQUID (HT SQUID). The main difference between the two is that the HT SQUID is filled with liquid nitrogen operating at  $-169^{\circ}\text{C}$  while the LT SQUID is filled with liquid helium and operates at  $-269^{\circ}\text{C}$ . The main advantage of LT SQUID is that it gives data of higher signal to noise ratio giving higher quality data than that acquired by a HT SQUID because of its lower operating temperature. However, its main disadvantage is that liquid helium is more expensive than liquid nitrogen, making LT SQUID surveys expensive to run.

Following correct procedure when filling liquid helium (Figure 3.2) into the cryostat of the LT SQUID is very important when preparing the system for measurement. The cryostat needs to be filled sufficiently to ensure that the sensor remain immersed in liquid helium throughout the day's surveying. Once the liquid helium level drops too low the sensor loses its superconducting properties. The procedure is provided in the manual which outlines the handling of liquid helium. The cryostat used at Jacomynspan project needed to be filled with liquid helium after every two days of field work.



**Figure 3.2** - Jessy Deep Low Temperature SQUID magnetometer in orange colour being filled up by liquid helium in order to cool the sensors down to  $-269^{\circ}\text{C}$  (Jessy Deep Manual).

The LT SQUID is a fast sampling **B**-field sensor that can measure the time-integral of the impulse response which is called “step response”. This time integral is an important ‘filter’ which attenuates fast decays from weaker or unconfined conductors in preference to decays from strong conductors which are slow. This makes it easier to discriminate a response from a good conductor in the presence of a weaker conductor such as a host, overburden or less conductive bedrock (EMIT, 2010). The main advantage of the SQUID sensor over a fluxgate is in its ability to measure at very late times (low frequencies, i.e. greater depths or larger conductivities). Since the sensors operate as super conductors due to their low operating temperature, the LT SQUID has a high signal to noise ratio providing very clean data when compared to a fluxgate sensor.

### **3.3.3 The 3 Component Fluxgate Magnetometer System**

The Australian ElectroMagnetic Imaging Technology's® (EMIT) Fluxgate Magnetometer System shown in Figure 3.3 consists of a sensor mounted on a platform and a control

box. The 3-component low-noise fluxgate magnetometer converts magnetic flux density, measured in three axes to analog voltages proportional to the magnetic flux density. The sensors are mounted in non-magnetic, non-conductive housings for protection against impacts and weather extremes, and to allow for rapid and accurate orientation. Power to the sensor is supplied by a separate controller box. This controller box also removes the DC geomagnetic signal from each component and amplifies the EM signals from the magnetometer.



**Figure 3.3** - EMIT's 3-component fluxgate magnetometer taking measurements at Jacomynspan project.

The 3 components can be measured simultaneously using the SMARTem receiver system. The fluxgate sensor is capable of measuring magnetic field in the frequency range from DC to 3 kHz. The fluxgate measures the **B**-field rather than dB/dt as is the case with conventional coils. The main advantage is that any slowly-decaying signal can be observed earlier in time in a **B**-field measurement than in a dB/dt measurement. It also measures the time integral of the impulse response which is called "step response" as for a SQUID. This time integral is an important filter which can discriminate between weak and stronger conductors. However, the fluxgate has a lower signal to noise ratio than the LT SQUID.

#### **3.3.4 The SMARTem V Receiver**

The SMARTem V receiver system was developed by ElectroMagnetic Imaging Technology® (EMIT) commencing 1995. It is a new, electrical method receiver system, which is designed around a purpose-built, rugged, weatherproof, dustproof Pentium PC. It is a completely programmable instrument that can acquire, record, process and display

TEM data using Zonge, Geonics and other transmitters. A complete SMARTem V system unit (Figure 3.4) which includes a transmitter controller unit allows data collection in a direct trigger mode and a synchronised (remote transmitter) mode.



**Figure 3.4** - Crystal synchronisation of the SMARTem V receiver and a transmitter controller before the start of field work at Jacomynspan.

It achieves high signal-to-noise ratios by virtue of rapid sampling of receiver voltages and digital signal processing techniques implemented in its control software.

Synchronisation of crystal oscillators in the receiver and transmitter controller is carried out with software and this procedure may take several minutes to complete and no manual tuning of either crystal is required. The crystals in the SMARTem transmitter controller and receiver must be turned on at least one hour prior to the crystal synchronisation operation to allow internal temperatures to stabilize.

### **3.3.5 Ground EM Survey Design**

Time Domain Ground EM (TDEM) surveys were carried out on a total of 35 lines at 100m spacing over the main target body (Figure 3.5). Both the fixed loop and the moving loop modes were executed.



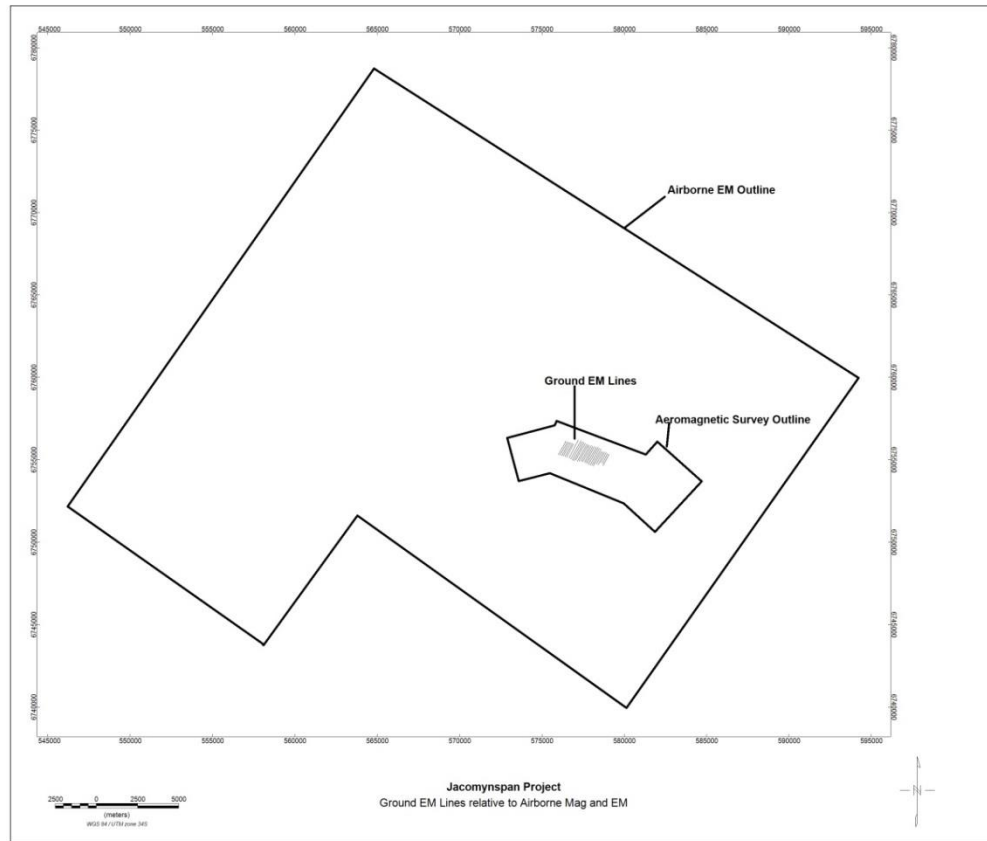


**Figure 3.5** - Ground EM traverses for both fixed loop and moving loop methods relative to the outline of the Airborne EM and Aeromagnetic survey.

### 3.3.6 Fixed Loop Survey Design

The position of the transmitter loop for the fixed loop mode is very critical. It must be positioned in such a way that there is maximum coupling with the target body. In order to come up with the best transmitter loop position for maximum coupling with the target body and also to get a feel of the anticipated theoretical EM response, forward modelling was carried out using EMIT's Maxwell software (Figure 3.6). Forward modelling however assumes a *priori* knowledge of the position of the conductor. When possible dip and position of the conductor is unknown, it is essential to use more than one transmitter loop position to avoid a zero coupling situation. In this study, from the drilling programme, it is known that the target mineralisation extends down to approximately 900m or deeper and dips  $\sim 68^{\circ}\text{SW}$ . Ground magnetic data acquired by the author prior to ground EM surveying also indicated the sub-outcrop position of the ultramafic body. All this information was used in the forward modelling in order to position the fixed loops. The dipping plate formulation for Maxwell is based on Lamontagne and West, (1971). The forward model for the fixed loop mode is shown in Figure 3.6.

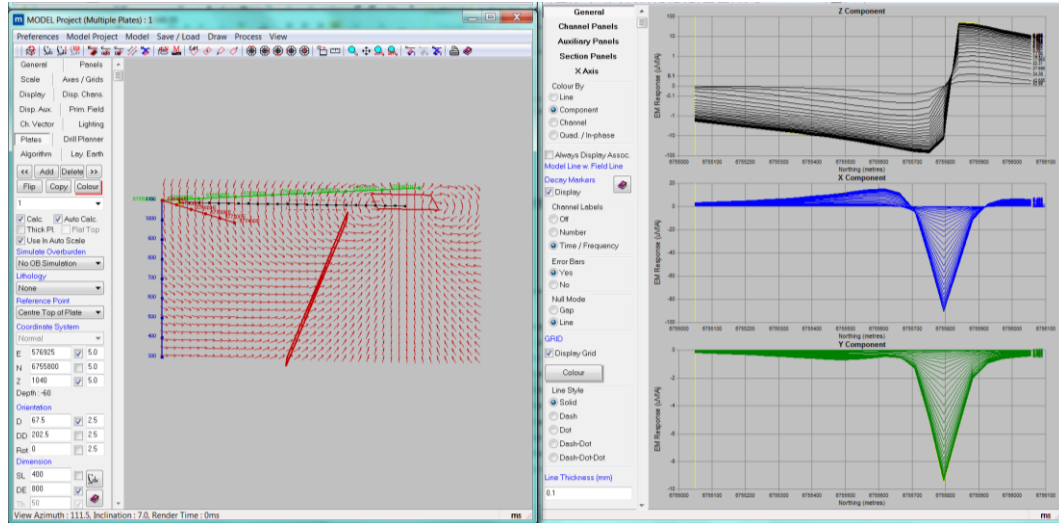


**Figure 3.6** - EM forward model for the Fixed Loop survey for the Jacomynspan conductive mineralisation scenario, showing the Primary field lines and coupling with the plate for the transmitter loop location in the left, the anticipated EM response for the Z, X, and Y components on the right.

Three 600m x 400m fixed transmitter loop positions were planned to the northern side of the intrusion to cover the main target (Figure 3.7). The primary influence of the transmitter loop size is in the amplitude of the primary pulse induced in the sub-surface. The amplitude of this pulse is determined by what is referred to as the magnetic dipole moment of the transmitter loop. This magnetic dipole moment is given by:

$$\mathbf{M} = n\mathbf{A}\mathbf{I} \quad (3.8)$$

where  $\mathbf{M}$  is the dipole moment,  $n$  is the number of turns of the loop,  $\mathbf{A}$  is the surface area of the transmitter loop and  $\mathbf{I}$  is the transmitter current.

For the fixed loop, the survey was carried out using a SMARTem V receiver with a SQUID sensor for loop 1 (See Fig 3.7). The fluxgate was available for the loop 2 and 3 survey. A generator powered GGT10 transmitter capable of producing time domain square waveforms into resistive loads was used to transmit a 50% duty cycle waveform at a base frequency of 0.5Hz into the fixed transmitter loop. The transmitter controller was synchronised to the SMARTem V receiver via the crystal clocks. At each station, three components X, Y, and Z were measured and stored. By convention, X points along the survey line positive to the north, Y points perpendicular to the survey line, being positive to the west while Z is positive up.

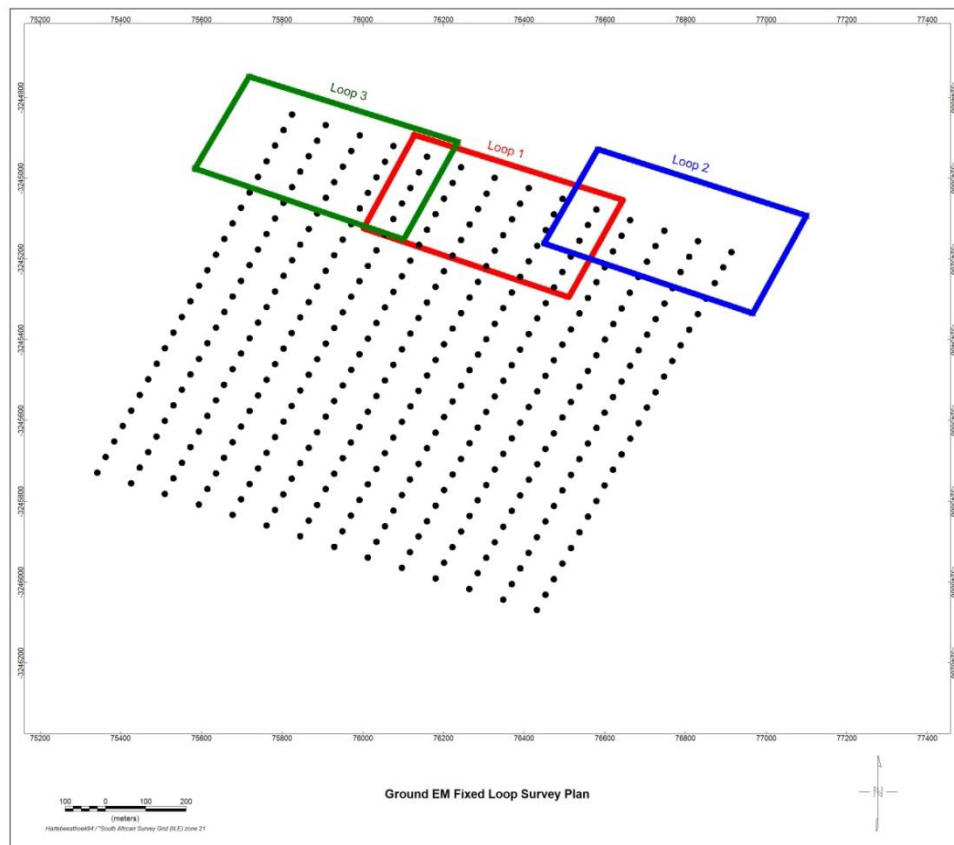


**Figure 3.7** - TDEM fixed loop survey plan over the main target showing the position of the 3 transmitter loops and stations as black dots.

The station spacing was chosen in such a way that the anomaly is sufficiently delineated to enable reliable interpretation of the data for a minimum of 5 stations on the anomaly. In this case the station spacing was 50m and the line spacing was 100m.

### 3.3.7 Moving Loop Survey Design

A moving loop time domain ground EM survey was carried out over the main target area at 100m line spacing and 50m station spacing. Since the transmitter loop for this mode moves along the survey line at the same time as the receiver in the middle, the position of the loop keeps changing with each station measured (Figure 3.8). However, forward modelling was also carried out in order to get a feel of the anticipated EM response.



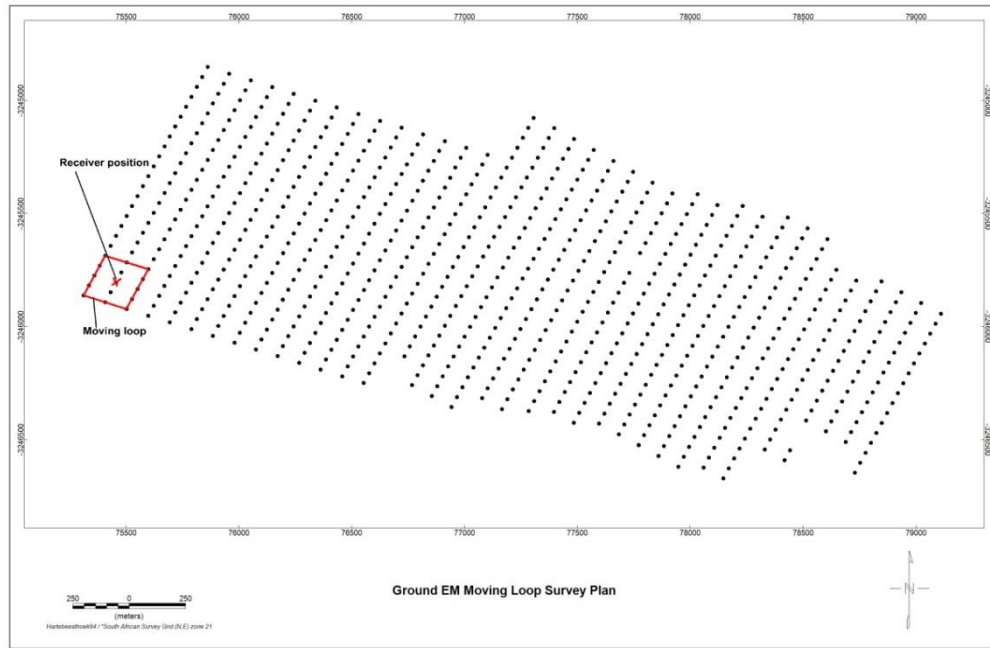


**Figure 3.8** - TDEM moving loop survey plan showing the moving transmitter loop, position of the receiver in red and station positions as black dots covering the main target.

Although moving loop surveying has a much lower production rate in data acquisition than the fixed loop method, its main advantage is a constant host rock response making the isolation of anomalies easier. The whole survey was conducted this time using a SMARTem24 receiver. Since the LT SQUID sensor was not always available part of the survey was carried out using a fluxgate sensor. A battery powered Zonge ZT-30 transmitter capable of producing time-domain square waveforms into resistive loads was used to transmit a 50% duty cycle square waveform at base frequency of 1Hz into a 200m x 200m moving transmitter loop. The transmitter controller was synchronised to a receiver via GPS. The readings were taken at the centre of the loop. At each station, three components **X**, **Y**, and **Z** were measured. Similar to, for the fixed loop mode, **X** points along the survey line positive to the north, **Y** points perpendicular to the survey line, positive to the west while **Z** is positive up.

### 3.3.8 Quality Control

Transmitter controller synchronisation to the receiver via the crystal clocks at the beginning of each survey day when using the SMARTemV has been emphasized before. As for the SMARTem24, synchronisation of the receiver and the controller is via the GPS and is automatic once the two instruments are switched on. After synchronisation, the SMARTem software must be configured to suit the particular survey parameters and all the configurations are saved to be available the following day.

For both the moving and fixed loop modes, the polarity of the signals being measured should be understood prior to undertaking the survey. The manner in which the loop has

to be connected to the transmitter has to be strictly adhered to or the response is opposite to what it should be. It is important that consistency must be maintained from one measurement to the next. One way of ensuring that current is flowing in the correct direction is that a **Z** component measurement in the centre of the loop, must always be positive and of relatively high amplitude and should have a well behaved decay curve. If one realizes in the middle of the survey that polarity has been accidentally reversed, it is recommended, for purposes of consistency to continue taking the measurements the same way and then the mistake can easily be corrected during processing. When judging the validity of a sign change in the data, it should be considered that a significant anomaly will never occur over just one or two stations only and will never manifest itself in a sharp change from one station to the next.

When using the SQUID system, sufficient liquid helium has to be in the cryostat. The SQUID is a highly sensitive instrument and therefore care must be taken during its transportation to make sure it does not fall over. Care must also be taken when moving the SQUID from one station to the next and it must be placed on a flat surface making sure it is standing stable as noise due to the smallest movement (wind noise or trees moving in the wind) could adversely affect the measurement drastically. The **X**, **Y** and **Z** components must face the right direction as explained previously. A weighted plastic windshield free of metals must be placed over the SQUID to avoid offset drift due to the wind. SQUIDS are very sensitive to radio-frequency interference and therefore no mobile and other communication devices must be used while taking readings.

The fluxgate sensor needs the same care in being placed in a stable environment as described for the SQUID to avoid generating noisy measurements.

### **3.4 Data Processing**

#### **3.4.1 Airborne Electromagnetic Data Processing (SPECTREM)**

The airborne EM data were processed by SPECTREM using both Geosoft Oasis Montaj and Spectrem® proprietary software. Some of the most important data processing procedures were carried out on the aircraft as it acquired the data with the first processing stage being stacking of the data to 512 time samples. The data were then deconvolved to remove the system response and then transformed to a square wave response. Spectrem uses a square 100% duty cycle transmitter waveform (i.e. the current is always on) as a periodic approximation of the step response (Klinkert *et al.*, 2012).

The data were then binned into 8 channels or time windows. Since Spectrem is an 'on-time' system it makes its measurements while the current is flowing and it records the complete waveform because the aim in the end is to also determine the B-field response.

(The integration of the coil response into a B-field 'magnetometer' response is a patented process developed by Prof James Macnae of RMIT University in Melbourne Australia for Spectrem). Spectrem measures a total of 10 channels; an assumption is made that the induced field will have decayed to a minimal amount at the time the last channel is sampled. As the last channel is assumed to have only measured the primary field, it can be subtracted from the other channels to separate the secondary field. Hence there are actually 8 channels with geological information in the final data (Klinkert *et al.*, 2012).

The spikes in the line data are removed using a 3 point Naudy filter (Klinkert *et al.*, 2012), then drift corrected and micro-levelled. Decorrugation and micro-levelling is applied to all channels to reduce small residual errors that will not have been corrected through the drift correction method. The data are then be gridded in Geosoft Oasis Montaj and analysed.

#### **3.4.2 Ground Electromagnetic Survey Data processing**

Data collected were stored in the SMARTem machine memory. The data can then be transferred to a memory stick and copied to a personal computer for processing at the end of each survey day. The copied files can easily be imported into Maxwell software as either \*.DAT or \*.TEM files for further manipulation. A separate configuration file for the particular survey can be imported into Maxwell if it is available. The configuration can however be created via the line editor dialog box in Maxwell software. In this dialog box, parameters such as loop size, base frequency, **X**, **Y**, **Z** effective component sensor area etc. are entered. If the polarity was accidentally reversed during data collection, this can also be corrected in Maxwell software. Since 3 readings were taken at each station when using either a fluxgate or SQUID, there is need to average these readings. But first, there is need to manually check the decay curves of each measurement for noise as shown in Figure 3.9. Readings that are considered to be noisy can be manually deleted.

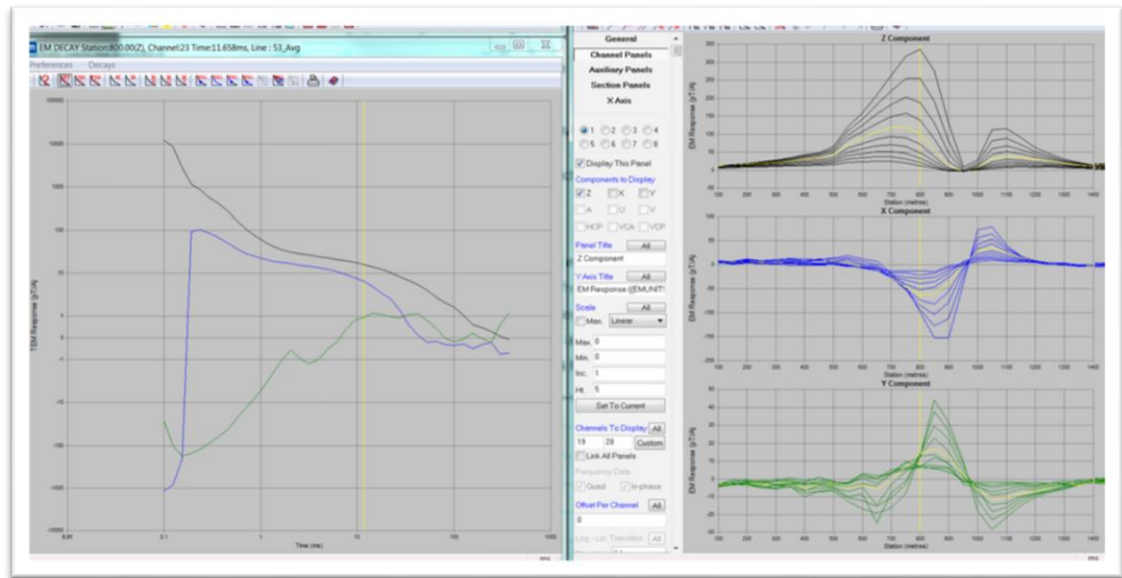


**Figure 3.9** - The moving loop data in Maxwell. The profiles for the measured components X, Y, and Z for Line 5300 are shown in the profile window on the right while the decay curves at station 800 for the three components are shown on the decay curves window on the left. Black is the Z component, blue is the X component and green is the Y component while the vertical yellow line shows the station position.

The loop polarity can be reversed here if necessary using the line editor. Decay curves can be plotted for each station and noisy readings manually deleted. The remaining 'not noisy' data are then averaged. The averaged data are in units of  $\mu\text{V}/\text{A}$  when using the fluxgate sensor and these are normally converted into more meaningful readings of  $\text{pT}/\text{A}$  as follows (only applicable to calibrations done for the survey at Jacomynspan):

$$1 \text{ pT field at sensor} = 2.857 \mu\text{V into receiver, or}$$

$$1 \mu\text{V into receiver} = 0.35 \text{ pT at sensor}$$

Therefore the fluxgate readings need to be multiplied by a factor of **0.34965** in order to convert the response from  $\mu\text{V}/\text{A}$  (micro volts per Amp) to  $\text{pT}/\text{A}$  (pico Teslas per Amp).

The LT SQUID sensor readings also need to be multiplied by certain calibration factors for each component. These calibration factors keep changing each time the LT SQUID goes for service and are specific to one sensor. The calibration factors for the Jessy Deep SQUID sensor that were used for this survey are:

- **X**= 1.562
- **Y**= 1.546
- **Z** = 1.543

where **X**, **Y** and **Z** are the measured components.

The data are now ready for display and further manipulation in Maxwell software.

## **CHAPTER 4: METHOD – DOWNHOLE ELECTROMAGNETICS (DHEM)**

### **4.1 Introduction**

This chapter covers the basic principles of Downhole Electromagnetics (DHEM) surveying as applied to geophysical investigations. Survey design will be illustrated and also the instruments used will be described. Data processing procedure will be explained later towards the end of the chapter.

DHEM surveying was conducted on selected boreholes surrounding the harzburgite in an attempt to try to map and delineate this well mineralised harzburgite from a distance away from the boreholes drilled into the harzburgite body, which is highly conductive in comparison to its host.

DHEM surveying has become a very important exploration tool for conductive mineralisation, particularly in areas where the ability of surface EM to define a target is limited by large depths or by interfering conductive bodies such as overburden, shallow occurring sulphides and peripheral mineralised horizons (Eadie and Staltari, 1987). Eadie and Staltari (1987) noted that in recent years, economic considerations have forced most mining companies to focus massive sulphide exploration expenditure on properties close to infrastructure and known mineralisation at the expense of reconnaissance work in new areas. As a consequence, deep and relatively small lenses in very complicated geological environments are often the target of an exploration programme. These are usually outside the detection capabilities of surface geophysical methods due to large depths, interference from shallower conductors or interference from large, peripheral, weakly mineralised horizons. In addition, pattern drilling for these targets is very expensive because of the depth involved and the necessity to drill closely spaced holes over large areas to ensure that no economic mineralisation is missed (Eadie and Staltari, 1987). This applies very well to the current study area where the well mineralised harzburgite appears to occur in pods at great depths and there is also interference from the poorly mineralised tremolite schist which hosts these pods.

#### **4.1.1 Basic theory of DHEM**

The power of DHEM is based on the fact that the receiver is lowered into the exploration drillhole, generally placing it closer to the target than most of the interfering bodies. From this position, it can detect conductive bodies at distances greater than 100m from the drillhole (depending on the size of the target), at depths well over 1000m (Eadie and Staltari, 1987).

According to Eadie and Staltari (1987), DHEM makes use of a large rectangular transmitter loop as an energising source with diameter dimensions varying from tens of

meters to hundreds of meters usually approximating the depth of interest. A 50% duty cycle waveform at a certain base frequency (e.g. 2Hz) is transmitted into the loop wire for impulse response systems. The receiver is synchronised to the transmitter through a hard-wire or radio timing link, or clock synchronisation. The sensing device (receiver coil(s)) is lowered down the drill-hole, taking readings at regular intervals, usually 5 or 10m. The coil measures the voltage, which is proportional to the time rate of change of the magnetic field, and is composed of the primary field contribution (derivative of transmitted field) and the secondary field for the complete recording of the waveform.

The primary field contribution is simply a series of pulses while the secondary field is derived from induced current flow decaying in the target. This transient decay is sampled during the interval between current pulses. The anomaly at a given time (Figure 4.1) below is positive at C, zero at B and negative at A, tracing a positive-negative-positive profile for the off-hole configuration illustrated.

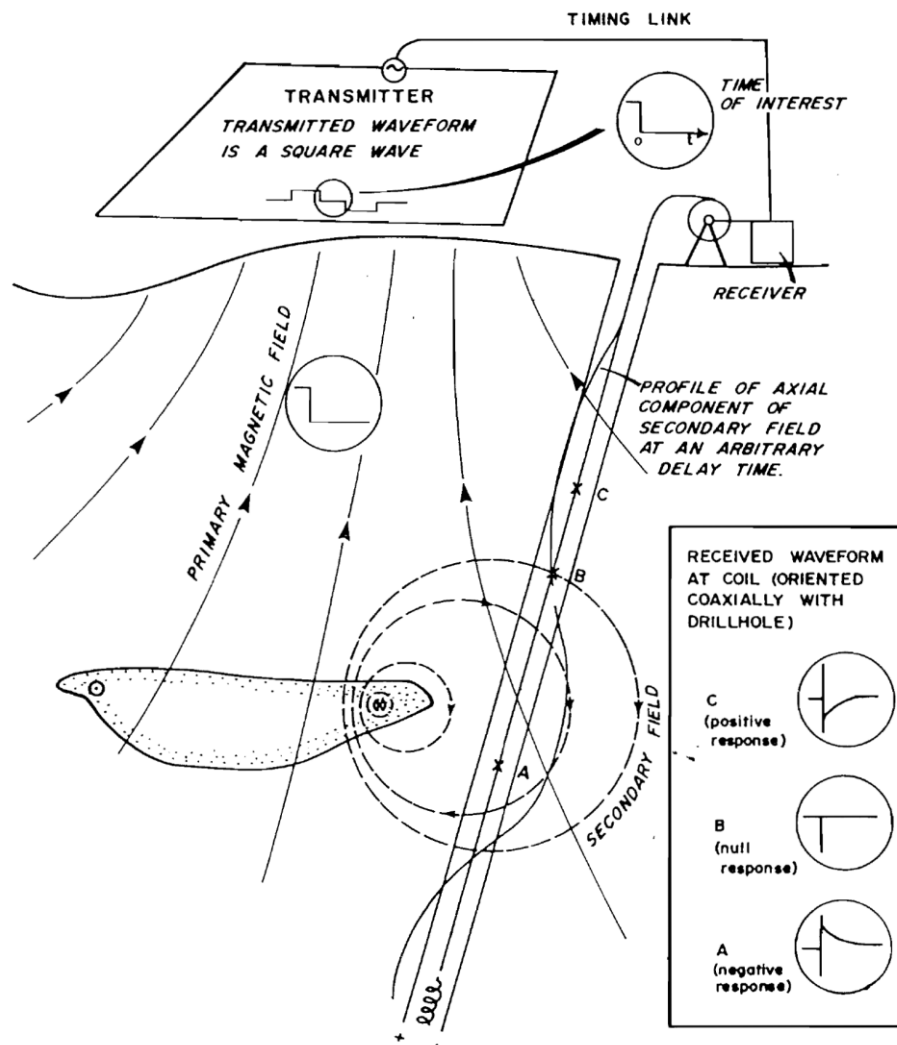


**Figure 4.1** - Basic principle of DHEM surveying (Dyck and West, 1984).

Despite the many benefits of DHEM surveys, Eadie and Staltari (1987), noted that there are a number of ambiguities and uncertainties which occur during the interpretation process. For example in this study, the well mineralised pods occur within a conductive host and the 3D complexity of the host response can cause uncertainty. The late time behaviour of the host response may be misinterpreted as due to an off-hole conductor (Macnae and Staltari, 1987). Furthermore, the host response modifies the early time behaviour of the target anomaly and can, in the case of current channelling, be responsible for a change in sign of the anomaly (Irvine, 1987).

#### **4.2 Instruments for DHEM Survey**

The DHEM survey data at Jacomynspan were acquired using the Atlantis DHEM system manufactured in Australia. It consists of a downhole sensor probe which is basically a fluxgate magnetometer DHEM logging system developed by EMIT® and a surface control box. The Atlantis system consists of a tri-axial fluxgate magnetometer housed in a slim-line probe used as a receiver sensor for borehole TEM and other borehole geophysical survey types requiring the accurate measurement of magnetic EM fields in the frequency range from DC to 3 kHz (EMIT User Guide, 2015). The probe can carry out a range of automated operations that include the automatic nulling of the DC geomagnetic response from the magnetometer so that the small AC signals desired can be isolated and amplified. The probe electronics consists of tri-axial accelerometers for orienting the probe and a temperature sensor for calibration of the temperature drift of the magnetometers and accelerometers. The probe runs on standard 4-core logging systems common in the geophysical industry (EMIT User Guide, 2015).

A measurement of 3 components of magnetic field can be undertaken with specialised software developed for the SMARTem Receiver system manufactured by EMIT®. The probe also houses its own CPU which is capable of accepting instructions from the SMARTem receiver or from a stand-alone computer. The SMARTem receiver automates the process of taking a measurement. The results of a measurement of the 3 components are automatically processed and rotated into borehole-referenced directions (EMIT User Guide, 2015).

A SMARTem V receiver which has been described previously under the ground EM chapter was used for data acquisition.

#### **4.3 Survey Design**

A number of 12 boreholes in total were selected for the DHEM survey over the main target area. The data were acquired using a single 600m by 300m fixed transmitter loop located to the north of the boreholes to enable maximum coupling with the body. From

the ground EM surveys carried out on the area and the drilling results, information regarding the target was available and positioning of the fixed loop was optimized to ensure maximum coupling with the target.

A 50% duty cycle square waveform was transmitted at a base frequency of 1Hz using a Zonge GGT-10 transmitter synchronised to the SMARTem receiver via the crystal clocks. A constant peak current of 20A was transmitted into the transmitter loop wire. The probe was lowered down the borehole using a winch. Measurements of all the surveyed boreholes were taken at 20m intervals in the country gneiss rock and at 10m intervals within the intrusion (tremolite schist and harzburgite). The Atlantis DHEM system also measures borehole azimuth and direction as it takes readings. There is therefore no need to survey the hole separately. Three components **U**, **V**, and **A** were measured at each depth interval. These 3 components form a right-handed set; **A** is axial up-hole, **U** is at 12 o'clock looking downhole and **V** is at 9 o'clock looking downhole.

#### **4.4 Quality control**

The probe is a very sensitive instrument and must be carefully lowered down the hole using a winch. Measurements should only be acquired after the probe is completely stationary.

#### **4.5 Data processing**

Acquired data were written to a \*.DAT file and copied from the SMARTem receiver using a memory stick and then transferred to a computer for processing at the end of each survey day. The \*.DAT file can be easily imported into EMIT's Maxwell software for further processing. The data are first checked for quality by scrolling through all the decay curves identifying all the noisy readings and manually deleting them. Since at each depth at least 3 measurements were taken it is possible to delete noisy data sets and thereafter the acceptable readings are then averaged. A configuration file for the survey can be imported if it is available but it can however also be created in Maxwell via a Line editor (Figure 4.2) as for the ground EM data as explained before. Parameters such as transmitter loop size, base frequency, transmitter current and so on are entered into the line editor dialog box as shown in Figure 4.2.



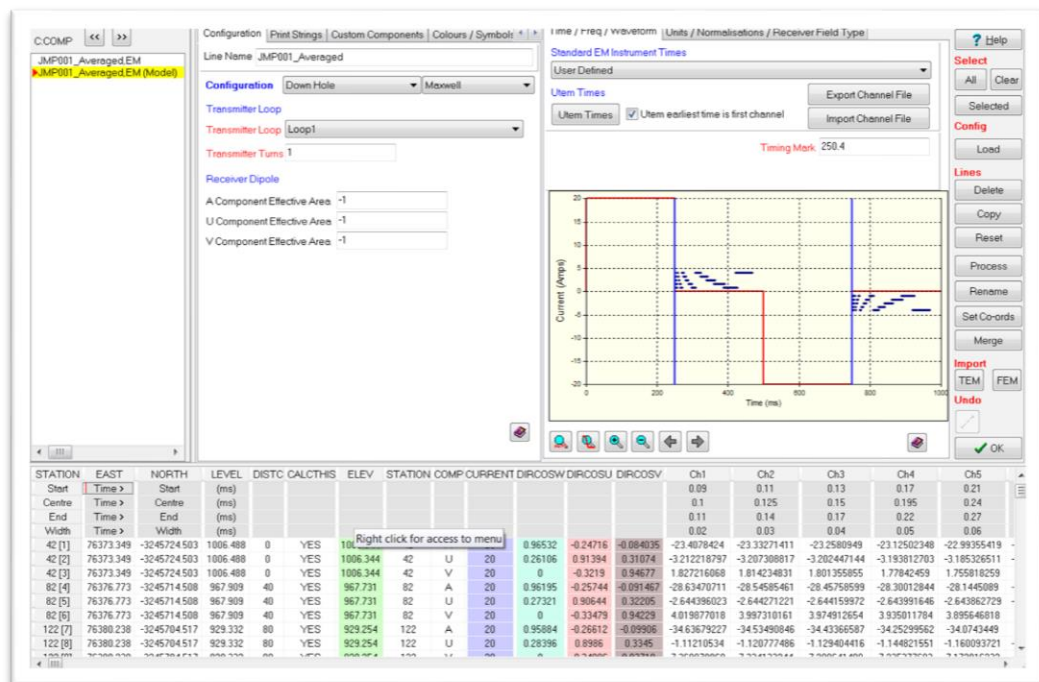


**Figure 4.2** - Line editor dialog box for Maxwell which can be used to create a configuration file for the survey.

The **A**, **U**, and **V** measured components are then displayed in Maxwell for further manipulation and modelling.

## CHAPTER 5: METHOD – AUDIO-FREQUENCY MAGNETOTELLURICS (AMT).

### 5.1 Introduction

This chapter covers the basic theory of the Audio-frequency Magnetotellurics (AMT) method. The instruments used in the data acquisition are described. Survey design and processing of the data is explained towards the end.

Natural source AMT surveying was carried out at Jacomynspan because it has a superior depth penetration than Time Domain Electromagnetics and is logistically simpler to carry out – no transmitter, generator or large wire loops are required. AMT better discriminates resistivity contrasts in a more resistive environment than TDEM which is mostly sensitive to conductors. The survey was carried out over the main target zone with the objective being to image deep geological structure, near-surface geology, and to map the intensity of mineralisation.

#### 5.1.1 Basic theory of AMT

Determining subsurface conductivity (or its inverse, resistivity) at crustal scales can be carried out using magnetotelluric methods that involve surface measurements of orthogonal electric and magnetic field variations. The Audio-frequency Magnetotellurics (AMT) method that was executed on the study area involves measurement of electromagnetic fields that are generated in the atmosphere and magnetosphere. Magnetotelluric (MT) signals which are low frequencies (<1Hz) are generated by the interaction between the earth's magnetosphere and the solar wind, sunspot activity and auroras (Bedrosian, 2007). High frequency sources (> 1Hz) in the Audio range (AMT) are generated by worldwide thunderstorms and lightning (Zonge, 2012). The large conductivity contrast at the air-earth boundary strongly refracts the inducing electromagnetic fields causing them to propagate vertically within the earth irrespective of the incident angle. Relative to the incident magnetic field, the amplitude and phase of the measured induced electric field depend upon the conductivity of the medium it travels through (Bedrosian, 2007).

The propagation of electromagnetic energy in the earth at magnetotelluric frequencies was described by Bedrosian (2007), with a diffusion equation of the same form as that governing heat diffusion through a solid. The solutions to this equation are electric and magnetic fields which decay exponentially within the earth over a characteristic distance  $\delta$  termed the skin depth. Over a homogeneous earth, the skin depth is related to the frequency ( $\omega = 2\pi f$ ) of the incident field and the resistivity ( $\rho$ ) of the subsurface by

$$\delta = \sqrt{2\rho/\mu\omega} \approx 500\sqrt{\rho/f} \text{ meters,} \quad (5.1)$$

where  $\mu$  is magnetic permeability typically assumed equal to its free space value,  $\mu_0$ .

Equation 5.1 is a statement of penetration depth, with lower frequencies penetrating deeper within the earth. For a typical survey, the depth of investigation is additionally dependent upon sampling rate, recording time, signal strength, and profile length (Bedrosian, 2007).

The aim of magnetotelluric analysis is to estimate the earth's heterogeneous and sometimes anisotropic resistivity structure from surface field measurements. The measured fields are transformed to the frequency domain where cross- and auto-power spectra are computed (Bedrosian, 2007). These are then used to estimate transfer functions relating the frequency-domain fields:

$$\begin{bmatrix} Ex \\ Ey \end{bmatrix} = \begin{bmatrix} Z_{xx} & Z_{xy} \\ Z_{yx} & Z_{yy} \end{bmatrix} \begin{bmatrix} Hx \\ Hy \end{bmatrix} \quad (5.2)$$

In Equation 5.2, the four elements  $Z_{ij}$  form the impedance tensor, a complex, frequency-dependent tensor containing the amplitude and phase relations between  $E(\omega)$  and  $H(\omega)$ . From each element of the impedance tensor the magnetotelluric response functions can be derived, such as apparent resistivity ( $\rho_a$ ) and phase ( $\phi$ ) (Bedrosian, 2007).

By Faraday's Law of Induction, the time varying magnetic field induces an electric current within the earth, and by Ohm's Law this current generates an electric (called "telluric") field. The strength of the electric field is dependent on the conductivity of the medium and the strength of the inducing source magnetic field. Therefore by observing the magnetic and electric fields simultaneously, and determining their ratios at varying frequencies (equivalent to depths by the skin depth phenomenon), one can derive the conductivity variation with both depth and distance (Jones, 2002).

On the surface of the Earth, one measures the time variations of the three components of the magnetic field ( $Hx$ ,  $Hy$  and  $H_z$ ), and the two horizontal components of the Earth's electric field ( $Ex$  and  $Ey$ ).

## 5.2 Instruments used

The AMT data were acquired using a Zonge® AMT system consisting of a multichannel analog GDP-32<sup>II</sup> geophysical data processor which is the receiver, ANT/6 magnetic field sensors, electric field array cabling and non-polarizing electrodes used for measuring ground potentials.

### 5.2.1 The GDP-32<sup>II</sup> Receiver

The Zonge GDP-32<sup>II</sup> Geophysical Data Processor (Figure 5.1) is a universal, multi-channel receiver designed to acquire virtually any type of electromagnetic or electrical data within the DC to 8 kHz bandwidth. It is an integrated, 24-bit multi-channel receiver for acquisition of controlled and natural source geoelectric and EM data (Zonge, 2010).



**Figure 5.1** - Zonge GDP 32<sup>II</sup> Receiver used to acquire AMT at Jacomynspan.

Programs are stored on an internal flash disk and are software-selectable. It can operate in both the frequency domain and time domain. Twenty six frequencies can be selected in binary intervals between 0.000121 Hz and 8 kHz.

### 5.2.2 ANT/6 Magnetic Antenna

The AMT survey was carried out using the ANT/6 as the magnetic antennas. They are highly flexible instruments, built to withstand the difficult conditions encountered in the field. They are extremely low noise instruments that use feedback amplifier technology including carefully designed mu-metal cores. The following are the specifications for the ANT/6 antenna

- Length: 91 cm
- Diameter: 4.8 cm
- Weight: 3.2 kg
- Frequency Range: 0.1 – 10 000 Hz
- Sensitivity in Passband: 250mV/γ (250mV/nT)
- Noise level: 200 μV (200fT) per √Hz at 1 Hz  
1μV (1fT) per √Hz nominal > 200 Hz
- Application: MT/CSAMT

### 5.3 Survey design

A total of 21 lines 2km long with a line spacing of 200m were surveyed using the Zonge AMT/MT system at 50m station spacing. The lines were planned with different orientations due to strike changes in geology (Figure 5.2) and overlap partly with the TDEM work.

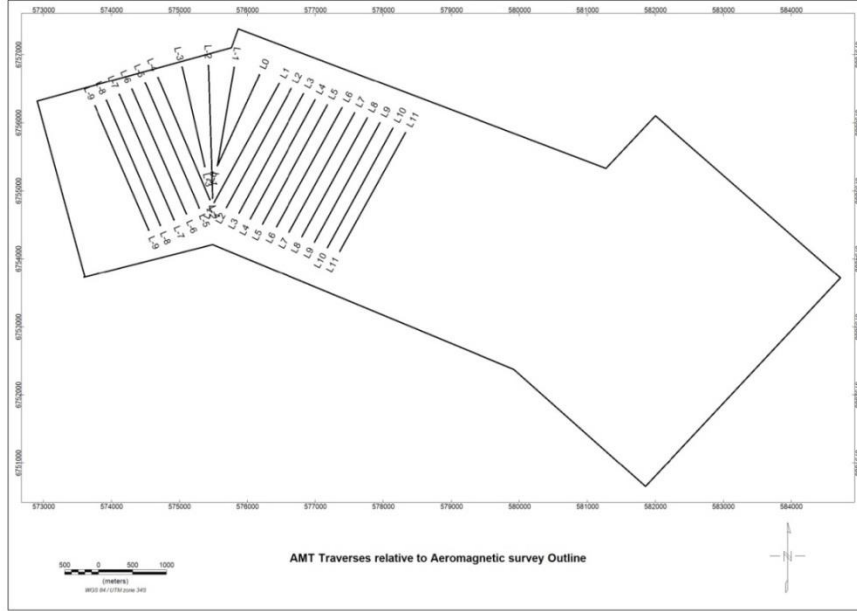


**Figure 5.2** - AMT traverses relative to aeromagnetic survey outline.

AMT is measured by calculating the ratio of the electric field (recorded with a dipole) and the orthogonal magnetic field (measured with an antenna). **Ex** and **Ey** refer to the directions of the array used to measure the electric field while **Hx** and **Hy** refer to the directions used to measure the magnetic field. Every **Ex** has an associated orthogonal **Hy** measurement, and every **Ey** has an associated **Hx**. Different array types are considered for acquiring the most beneficial data for a particular survey area. Typically, in a scalar survey only a single component, usually **Tm (Ex/Hy)** is measured while in a vector survey both **Tm** and **Te (Ey/Hx)** are measured. Vector AMT data measure additional components **Ey** and **Hx** which provide information about directionality. Vector array methodology was used at the study area.

The 100m spread used in the study area shown in Figure 5.3 measures:

$$Tm1 = Zxy1 = Ex1/Hy \quad (5.3)$$

$$Tm2 = Zxy2 = Ex2/Hy \quad (5.4)$$

$$Te1 = Zyx1 = Ey1/Hx \quad (5.5)$$

$$Te2 = Zyx2 = Ey2/Hx \quad (5.6)$$

The orientation of **X** is along the line while the orientation of **Y** is always perpendicular and the best response is achieved if **Y** is along the anticipated strike of the target conductor.

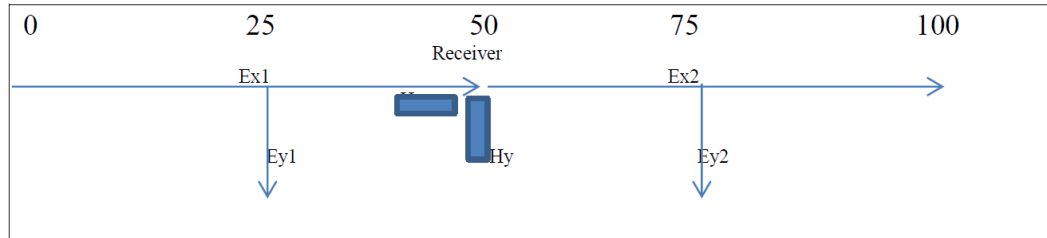


**Figure 5.3** - Typical 100m spread for the vector survey carried out at the study area.

The two horizontal magnetic field components **H<sub>x</sub>** and **H<sub>y</sub>** were measured by calibrated ANT/6 AMT coils. They were placed horizontally on stable ground making sure they are not affected by surface noise such as wind. Metal stakes were used as electrodes to measure the electric field. Contact resistance should be low and can be minimized by pouring water into the small prepared pit where the electrodes had been placed. Time series data were then collected in discrete bands from 3Hz to 8192Hz over 20 – 30 minute periods for each spread.

#### 5.4 Quality Control

Lightning storms can cause noise and will travel further where the surface material is resistive. Energy from lightning storms can damage equipment if it strikes near a station. Therefore recording should be ceased and equipment ‘unhooked’ when severe electrical storms are present or threatening. Wind vibrations on both the coils and the **E**-lines can seriously affect measurements, creating noise. Stations must not be located on topographic high as this will cause stripy effects in the data, primarily caused by distortion of the fields by the high topographic feature. Terrain also influences the **E**-lines if they are laid out on extreme slopes, effectively shortening the length of the **E**-lines without the acquisition unit recognizing the problem.

#### 5.5 Data Processing

All Audio-frequency Magnetotelluric (AMT) data processing and inversion for this study were carried out using a combination of Zonge® internal software and Geosoft® for mapping products. The aim of processing AMT/MT data is to image the subsurface distribution of conductors at depth. This is a multistage process in which Cagniard Resistivity (a frequency-dependent apparent resistivity calculation) and Impedance Phase data are calculated from electric **E**-field and magnetic **H**-field data (Zonge, 2010). The phase difference between the **E** and **H** components of the electromagnetic field is defined as the Impedance Phase. Both Cagniard resistivity and Impedance phase were used in

Zonge 1-D and 2-D inversion models to image actual resistivity changes associated with geology (Zonge, 2010).

## CHAPTER 6: GEOPHYSICAL DATA ENHANCEMENT

### 6.1 Introduction

This chapter looks at the various ways of geophysical data enhancement focusing mainly on magnetic data by making use of a range of linear and non-linear filtering algorithms. These algorithms can selectively enhance the anomalies due to one group of geological sources relative to other groups. Emphasis will be on the principles behind the enhancements and the usefulness of the enhancements in the interpretation of the data. After data are collected from the field (ground or airborne), several corrections can be applied to the data to produce profiles, contours and grid versions of 'processed' images like the total magnetic intensity, total radiometric count rate, and count rates for the potassium, thorium and uranium energy windows (Milligan and Gunn, 1997). It is however possible in many cases to apply various filtering and transformation processes in order to enhance the data and produce secondary products with improved visual information.

### 6.2 Linear transformations (filters)

The two most popular ways of filtering data are via the Fourier transform (frequency domain) and convolution (time domain). A linear filtering process in the frequency domain changes in a predetermined way, the amplitude and/or phase relationships of the assemblage of sine waves that constitutes every profile or gridded data set (Milligan and Gunn, 1997).

#### 6.2.1 Fourier transform

According to Dobrin and Savit (1988), Fourier transformation is based on the Fourier series, which expresses any function, such as a time signal of unlimited length (but in practice of limited length), as a summation of an infinitely long series of sine and cosine waves. As the series becomes infinitely long, the fundamental frequency which can be explained as the basic repetition frequency approaches zero. All harmonics (i.e. simple multiples of the fundamental frequency) are separated by infinitesimal increments and Fourier series, consisting of amplitude and phases for successive harmonics, become a continuous function after summation. Fourier transforms convert a data set into the frequency domain resulting in an in and out-of-phase spectrum, where a filter operation is applied by multiplication of some function to both spectra before converting the spectra back to the spatial domain.

Dobrin and Savit (1988) illustrated that the integral expression for a Fourier transform is in two parts, one for frequency spectrum  $F(n)$  in terms of the time function  $f(t)$ , and the



other for the time function in terms of frequency spectrum. The frequency function  $F(n)$  can be obtained from the time function  $f(t)$  by the integral:

$$F(n) = \int_{-\infty}^{\infty} f(t) \cos 2\pi n t dt - i \int_{-\infty}^{\infty} f(t) \sin 2\pi n t dt \quad (6.1)$$

where time is designated by  $t$  and frequency by  $n$

The transform  $f(t)$  of the frequency function  $F(n)$  can be similarly expressed by the integral:

$$f(t) = \int_{-\infty}^{\infty} F(n) \cos 2\pi n t dn + i \int_{-\infty}^{\infty} F(n) \sin 2\pi n t dn \quad (6.2)$$

The integral containing the cosine term is designated as real, while that containing the sine term is designated imaginary (i.e.  $i$ ). This complex representation is a mathematical convenience, as the two terms cannot be added directly but must be added vectorially.

Kearey *et al.*, (2002) described the time and frequency domain representations of a waveform,  $F(n)$  and  $f(t)$  as a Fourier pair, represented by the notation:

$$f(t) \leftrightarrow F(n) \quad (6.3)$$

Components of a Fourier pair are interchangeable meaning if  $F(n)$  is the Fourier transform of  $f(t)$ , then  $f(t)$  is the Fourier transform of  $F(n)$ .

When the number of data points can be confined to  $2^n$ ,  $3^n$ , or  $5^n$  ( $n$ =integer) then the process of calculating a Fourier Transform and its reverse can be very much expedited as discovered originally by Vern Herbert in 1962 and later widely publicized by Cooley and Tukey (1965) and others e.g. Claerbout (1976). It is then referred to as a Fast Fourier Transform (FFT) and using the identical algorithm twice transforms time domain data into the frequency domain and back into the time domain.

There are a multitude of mathematical expressions that can be applied to the data once in the frequency domain that are capable of enhancing or suppressing different frequencies. Low pass filters attenuate high frequency data and accentuate low frequency data while high pass filters do the opposite and these filters can even be directional (Heath, 2007). Fortunately the application of these filters is very easy in today's data manipulation software such as Geosoft® and Intrepid®.

### 6.2.2 Convolution

Another way of filtering is by convolving the data set in the space domain with a set of filter coefficients whose frequency response (i.e. Fourier transform) is the same as the desired amplitude and phase changes. This method is referred to as convolution (Milligan

and Gunn, 1987). In the convolution method, data are filtered in the space domain using a moving window with an associated filter response,  $w(x,y)$ , which is convolved with the data,  $D(x,y)$ . The result of the convolution is a new dataset  $D'(x,y)$ . This filter is explained below in Figure 6.1:

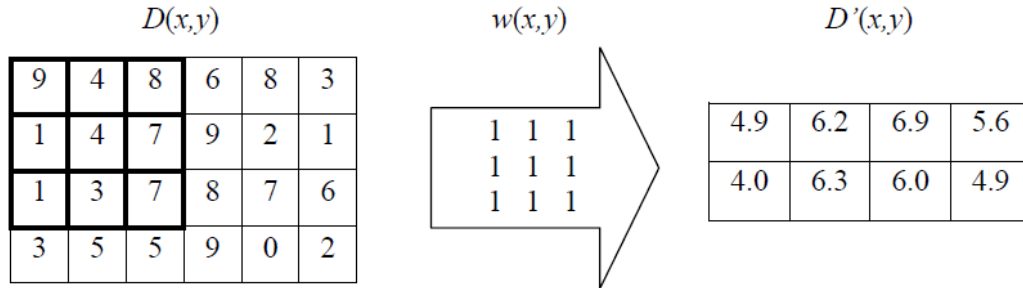


**Figure 6.1** - Schematic example of a spatial 3 x 3 smoothing filter kernel. Note the 6 x 4 input grid is reduced to a 4 x 2 filtered grid, after Cooper (2004).

The data point in the centre of the highlighted 3 x 3 window above (i.e. 4) undergoes a mathematical process, relating to the window and surrounding data points. In this case, each of the nine points are multiplied by the corresponding value in the window (i.e. 1), summed and then divided by the number of points in the window (i.e. 9). This produces an average of the surrounding points. The window then moves on to the next point (i.e. 7) and the mathematical averaging is repeated. This is continued through the dataset, thus producing a newly filtered dataset (Coomber, 2008). However it must be appreciated that filtering via convolution is much slower than filtering in the frequency domain.

### 6.3 Upward and downward continuation

Computing potential fields at higher or lower levels is referred to as upward or downward continuation. Upward continuation is usually applied to ground survey data when comparing it to airborne data or to remove high frequency noise. Vertical continuation can be applied when smoothing data and merging airborne surveys that have been flown at different heights (Coomber, 2008).

According to Dean (1958), the filter operator for profile data in the frequency domain is:

$$F'(u) = F(u)e^{-uz} \quad (6.4)$$

Where  $u$  is the frequency and  $z$  is the distance above or below the point of measurement ( $z$  being positive or negative, respectively).

This means that upward continuation smooths out high-frequency anomalies relative to low-frequency anomalies. It is considered a clean filter because it produces almost no side effects that may require the application of other filters or processes to correct. This

can be useful in suppressing the effects of shallow anomalies while enhancing deeper anomalies.

Downward continuation is a high pass filter which sharpens the effects of high frequencies by bringing them closer to the plane of observation (flying the survey closer to the ground). But this filter enhances high frequency noise as well as geological anomalies, and it is normally difficult to continue a field downward very far with the practical limits depending on the sample interval and the quality of the dataset (Milligan and Gunn, 1997).

#### **6.4 Reduction to the pole**

This process involves converting the magnetic field from a magnetic latitude where the Earth's magnetic field is inclined, to the field at a magnetic pole, where the inducing field is vertical. When the earth's field is inclined, magnetic anomalies due to induction have forms that are asymmetrically related to their sources, but when the inducing field is vertical (magnetic pole), the induced anomalies are directly over their sources (Milligan and Gunn, 1997). This process is important in simplifying the interpretation of magnetic data. According to Milligan and Gunn (1997), there are problems which can arise in the reduction to pole process at magnetic latitudes that are less than  $15^{\circ}$  since the Fourier domain transformation process becomes unstable owing to the need to divide the spectrum by a very small term.

#### **6.5 Derivatives**

##### **6.5.1 Vertical Derivatives**

The first vertical derivative (vertical gradient) is physically equivalent to measuring the magnetic field simultaneously at two points which are vertically above each other, subtracting the data and dividing the result by the vertical spatial separation of the measurement points. The vertical gradient of the first vertical derivative is referred to as the second vertical derivative and so on (Milligan and Gunn, 1997). This process enhances high frequencies as compared to low frequencies and this property forms the basis for the application of the derivative process which eliminates long-wavelength regional effects and resolves the effects of adjacent anomalies. The second vertical derivative has even more resolving power than the first vertical derivative but must be applied to high quality data because its greater enhancement of high frequencies results in greater enhancement of noise (Milligan and Gunn, 1997). As with other filters that enhance the high wavenumber components of the spectrum, it is often necessary to apply an additional low-pass filter to remove high wavenumber noise.

### 6.5.2 Horizontal Derivatives

According to Milligan and Gunn (1997), this process involves a phase transformation as well as an enhancement of high frequencies. The phase transformation generally has the result of producing anomaly peaks approximately located over the edges of wide bodies and the enhancement of high frequencies sharpens these peaks to increase the definition of the body edges. This can be used in mapping body outlines but becomes extremely ambiguous for narrow bodies.

### 6.5.3 Tilt Angle Derivative

The tilt angle derivative is denoted by the following formula (Nabighian, 1972)

Tilt Angle Derivative (TDR) = arc tan (Vertical Derivative / Total Horizontal Derivative)

where Vertical Derivative =  $dT/dz$ , and the total horizontal derivative is (THDR) =  $\sqrt{(dT/dx)^2 + (dT/dy)^2}$  and Total magnetic Intensity is represented by T.

TDR derivative is restricted within range  $+\pi/2$  to  $-\pi/2$  (Salem & Fairhead 2007; Ghosh and Dasgupta, 2013)

This filter is useful for mapping shallow basement structures and targets as can be seen in Figure 7.11.

## 6.6 Analytic Signal

The analytic signal (Milligan and Gunn, 1997) is a function related to magnetic fields by the derivatives. It is the square root of the squares of the derivatives in the x, y, and z directions, i.e.

$$\text{Analytic signal: } |A(x,y)| = \sqrt{\left(\frac{\partial m}{\partial x}\right)^2 + \left(\frac{\partial m}{\partial y}\right)^2 + \left(\frac{\partial m}{\partial z}\right)^2} \quad (6.5)$$

where  $m$  = magnetic anomaly

Milligan and Gunn (1987) noted that although function 6.5 is not a measurable parameter it is quite interesting in the context of interpretation. It is completely independent of the direction of both the magnetization and that of the Earth's field which means all bodies with the same geometry have the same analytic signal. The peaks of analytic signal functions are symmetrical and occur directly over the edges of wide bodies and directly over the centres of narrow bodies (Figure 7.10). This makes the interpretation of analytic signal maps simple, and provides easily understood indications of magnetic source geometry.

## **CHAPTER 7: GEOPHYSICAL DATASETS**

This chapter presents the different datasets used for this study.

Ground magnetic survey data as well as high resolution aeromagnetic survey (1496 line-km) data and the different types of data enhancement will be given.

SPECTREM Air Limited simultaneously collects electromagnetic, total field magnetic (TMF), gamma-ray radiometric and digital elevation measurements. Late time channel TDEM data and also late time constants as interpreted grids are part of the output. Total field magnetic and radiometric data collected by SPECTREM® are presented as gridded colour images.

Ground EM datasets for both the Low-temperature SQUID and the Fluxgate sensor in separate surveys are depicted for the late time channels as well as gridded images of the late time data. DHEM data from selected boreholes augment the above.

Drilling results will be presented and used to create a 3D starting model for geophysical modelling.

The entire processing, data enhancement and presentation in this chapter was done using Geosoft Oasis Montaj, EMIT's Maxwell software and Zonge internal software.

### **7.1 Physical Property Measurements Data**

It has been mentioned earlier that the successful application of geophysics depends on gaining knowledge of the physical properties of the Earth section being examined. Contrasting physical properties between host environment and the target must be identified in order to enable selection of the appropriate geophysical technique.

#### **7.1.1 Magnetic Susceptibility and Relative Conductivity**

Physical property measurements (magnetic susceptibility and conductivity) were carried out on the drill core by the author. Magnetic susceptibility measurements were carried out using a Kappameter KT6 while the conductivity measurements were carried out using a Scintrex CTU-2 testing unit. Figure 7.1 shows borehole JMP001 results as strip logs.

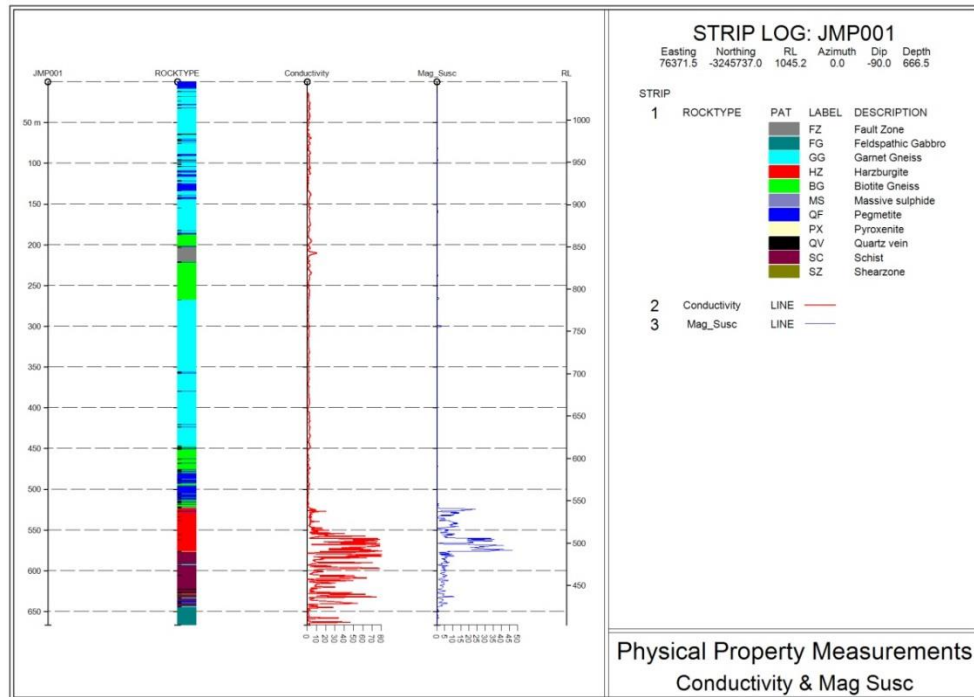


**Figure 7.1** - Strip log of borehole JMP001 showing how the relative conductivity (red trace) and magnetic susceptibility (blue trace) (in  $10^{-3}$  SI units) varies for the different rock units. Massive sulphide stringers and net textured sulphides are highly conductive as well as highly magnetically susceptible.

It can clearly be seen from the profiles for borehole JMP001 that the country gneiss rock is neither conductive nor is it magnetically susceptible. However, the results show elevated values of magnetic susceptibility and relative conductivity for the intrusion with higher values for the net textured harzburgite and massive sulphide stringers. The poorly mineralised tremolite schist is more magnetically susceptible than the gneiss host rock but less magnetically susceptible than the well mineralised harzburgite. The well mineralised harzburgite is more conductive than both the gneissic country rock and the poorly mineralised tremolite schist. An assumption was made that for Transient Electromagnetics (TEM) techniques, at late decay times current will gather in the more conductive, well mineralised net-textured harzburgite and massive sulphide stringer zones. Therefore modelling EM and magnetic data could potentially indicate the higher grade zones rather than the lower grade tremolite schist mineralisation making it possible to map and delineate these well mineralised zones (Ushendibaba *et al.*, 2013).

## 7.2 Palaeomagnetic Laboratory Measurements

Remanent and induced magnetizations are both significant contributors to almost all magnetic anomalies. It was therefore necessary to carry out some palaeomagnetic laboratory analysis. Measuring remanent magnetization is crucial to determining confidence in the targeting model because, in conjunction with magnetic susceptibility determinations, it provides a sound basis for calculation of the resultant (induced +

remanent) magnetisation of the source (Austin and Foss, 2014). All the laboratory procedures and measurements on core samples were carried out by the author under the guidance of Dr Leonie Mare at the Council for Geoscience (CGS) based in Pretoria. Borehole JMP001 was selected for the palaeomagnetic studies since it intersected the country rock, the tremolite schist as well as the well mineralised harzburgite. The samples were prepared by cutting them into smaller specimens, cubes in shape measuring 2cm x 2cm x 2cm (Figure 7.2) using a copper disc cutter (to prevent introducing magnetisation).

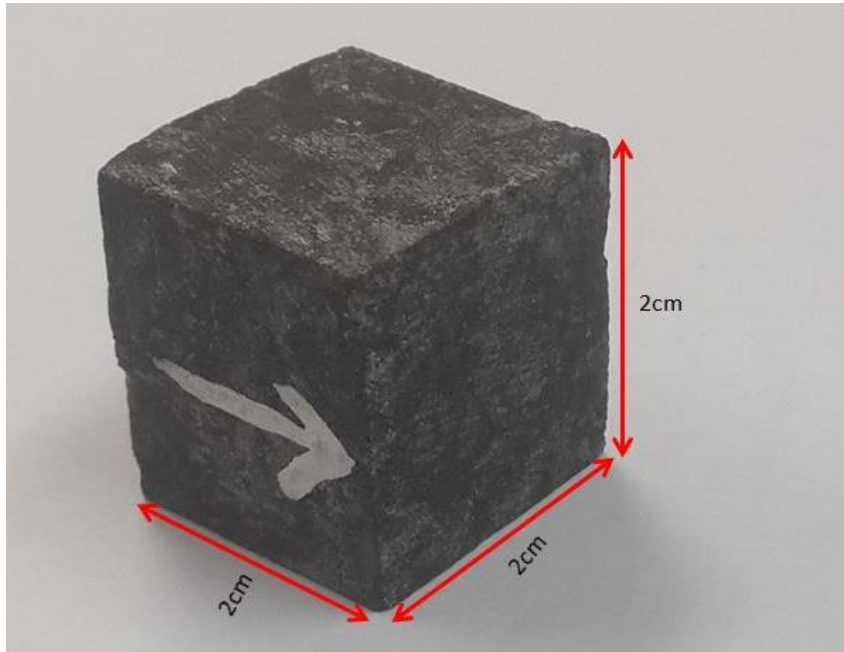


**Figure 7.2** - Prepared specimen of the well mineralised harzburgite for Palaeomagnetic measurements. The white arrow shows the orientation of the specimen going down.

The aim of the analysis was to determine the presence of remanent magnetisation and if it existed measure its intensity and direction. This procedure involves measurement of Natural Remanent Magnetisation (NRM), susceptibility and finally progressively demagnetising the specimens using alternating field (AF). The information gathered was then used during modelling of magnetic data.

### **7.2.1 Magnetic Susceptibility Measurements**

Bulk magnetic susceptibility determinations were carried out using the MFK1 Kappabridge meter before the demagnetisation process was performed. Four prepared core specimens collected from borehole JMP001 were analysed (i.e. well mineralised harzburgite, tremolite schist which hosts disseminated mineralisation, feldspathic gneiss and quartz feldspar gneiss which forms part of the country rock). The bulk susceptibility measurements results are presented in Table 7.1.

**Table 7.1** - Bulk Susceptibility measurements of core samples for borehole JMP001 in SI units.

<b>Specimen</b>	<b>Bulk Susceptibility</b>
Harzburgite	$3.3 \times 10^{-2}$
Tremolite Schist	$1.24 \times 10^{-2}$
Feldspathic Gneiss	$4.31 \times 10^{-3}$
Quartz Feldspar Gneiss	$8.71 \times 10^{-4}$

The net susceptibility resulting from contributions of all minerals but usually dominated by the ferromagnetic minerals is referred to as bulk susceptibility (Butler, 1992). It can clearly be seen that the well mineralised harzburgite is two times more susceptible than the tremolite schist that hosts disseminated style mineralisation. The well mineralised harzburgite is also 7 times more magnetically susceptible than the country rock. It was therefore anticipated that it is possible to model the well mineralised harzburgite using magnetic data.

### **7.2.2 Demagnetisation of rock specimens**

NRM is total remanent magnetisation present in a rock sample prior to laboratory treatment. After measuring the bulk susceptibility, the specimens were subjected to Alternating Field (AF) demagnetisation to remove components of NRM using a progressive AF demagnetiser (Figure 7.3). The demagnetisation process was conducted in a Faraday cage shown again in Figure 7.3 which shields Earth's magnetic field. All specimens were incrementally demagnetized using an alternating field by increasing intensity at each stage to progressively demagnetise the specimens and remove components of NRM. There are components that can easily be removed and these are referred to as low-stability components. Removal of low-stability components by partial demagnetisation allows isolation of the more resistant high stability components. In many cases, the high-stability component can logically be inferred to be a primary NRM, while the low-stability component is inferred to be a secondary NRM (Butler, 1992).

However, according to Butler (1992) it is not always the case that the high stability component is the primary NRM. A terminology has been introduced to deal with this potential difficulty. These high-stability components of NRM are referred to as the characteristic component (ChRM) of NRM. ChRM direction can be determined by partial demagnetisation but this process cannot directly determine whether it is primary ChRM or not; additional information is needed in order to infer whether the ChRM is primary. The purpose of the term characteristic component is that this term can be applied to results of partial demagnetization experiments without the connotation of origin time attached to the term primary NRM (Butler, 1992). The demagnetisation processes was performed progressively by increasing the intensity of the demagnetising field and then measuring



the intensity of magnetisation of the specimen using the JR-6A spinner magnetometer shown in Figure 7.4 at each stage.

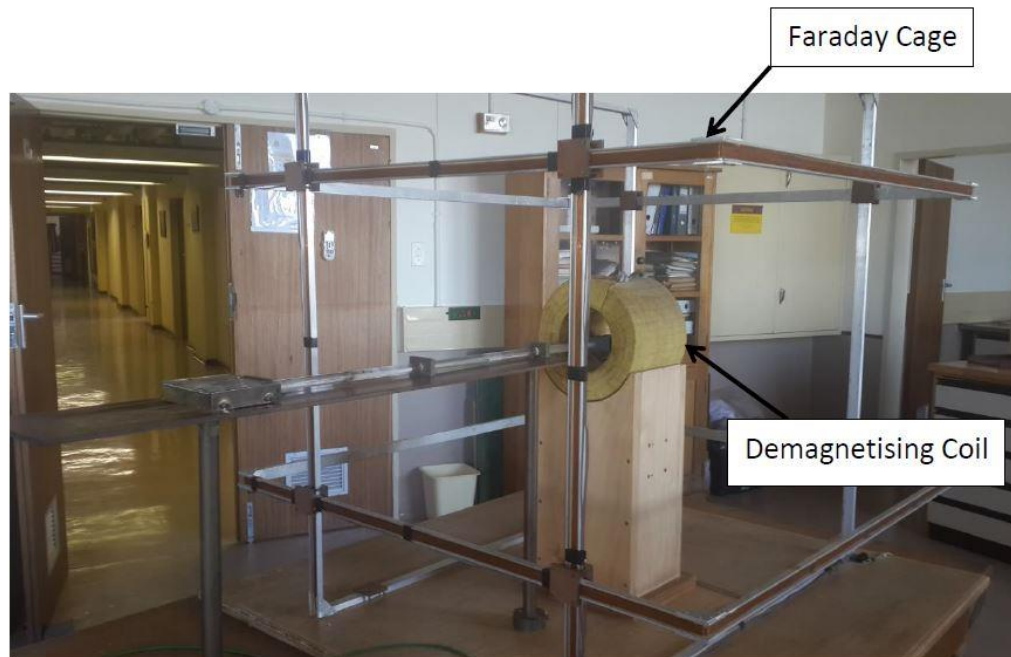


**Figure 7.3** - The AF demagnetiser used for progressively demagnetising samples at CGS by applying alternating fields.

### 7.2.3 Measurement of NRM

After each stage of demagnetising the specimen, a measurement of the remanent magnetisation was carried out using a JR-6A spinner magnetometer. The JR-6A spinner magnetometer (Figure 7.4) is used as a laboratory instrument for measurements of remanent magnetisation of rock specimens in studies of magnetic properties of rocks. A rock specimen of defined size and shape is rotated at a constant angular speed in the pick-up unit inside a pair of coils. An AC voltage is induced in the coils whose amplitude and phase depend on the magnitude and direction of the remanent magnetisation (RM) vector of the specimen. The voltage is amplified, filtered and digitized. By fourier analysis the computer calculates two rectangular components of the projection of RM vector into the plane perpendicular to the axis of rotation (JR-6A User's Manual, 2004).



**Figure 7.4** - The JR-6A spinner magnetometer used for measuring NRM at CGS showing the sample position.

Three components  $M_x$ ,  $M_y$  and  $M_z$  of the magnetic moment are measured in sample coordinates. This involves taking a number of measurements for each component, allowing evaluation of homogeneity of NRM in the specimen and a measure of signal-to-noise ratio. Data are fed into a computer that contains orientation data for the sample, and calculation of the best-fit direction of NRM in sample coordinates and in geographic coordinates is performed (Butler, 1992).

The results for NRM in A/m are shown for each demagnetising field intensity measured in mT as shown in Table 7.2 and as normalised values in Table 7.3.

**Table 7.2** – NRM results in A/m for each demagnetising field intensity measured in mT for the four specimens.

Intensity (mT)	Harzburgite NRM(A/m)	Tremolite Schist NRM(A/m)	Feldspathic Gneiss NRM(A/m)	Quartz Feldspar Gneiss NRM(A/m)
0	1.825	3.215	3.243	0.3085
3	1.379	1.824	2.408	0.2387
5	0.88	1.25	1.761	0.08335
7.5	0.7032	1.058	0.6899	0.09319
10	0.6533	0.4678	0.398	0.03539
12.5	0.4694	0.7252	0.03808	0.06569
15	0.5382	0.8974	0.1234	0.03114
17.5	0.6805	0.3732	0.09626	0.03692
20	0.876	0.4234	0.2012	0.01774
25	0.6734	0.3313	0.2146	0.08828
30	0.646	0.413	0.2548	0.07557

**Table 7.3** – Normalised NRM values for the four specimens.

Intensity (mT)	Harzburgite (normalised)	Tremolite Schist (normalised)	Feldspathic Gneiss (normalised)	Quartz Feldspar Gneiss (normalised)
0	100	100	100	100
3	75.561644	56.734059	74.252236	77.374392
5	48.219178	38.880249	54.301573	27.017828
7.5	38.53151	32.90824	21.27259	30.20746
10	35.79726	14.55054	12.27259	11.47164
12.5	25.72055	22.55677	1.174221	21.29335
15	29.49041	27.91291	3.805119	10.0994
17.5	37.28767	11.60809	2.968239	11.96759
20	48	13.16952	6.204132	5.750405
25	36.89863	10.30482	6.61733	28.61588
30	35.39726	12.84603	7.856923	24.84603

The results show a decrease in the value of NRM for each sample after every demagnetization stage. The results can be plotted using Rema6w software as shown in Figure 7.5 for further analysis.

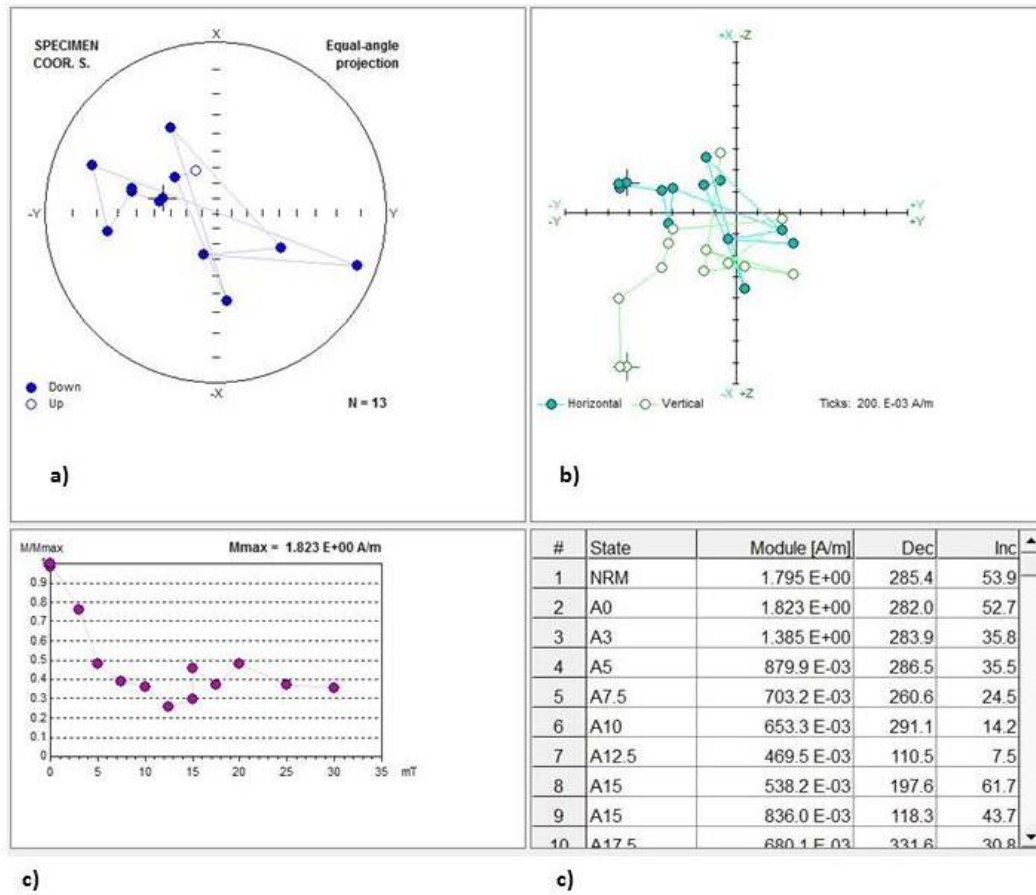


**Figure 7.5** – Demagnetization results of the well mineralised harzburgite plotted in Rama6w software.

By plotting the NRM vectors it is possible to recognise different components of NRM, and ultimately determine the ChRM in the samples. In order to pick the NRM and ChRM components, one has to examine the horizontal and vertical plots in Figure 7.5b. A component may be identified if the horizontal and vertical projections are co-linear over the same measurements. The ChRM component also has to be co-linear but at the same time the points have to project towards the origin (Butler, 1992) in Figure 7.5b. If they do not project towards the origin as in this case, they are considered as a younger overprint and not the ChRM components i.e. not the magnetisation acquired at time of formation. The plot for the synthetic data in Figure 7.5b for the well mineralised harzburgite does not show different components of the NRM. Therefore the NRM of the deposit is very weak and will not affect the modelling results.

#### 7.2.4 Calculating the Koenigsberger Ratio

In general, the Koenigsberger ratio is used as a measure of the stability to indicate a rock's capability of maintaining a stable remanent magnetisation. Low value of the Koenigsberger ratio indicates that minerals have unstable remanent magnetisation and are more susceptible to an external magnetic field (Irving, 1964). An example of calculating the Koenigsberger ratio is given below for the well mineralised harzburgite:

At Jacomynspan project area, the geomagnetic field is approximately 26800 nT, the magnetising force  $H$  is given by:

$$H = \frac{B}{\mu(1+k)} \quad (7.1)$$

where  $B$  is Magnetic field in Tesla,  $\mu_0$  is magnetic permeability of free space given by  $4\pi \times 10^{-7}$  H/m and  $k$  is magnetic susceptibility of air which  $\sim 0$ .

$$\text{Magnetising force } H, \text{ at Jacomynspan} = \frac{2.6800 \times 10^{-5}}{4\pi \times 10^{-7}} = 21.3268 \text{ A/m}$$

The Koenigsberger Ratio for the well mineralised harzburgite with magnetic susceptibility  $k = 0.033$  and NRM = 1.825 A/m is given by:

$$Q = \frac{J}{kH} = \frac{1.825}{0.033 \times 21.3268} = 2.59$$

NRM value used (1.825) is the value when no demagnetization has been applied i.e. demagnetizing intensity is zero.

The calculated Koenigsberger ratios for all the tested specimens are shown in Table 7.4:

**Table 7.4** – Koenigsberger Ratios for the four different specimens

Specimen	Koenigsberger Ratio
Well mineralised Harzburgite	2.59
Tremolite Schist	12.16
Feldspathic Gneiss	35.28
Quartz Feldspar Gneiss	16.61

The significance of these Koenigsberger ratios will be explained in the next section.

#### 7.2.5 Summary of the Palaeomagnetic Results

Looking at the Koenigsberger ratios in Table 7.4, it is apparent that the well mineralised harzburgite has a much lower Koenigsberger ratio than the tremolite schist and the country gneissic rocks. This indicates that the well mineralised harzburgite has unstable remanent magnetisation and is more susceptible to an external magnetic field (Irving,

1964). This can be explained in terms of shape anisotropy of the individual grains. The capability of maintaining a stable remanent magnetization can be explained in terms of anisotropies. Single-domain (SD) grains have uniform magnetization with  $\mathbf{j} = \mathbf{j}_s$  (saturation magnetisation). Therefore application of a magnetic field cannot change the intensity of magnetization but can only rotate  $\mathbf{j}_s$  towards the applied field but there are resistances to a rotation of  $\mathbf{j}_s$ . These resistances are known as anisotropies that lead to energetically preferred directions for  $\mathbf{j}_s$  within individual SD grains (Butler, 1992). The dominant anisotropies are shape anisotropy and magnetocrystalline anisotropy. A highly elongated ferromagnetic grain has much lower magnetostatic energy if magnetized along its length (Figure 7.6a) rather than perpendicular to its length (Figure 7.6b).



**Figure 7.6 – a)** Surface magnetic charge produced by magnetization of a Single Domain (SD) grain along the long axis of the grain. The arrow indicates the direction of saturation magnetization  $\mathbf{j}_s$ ; plus and minus signs indicate surface magnetic charges; note that magnetic charges are restricted to the ends of the grain, **b)** Surface magnetic charge produced by magnetization of an Single Domain (SD) grain perpendicular to the long axis of the grain. The arrow indicates the direction of saturation magnetization  $\mathbf{j}_s$ ; plus and minus signs indicate surface magnetic charges; note that magnetic charges appear over the entire upper and lower surfaces of the grain. (Butler, 1992).

This can be explained in terms of the percentage of surface covered by magnetic charges which is small when  $\mathbf{j}_s$  points along the long dimension of the grain (Figure 7.6a). As can be seen in Figure 7.6b, magnetization perpendicular to the long axis leads to a substantial surface charge. This therefore means the internal demagnetizing factor along the long axis is much less than the internal demagnetizing factor perpendicular to the long axis (Butler, 1992). The microscopic coercive force for elongate grains of magnetite is dominated by shape anisotropy. Maximum shape anisotropy is displayed by needle-shaped grains. The grains of the tremolite schist are needle-shaped thus explaining their higher Koenigsberger ratios than the harzburgite. Using both the NRM vector plots and the Koenigsberger ratios, the Jacomynspan deposit does not show significant NRM and this will not be considered during modelling.

### 7.3 Ground Magnetic Survey Data

A ground magnetic survey was carried out over the study area at 50m line spacing and 10m station spacing. The total field magnetic intensity image maps the sub-outcrop of the east-west trending ultramafic rocks.

### 7.3.1 Total Magnetic Field Intensity Data

Ground magnetic survey data are prone to surface magnetic noise due to the close proximity of the sensor to the ground. It is therefore essential to level the data using algorithms available in Geosoft. The levelled data are shown in Figure 7.7.

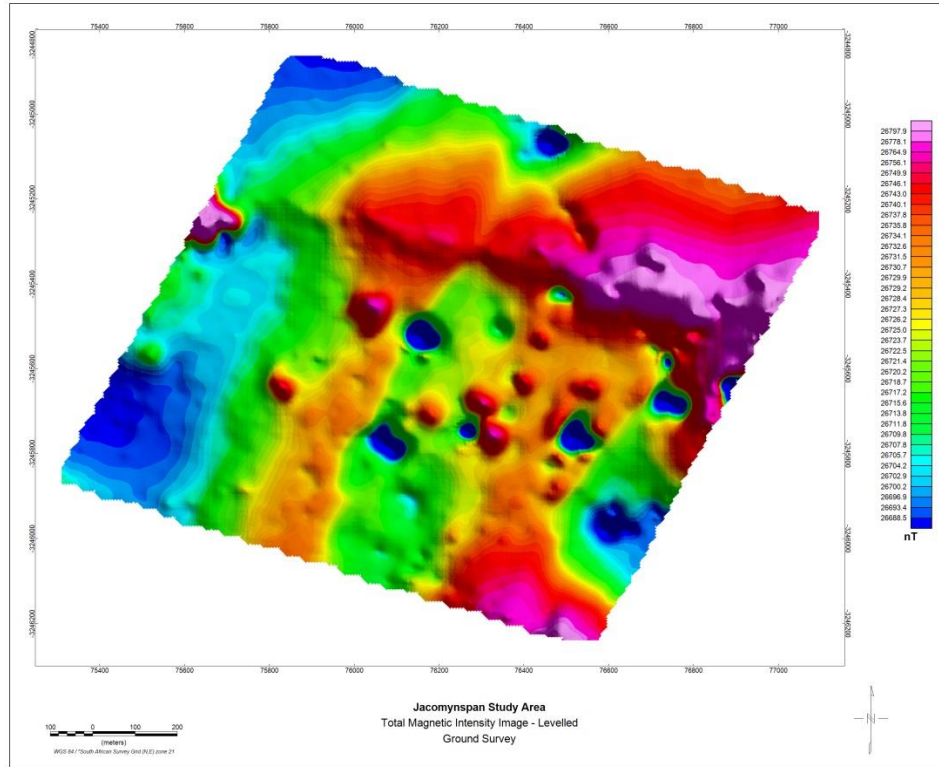


**Figure 7.7** - Levelled Total Field Magnetic Intensity Image – ground survey.

As will be seen later in this chapter, the airborne data are superior in quality to the ground data and the anomaly of interest stands out better on the airborne data. “It is a well-known fact that airborne magnetic data at a low flying height is much superior to data collected on the ground. On the ground you are much too near local sources of noise, the effects of which are never completely removed with whatever magical filter” (Stettler, personal communication 2015). Therefore the high resolution airborne data was used in the modelling of the magnetic data. However, the ground magnetic data were useful in positioning the fixed transmitter loop for ground EM survey since the survey was carried out before the airborne survey.

### 7.3.2 Upward continuation of ground magnetic data

The ground magnetic data were upward continued to 30m which is the height at which the high resolution aeromagnetic data were flown for comparison (Figure 7.8).



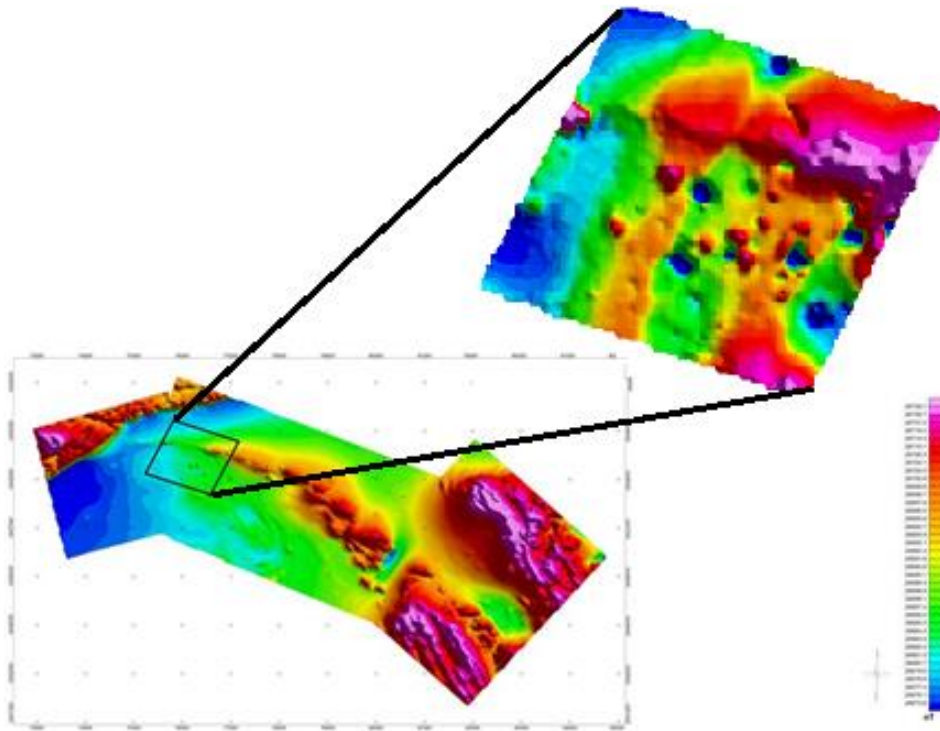


**Figure 7.8** - High resolution Total Magnetic Intensity image (*bottom*) and the ground Total magnetic Intensity upward continued to 30m above ground (*Top*).

The upward continuation filter does smooth out high-frequency anomalies relative to low-frequency anomalies. It is considered a clean filter because it produces almost no side effects that may require the application of other filters or processes to correct. This can be useful in suppressing the effects of shallow anomalies while enhancing deeper anomalies.

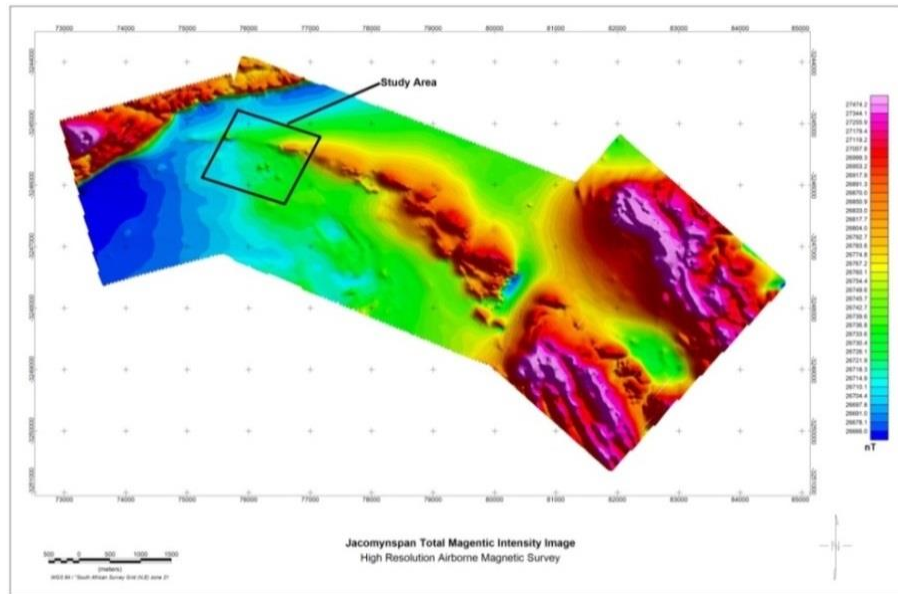
#### **7.4 High Resolution Aeromagnetic Survey Data**

The high resolution survey was carried out by Xcalibur Airborne Geophysics during June 2011. The data collected consisted of magnetic and digital terrain/elevation measurements (DTM). The line spacing was 30m and 3 blocks were flown in different line orientations due to anticipated strike changes in geology. The technical specifications for the survey have already been given in section 2.2. The aim of the airborne survey was to cover the strike extent of historical drilling and determine the structure and setting of the intrusion.

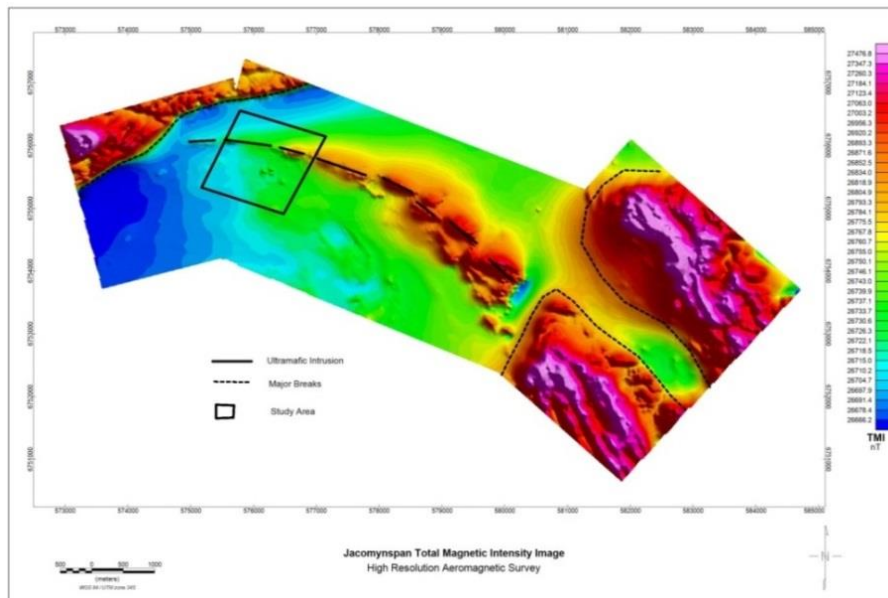
##### **7.4.1 Total Magnetic Field Intensity Data**

The Total Magnetic Intensity (TMI) image (Figure 7.9a) was produced by gridding the diurnally corrected and levelled TMI readings from the database supplied by Xcalibur. The gridding was performed using Geosoft Oasis Montaj software. Major annotations like major breaks and the ultramafic intrusion are shown in Figure 7.9b.





a)



b)

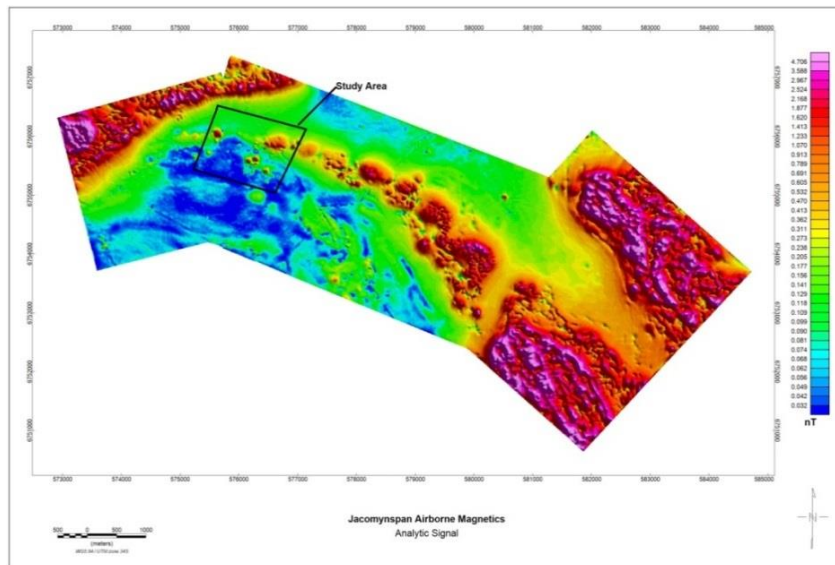
**Figure 7.9** a) - High resolution Total Magnetic Intensity image for the Jacomynspan project. b) - High resolution Total Magnetic Intensity image for Jacomynspan project showing the outline of the ultramafic intrusion and some major breaks.

As stated earlier, total magnetic intensity responses can give an idea of the major changes in the magnetite or other magnetic minerals content in the underlying rocks and unconsolidated overburden. Major breaks indicated in the image are clearly evident in the airborne TMI image (Figure 7.9b). The amplitude of magnetic anomalies, relative to the regional background, helps in identifying specific magnetic and less-magnetic rock units related to, in this case, mafic to ultramafic intrusives, felsic intrusives, gneiss or sediments. However, differences in mineralogy of geological sources do not produce differences in magnetic signature unless it is accompanied by differences in magnetic

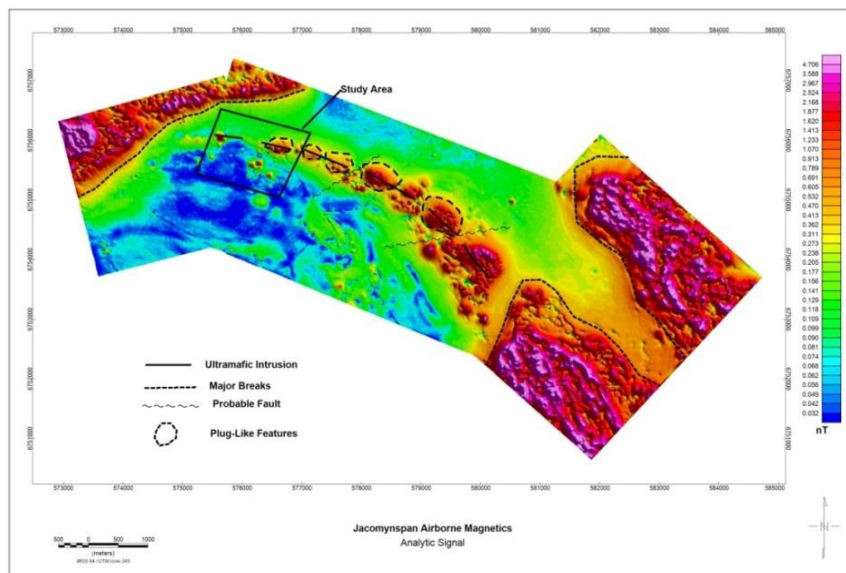
mineral content but this ambiguity has been reduced considerably because basic geological information is available.

#### 7.4.2 Analytic Signal of Aeromagnetic data.

The analytic signal was produced in Geosoft as one of the available modules and the result is shown in Figure 7.10a with annotations shown in Figure 7.10b.



a)



b)

**Figure 7.10 a)** - Analytic signal image of the Total Magnetic Intensity for Jacomynspan project. **b)**- Analytic signal image showing edges of the magnetic source bodies and major breaks.

The analytic signal was useful in locating the edges of magnetic source bodies especially where remanence and/or low magnetic latitude complicates interpretation. The Analytical Signal (AS) image mapped the boundaries of magnetic bodies. Subtle breaks in the harzburgite orebody are visible and interesting plug-like bodies suggesting that the

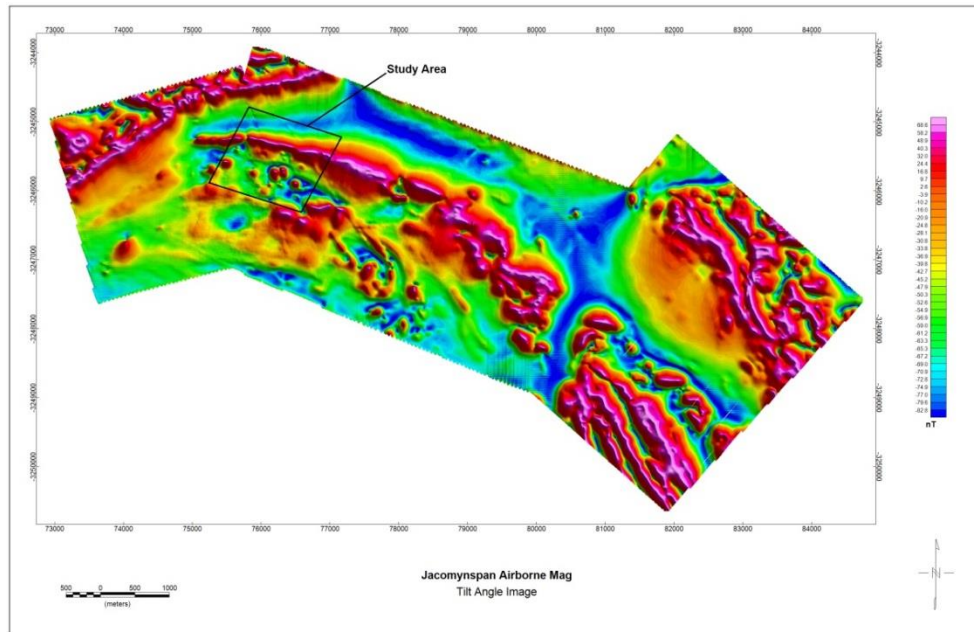
intrusion is not a continuous body. Major breaks are also indicated in Figure 7.10(b) image.

#### **7.4.3 Tilt Angle Vertical Derivative of the Aeromagnetic Data**

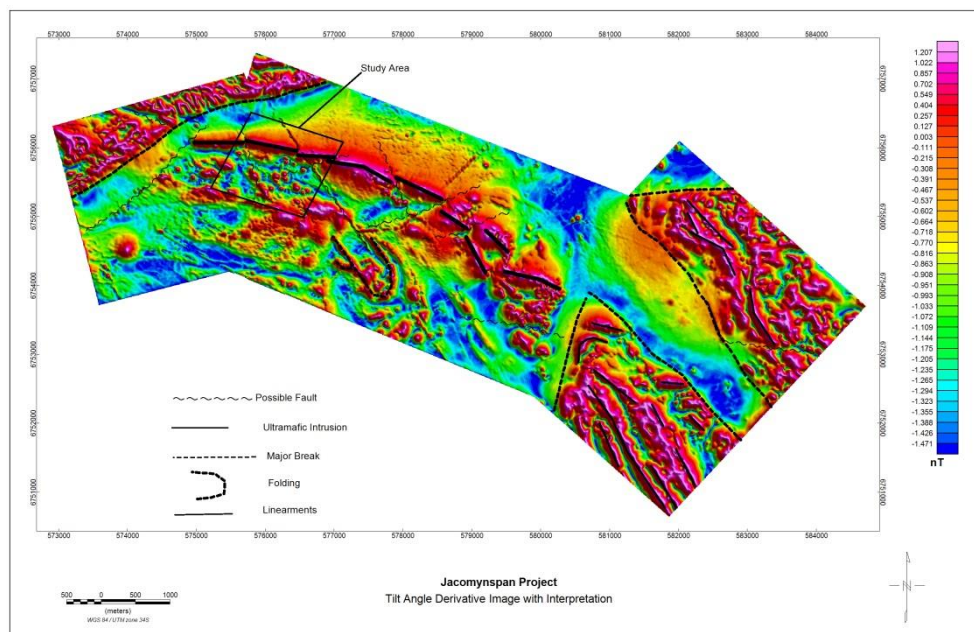
The tilt angle (TA) vertical derivative image was calculated with algorithms available in Geosoft and the image is shown in Figure 7.11(a) with annotations in Figure 7.11(b). Positive tilt angle values overlay a magnetic body, thus making it easier to identify the location and shape of the body as can be seen in Figure 7.11(b) where more detail appears. The 1<sup>st</sup> vertical derivative of the tilt angle sharpens the pattern and thus enhances the accuracy with which boundaries can be discerned.

The enhancement of shallow basement structures can clearly be seen in the image (Figure 7.11(a&b)). Since the total magnetic intensity (TMI) anomaly may represent the magnetic signal of two or more closely spaced bodies within such an anomaly, the tilt angle derivative of the TMI response was helpful in separating the individual anomalies of the closely spaced bodies. It is most useful in mapping near surface lineaments and other subtle magnetic structures that are partially masked by overbearing higher amplitude magnetic features.

The tilt angle vertical derivative image clearly maps the total strike length of the ultramafic intrusion. The east-west trending ultramafic rocks over the study area are clearly visible in the image. It mapped approximately 6km of highly prospective strike extend for the sulphide mineralisation. Other structures like folding and major breaks are now evident in the tilt angle image.



a)



b)

**Figure 7.11 a)** - The Tilt angle vertical derivative image for Jacomynspan **b)** - The Tilt angle vertical derivative image for Jacomynspan clearly mapping approximately 5km of highly prospective strike extent for the sulphide mineralisation.

From the TA the depth to source and the boundaries of the bodies can be calculated in an automated way by making use of the formula as published by Salem *et al.*, (2007) which is strictly only valid for vertical contacts. Figure 7.12 gives a plot of the boundaries as determined with a FORTRAN algorithm written by Stettler (personal communication, 2015) not available in Geosoft and that allows for dipping contacts. The boundaries are indicated by dots below and multi-edge dots indicate the bodies dipping to the south as is

well known from the borehole information. The stripeyness of the edge solutions along longitude 21° 47' are either due to noise in the magnetic grid because of a change in flight line direction or due to shallow dipping magnetic units being present here.

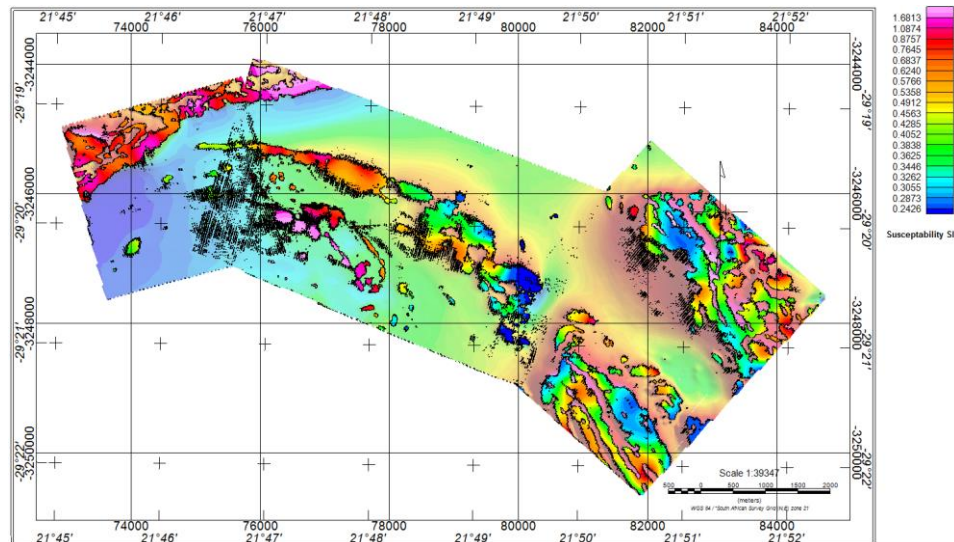


**Figure 7.12** – A plot of the boundaries as determined from the TA with a Fortran algorithm (Stettler, personal communication, 2015). It also depicts the calculated magnetic susceptibility for each body determined in an automated way.

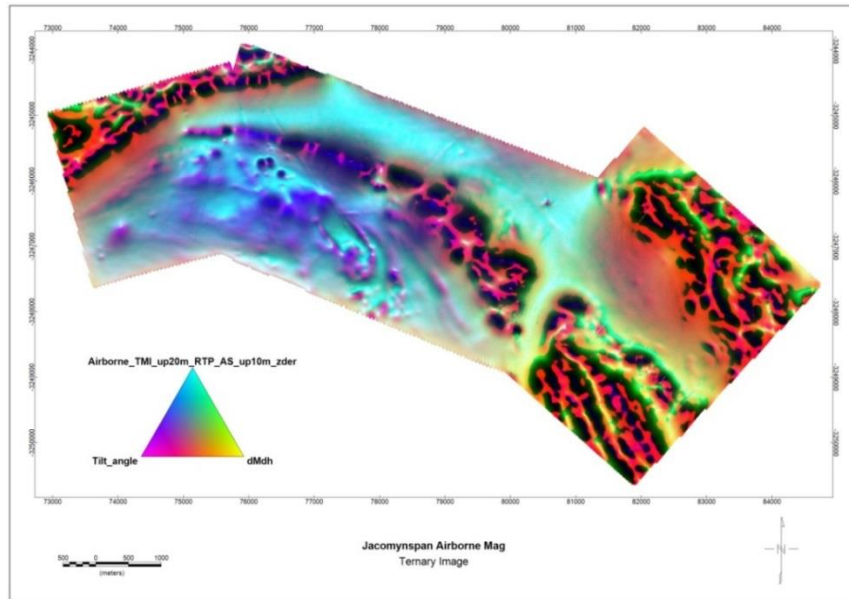
Figure 7.12 also depicts the magnetic susceptibility for each body also determined in an automated way and is calculated from an over determined solution from which both depth and susceptibility are obtained. Most of the depths came out shallow and have not been indicated on the map. An interesting feature is that the western segment of the Jacomynspan body has a lower calculated magnetic susceptibility than the central part which is again higher than the eastern segment. There are only a few boreholes in the central segment drilled by Anglo American in the 1970's but the susceptibilities' of the material are not known to the author and a possible reason for this phenomenon is that the material in the central segment is more serpentinised than the flanks.

#### 7.4.4 Magnetic Ternary Image of the aeromagnetic data

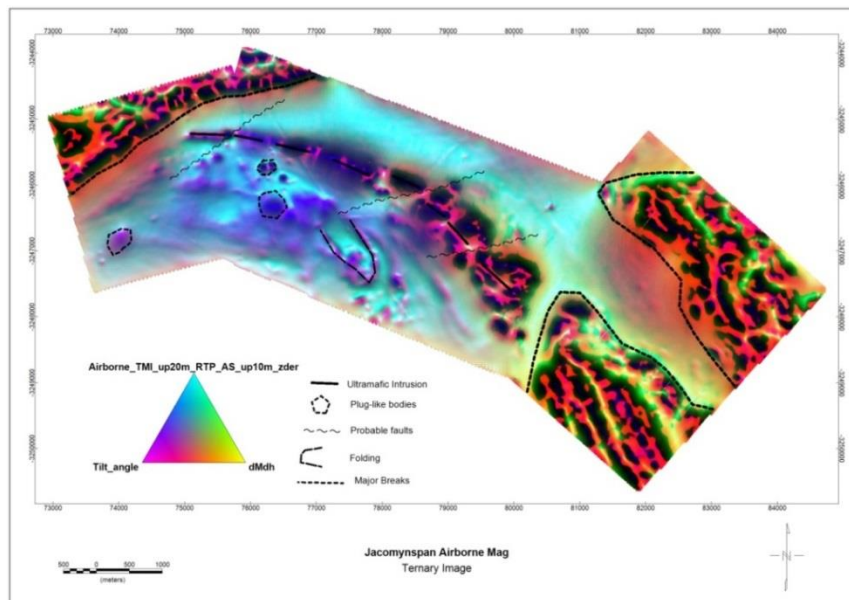
A magnetic ternary colour image was created by applying a sequence of Geosoft algorithms to the high resolution aeromagnetic survey data. The Analytical Signal (AS) maps the boundaries of a magnetic body and the vertical derivative of the tilt angle performs a similar function. If these two images are combined with the  $\text{SQRT}(X\text{-derivative}^2 + Y\text{-derivative}^2)$  which is similar to the analytic signal in a ternary plot then for the Cyan-Magenta-Yellow (CMY) colour scheme the magnetic bodies lie under the dark colours and breaks between bodies or faults and fractures underlie the lighter colours. The ternary image helps to enhance even the very weak structures not seen in the TMI and Figure 7.13 shows a) subtle breaks in the harzburgite orebody are visible, b)



a change in pattern character in the eastern part of the harzburgite intrusion which may indicate the favourable conditions for mineralization not being present here c) folding in the rocks south of the intrusive harzburgite, d) interesting plug-like bodies and e) similarities between the patterns of the magnetic geological units on the eastern and north-western boundaries which suggest that they are of similar nature and origin. Figure 7.13(b) is an annotated copy of Figure 7.13(a) and shows the features described above.



a)



b)

**Figure 7.13 a)** - Ternary image of the high resolution aeromagnetic data for Jacomynspan project. **b)** Ternary image clearly enhancing structures with annotations

#### 7.4.5 Interpretation of the Aeromagnetic Data

The high resolution aeromagnetic data provided valuable information regarding the structure and setting of the intrusion. Figure 7.14 shows the tilt angle derivative image.

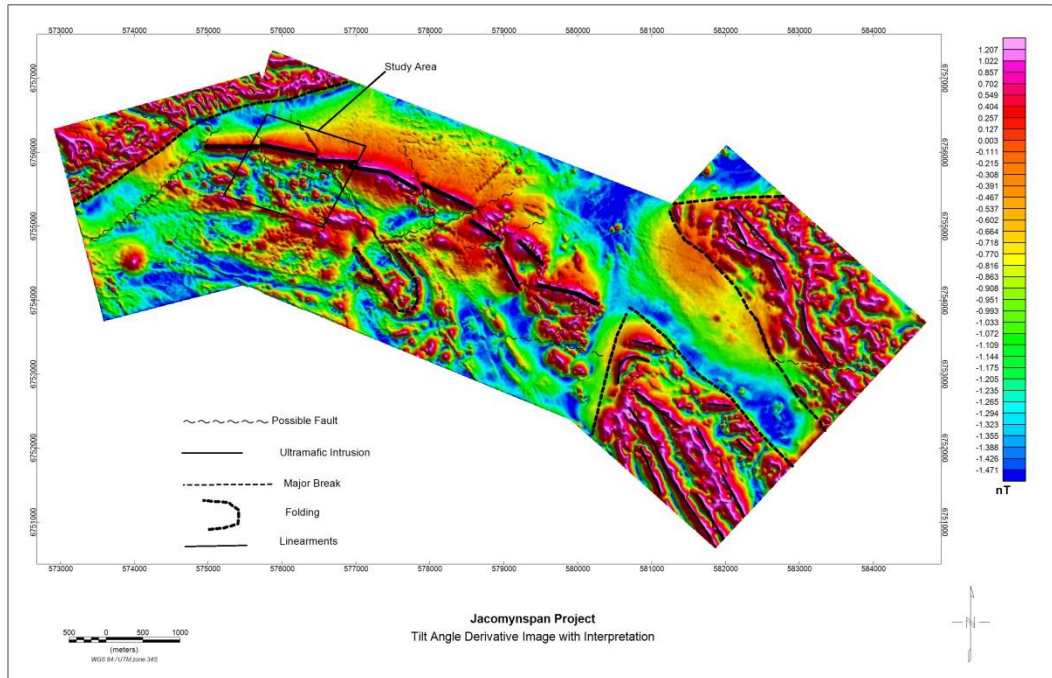


**Figure 7.14** - Xcalibur high resolution aeromagnetic data interpretation on a Tilt angle Derivative image.

The approximately 6km strike length of the known Jacomynspan intrusion is clearly visible in the tilt angle vertical derivative and the ternary images. The magnetic anomaly due to the intrusion is terminated against major breaks in the magnetic data at both the eastern and western boundaries, where folded magnetic rocks occur. These folded magnetic rocks could be magnetite quartzite. The ultramafic intrusion appears to become progressively more faulted and folded and possibly duplicated towards the east. Historically it has been reported that the intrusion is serpentinised towards the east of the farm Hartbeesfontein where Anglovaal drilled for asbestos in the 1970's. Serpentinization could explain the increasing amplitude of the magnetic anomaly towards the east (S du Plessis, 2012 personal communication).

#### 7.5 Airborne Electromagnetic survey data (SPECTREM)

An airborne electromagnetic survey was conducted by SPECTREM Air Limited over the Jacomynspan area in September 2012. The technical specifications for the survey have already been given in Table 3.2. The aim of the survey was to map and delineate the entire Jacomynspan intrusion and also map and delineate other possible conductors within the survey area due to the upside potential of the area. The area covered by Spectrem is much bigger than that flown by Xcalibur.

### 7.5.1 The Late-time Constant

The late-time constant data were calculated by Spectrem using proprietary software and was presented together with other datasets in the Geosoft database they provided. Late-time constants help to identify strongly conductive anomalies without looking at lateral plots of individual channels. The time constant, **Tau** can be explained as a decay constant which is the time required for an exponential function to decay to a value of  $1/e$  of the original value. It is the time required for the induced currents to decay to ~37% of their strength after switching off the source current in the transmitter loop. The late-time constant image (Figure 7.15) was produced by gridding the late-time constant channel in geosoft.

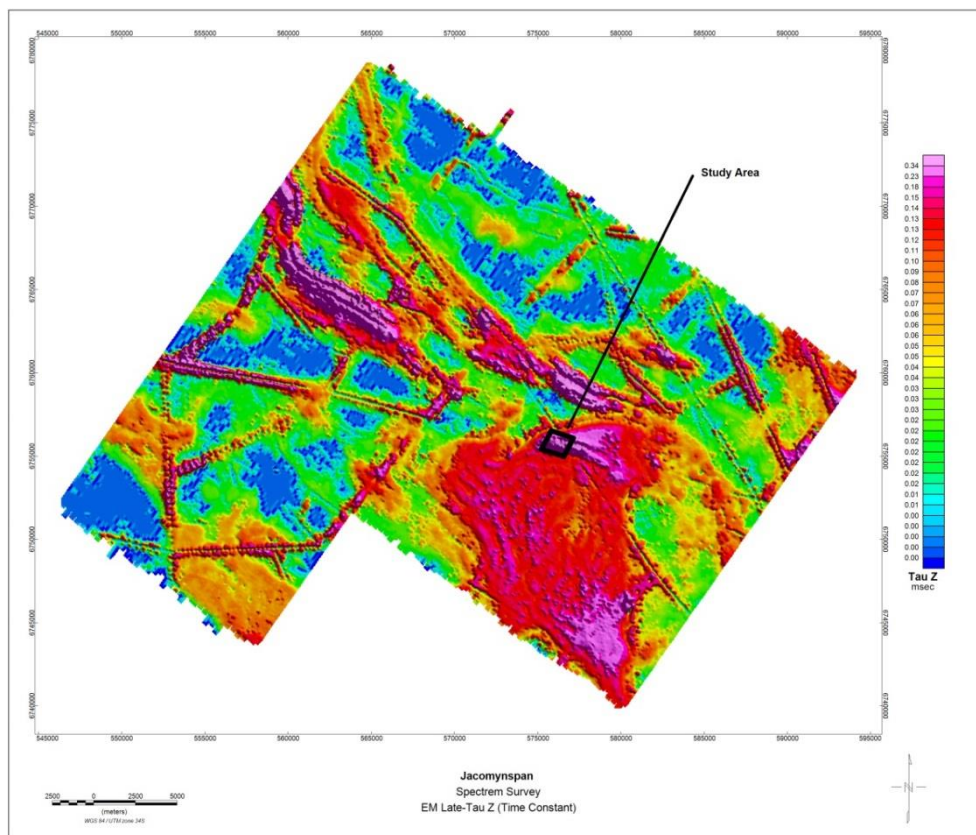


**Figure 7.15** - EM Late-time constant image for Jacomynspan project airborne EM data flown by Spectrem Air mapping the outline of the Jacomynspan ultramafic intrusion and other possible sulphide bodies within the area. The linear very obvious anomalous features are mostly due to fences and other anthropogenic structures.

### 7.5.2 Interpretation of AEM data

Interpretation of AEM follows two approaches, the first one being the use of profile data for EM anomaly selection and the second one being the use of gridded data especially from late-time channel and late-time constant data to produce images for augmenting the interpretation of profile data. According to Klinkert *et al.*, (2012), anomaly shapes



recorded by the Spectrem electromagnetic system can be classified into three types namely cultural, surficial, and bedrock:

- Cultural conductors are due to man-made conductors such as fences, power lines, buried pipes and other metal structures. These give rise to anomalies if they form closed conducting loops, either by being well grounded in a conducting environment, or due to their physical geometry.
- Surficial conductors are flat-lying conductors occurring on or just beneath the surface. The anomalies they generate are characteristically broad, of poor conductivity, and large in amplitude e.g. Quaternary cover and conductive regolith.
- Bedrock conductors are typically steeply-dipping narrow targets of high conductivity situated in a relatively resistive host environment. Strike length may be considerable.

The above is a classification that was used in interpreting the airborne EM data flown by Spectrem over the Jacomynspan project area (Figure 7.16).

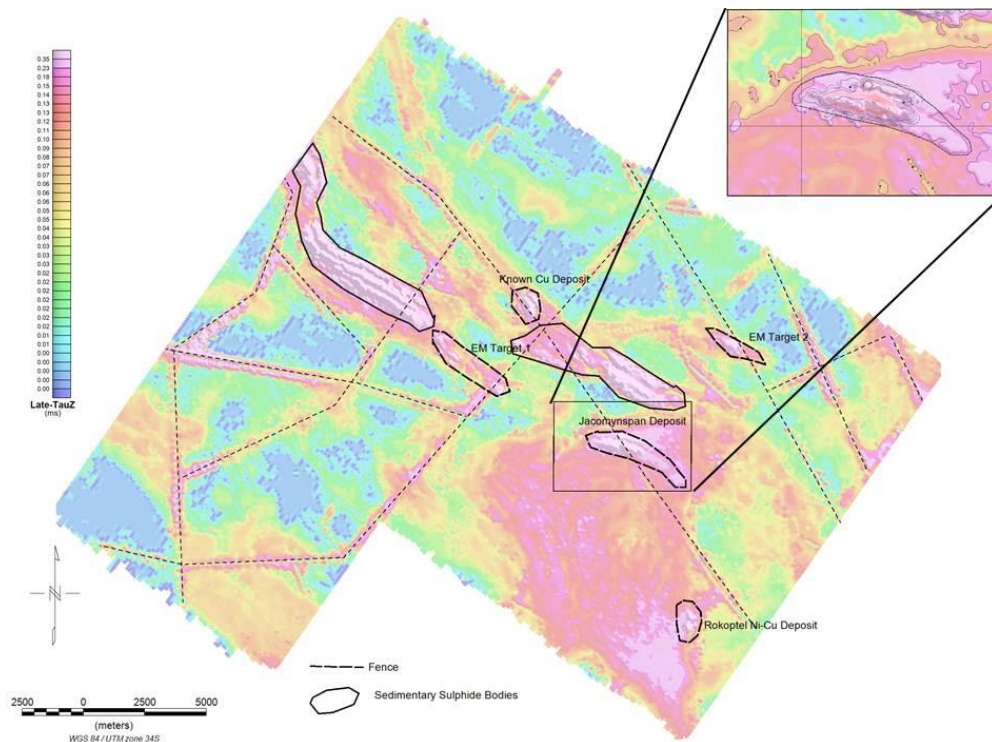


**Figure 7.16** - EM Late time-constant image for Jacomynspan project flown by Spectrem Air clearly mapped the outline of the Jacomynspan ultramafic intrusion, known deposits and prospective sulphide bodies within the area. Cultural features such as fences were also detected and make up the linear conductors indicated by broken lines.

The Jacomynspan sulphide body stands out clearly over a 5 km strike length as a good conductor. In addition, two known Cu and Ni-Cu sulphide prospects were also detected. Two more highly prospective targets were identified from the Spectrem data in Figure 7.16. Furthermore a number of extensive sedimentary sulphide bodies with low economic potential shown in Figure 7.16 were detected within the survey area. There are a number of grounded fences which clearly show-up by their linear narrow peak shapes from the profiles and have been highlighted in the interpretation by 'broken' pattern lines.

### 7.5.3 Spectrem Total Magnetic Intensity data

TMI data were collected simultaneously with the EM and radiometrics data. The TMI image was produced in Geosoft by gridding the levelled TMI channel which is part of the database supplied by Spectrem (Figure 7.17).

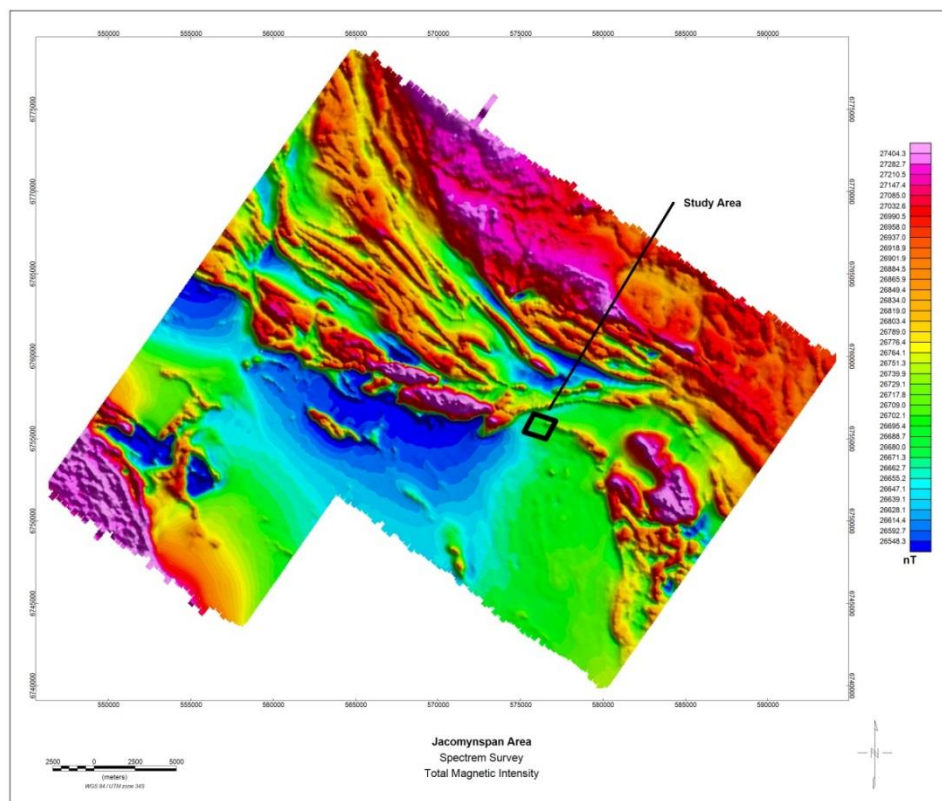


**Figure 7.17** - EM Total Magnetic Intensity image for Jacomynspan project flown by Spectrem Air clearly mapped the outline of the Jacomynspan ultramafic intrusion. Main contacts and structures within the area were also mapped.

Although the data were flown at 200m line spacing, the Jacomynspan intrusion is still visible as a minor magnetic high in the TMI image. This is because pyrrhotite which is the most abundant sulphide and its host, the mafic and ultramafic rocks, have an elevated magnetic susceptibility. The TMI data were complementary in identifying known Ni-Cu deposits and other prospective targets and shedding light on the structure and setting of the intrusion as will be revealed later.

#### 7.5.4 Radiometric Data (Spectrem)

Radiometric data were routinely collected simultaneously with the EM and magnetic data. The radiometrics RGB ternary image of potassium (Red), Thorium (green) and Uranium (yellow) for Jacomynspan is shown in Figure 7.18.

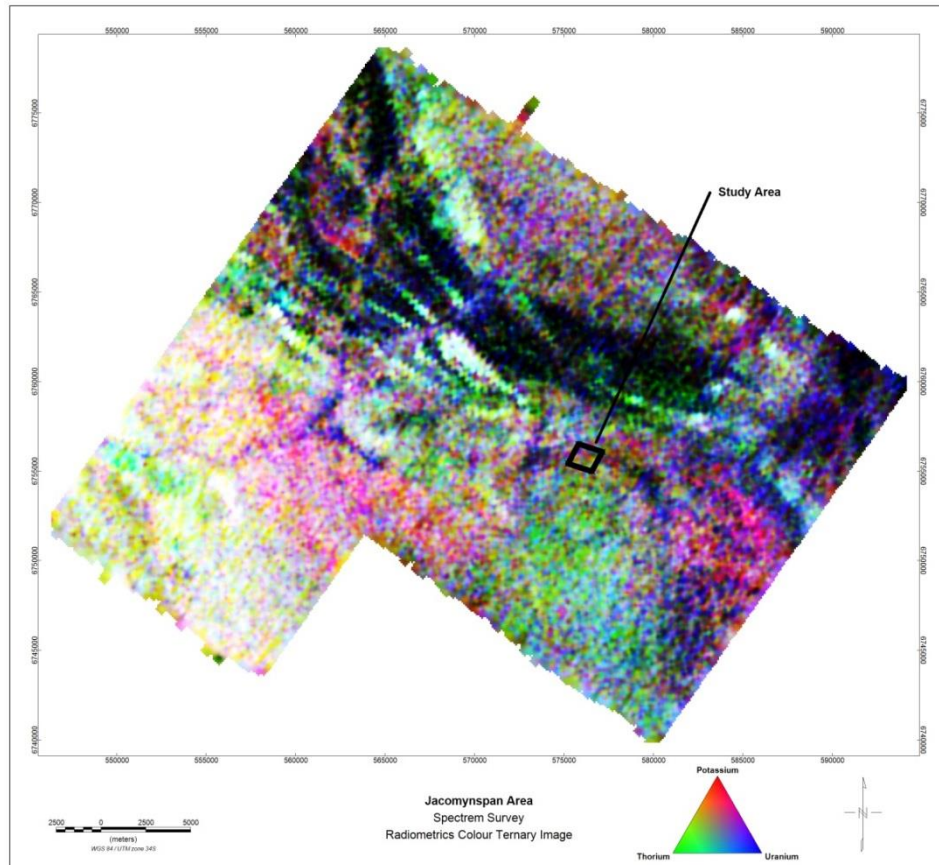


**Figure 7.18** - Radiometrics ternary image for Jacomynspan project flown by Spectrem Air. The image is very speckled and indicates mostly reddish hues due to elevated equivalent eK concentrations with the location of the target area. This may signify that the mineralization is due to hydrothermal enrichment. Purple crosscutting structures indicate the drainage pattern.

Although radiometrics has almost no ‘depth of penetration’ a radiometric survey can be of great use in areas of minimum overburden or in situ weathering as a geological mapping tool because different rock types have varying concentrations of potassium, uranium, and thorium and therefore have distinctive radioactive signatures. The total magnetic field image, other enhanced magnetic images together with the ternary colour image of the radiometric data can be used to identify geological units and produce a ‘geology’ map of an area (see for instance Paasche and Eberle, 2009). The mafic and ultramafic rocks usually have a relatively subdued radiometric response compared to the gneissic host rocks that are more K and U rich. The green hues of the ternary image are equated with the mapped mafic and ultramafic rocks.

The image (Figure 7.18) is very speckled which is due to the small crystal volume of only 16 litre of NaI looking down and no Noise Adjusted Singular Value Decomposition (NASVD) had been applied to the data by SPECTREM AIR. Mostly reddish hues due to elevated equivalent eK concentrations are associated with the location of the target area. K abundance may signify that the mineralization is due to hydrothermal enrichment. The purple crosscutting structures indicate the drainage pattern.

## 7.6 Ground EM survey Data

Both the moving loop and fixed loop modes for ground EM surveys were carried out over the study area. Both the Low-Temperature Superconducting Quantum Interference device (LT SQUID) and the fluxgate were used as sensors in separate surveys.

### 7.6.1 Moving Loop Time Domain ground EM survey Data

Using both the LT SQUID and the fluxgate gives an opportunity to analyse the quality of data between these two sensors. The survey design and specifications for the moving loop mode have already been given in Section 3.3.2. Downloaded data were imported into Maxwell software as either \*.DAT or \*.TEM file. Anomalies are easier to identify when data are presented in the form of profiles. The screen dump in Figure 7.19 shows the data after being imported into Maxwell. The left side of the screen dump depicts the lines surveyed and the stations in plan. The right side indicates the EM response for a single line (Line 5300 in this instance) for the three measured components i.e. **Z**, **X** and **Y** in that order going down. The EM response for each line can be viewed by toggling through the lines.

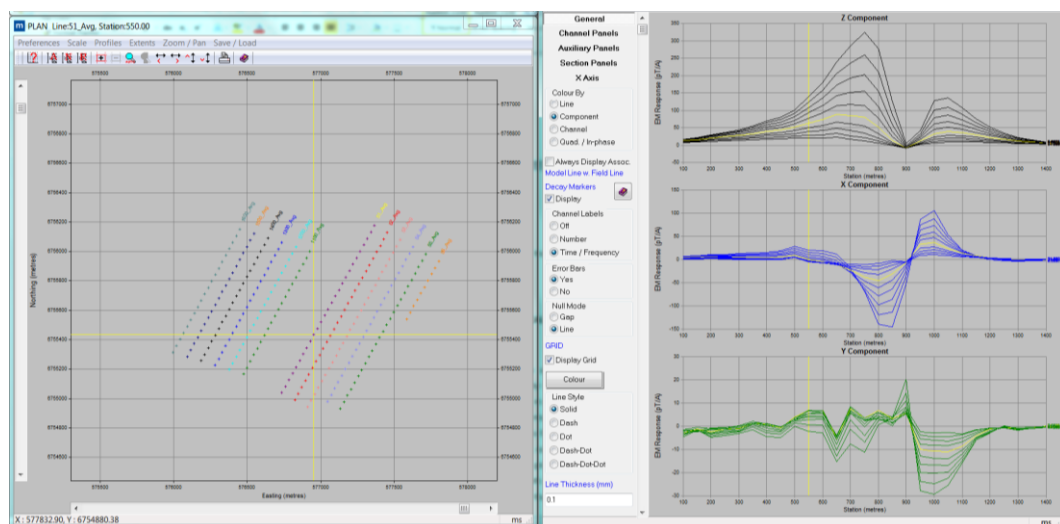


**Figure 7.19** - The moving loop data after importation into Maxwell Software showing the EM response profiles for the three components **Z**, **X**, and **Y** on the right side and surveyed lines on the left for line 5300 (indicated by a yellow cross) of the study area.

Each trace on one of the three plots on the right hand side represents a certain time channel with the earliest channel being the uppermost trace and time increasing as one move's down the plot. During the early times, the distribution of the induction currents in the finite conductor below depends primarily on the size and shape of the body and very weakly on its conductivity. In the late times, the current distribution is limited to a large extent to the largest surface of the conductor. As current distribution changes from early to late time, the orientation of the induced magnetic field vector will change thus changing the shape of the observed anomaly. For interpretation purposes it is therefore essential to interpret the shape of the anomaly only for the late time behaviour of the induction currents. Remembering that Maxwell can only model the TEM behaviour of conductive plates in a resistive host, the current distribution in a plate like conductor will be parallel to the largest surface of the conductor in late times (Southern Geophysical Exploration CC, 1995).

From the response curves for the moving loop as shown in Figure 7.19, the following interpretive conclusions can be drawn

- The top of the conductor is always located directly under the centre minimum amplitude point between the two shoulders of the **Z** component response.
- As the eddy currents move deeper into the conductive body this is equated with an increasing depth to the top of the conductive body and the shoulder peaks of the response become more separated for the **Z** component.
- The centre low point between the shoulders for the **Z** component does not change position with time.
- As the plate dips and departs from the vertical position, the peaks of the **Z** component become asymmetrical with direction of dip towards the high shoulder of the response and the centre of the plate remains under the central minimum.
- The most pronounced zero cross-over of the **X** component is always located on the centre of the conductor.

This cross-over position of the **X** component does not change position with time.

Figure 7.20 shows the gridded image of the Z component channel 20 for the moving loop. The conductive ultramafic to mafic intrusion was clearly mapped



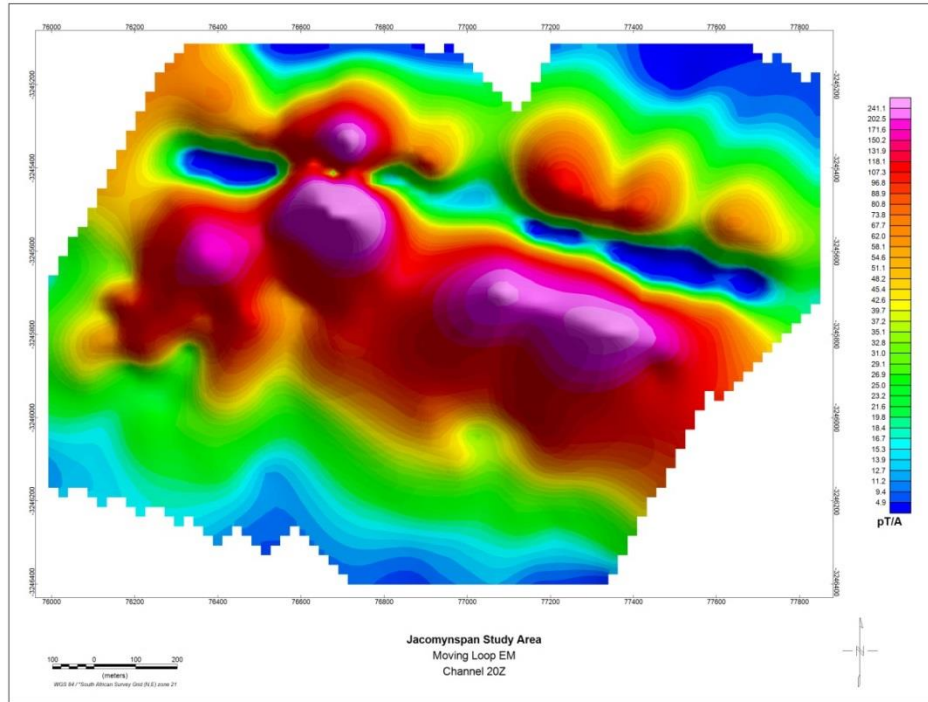


**Figure 7.20** - Channel 20 Z-component image of the moving loop mode mapping the conductive intrusion of the study area.

Since the sensors operate as super conductors due to their low operating temperature of  $-269^{\circ}$ , the LT SQUID has a high signal to noise ratio providing very clean data as compared to the fluxgate sensor used. The LT SQUID can also measure up to very late times (low frequencies) and compared to the fluxgate, thus can 'look' deeper than a fluxgate.

### 7.6.2 Fixed Loop Time Domain ground EM survey Data

The survey design and specifications for the fixed loop mode have already been given in Section 3.3.1. Downloaded data were again imported into Maxwell as either \*.DAT or \*.TEM files and presented below in profiles form (Figure 7.21).

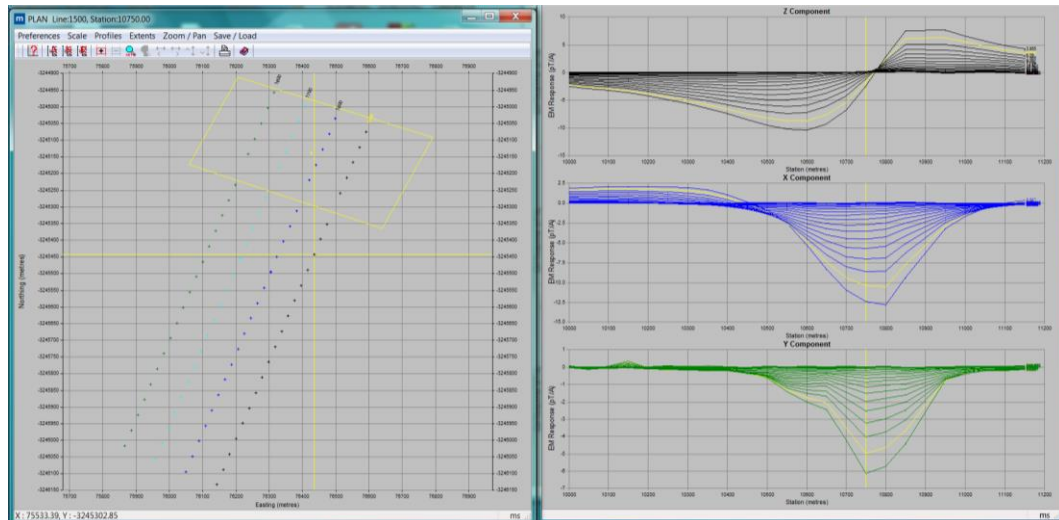


**Figure 7.21** - The fixed loop data (SQUID sensor) after importation into Maxwell Software showing the EM response profiles for the three components Z, X, and Y to the right and the fixed loop and surveyed lines to the left for line 5300 (indicated by a yellow cross) of the study area.

Almost the same principles as for the moving loop apply to the fixed loop mode. Each trace represents a certain time channel, from the early time channel through the intermediate to the late time. Only the late time behaviour of the induction currents as shown above is interpreted. In late times, the current distribution in a plate like conductor will be parallel to the largest surface of the conductor (Southern Geophysical Exploration CC, 1995).

From the response curves for the fixed loop like the one shown in Figure 7.21, the following interpretive conclusions can be drawn:

- The **Z** component is anti-symmetrical across the plate with a zero crossover above the centre of the plate.
- The zero cross-over does not change position with time.
- The **X** component is symmetrical across the plate, with the peak amplitude above the centre of the plate.
- The position of this maximum does not change with time.

## 7.7 Downhole EM data

A number of boreholes were selected for DHEM surveying using EMIT's Atlantis DHEM system. Three components **A**, **U** and **V** for borehole JMP001 are displayed as traces to the right side of Figure 7.22 with the **A** component in black, **U** component in blue and the **V** component in green. The 3 components measured form a right-handed set as explained before where **A** is axial up-hole, **U** is at 12 o'clock when looking downhole and

V is at 9 o'clock when looking downhole. The transmitter loop position (yellow rectangle) and the borehole trace (in black) are shown in plan view on the left hand side. The late time channel data are shown as traces in Figure 7.22 on the right hand side.

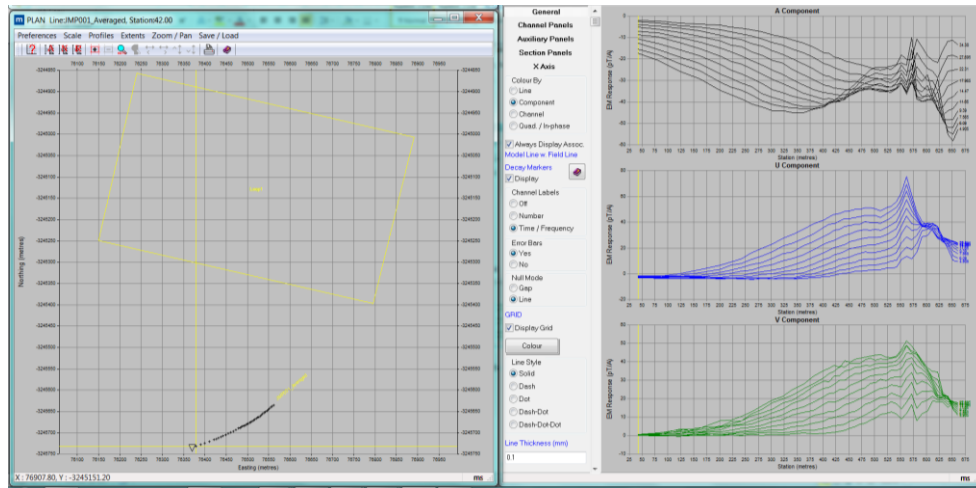


**Figure 7.22** - The DHEM data after importation into Maxwell Software showing the EM response profiles for the three components A, U, and V to the right and the borehole trace and fixed loop position to the left for borehole JMP001 located in the study area.

Interpretation of DHEM data can be carried out from the response curves shown in Figure 7.22. Different anomaly shapes are expected from different drillhole locations with respect to the conductor; a purely positive anomaly for the **A**-component is obtained from an intersection near the centre of the target, a predominantly positive anomaly from an edge intersection and a totally negative anomaly from a very distant target as shown in Figure 7.23 (Eadie and Staltari, 1987).

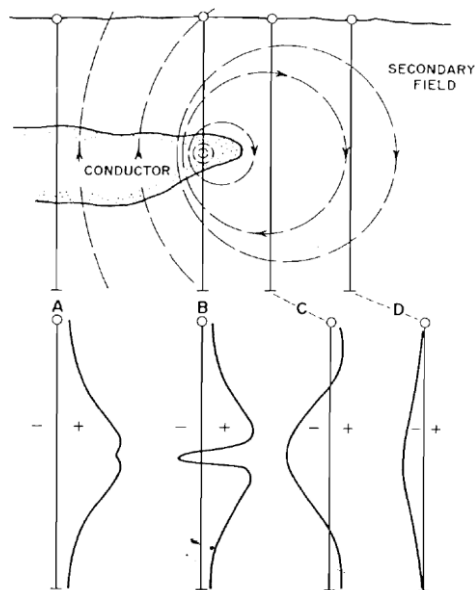


**Figure 7.23** - A purely positive anomaly is obtained from a borehole intersection near the centre of a conductor, a predominantly positive anomaly from an edge intersection, a negative anomaly with positive shoulders from a relatively close miss, and a totally negative anomaly from a very distant target (Crone, 1980).



## 7.8 AMT Data

The time-series data that were collected during field work in discrete bands from 3Hz to 8192Hz were downloaded onto computer. A computer screen dump showing the time series from each channel is shown in Figure 7.24.

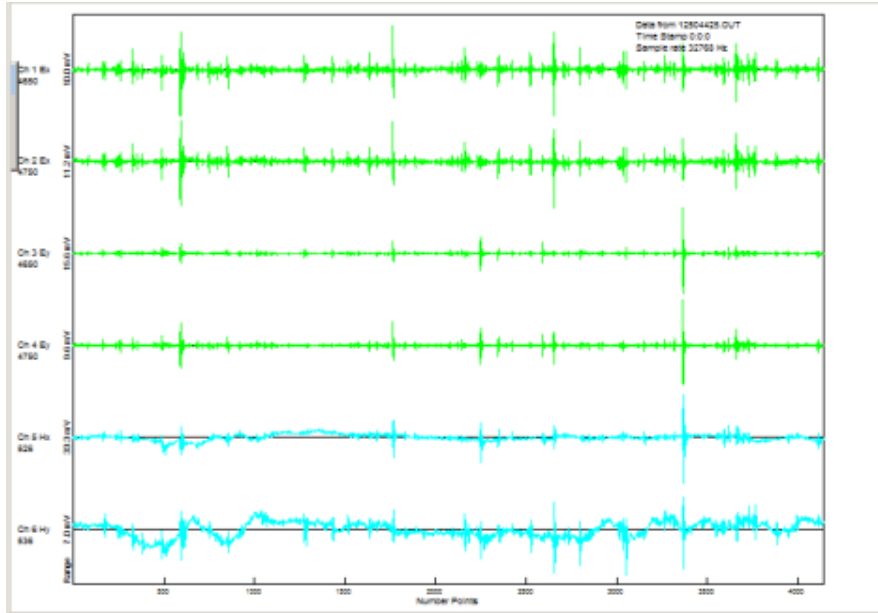


**Figure 7.24** - Time series from each channel on the instrument. Green is the electric field  $E$  while blue is magnetic field  $H$ .

Each trace is a channel on the instrument recording  $E$  and  $H$  fields as a function of time. Green represents the  $E$ -field dipoles and blue the  $H$ -field antennas and each spike is an event. A resistivity sounding curve is derived by converting the two  $E$  and two  $H$ -field time domain data streams into the frequency domain, where they are now represented by in and out-of-phase or real and imaginary components. These are used to calculate expectancy and complicated cross-correlation functions that determine which of these recorded events have sufficient correlation between  $E_x$  and  $H_y$  or  $E_y$  and  $H_x$  to be useful in determining an apparent resistivity. Traditionally more than one correlation coefficient is calculated from a single event and if an average of coefficients provide a correlation of better than 80 per cent then that event is accepted as being a contributor to a stack of other chosen events that are eventually used to calculate the apparent resistivity in two orthogonal directions. Ultimately, the apparent resistivity as a function of frequency depends on the ratio of  $E_x$  and  $H_y$  and  $E_y$  and  $H_x$  power spectra.

The sounding curve in Figure 7.25 shows two components,  $T_m$  in dark blue colour and  $T_e$  in light blue colour (these components have been explained before) and are measured at right angles to one another.

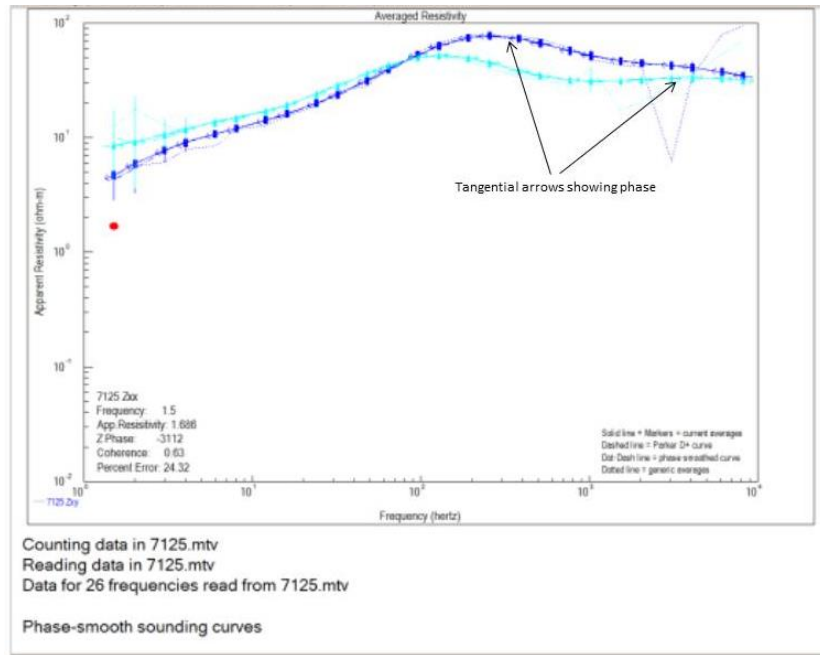


**Figure 7.25** - The sounding curves of the two components,  $T_m$  ( $\rho_{xy}$ ) in dark blue and  $T_e$  ( $\rho_{yx}$ ) in light blue.

The vertical scale is resistivity; the horizontal scale is frequency with high frequencies on the right. High frequencies penetrate shallow and low frequencies deeper depths. For each component both resistivity and phase are calculated, the phase is represented on the curves by the tangential arrows (shown in the picture) as an angle. The vertical bars represent error bars. The processing to this stage was undertaken using Zonge's MTFT24 and MTEDIT proprietary software.

The successive apparent resistivity sounding curves along a survey line can then be converted into a layered (1D) earth estimation of the subsurface and strung together into pseudo-sections constructed from the resistivity and phase for each of the components as shown in Figure 7.26. Successive soundings can be converted into a discretized model for the subsurface where a resistivity is calculated for each 'finite element' building block via a 1D starter model which is then inverted into a more representative 2D model of the Earth.

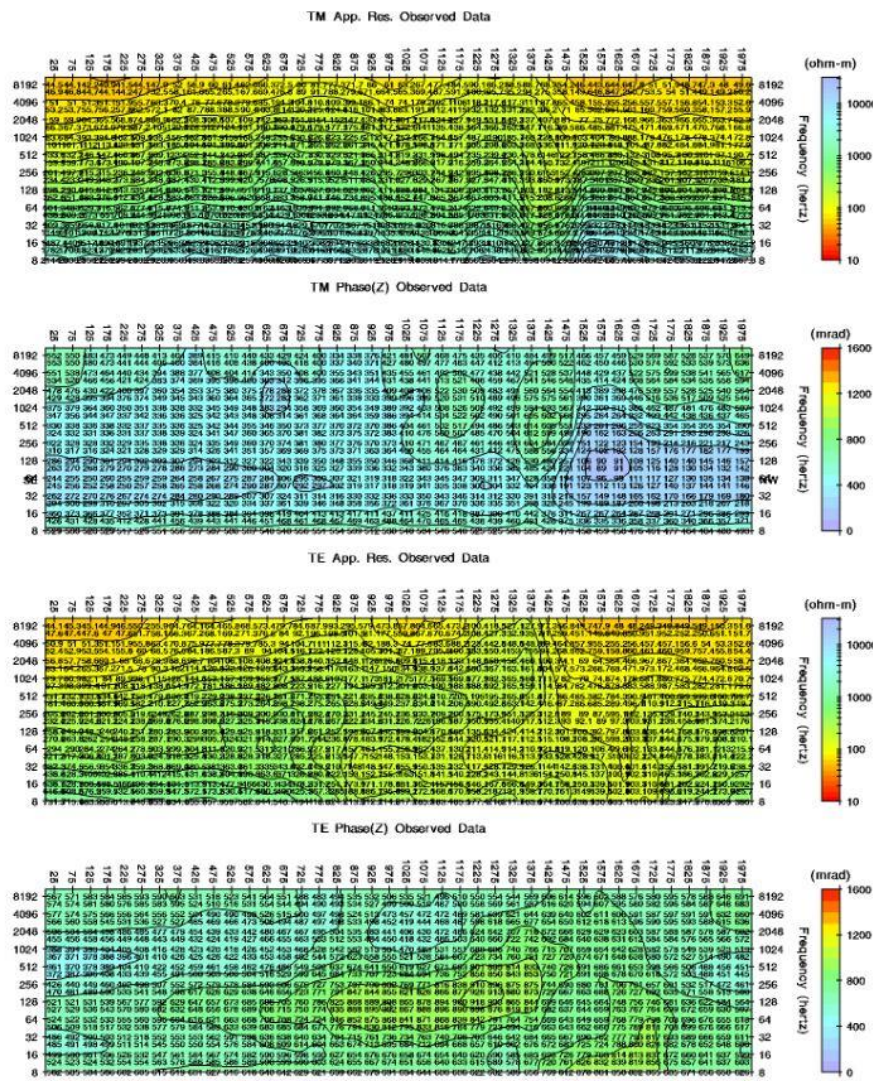


**Figure 7.26** – Line 4 2D Smooth-Model inversion strung together into sections showing resistivity and phase of the observed data. The successive apparent resistivity sounding curves along a survey line have been converted into a layered (1D) earth estimation of the subsurface and strung together into pseudo-sections constructed from the resistivity and phase for each of the components.

High frequencies are at the top (shallower) and lower frequencies at the bottom (deeper). The soundings may appear to be a bit stripy in 1D due to static effects (very local resistivity variations caused by thin geological bodies of limited strike extent at surface). The static effects are simple shifts between the **T<sub>e</sub>** and **T<sub>m</sub>** modes which can be manually removed or ignored as they are taken care of if 2D modelling is applied (Figure 7.26).

## 7.9 Drillhole Data

A total of 17 boreholes were drilled within the study area by African Nickel Ltd during the 2011 drilling programme. The drill programme was planned in order to delineate the sulphide mineralisation better and prove up a resource. Information gathered from drilling was used to create a 3D geological starting model for the ultramafic sill and the well-

mineralised harzburgite. The borehole positions have been plotted on the TMI image (Figure 7.27).

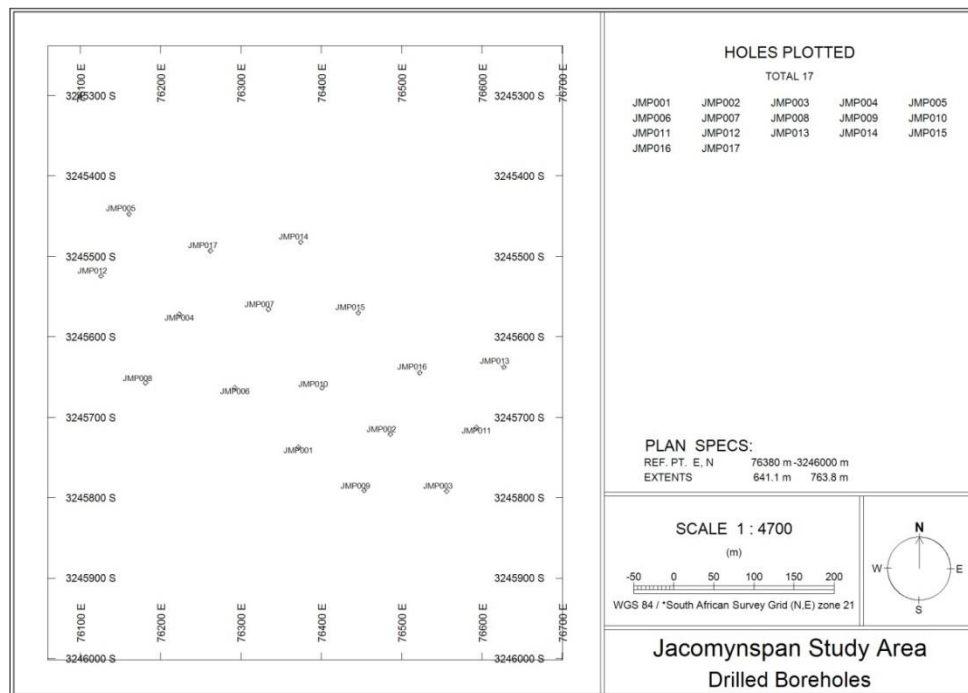
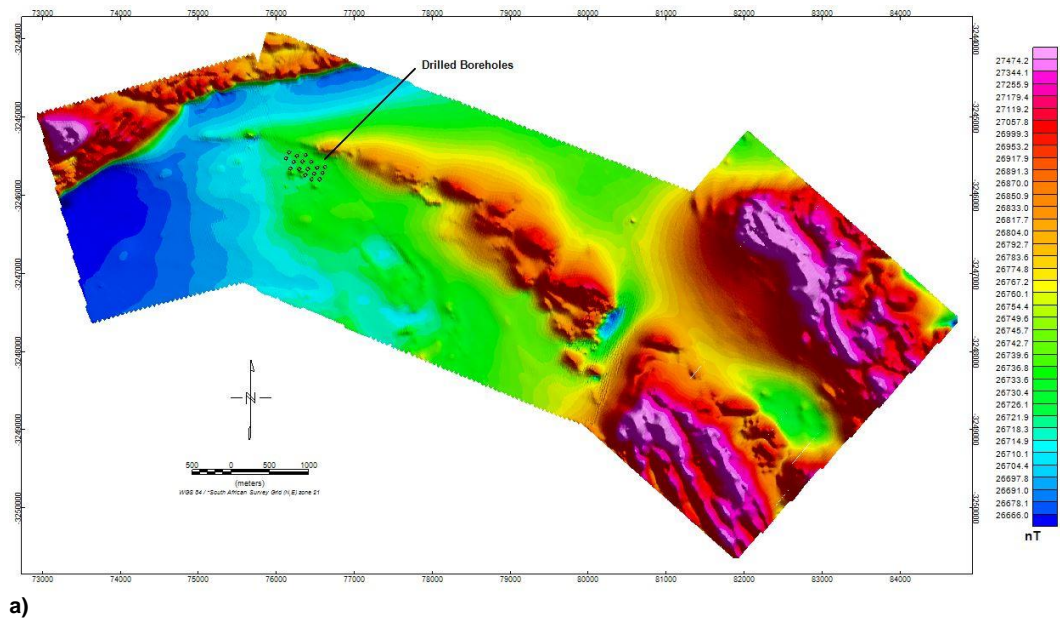


**Figure 7.27 – a)** Collar positions of the drilled boreholes on TMI image of the aeromagnetic data, **b)** Plan of the position of the boreholes drilled within the study area showing the borehole names.

The country rock alternates between quartz-feldspathic-biotite-garnet-gneiss, politic quartz-feldspathic-biotite-garnet-gneiss and a quartz-feldspathic-pegmatite, where a thick pegmatite unit is intersected just before the intrusion.

The same stratigraphic sequence is seen in all the holes as illustrated in Figure 7.28.



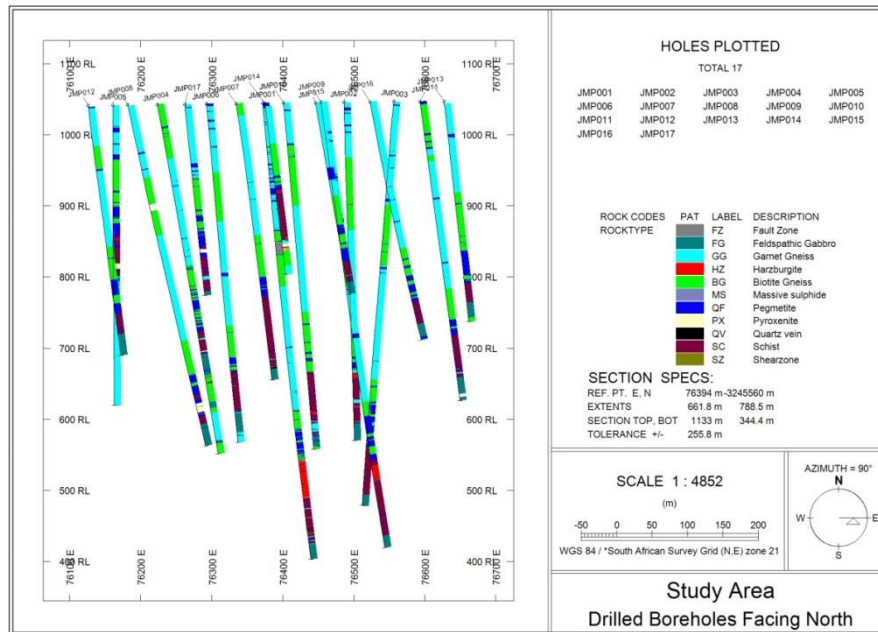


**Figure 7.28** - Cross section of all the drilled boreholes facing north showing the same stratigraphic sequence on all the drilled boreholes.

The intrusion is made up of tremolite-biotite schist (metamorphosed pyroxenite) and harzburgite. The body has an east-west trending curvilinear surface expression and dips at  $65^{\circ}$  –  $70^{\circ}$  to the south and has been drilled down to a vertical depth of 900m (Figure 7.29).

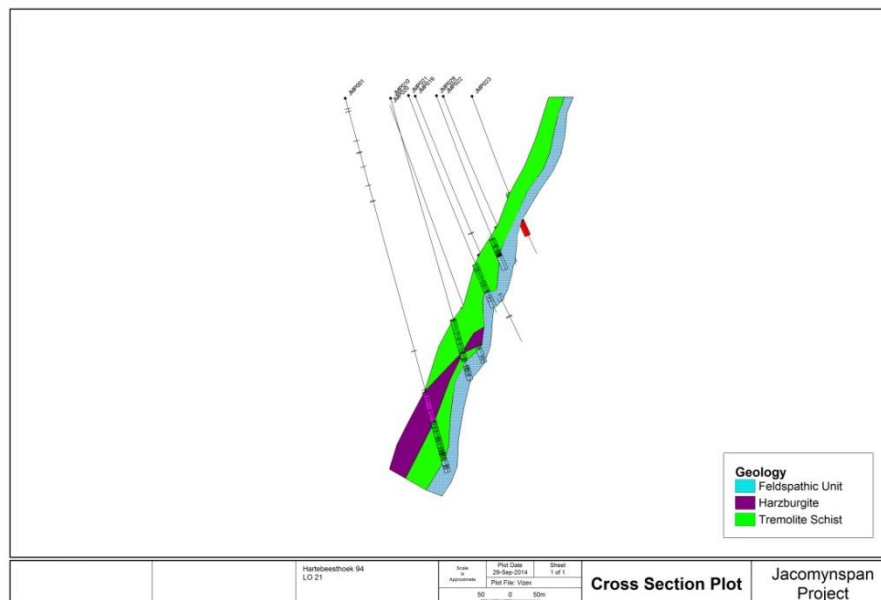


**Figure 7.29** - Cross section plot facing west of the Jacomynspan ultramafic sill showing well mineralised harzburgite and some of the borehole traces drilled within the study area.

### 7.9.1 Borehole JMP001.

Borehole JMP001 drilled within the study area is of great interest to this study because it intersected all the stratigraphic units. It was drilled to a depth of 666.51m located within

the study area. The country rock alternates between the already mentioned quartz-feldspathic-biotite-garnet gneiss (logged as garnet gneiss), a pelitic quartz-feldspathic-biotite-garnet-gneiss (logged as biotite gneiss) and a quartz-feldspathic pegmatite. The intrusion was intersected from 523.10 - 643.95m and two rock types can clearly be distinguished, harzburgite and tremolite schist units. The tremolite schist (Figure 7.30) in borehole JMP001 was intersected from 577.40 – 643.95m and the sulphide mineralisation decreases from the top in the schist as the borehole gets deeper.



**Figure 7.30** - Drill core for JMP001 between depth of approximately 581m and 586m showing tremolite schist (metamorphosed pyroxenite) which is host to disseminated sulphides.

Sulphide mineralisation is in the form of pyrrhotite, with lesser amounts of chalcopyrite and pyrite. Physical properties measurements carried out on core samples show that the tremolite schist has more elevated magnetic susceptibility values than the gneissic country rock but is less magnetically susceptible than the well mineralised harzburgite. Relative conductivity measurements also show that tremolite schist is more conductive than the host gneiss country rock but 4 times less conductive than the harzburgite.

The harzburgite was intersected from 523.10m – 577.40m and hosts the bulk of the sulphide mineralisation. It hosts net-textured mineralisation as can be seen in Figure 7.31.

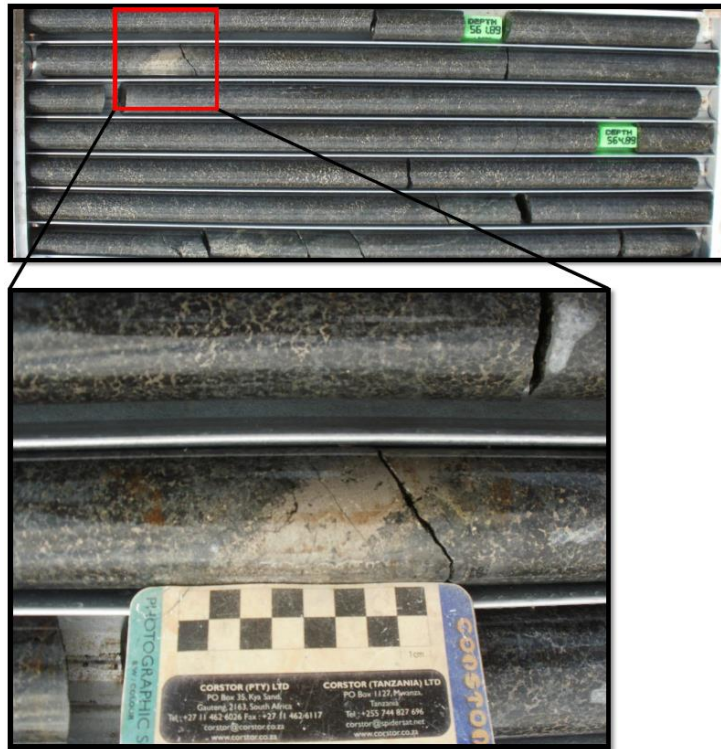


**Figure 7.31** - JMP001 drill core showing harzburgite with well mineralised net-textured sulphides and a stringer of massive sulphides.

As the drilling programme progressed, it became clear that the well mineralised harzburgite is not a continuous body but occurs most probably in pods since most of the boreholes drilled did not intersect the harzburgite. The physical property measurements showed that there is a substantial physical contrast in magnetic susceptibility and conductivity between the well mineralised harzburgite and the poorly mineralised tremolite schist. An assumption has consequently been made that at late decay times, the current would gather in the massive sulphide stringer zones and the net-textured higher grade mineralised harzburgite. Therefore the centre of the EM plate model targets could potentially indicate these units, rather than the lower grade tremolite schist mineralisation. It was also anticipated that the AMT will map the highly conductive well mineralised harzburgite at depth. It is therefore possible to produce a final geophysical model of the well mineralised harzburgite using the geological model from boreholes and combining that with the EM and magnetic data models.

## CHAPTER 8: THEORETICAL ASPECTS OF GEOPHYSICAL MODELLING

### 8.1 Preamble

Geophysical modelling incorporated all the available datasets in this study. In exploration, geophysical inversion usually means producing an earth model which is in agreement with geophysical survey data, in a timely and cost effective manner. The earth model must conform to other project information, in particular, geology and drilling (Long and Fischer, 2013). It is a process used to find the distribution of a physical property that caused a set of physical measurements recorded in a field survey enabling resource explorers to extract more insight from geophysical measurements into images of the subsurface that can be integrated with other surface and subsurface geological observations (Geosoft, 2013). It must, however be noted that:

- Geophysical inversion is a non-unique process meaning different models can produce the same response. For example, a broad dense body close to the surface creates a gravity response that is similar to a very dense compact body deeper in the earth.
- *A priori* information must be included in the inversion (e.g. smoothness, geology, drilling, geophysical data etc.) in order to constrain the process.
- Integrating other information improves reliability and greatly increases the acceptance of the inversion into the exploration process.
- From a practical perspective, these processes must be robust and easy to use.

According to Oldenburg and Pratt (2007), inversion applications can be divided into three categories:

- a. Type I – Discrete body inversion where a few parameters are sought.
- b. Type II – Pure property inversion where a voxel (cell) representation of the earth is invoked.
- c. Type III – Lithological inversion where the earth is characterised by specific rocks.

Again according to Oldenburg and Pratt (2007), in a typical inverse problem we are provided with observations, some estimate of their uncertainties, and a relationship that enables the computation of the predicted data for any model,  $\mathbf{m}$ . The model represents the spatial distribution of a physical property such as susceptibility or conductivity. Our



goal will then be to find the  $\mathbf{m}$  which gave rise to the observations (measurements). As such, the predicted data,  $\mathbf{d}^{pre}$ , should be “close” to the observations,  $\mathbf{d}^{obs}$ , but this requires that properties of the noise are estimated. From the perspective of the inverse problem, the noise accounts for repeatability, surveying, and modelling errors.

If a least squares criterion is used, the misfit functional  $\Phi_d$  is

$$\Phi_d = \sum_{i=1,N} \left( \frac{d^{obs} - d^{pre}}{\delta} \right)^2 \quad (8.1)$$

where  $\delta$  is standard deviation,  $N$  is the number of data and  $\Phi_d$  is the data misfit. When solving the inverse problem we want to find a model  $\mathbf{m}$  that produces an acceptably small misfit.

There are two methods of modelling geophysical data: forward modelling and inversion modelling as illustrated in Figure 8.1. Each method attempts to determine the model parameters (e.g. depth, thickness, density, etc.) via a different approach (Coomber, 2008).

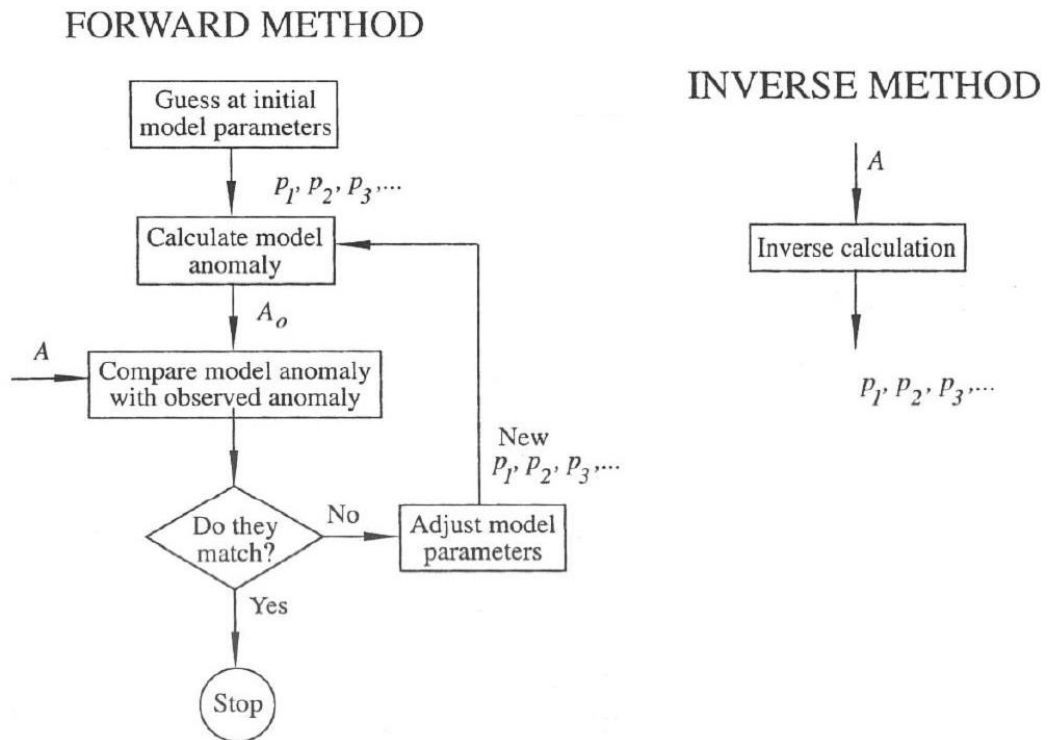


**Figure 8.1** - Comparing the forward and inverse method.  $A$  represents the measured anomaly, and  $A_o$  the calculated anomaly. Parameters  $p_1, p_2, \dots$  are the source attributes (e.g. depth, thickness, density), (Blakely, 1995).

Forward modelling (also referred to as the forward problem) is the process of computing a response (e.g. a gravity measurement) from a given earth model (e.g. a density distribution). It assumes *a priori* a mass and calculates the corresponding anomaly. Most important is that known geological units and structures are brought into the forward model to ensure a realistic model. This calculated anomaly is in turn compared to the measured anomaly and the model is manipulated until the calculated anomaly mimics the observed anomaly to an acceptable degree. It also helps in planning geophysical surveys by calculating the response of various types of geophysical surveys making it easier to choose the best method (Coomber, 2008).

The inverse problem is complementary to forward modelling. It helps determining what distribution of physical properties yields a measured field response best. It needs and allows the inclusion of a 'starter model' which is given by the forward model into which has been incorporated the *a priori* information on the source body. For the interpretation of large volumes of airborne data a standard 'starter model' such as a dipping plate or cylinder is sometimes assumed and the inversion calculates best estimates for depth, dip and conductivity/susceptibility. Model parameters are computed directly from measurements. However, many models can create the same surface response and this is referred to as non-uniqueness. To create a model which is useful we have to make use of known information (*a priori*) like overburden thickness, known geology, lithology from drill data etc. in order to constrain the inverse problem to a limited number of plausible models.

## **8.2 Inversion of Magnetic Data**

Since the Jacomynspan Ni-Cu sulphide deposit has a coincident magnetic and EM response, VOXI Earth Modelling software and Prof Gordon Cooper's Mag2dc will complement each other in modelling the high resolution aeromagnetic data for this study. The principal difficulty in finding a solution to the magnetic inverse problem is its inherent non-uniqueness mentioned before. There are an infinite number of models that could adequately reproduce the data and there are also a number of different sources of this non-uniqueness. This can be explained, first by Gauss's theorem which states that if a field distribution is known on the boundary surface of a region, there are infinitely many possible equivalent source distributions in the region that can produce the known field. The other reason is that the number of survey measurements is finite and the data will contain some level of inaccuracy. Therefore, the data only need to be fitted to a certain degree, defined by their expected errors (Lelievre, 2003).

However, although there are an infinite number of possible models that can adequately reproduce the data many of these will be unreasonable for a specific situation. The

number of acceptable models can therefore be reduced by considering the requirements for a feasible model. The data predicted by the recovered model should fit the observed survey data to within a degree justified by their estimated uncertainties. The second requirement is that the recovered model should be compatible with any *a priori* knowledge of the subsurface geology or physical property distribution (Lelievre, 2003).

### 8.2.1 VOXI Earth Modelling theory

VOXI Earth Modelling is a Geosoft® geophysical inversion software service that generates 3D voxel models from airborne or ground gravity and magnetic data using cloud computing (Geosoft, 2013). The utility of magnetic field data in many areas of geophysical exploration is well-known as is the application of 3D voxel inversion to aid in magnetic data interpretation (Pilkington, 1997). Geosoft's VOXI Earth Modelling software was used for modelling the high resolution airborne magnetic data for this study. Below is a brief description of how it works.

The inversion process of VOXI Earth modelling software can be explained starting with the forward and inverse problem represented by the following equations:

$$\mathbf{G}[\mathbf{m}] = \mathbf{d} \text{ forward problem} \quad (8.2)$$

$$\mathbf{G}^{-1}[\mathbf{m}] = \mathbf{d} \text{ inverse problem} \quad (8.3)$$

where  $\mathbf{G}$  is some geophysical phenomena,  $\mathbf{m}$  is the earth model and  $\mathbf{d}$  is the geophysical data.

However  $\mathbf{G}^{-1}$  does not exist, therefore the inverse problem becomes one of optimising the closeness of the predicted model and its forward calculated response to what we have observed and what we assume in the model to look alike (Geosoft, 2013). In VOXI, the idea is therefore to quantify the closeness between the predicted model response and the observed data using the data misfit equation:

$$\boldsymbol{\varphi}_d = \frac{1}{N} \sum_{i=1, N} \left( \frac{d^{obs} - d^{pre}}{\delta d} \right)^2 \quad (8.4)$$

when  $d^{obs} - d^{pre} = \delta d$ ,  $\boldsymbol{\varphi}_d = 1 \equiv$  “which fits the data”

where  $\boldsymbol{\varphi}_d$  is the data misfit,  $N$  is number of observations,  $d^{obs}$  is the observed geophysical data,  $d^{pre}$  is the predicted model response and  $\delta d$  is the error.

It is possible to also quantify how closely the predicted model is to the preferred reference model with the model norm equation for  $M$  voxels:

$$\boldsymbol{\varphi}_m = \frac{1}{M} \sum_{i=1, M} \left( \frac{m^{ref} - m^{pre}}{\delta m} \right)^2 \quad (8.5)$$

$$\boldsymbol{\varphi}_m = 0 \equiv \text{“conforms to geology”}$$

where  $\boldsymbol{\varphi}_m$  model norm,  $M$  is the number of voxels,  $m^{ref}$  is the reference earth model,  $m^{pre}$  is the predicted model and  $\delta m$  is the error or the confidence in the reference model.

When the confidence in the reference model is high,  $\boldsymbol{\varphi}_m = 0 \equiv \text{“conforms to geology”}$ .

It was shown that for geophysical inversion

$$\boldsymbol{\varphi}_d \sim 1 \text{ in agreement with survey data}$$

$$\boldsymbol{\varphi}_m \rightarrow 0 \text{ earth model must conform with geology}$$

In practice the idea is to seek for a model which satisfies both the observed data and the known geology therefore the inversion seeks to balance these two quantities before arriving at the final model (Geosoft, 2013). One can quantify this balancing act with an objective function:  $\boldsymbol{\varphi}_T = \boldsymbol{\varphi}_d + \lambda \boldsymbol{\varphi}_m$  (8.6)

where  $\boldsymbol{\varphi}_T$  is the total objective function,  $\boldsymbol{\varphi}_d$  is the data misfit,  $\boldsymbol{\varphi}_m$  is the model norm with a regularization parameter  $\lambda$  that is adjusted by the inversion algorithm in successive steps. During each step calculation, the inversion tries to find a model that minimises the objective function so that the data misfit  $\boldsymbol{\varphi}_d \sim 1$

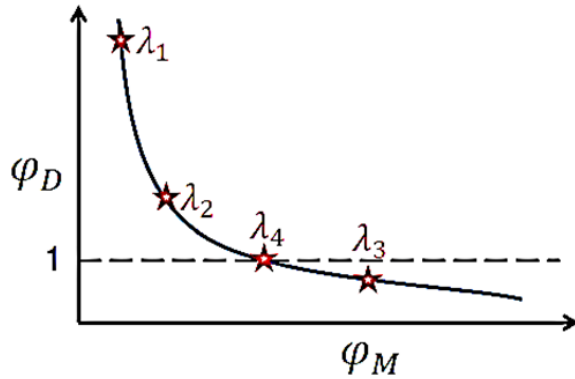
Therefore VOXI solves for

$$\text{Minimize } \boldsymbol{\varphi}_T = \boldsymbol{\varphi}_d + \lambda \boldsymbol{\varphi}_m \text{ and choose } \lambda \text{ so that } \boldsymbol{\varphi}_d \sim 1$$

To solve the problem numerically, the earth volume is divided into a number of cubic cells each of which has a constant, but unknown value of the physical property. The model objective function and forward modelling equations are discretized using the gridded earth volume and the total objective function minimized (Pilkington, 1997).

When the total objective function is minimized for a specific  $\lambda$  it produces a model that has quantifiable misfit and model norm. When the optimization is carried out for many

values of  $\lambda$  the results of these step calculations can be plotted to produce a Tikhonov, or trade off, curve shown in Figure 8.2:



Minimize  $\varphi_T = \varphi_D + \lambda \varphi_M$  choose  $\lambda$  so that  $\varphi_D \sim 1$

**Figure 8.2** - Tikhonov or Trade-off curve showing how optimization is carried out for the values of  $\lambda$ .

where each  $\lambda$  represents an iteration in the inversion process. The final model is the one that minimizes the objective function with the condition specified above that is the data misfit  $\varphi_d \sim 1$ .

According to Oldenburg and Pratt (2007), the left hand side of the curve in Figure 8.2 corresponds to large  $\lambda$  and significant decrease can be obtained in the misfit without greatly increasing the model norm  $\varphi_m$ . This area of the curve is fitting the geophysical signal. But on the right hand portion of the curve, the model norm (i.e. structure) increases significantly with only a small decrease in misfit thus in this realm fitting the noise. Therefore, the best fit can be obtained somewhere near the kink of this curve (i.e. between  $\lambda_2$  and  $\lambda_4$ ).

### 8.2.2 VOXI's Magnetization Vector Inversion (MVI) Theory

McEnroe *et al.*, (2009) noted that in the majority of voxel based inversions it is assumed that the magnetic response arises entirely from magnetic induction but in the last decade or so, several studies have discovered that remanent magnetisation is far more prevalent than previously thought and affects crustal rocks as well as zones of mineralisation. It has been stated earlier that magnetism within most rocks containing magnetic minerals can be comprised of two components i.e. induced and remanent magnetisation, and therefore it is very important to consider both when modelling geological bodies (Austin *et al.*, 2013). Magnetisation Vector Inversion (MVI) allows the magnetization direction to vary within the model and thus take into account the combined effects of remanence, demagnetization, anisotropy and induced magnetization. The result is a more realistic representation of rock magnetization, which is the fundamental rock property measured

with the magnetic method (Burns, 2012). Remanent magnetisation can seriously distort inversion outcome results, based on the assumption that only induced magnetization is present. The severity of this distortion is due to the highly non-unique nature of potential field inversion making it very easy for a potential field inversion to produce a seemingly plausible model which agrees satisfactorily with the observed data although a fundamental assumption in the inversion is flawed (Ellis *et al.*, 2012).

In order to understand VOXI's MVI the starting point is a brief overview of the magnetization vector. The magnetization of a rock is a vector quantity measured in SI units of Ampere per meter (A/m). For a given volume, shown in Figure 8.3

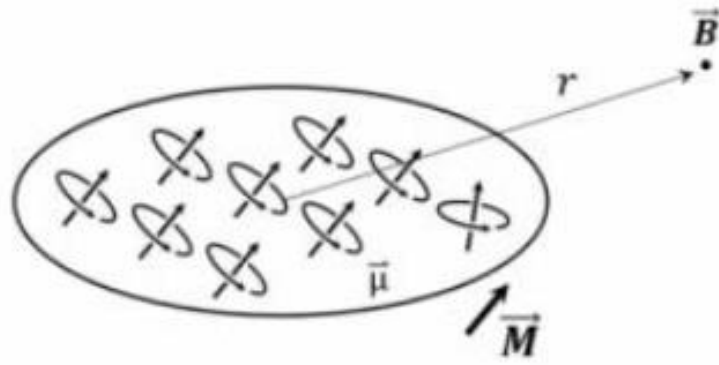


**Figure 8.3** - Volume of rock showing that the magnetization is a vector quantity.

The volume above is defined by  $\mathbf{M} = \frac{N}{V} \langle \boldsymbol{\mu} \rangle$

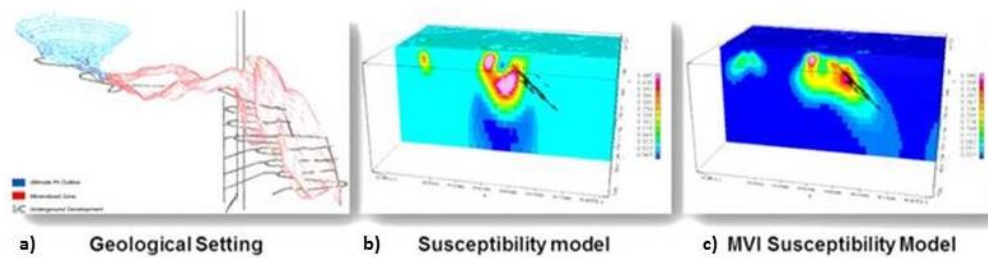
where  $\mathbf{M}$  is the Magnetization (A/m),  $N$  is the Number of moments,  $V$  is the volume of the sample ( $\text{m}^3$ ) and  $\boldsymbol{\mu}$  is the mean of moment vectors ( $\text{A.m}^2$ ).

The key importance of the above equation is that it allows the magnetic properties of the rock to be represented without making assumptions of source and direction of magnetization. According to Ellis *et al.*, (2012), from magnetostatics the magnetic field  $\mathbf{B}$  observed at some point  $\mathbf{r}$  resulting from a volume  $V$  with a magnetization  $\mathbf{M}$  is represented by the expression:

$$\mathbf{B}(\mathbf{r}) = \nabla \int_V \mathbf{M}(\mathbf{r}') \cdot \nabla \frac{1}{|\mathbf{r} - \mathbf{r}'|} d\mathbf{r}'^3 \quad (8.7)$$

Solving for  $\mathbf{M}$  does not require any prior knowledge of the strength and direction of any possible remanent magnetization. The above expression shows directly that given an observed magnetic field  $\mathbf{B}$  the natural parameter for inversion is the magnetization vector  $\mathbf{M}$ . MVI returns the magnetization vector with both its direction and amplitude being defined for interpretation purposes.

Ellis *et al.*, (2012) as a case study, discussed where MVI was applied to TMI data collected over the Osborne deposit in Australia. Exploration since 1995 has delineated high-grade primary mineralisation dipping steeply east to some 1100m vertical depth. Current exploration is focussed on mapping the high grade mineralisation to greater depths and mapping similar structures in the surrounding area. This includes total magnetic intensity (TMI) data over the property as shown in Figure 8.4 below (Ellis *et al.*, 2012):



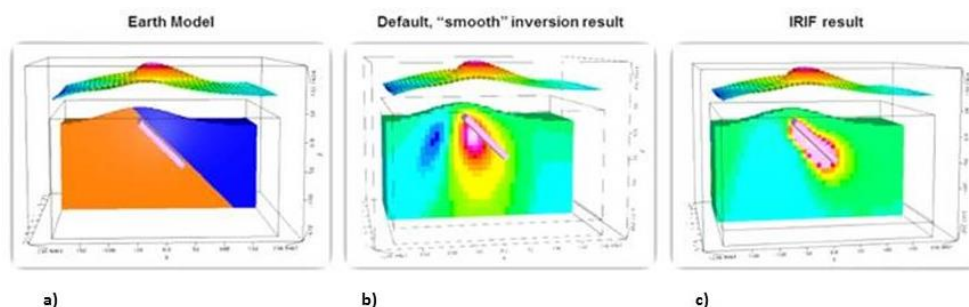
**Figure 8.4** - An example of Osborne IOCG deposit model with the now known mineralisation shown in black – comparing MVI with Susceptibility inversion. a) Geological Setting, b) Susceptibility model, c) MVI Susceptibility (Ellis *et al.*, 2012).

Figure 8.4 above shows that inverting for the magnetization vector provides a much better model which is consistent with the drilling results indicating a steeply dipping volume on the Eastern flank.

Magnetization Vector Inversion (MVI) therefore takes into account both remanent and induced magnetization even without prior knowledge of the direction or strength of remanent magnetization. This is essential for correct interpretation of magnetic field data. MVI technique was applied in this study.

### 8.2.3 Iterative Reweighting Inversion Focusing (IRF)

Iterative reweighting inversion (IRI) in VOXI is a powerful technique that can be used to constrain inversion results to better agree with known geology or geophysics. It can be used to simultaneously sharpen, smooth inversion results and to control the depth of the recovered targets as can be seen in the following example in Figure 8.5.



**Figure 8.5** - A Geosoft example of Iterative Reweighting Inversion Focusing (IRI) showing the focusing of the model to the actual known deposit compared to the smooth model. a) Earth Model, b) Smooth inversion model, c) Iterative Reweighting Inversion (VOXI training manual).

The default, “smooth” inversion result above can be considered to be too smooth and can be sharpened by taking the default inversion result and entering it as an iterative reweighting constraint and then rerunning the inversion. To further sharpen the model, this procedure can be repeated by taking the output from the last inversion and using it as the Iterative Reweighting input in the next inversion.

#### **8.2.4 Mag2dc Software**

To obtain an initial understanding of whether the magnetic data actually supports the geological model as obtained from the extensive drilling information and physical parameter data already determined, the aeromagnetic data were modelled in the forward solution way just using Cooper’s Mag2dc modelling software. Mag2dc is a simple 2.5D algorithm that allows the forward modelling and inversion of magnetic data assuming a flat horizontal surface topography. Of-course a magnetic topography could be added as just a separate body mimicking the surface if required.

#### **8.3 Inversion of Electromagnetic data**

The dominant physical property for the inductive EM methods used in this study is the electrical conductivity which allows the movement of electrical charges i.e. current flow inside matter. As shown by the relative conductivity measurements on borehole JMP001 for this study, there is a very large conductivity contrast between the well mineralised harzburgite and the tremolite schist which hosts disseminated mineralisation with the host gneissic rock not being conductive at all. This will produce a strong anomalous EM response from the harzburgite. The aim of the geophysical interpretation in this study is to invert the measured EM data into knowledge about the spatial distribution of conductivity within the deposit, and to use that information in geological interpretation. It must be noted that the inverse problem can have many solutions because conductivity is a complex, continuous function and the data were collected using finite sampling (Hohmann and Raiche, 1988). All the EM data for this study (fixed loop, moving loop and DHEM) excluding the AMT will be processed and modelled using ElectroMagnetic Imaging Technology’s (EMIT) Maxwell Electromagnetic software (Duncan, 2007) which limits one to a more than one dipping conductive plate model in a resistive host.

Parametric modelling using EMIT’s Maxwell was performed on both the ground EM and the Downhole Electromagnetic data. The Maxwell algorithm is a 32-bit Windows application that provides fast forward iterative modelling of single and multiple conductors in free space or with simple flat overburden sheets. At its core Maxwell uses the plate formulation of Lamontagne and West (1971). It handles all EM geophysical data such as time and frequency domain, downhole EM, ground and airborne EM data,  $\frac{dB}{dt}$  and **B** field measurements. Maxwell software automates the handling of large datasets with



inversion and forward modelling of plate targets and conductive overburden responses. It uses a thin plate model to represent many geologically and economically interesting conductive targets that appear as intrusive dipping dikes or nearly horizontal layers of finite size especially when prospecting for base metals (e.g. Ni, Cu) or mineral deposits that are often isolated, massive sulphide bodies. Here Maxwell thin plate modelling is used to represent the highly conductive well mineralized harzburgite pods. The schematic view of the thin conductive plate is illustrated in Figure 8.6.

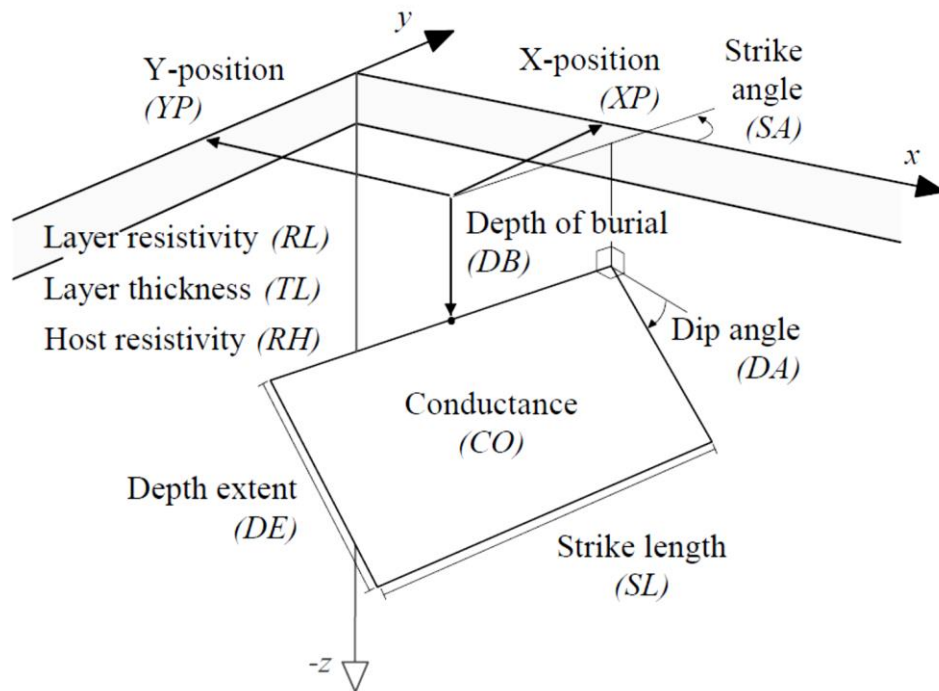


**Figure 8.6** - Schematic view of thin conductive plate in a resistive host below a conductive overburden. No plunge angle (Pirttijarvi, 2003).

Pirttijarvi (2003) illustrated a schematic view of a thin plate model in the lower part of a two-layered host medium (Figure 8.6). In the rectangular coordinate system the plane  $z = 0$  represents the earth's surface and the  $x$  and  $y$  coordinates refer to the geographical coordinates (north and east). The position of the plate is defined by the  $x$ ,  $y$ , and  $z$  coordinates of the centre of the upper side of the plate. One side of the plate is always parallel to the surface, and the orientation of the plate is defined by the (vertical) dip angle and the (horizontal) strike angle but no plunge angle. The size of the plate is defined by parameters like the strike length, which is the plate width along the strike direction, and depth extent, which is the plate height along the dipping side of the plate. Since the plate is considered to be thin, its thickness and conductivity are strongly correlated and cannot be determined separately. Therefore their product, conductivity thickness or conductance, is used to characterize the electrical property of the thin conductor (Pirttijarvi, 2003).

## 8.4 Inversion of AMT data

Inverting AMT Cagniard Resistivity and Impedance Phase data provide detailed images of the conductivity structure at depth. 1-D and 2-D modelling programs were used to convert the measured results to profiles of resistivity versus depth. Smooth-model inversion mathematically “back-calculates” from the measured data to determine a likely location, size and depth of the source or sources of resistivity changes. Zonge 2D inversion algorithms allow for various types of input model parameters and geometry constraints to yield the most reasonable model (Zonge, 2010). 2D inversion models have several advantages over 1D models in that the 2D inversion shows two dimensional shaped structures (for example, edges associated with contacts at depth) (Zonge, 2010). Also, the 2D inversion removes the need to perform static-shift corrections normally required for the 1D inversion. The 2D inversion is also able to successfully model any dipole orientation, but assumes the survey line crosses geologic strike perpendicularly to the section (Zonge, 2010).

### 8.4.1 AMT Model Types

Dobrin and Savit (1988) described a 2D geo-electrical structure as one for which the electrical conductivity varies as a function of depth ( $z$ ) for only one horizontal coordinate, for example  $X$ , while the resistivity is not a function of the other coordinate,  $Y$ . The direction along which the electrical properties do not vary,  $Y$ , is called the strike direction, and the perpendicular direction,  $X$ , is called the dip direction. For 2D models the equations describing the interaction of plane EM waves with such a medium separate completely into two sets of equations. One describes the case for which the electric field component is parallel to the strike while the magnetic field component is perpendicular to it. The first mode of interaction is called **E-parallel** ( $E_{||}$ ) or transverse electric (**Te**) mode. The other set of equations describes the normal or perpendicular mode in which the electric field component is perpendicular to the strike or in the dip direction, while the magnetic field component is in the strike direction. This is called **E-perpendicular** ( $E_{\perp}$ ) or the transverse magnetic (**Tm**) mode (Dobrin and Savit, 1988). These two modes of EM wave propagation in 2D media behave differently.

Dobrin and Savit (1988) examined the behaviour of these two modes for a simple, single-vertical-contact model which can shed light on other models that are significantly more complicated. If a number of MT stations are measured along the  $X$  axis, i.e., along the line traversing the model from left to right, and plot the apparent-resistivity information for the two fundamental modes for a single frequency as a function of  $X$ , we obtain the apparent resistivities as described in the middle part of Figure 8.7.

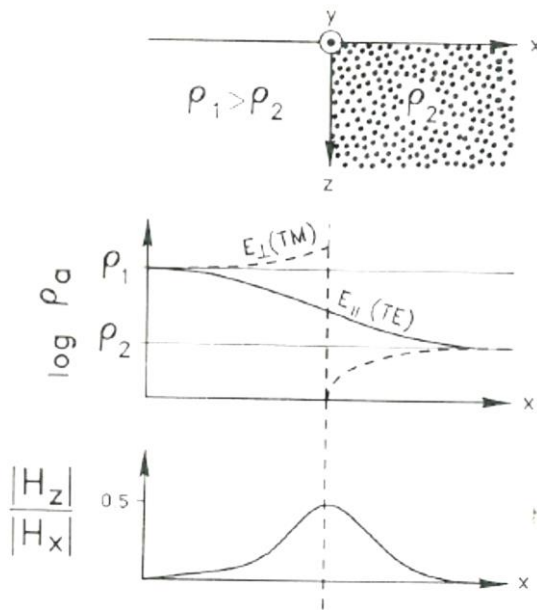


**Figure 8.7** - Natural-field electromagnetic response to a two-dimensional, single lateral contact, model (d'Ecreville and Kunetz, 1962).

For the **Te** mode, the response of the stations to the left removed from the contact, are where the asymptotic value of this apparent resistivity is equal to the resistive value of the block on the left or  $\rho_1$ . As we move along the **X** axis to the right towards the vertical contact of the resistivity discontinuity, the **Te** mode senses the existence of the discontinuity and smoothly plunges down due to the effect of the more conductive block to the right. The curve goes smoothly through the location of the discontinuity and eventually asymptotically converges to the true value of the resistivity for the block on the right (Dobrin and Savit, 1988).

The **Tm** mode exhibits an entirely different behaviour. It starts as for the **Te** mode from the true value of the resistivity for the resistive block on the left. However as we approach the point of discontinuity from the resistive side the **Tm** mode exhibits an even more resistive response than does the resistivity of the block on the left. As we move across the discontinuity, the **Tm** drops and has a discontinuous behaviour (Figure 8.7). Again, as we move to far right, it converges to the true value for that block (Dobrin and Savit, 1988).

The physical reason behind this characteristic behaviour is that, for the **Te** mode, the electric field is in the direction of the geoelectric strike. Electric currents, which tend to follow the direction of the electric field component, are flowing in the structure parallel to the strike, never trying to cross the lateral resistivity discontinuity. Consequently, although this current flow senses the presence of the discontinuity as we get closer to it, it passes through the discontinuity in a smooth fashion. This means that the information carried by the **Te** mode response is less distorted by lateral discontinuities but also less sensitive to

them. On the other hand, the **Tm** mode has an electric field component in the **x** direction. That electric field component drives electric currents across, perpendicular to the vertical contact. There is a discontinuity in the magnitude of this electric current due to the contrast in resistivities (Dobrin and Savit, 1988).

## CHAPTER 9: GEOPHYSICAL MODELLING OF THE DATA

The main objective of this research project is to derive a 3D model of the well mineralised harzburgite which is hosted within the Jacomynspan Ni-Cu mineralised mafic to ultramafic sill in order to guide further drilling. This model was developed by modelling different geophysical datasets collected over the study area. The 3D geology model generated in Micromine from drilling results was used as a starting model.

Since the Jacomynspan Ni-Cu sulphide deposit has a coincident magnetic and EM response, Prof Cooper's Mag2dc software was used for modelling the high resolution aeromagnetic data for this study. Geosoft's VOXI Earth Modelling software was used to model of the magnetic data to compliment the modelling from Mag2dc.

The dominant physical property for the inductive EM methods used here is the electrical conductivity. As shown previously, there is a very large physical contrast between the electrical properties of the well mineralised harzburgite and the host rocks. Maxwell Electromagnetic software was used in the modelling of all the ground EM data and Downhole Electromagnetics (DHEM) data.

All Audio-frequency Magnetotelluric (AMT) data processing and inversion were carried out using a combination of Zonge proprietary software and Geosoft as described in the previous chapter.

Geological information was incorporated via the model objective function. The geology model created in Micromine software using the drilling results and the associated measured physical property values were combined to make the reference model  $m_{ref}$ . This model represents the best guess for the true distribution of the physical properties. During the inversion process, the challenge is to find a model that fits the data, is close to this reference model but improves the knowledge about the mineralized body, i.e. indicate where the mineralized pods are if possible.

### 9.1 Modelling Magnetic Data.

The underlying basic principle behind magnetic modelling is that all magnetic anomalies caused by rocks are superimposed on the geomagnetic main field that originates in the core of the Earth (Lelievre, 2003). The shape, dimensions, and amplitude of an induced magnetic anomaly is a function of the orientation, size, depth, and magnetic susceptibility of the body as well as the intensity and inclination of the Earth's main magnetic field (Mariita, 2007). It has been explained before that the forward modelling process involves calculating a corresponding magnetic response from a starter model which in turn is compared to the observed magnetic field response. The model is manipulated until the

calculated magnetic response mimics the observed magnetic response to an acceptable degree.

#### 9.1.1 The Three-Dimensional Starting Model

From the drilling results carried out so far, it is known that the Ni-Cu mineralisation is hosted within a mafic to ultramafic sill intruded into gneissic rocks and dips steeply to the south and extends down to depths of over 900m. The sill is predominantly composed of a poorly mineralised tremolite schist (metamorphosed pyroxenite) containing lenticular bodies of the well mineralised harzburgite. The harzburgite generally hosts net-textured mineralisation with the mineralisation up to 50% by volume of the rock. Massive sulphide veins and stringers are occasionally present. The aim is to map and delineate the well mineralised harzburgite with its elevated magnetic susceptibility and conductivity values against that of the tremolite schist. The Micromine model of this sill using drilling results from historical (1970s) and the recent (2011,2012) drilling was exported as a DXF file and imported into Geosoft as shown in Figure 9.1.

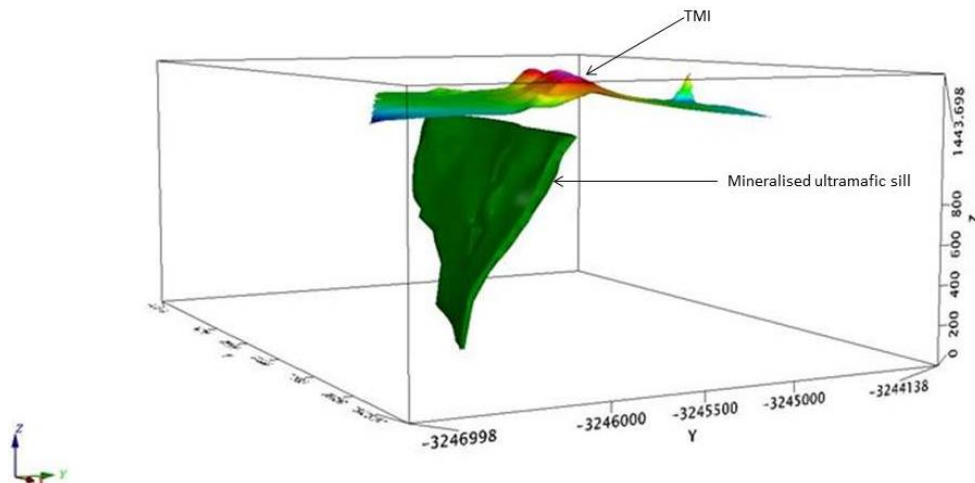


**Figure 9.1** - 3D view of the Micromine model (in green) showing the mineralised ultramafic intrusion steeply dipping to the south with the TMI image on top. This model was used as a starting model during the modelling process.

As can be seen from Figure 9.1 above, the mafic to ultramafic sill has elevated values of magnetic susceptibility in comparison to the surrounding country gneissic rocks (TMI image above the sill). The sill is host to disseminated mineralisation as well as the well mineralised harzburgite which also has elevated values of magnetic susceptibility and occurs in pods. Of course this 'starter model' is limited to the drilling information and does not consider the possibility of similar ore-bearing bodies being present at greater depth down dip from the present body. That is where the geophysical data sets with associated inversion models would be most useful in delineating possible further bodies with similar physical properties.

### 9.1.2 Mag2dc Modelling of the High Resolution Aeromagnetic data

The aeromagnetic data were modelled using Mag2DC that allows the forward modelling and inversion of magnetic data. A total of 19 synthetic lines were created over the TMI grid of the high resolution aeromagnetic survey data for the study area (Figure 9.2). The lines were selected to intersect the sill at approximately right angles. X, Y coordinates and the TMI data were then sampled from the TMI grid along the synthetic lines at 25m intervals in Geosoft.

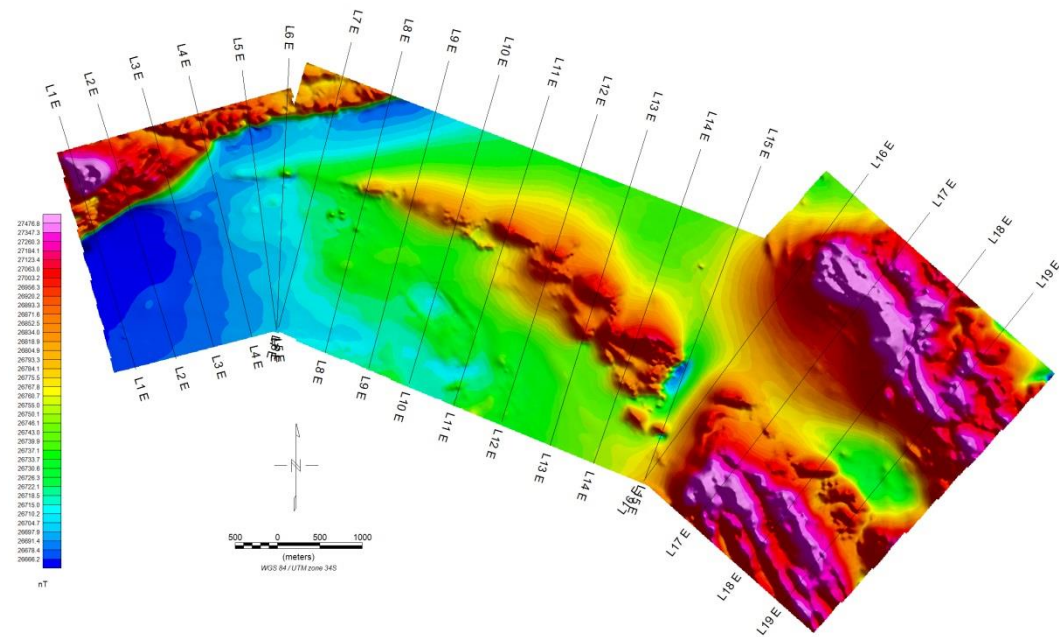


**Figure 9.2** – The airborne TMI image showing the 19 synthetic lines created for modelling.

For each sampled line, data were then imported as an ASCII file separately into Mag2dc software for forward modelling. The forward modelling process involves calculating a corresponding magnetic response from a postulated geological 'starter' model which in turn is compared to the observed magnetic field response while adjusting the regional field during the process. The main obstacle here is that the regional field, which is the field observed if the anomaly is not present, is unknown. Furthermore the regional field must be a slowly varying smooth function represented by geology at much greater depth than dictated by the present near surface geology of interest. At first, the postulated model is manipulated to represent the known geology in terms of shape and the bulk magnetic physical parameters determined and still agree with the measured interpolated total field magnetic data until the calculated magnetic response mimics the observed magnetic response to an acceptable degree as shown in Figure 9.3.

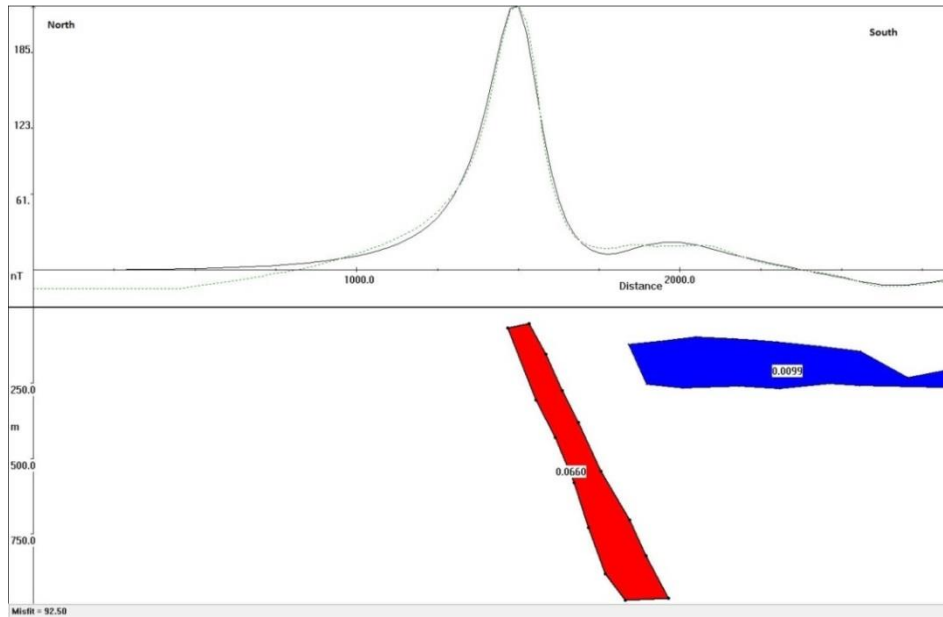


**Figure 9.3** - Mag2dc modelling results for Line 11 showing the mineralised ultramafic sill in red steeply dipping to the south. The green dotted profile above represents the observed magnetic field while the continuous black profile represents the field due to the model. A second shallow magnetic body with very much lower magnetic susceptibility is present down-dip (south) of the dipping sill which is not present in the Micromine 3D 'starter' model. Susceptibilities are in SI units.

The modelling results produced a close fit between the calculated response (green dotted profile) and the measured TMI response (black profile). A body representing the ultramafic sill which steeply dips to the south at around  $68^\circ$  with a large depth extend of over 900m was modelled in agreement with the known geology.

### 9.1.3 Calculating the Regional Field and Levelling

After all the 19 lines were modelled and the regional field for each line adjusted during modelling, the regional field was abstracted for each line and gridded for the whole area in Geosoft. More specifically, first the regional field for each line was exported as an ASCII file from the Mag2dc software. The ASCII regional file for each line was then imported into a Geosoft single database. The data were then gridded and since the regional field for each line was adjusted separately the gridded data are stripy along the lines (Figure 9.4a) and need levelling.



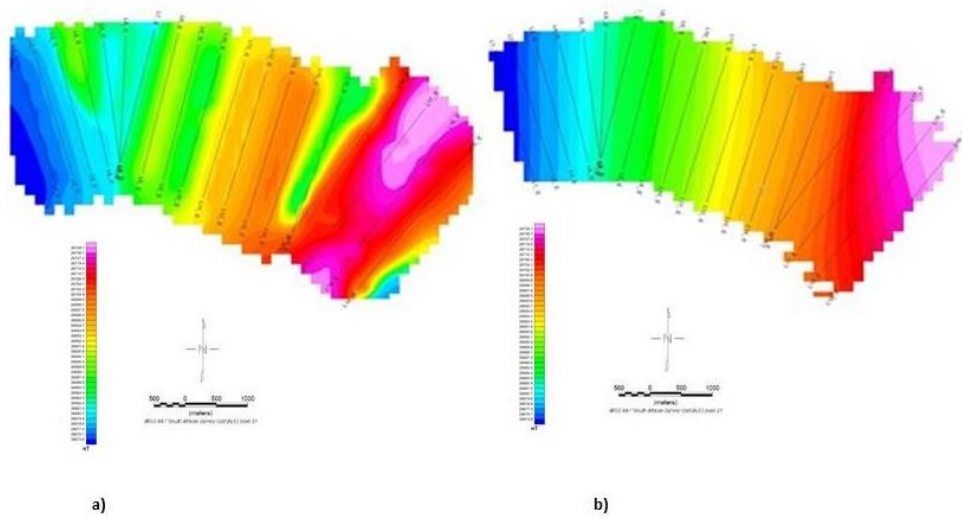


**Figure 9.4** - a) Regional field data for each line gridded into a single grid which is stripy and needs levelling. b) The levelled Regional field.

The regional field for the whole grid was levelled in Geosoft (Figure 9.4b) using the Micro-levelling procedure. This procedure involves using Bi-directional Line Gridding which changes the storage sense of the data while applying filters. The procedure was carried out using the Row Orientation option in Geosoft. The output grid direction parameter **KX** determines whether the output grid lines will be parallel to the output grid **X**-axis (**KX=1**) or the **Y**-axis (**KX=-1**). As an example, if the lines are oriented in the **X** direction and one runs line gridding, the output grid is oriented in the **Y** direction with the **KX** parameter controlling the storage direction of the grid.

#### 9.1.4 Calculating the Residual Grid

The final residual data were calculated by subtracting the levelled regional field data from the TMI data. This procedure was carried out using the Geosoft database tools via the channel math utility.

The residual field map (Figure 9.5b) was then produced in geosoft by subtracting the levelled regional field from the original TMI.

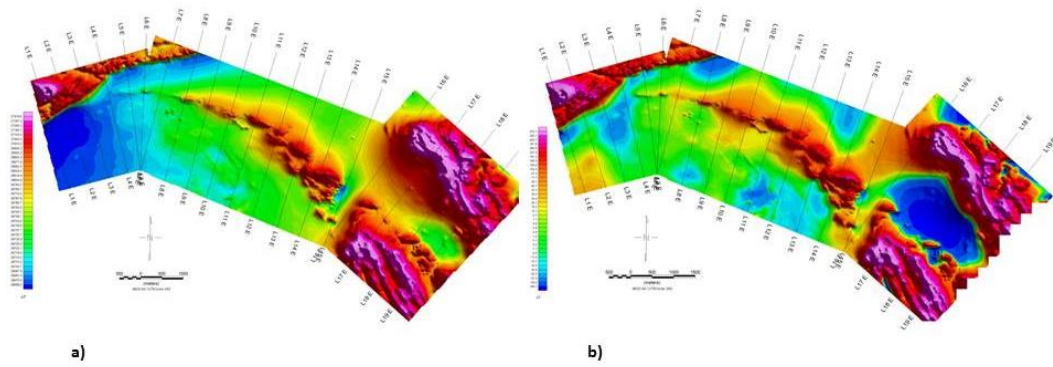


**Figure 9.5** a) The aeromagnetic TMI image. b) The calculated Residual field map after subtracting the Levelled Regional Field from the TMI.

### 9.1.5 Modelling of the Final Residual Data

The final residual field data in the database together with the X and Y coordinates were exported in Geosoft as an ASCII file and imported again into Mag2dc software. The BOD files which define the shape of the modelled bodies were also imported into Mag2dc for final modelling. The final model (Figure 9.6) which now takes into account the levelled regional field was then obtained for each line by a combination of minor adjustments to the model of inversion.

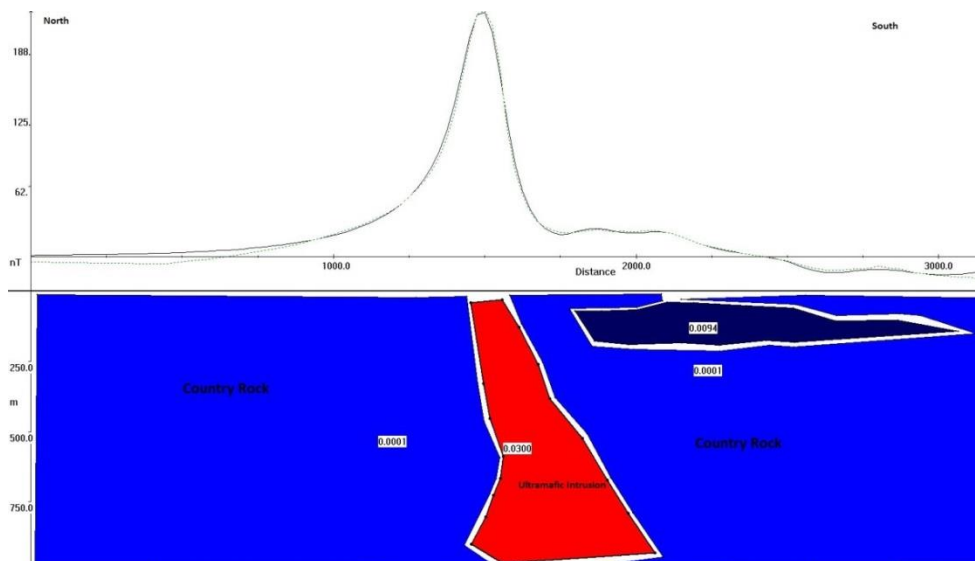


**Figure 9.6** - Line 11 final model of the residual field showing the ultramafic intrusion steeply dipping to the south.

The 2.5D model for line 11 again shows a body steeply dipping to the south. This correlates very well with our starter model which is the ultramafic sill which steeply dips to the south and has elevated magnetic susceptibility compared to the country rocks. However note that this model now predicts a widening of the sill body at a depth below 700m and has halved the bulk magnetic susceptibility from 0.06 to 0.03 SI units. The

widening of the sill body is probably an artefact as it is notoriously difficult to obtain the 'true' lower contact or interface of a magnetic model through modelling.

#### 9.1.6 Creating a 3D Model Representation from Mag2dc Models

The final 2.5D model for each line was exported in Mag2dc as an ASCII file. The algorithm 'Magmodintrp' written in FORTRAN 77 (E Stettler, personal communication) was then used to extract the cross sections of the final model. The output of this application is an X,Y,Z,val file where X and Y are the coordinates of the lines and Z is the depth with corresponding magnetic susceptibility values for the modelled bodies at each depth and distance. This XYZ file was then imported into geosoft and gridded in 3D to come up with a 3D magnetic susceptibility starter model representation of the study area shown in Figure 9.7.

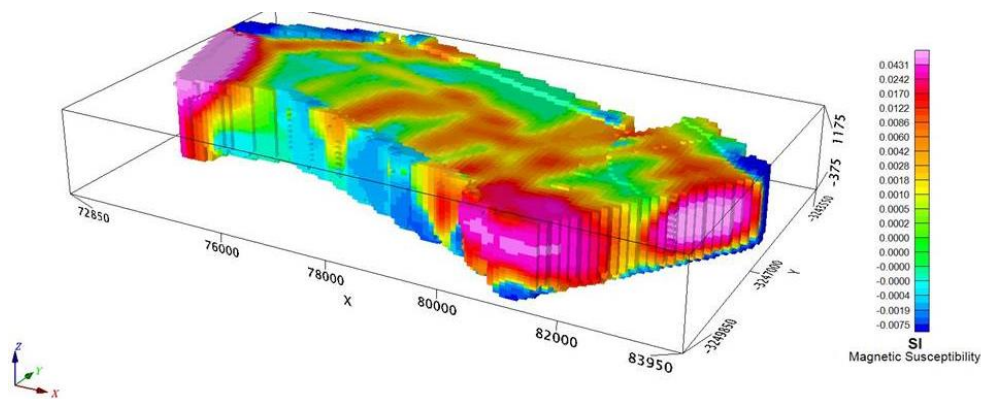


**Figure 9.7** - Final 3D susceptibility smooth model representation of the Jacomynspan area.

This 'starter' has the advantage that *a priori* information especially about the geology and physical parameters can be incorporated into the model and experimentation can be done with possible geological scenarios to determine what is a likely acceptable model. The smooth model can be clipped along the X-axis to the mineralised mafic to ultramafic intrusion of the study area (Figure 9.8a). A colour tool was also applied in Geosoft to the clipped model (Figure 9.8b) to clearly map the intrusion.

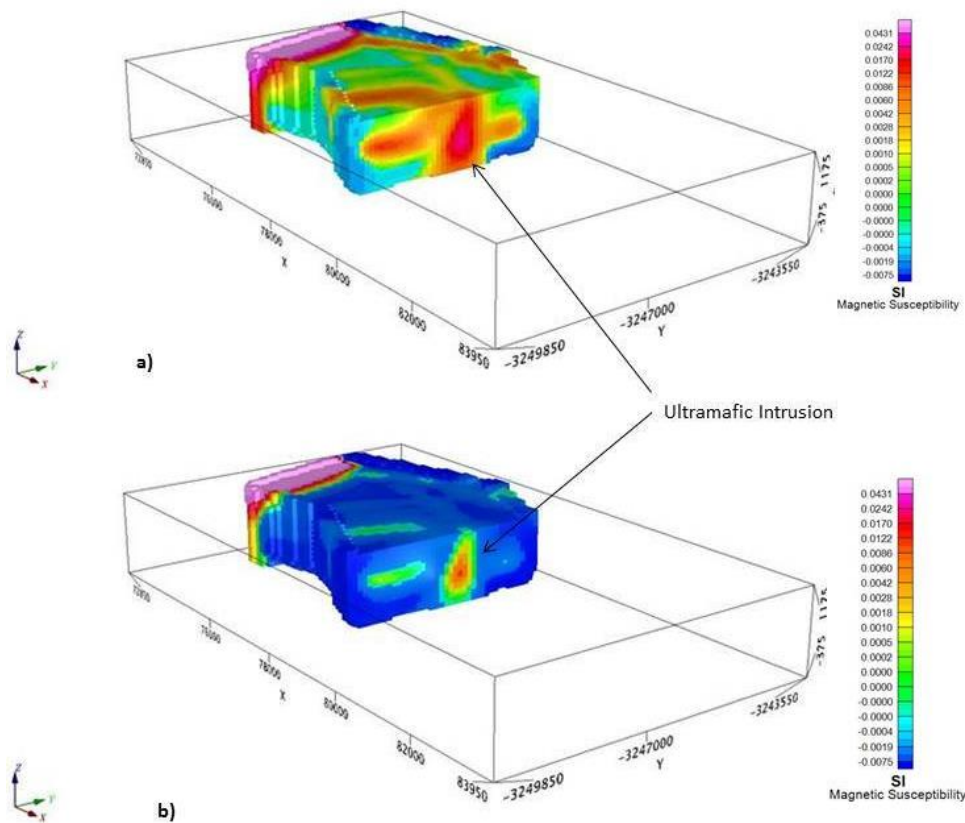


**Figure 9.8** – Final 3D model representation of Jacomynspan clipped to the mineralised ultramafic sill of the study area. a) Smooth model showing the mineralised ultramafic sill, b) Smooth model with the colour tool applied to clearly map the mineralised ultramafic sill.

The mineralised ultramafic sill was clearly mapped in this 3D model representation. Note the slightly magnetic material south of the sill which has been resolved by the inversion process. However note that this is still only a ‘starter’ model and this model can now be subjected to 3D least squares or other inversion techniques such as the ones available in Geosoft. However the 3D model already represents the interpreter’s best information on the most likely imitation of the true geology and the inversion only needs to make final minor corrections to obtain the best fit between observed and calculated total magnetic field values.

## 9.2 VOXI Modelling of the Aeromagnetic Data

Voxel inversion, by definition, divides the earth into a number of voxel (cubic) elements and solves for their associated physical properties (magnetic susceptibility in this case). Ideally, the output from a voxel inversion should be free from discretisation artefacts, i.e. it will depend only on the data and the regularisation method and not on the specific locations of voxel elements or their finite sizes (Geosoft, 2012).

### 9.2.1 VOXI modelling of the study area

VOXI's unconstrained smooth model inversion was applied to the study area. A new VOXI session was created by first defining the geographical Area of Interest (AOI) using a polygon file outlining the study area. A Digital Elevation Model (DEM) for the area was also created and entered into the new VOXI session as a grid. A mesh showing the area of interest and depth of investigation was then created as shown in Figure 9.9.

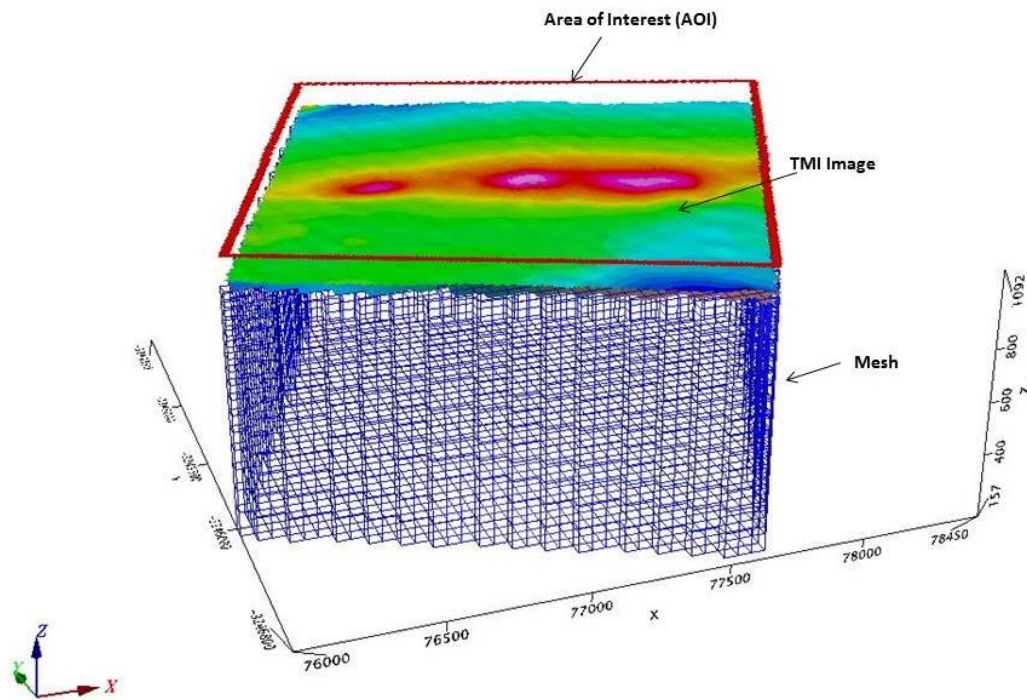


**Figure 9.9** - A mesh showing the Area of Interest (AOI) and the depth extent of modelling.

The type of the potential field data is also entered and in this case it is magnetic and the model type is susceptibility. A linear background trend is removed automatically and then the inversion is conducted. The inversion process runs for some minutes depending on the size of the AOI and the number of constraints being applied. When complete the final result is displayed and appears as shown in Figure 9.10.



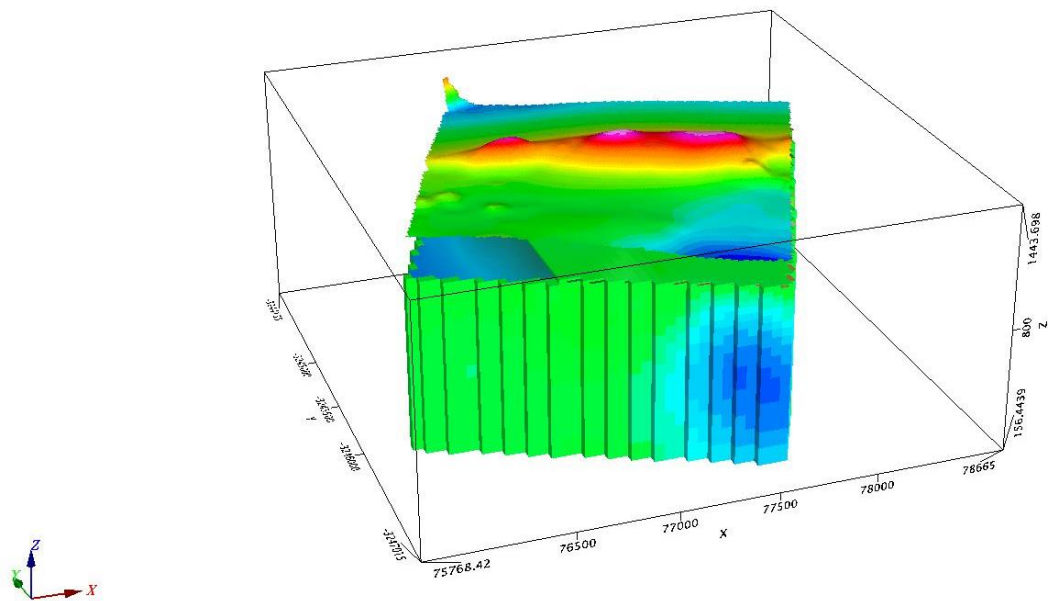


**Figure 9.10** – Unconstrained smooth model inversion results after performing the inversion. The straight black lines in the susceptibility are a result of the created voxels.

The results can be exported and displayed in 3D as shown in Figure 9.11 for further manipulation.

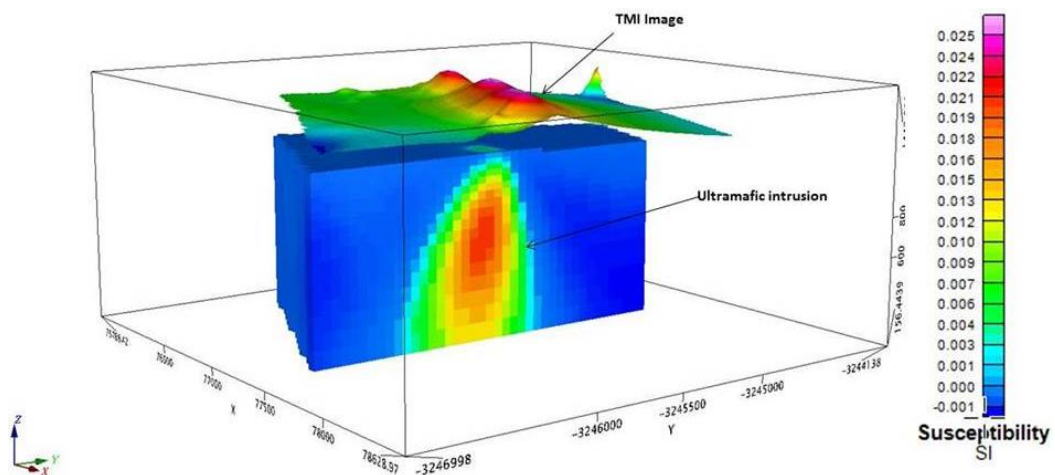


**Figure 9.11** – 3D unconstrained smooth model inversion results of the study area showing the mineralised Jacomynspan ultramafic intrusion.

The unconstrained smooth model inversion results for the study area above clearly maps the Jacomynspan ultramafic intrusion which has elevated values of the magnetic susceptibility. However the slightly magnetic material south of the sill mapped in Mag2dc has not been resolved by this inversion process but the maximum susceptibility is in the same ball-park as obtained by the final Mag2dc modelling and a widening of the magnetic body is also predicted which, as already stated, is most probably an artefact.

3D iso-surfaces for the susceptibility can be created in Geosoft to clearly outline the modelled magnetic bodies of different susceptibility as shown in Figure 9.12.

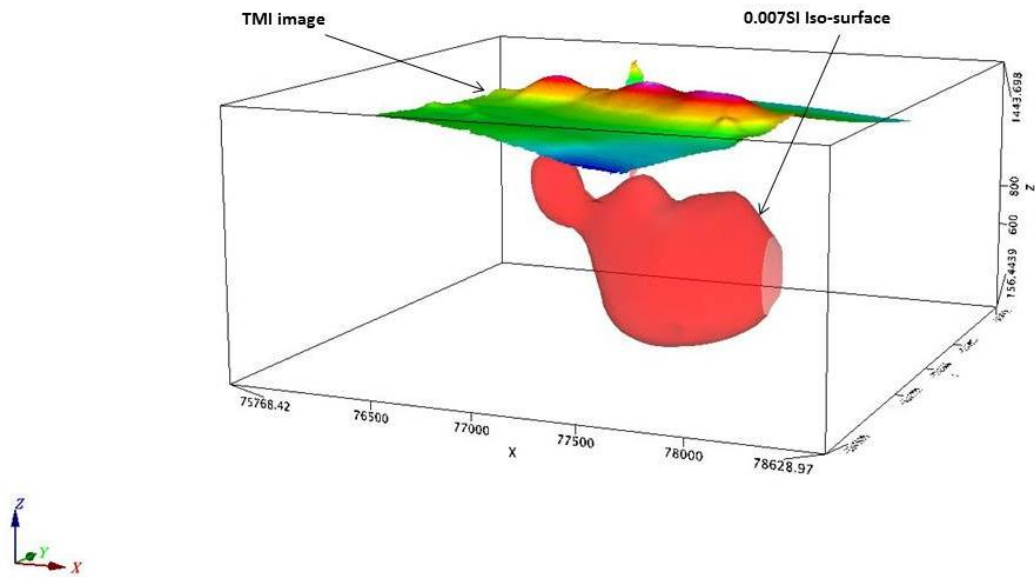


**Figure 9.12** - The 0.007SI magnetic susceptibility iso-surface of the ultramafic intrusion.

### 9.2.2 Iterative Reweighting Inversion Constraint (IRI)

VOXI's Iterative Reweighting Inversion (IRI) Focus was applied to the study area in order to refine the smooth model inversion and emphasize a desirable model characteristic. The IRI Focus constraint normalizes and sets the outcome of the previous inversion as the weight constraint for the next inversion. It allows the model to be refined in order to emphasize positive or negative anomalies. For the study area, since the intrusion has more elevated magnetic susceptibilities than the country rock, the positive was emphasised.

The unconstrained smooth model inversion results were compared to the IRI Focus results in Figure 9.13.

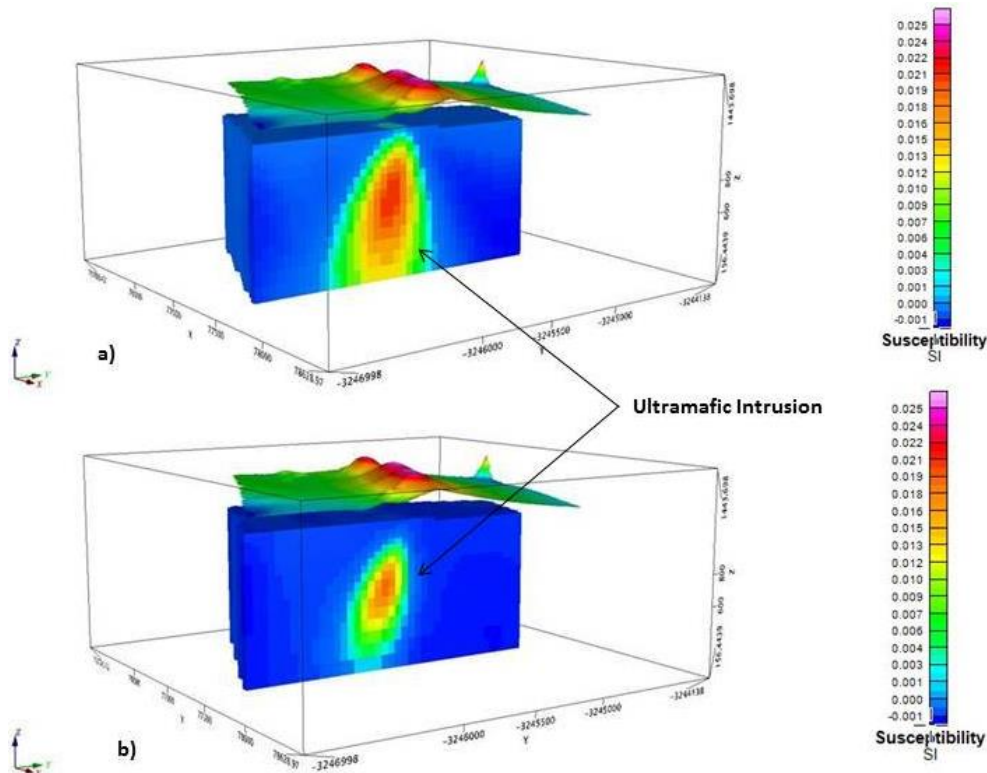


**Figure 9.13** - a) Smooth Model Inversion for the study area, b) IRI focus applied to the smooth model. The results are more focused showing the body steeply dipping to the south.

The IRI Focus results (Figure 9.13b) show a more compact and focused but deeper magnetic susceptibility distribution of the mineralised mafic to ultramafic intrusion compared to the smooth model inversion results. It can clearly be seen that the intrusion is now more focused and dips to the south.

### 9.2.3 Magnetization Vector Inversion (MVI)

Although the palaeomagnetic results have shown that there is little remanent magnetism at Jacomynspan to consider during modelling, VOXI's Magnetisation Vector Inversion (MVI) was however applied to the study area. The reason being that MVI allows the magnetization direction to vary within the model not only taking into account the effects of remanence, but also demagnetization, anisotropy and induced magnetization. Both remanent and induced magnetisations are incorporated even without prior knowledge of the direction or strength of remanent magnetization. This is essential for correct interpretation of magnetic field data (Ellis *et al.*, 2012).

Most vector magnetization models in 3D are difficult to interpret directly except for very simple cases. In real-world exploration some simpler derived scalars are needed which highlight the important information in the vector model. There are many possibilities but Ellis *et al.*, (2012) found that there are three useful derived scalars for exploration which are: the amplitude of the magnetization, the earth field projection of the magnetization,



and the amplitude of the perpendicular-to-earth-field components of the magnetization. Their vectors are explained diagrammatically as shown in Figure 9.14.

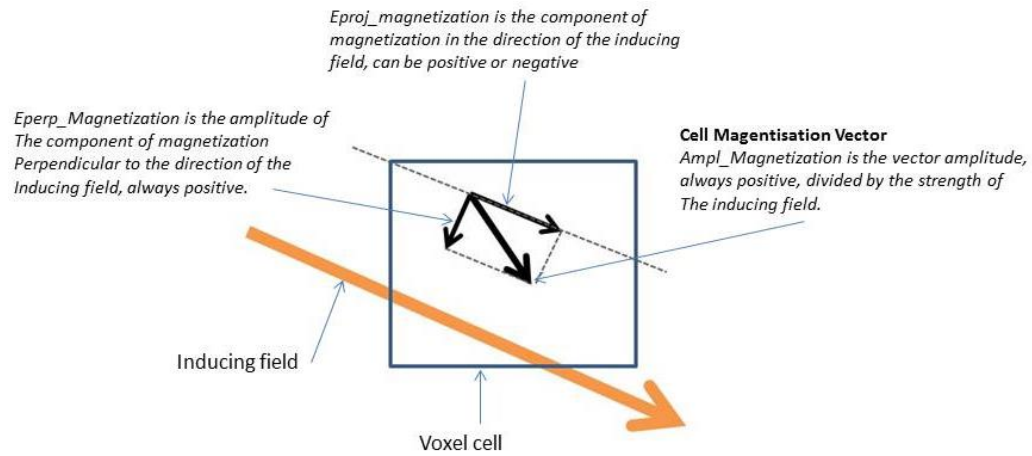


**Figure 9.14** - Magnetization vector orientation of the Amplitude Magnetization, Eperp\_Magnetization and Eproj\_Magnetization (VOXI Training manual).

In exploration problems, the amplitude is robust by being independent of any assumptions regarding the Earth's field, while the amplitude perpendicular to the Earth's field is an approximate indicator of magnetization not induced by the earth's present field. The derived scalars of the magnetisation vector inversion for the study area are shown in Figure 9.15.

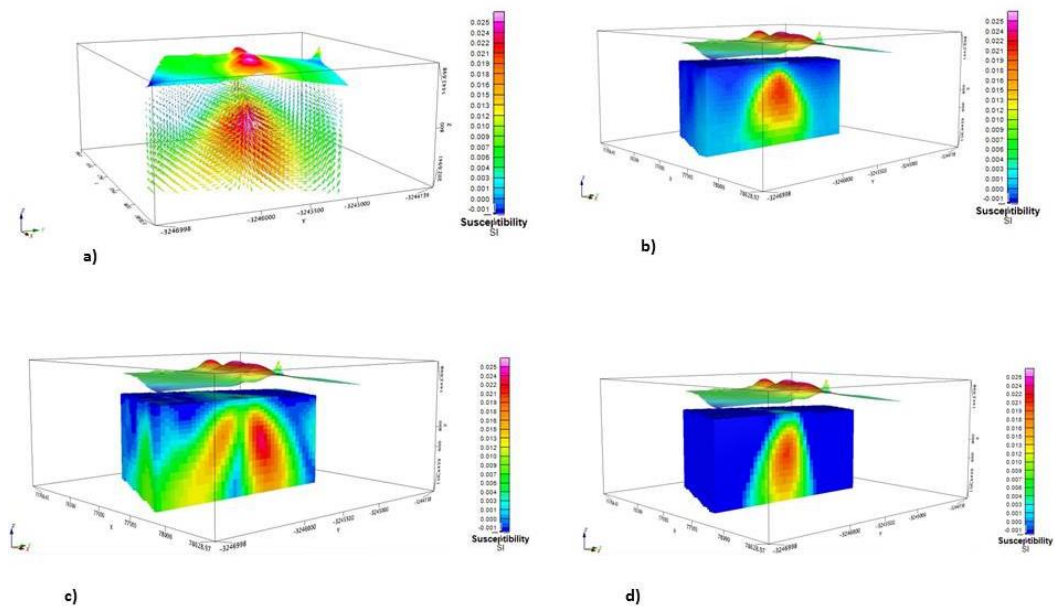


**Figure 9.15** - Derived scalars of the Magnetisation Vector Inversion for the study area. a) magnetisation vector orientation, b) the recovered amplitude of the magnetization vector, c) the amplitude of the perpendicular "Eperp" to earth field components of the magnetization, and d) the projection of the magnetization "EProj" on to the earth field direction.

The Eperp\_Magnetization and Eproj\_Magnetization voxel models can then be compared. If  $Eperp \gg Eproj$  and  $Ampl \gg 0$ , then remanence is more pervasive in the area of interest.

The “Amplitude” voxel represents the vector magnetization amplitude divided by the strength of the inducing field and is analogous to susceptibility and is always positive. The “Eperp” voxel represents the amplitude of the component of magnetization perpendicular to the direction of the inducing field and is always positive. The “Eproj” voxel represents the component of magnetisation in the direction of the inducing field, and can be positive or negative.

#### 9.2.4 VOXI Constrained Inversion

Drilling constraints, with wire-framing, can be used with VOXI inversion. VOXI inversion can be used to validate the geologic interpretation deduced from drilling and to indicate where unrecognised additional mineralization may be located. Since the objective of this study is to map and delineate the well mineralised harzburgite, the Micromine geology model of the harzburgite (Figure 9.16a) was used to create a geo-surface (Figure 9.16b) which was then used as a guide during the constrained inversion.

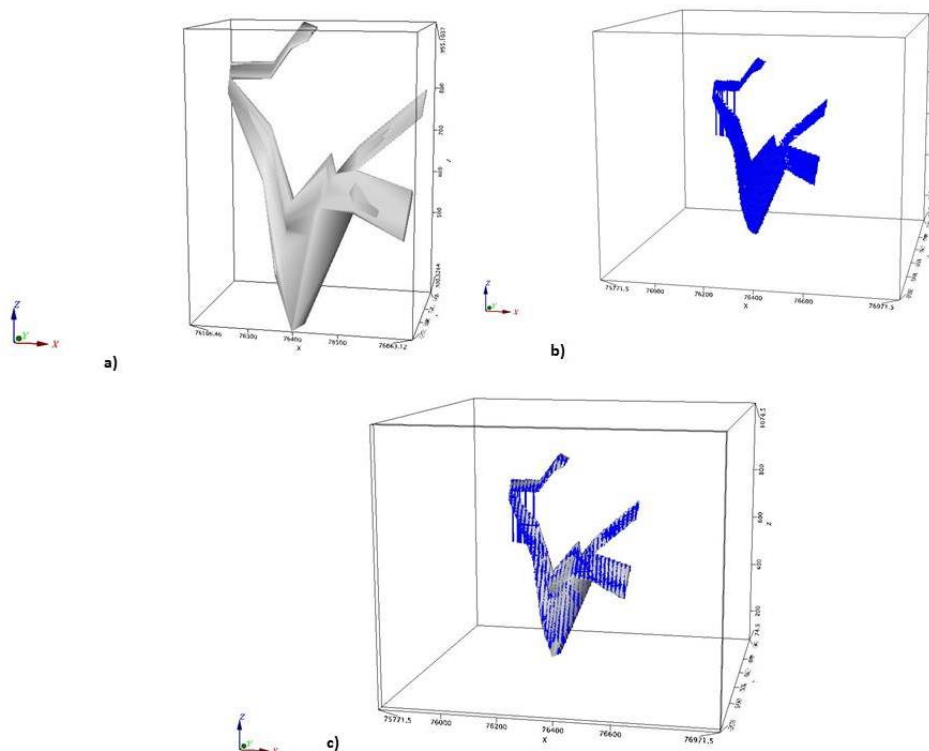


**Figure 9.16** – a) Well mineralized harzburgite model from Micromine, b) well mineralized harzburgite voxel created from geo-surface in geosoft, c) Well mineralized harzburgite model integrated with the voxel in Geosoft.

The constrained inversion that was carried out uses the following constraints:

- A parameter reference model defined by the drilling-wireframe. This encourages the inversion to replicate the drilling-wireframe harzburgite volume, subject to fitting the TMI data. The global reference parameter weight was increased to 1 to force the parameter reference model to affect the inversion.

- There must be an abrupt transition in the susceptibility from the well mineralised harzburgite to the host tremolite schist, therefore gradient weights were introduced to break the smoothness across the boundary of the harzburgite. Four consecutive IRI-Focusing runs were applied for the same reason.

The constrained inversion results suggest a possible extension of the well mineralised harzburgite to the west if a conductor is present as shown in Figure 9.17.

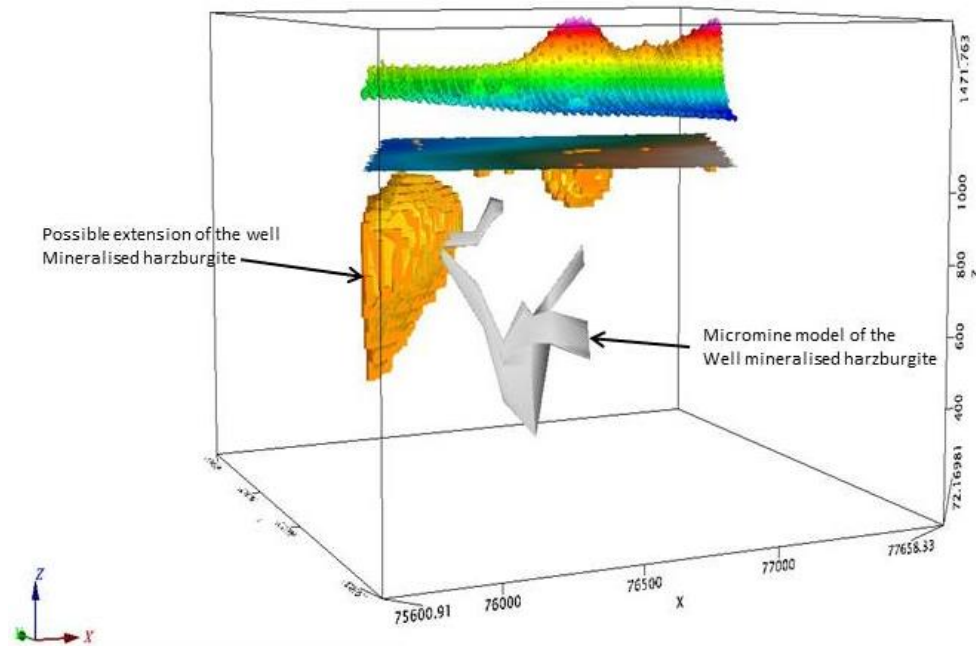


**Figure 9.17** – Constrained inversion results showing the Micromine modelled well mineralised harzburgite and its possible extension to the west.

### 9.3 Modelling of Ground EM data in Maxwell Software

Ground EM data for both the fixed loop and moving loop modes for the study area were modelled using Maxwell EM software. The imported field data as explained before were first interrogated and cleaned up in Maxwell by deleting noisy readings and averaging. The configuration file was then modified according to waveform and survey parameter dictates before modelling.

#### 9.3.1 Waveform Parameters

It is of fundamental importance that before any modelling of the EM data can be carried out, one must have a clear understanding of the waveform parameters such as on-time, off-time, timing mark, duty cycle etc. to enable creating the configuration file. Some of the waveform parameters are explained diagrammatically in Figure 9.18.

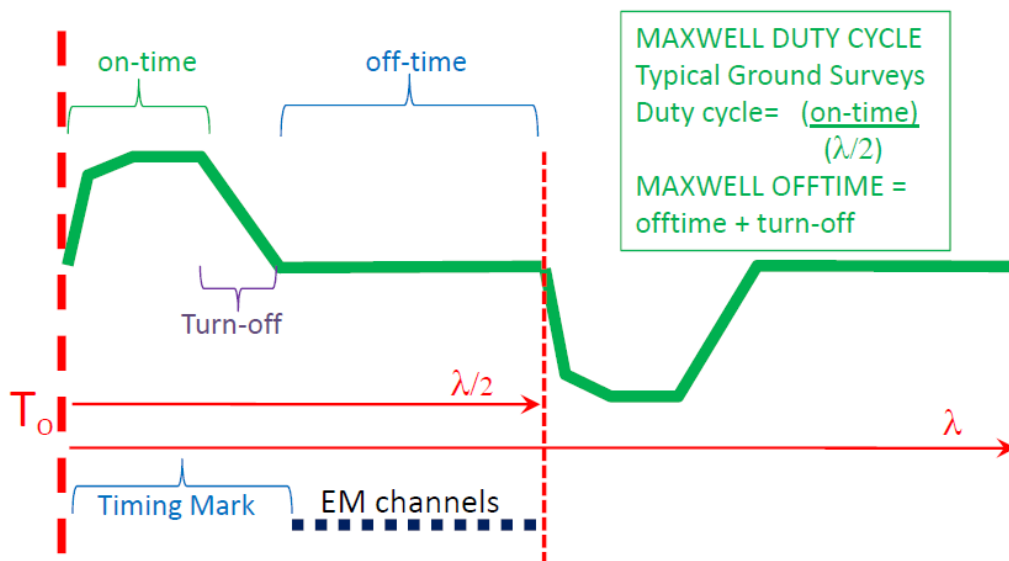


**Figure 9.18** - Waveform parameters used during modelling (Maxwell Training Manual, 2013).

The Timing Mark (Figure 9.19) is important as it sets the timing reference for TEM channel times. This referencing depends on the acquisition system and allows for the same window/channel sampling scheme to be used from survey to survey whilst accounting for variations in the transmitter waveform.



**Figure 9.19** - A window in the line editor display view showing the timing mark, base frequency, on-time, off-time and turn off time. The transmitted current waveform is shown in red while the horizontal blue lines represent receiver time gates.

### 9.3.2 Decay Analysis

After creating the configuration file, there is a need to first determine the best time channels to model. This can be done by making use of time constant decay analysis which can be performed in the Decay Window of the Maxwell software shown in Figure 9.20. The time constant fit to the selected decay is shown by the asymptotic red line and the channels to be modelled are displayed in the Decay window status bar at the bottom.

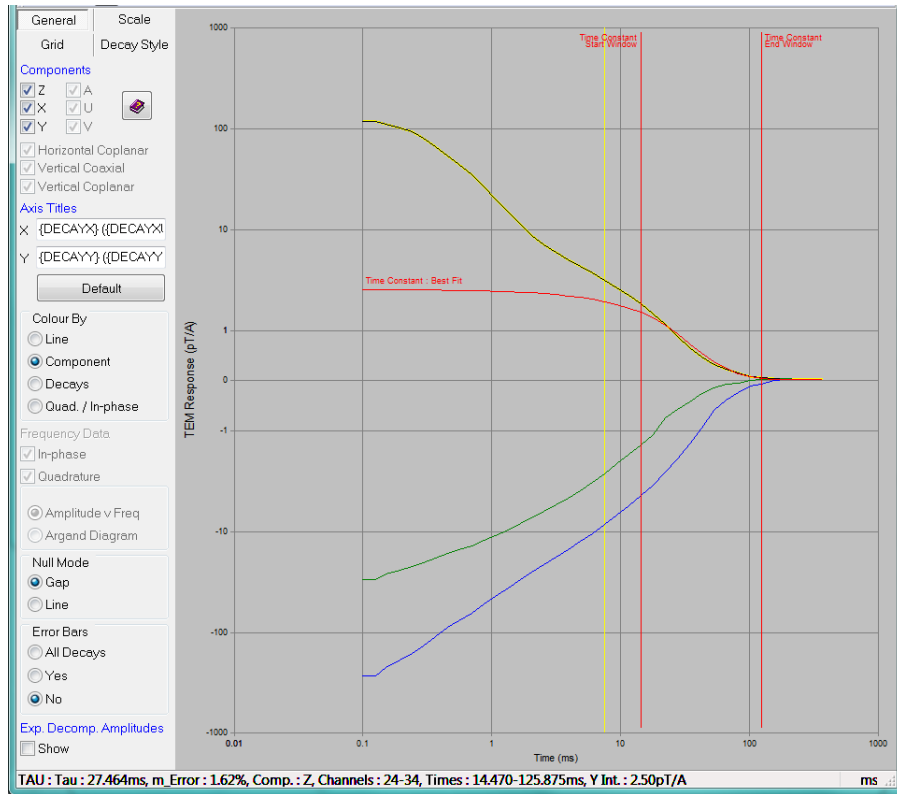
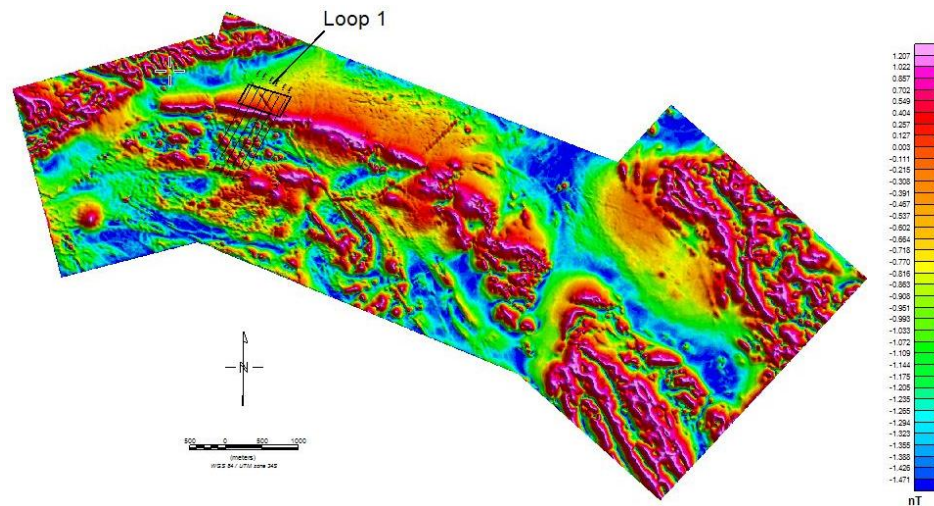


**Figure 9.20** - Decay analysis window showing the Z component fit used to determine the best time channels to model. The Z component decay curve is shown in black(with yellow hue), the X component decay curve is in green while the Y component is in blue.

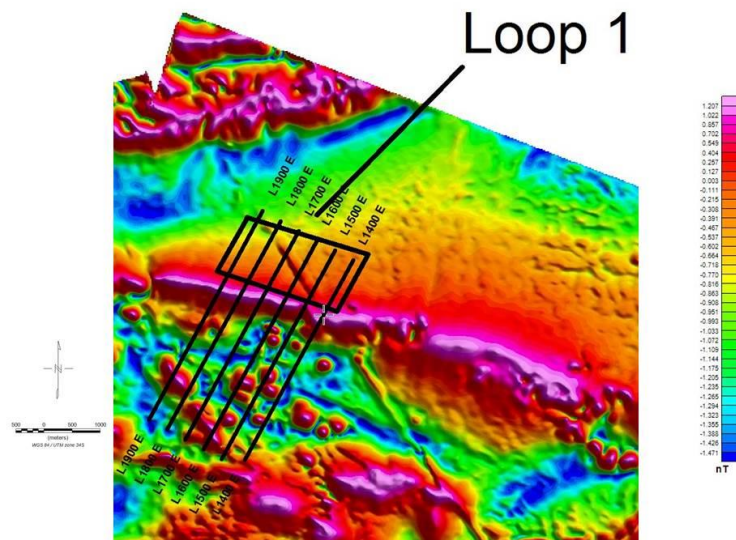
For the fixed loop data, a time constant of 27.464ms was obtained and channels 24 to 34 are the best for modelling.

### 9.3.3 Modelling Fixed Loop EM Data – Loop 1

Three fixed transmitter loops measuring 600m x 400m were surveyed over the Jacomynspan intrusion. However, this study only covers the main target area which was drilled by African Nickel. Therefore only Loop 1 data will be considered. The data for Loop 1 were acquired with the LT SQUID sensor. The data cover the main target area which is also the study area. A total of six lines of about 1.1km long each at 50m station spacing were surveyed over the main target area for transmitter Loop1 (Figure 9.21). The data were modelled using Maxwell with each line being modelled separately.



a)



b)

**Figure 9.21** – a) position of loop 1 relative to the Tilt Angle Derivative image of the high resolution aeromagnetic survey, b) surveyed lines showing the line numbers on Tilt Angle Derivative image.

Before any modelling can be carried out in Maxwell, a configuration file for the survey must be created. Table 9.1 shows the waveform parameters used in creating the configuration file for modelling fixed loop data.



**Table 9.1 – Waveform parameters used for fixed loop survey**

Duty cycle	50%
Base Frequency	0.5Hz
On Time	500ms
Off Time	500ms
Turn On time	0.4ms
Turn Off time	0.4ms
Timing Mark	500.4ms
Transmitter Current	20A

Figure 9.22 shows the EM results in Maxwell for line 1600 (indicated by a yellow cross) after creating the profile plots and the configuration file. On the left side is the plan window which shows the surveyed lines and the transmitter loop position in yellow. On the right, line 1600 profiles for the measured EM response are shown for the **Z**, **X** and **Y** components in that order going down.

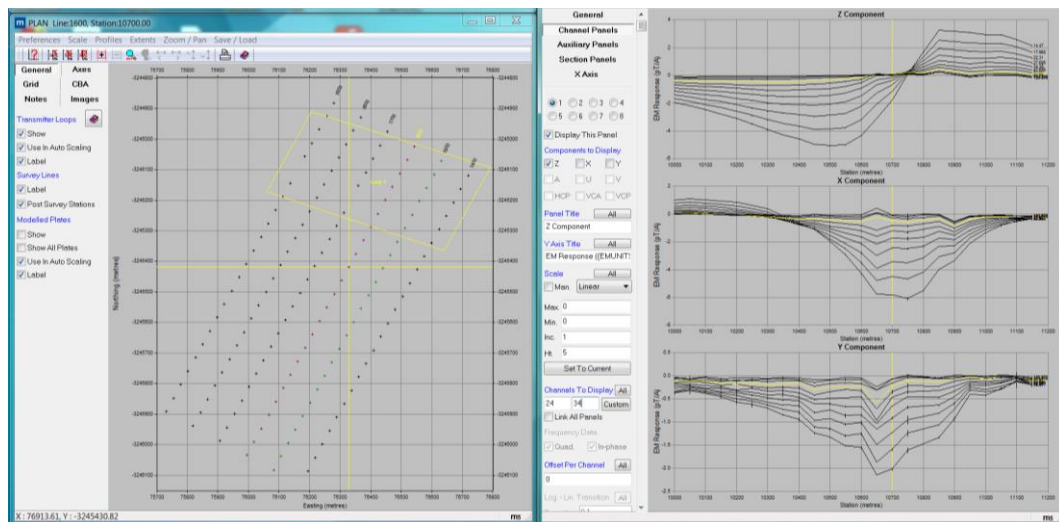


**Figure 9.22 - Fixed loop data after importation into Maxwell Software.** On the left side is the Plan window which shows the surveyed lines and the transmitter loop position (yellow rectangle). On the right, the profiles for the measured EM response are shown for the Z, X and Y components in that order going down for line 1600 which is indicated by a yellow cross.

Modelling of EM data like any other geophysical modelling is a non-unique process i.e. many models can produce the same model response. From the drilling results, we know that the mineralised ultramafic sill has a strike length and depth extent of over 1000m. Physical property measurements also show that the sill has elevated conductivity values compared to the country rocks. We also know from drilling results that the sill dips steeply to the south. This information was used as a starter model in order to constrain our model.

Decay analysis to determine the best time channels carried out in section 9.2.3 showed that the best time channels to model are from channel 24 to channel 34. The next step was to modify the plate parameters to represent the target based on the anomalous data

taking into account the *a priori* information that is available from drilling and physical property measurements. A forward model was then calculated while:

- Adjusting the conductance until there is a response.
- Moving the plate until a reasonable fit is obtained for a single line.

With these forward ‘starting’ parameters determined, the EM plate can now be inverted for the Easting of Plate Centre (E), the Northing of Plate Centre (N), Elevation of Plate Centre (Z), Dip (D) and Dip Direction (DD) while constraining the inversion. Continued necessary adjustments are made until the model response mimics the measured EM response as shown to the left window in Figure 9.23. The black traces show the measured EM response while the red traces depict the model response.

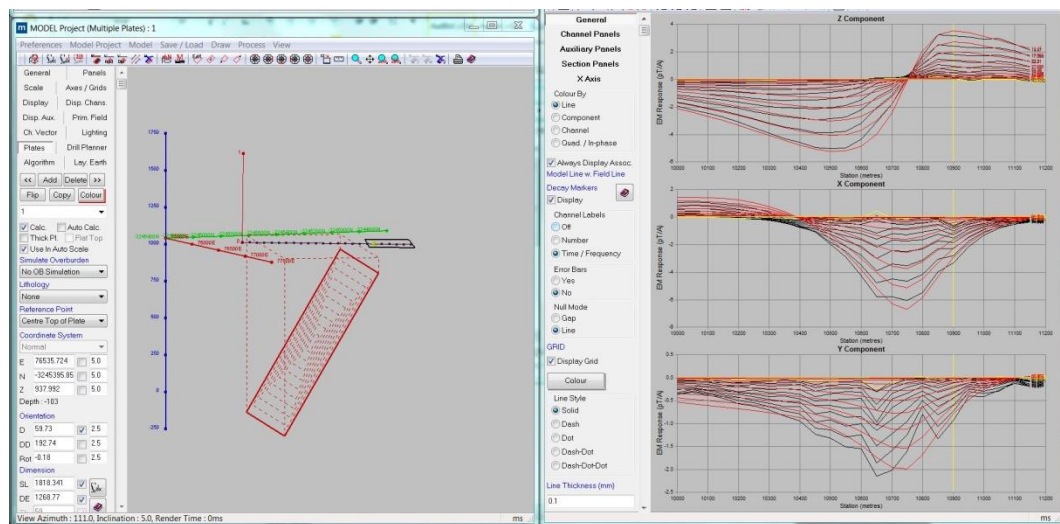


**Figure 9.23** – Modelling results for Line 1600. The left window shows the modelled EM plate steeply dipping to the south correlating with the mineralised ultramafic sill. The right window depicts the measured EM response traces in black and the modelled EM response in red for the three components Z, X and Y.

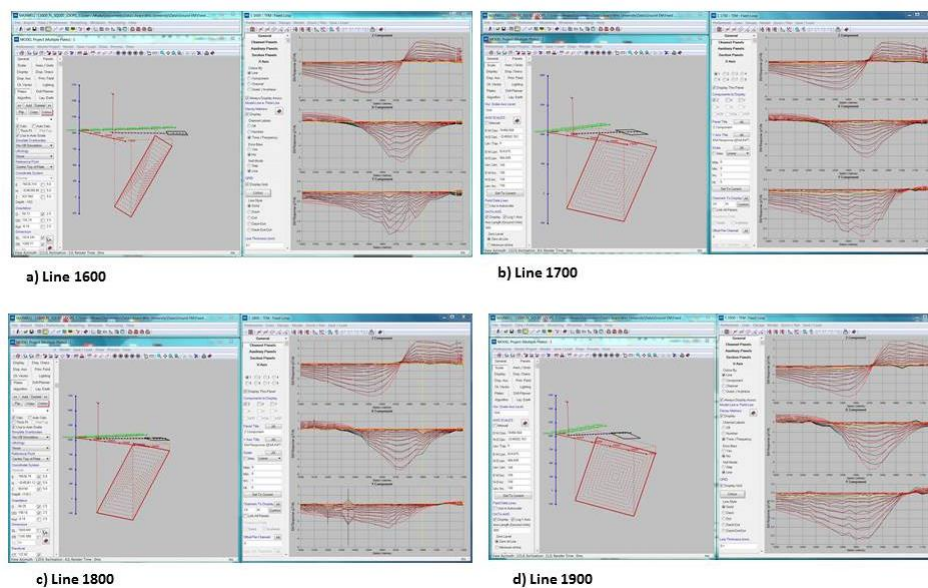
The size of the plate is defined by parameters like the strike length, which is the plate width along the strike direction, and depth extent, which is the plate height along the dipping side of the plate. Since the plate is considered to be thin, its thickness and conductivity are strongly correlated and cannot be determined separately and therefore their product, conductivity thickness or conductance, is used to characterize the electrical property of the thin conductor (Pirttijarvi, 2003). The EM plate parameters for all the modelled loop 1 lines are shown in Table 9.2.



**Table 9.2 – EM plate parameters for all the modelled Loop 1 lines**

Line Number	Strike Length (m)	Depth Extent (m)	Depth to Top (m)	Dip (Degrees)	Conductance(S)
1400	2151.8	1093	66	55.6	104
1500	1803.1	1269.5	95.9	61.71	105.54
1600	1818.3	1268.8	103	59.73	111.24
1700	1811.4	1371.6	102.1	62.01	112.56
1800	1820.9	1341.6	116.1	60.25	122.62
1900	1806	1207.3	125.7	66.32	142.62

All 6 lines for fixed loop 1 were modelled in Maxwell separately and they all show a large EM plate steeply dipping to the south with large strike and depth extent in agreement with the starter model. Figure 9.24 shows modelling results of four of the modelled lines.

**Figure 9.24 – Modelling results for four of the surveyed lines.**

It is known from drilling that the mineralised intrusion is a steeply dipping sheet with a large strike and depth extent and so are the EM modelled plates. An assumption can be made that at late decay times the currents would be focused in the centre of the large EM plate giving an indication of the most conductive part of the intrusion. In order to better constrain the targets, smaller 'Resultant EM plates' of dimensions, 300mx300m that coincide with the centre of the large EM plates (with a conductance above 100S) where current will be focused at late decay times were constructed in Maxwell (Figure 9.25a). Since the physical property measurements (conductivity) taken on the drill core indicate that the net-textured well mineralised harzburgite is more conductive than the disseminated mineralised tremolite schist, the constructed centre of EM plates with conductivity thickness above 100 Siemens were interpreted to give an indication of the well mineralised net-textured harzburgite and massive sulphide stringers. It must be noted that the centre plate is just a dummy plate with no effect on the modelling results

but simply to give an indication of where the currents will be concentrated at late decay times. The constructed 'resultant' EM plate is shown in Figure 9.25 (in blue).

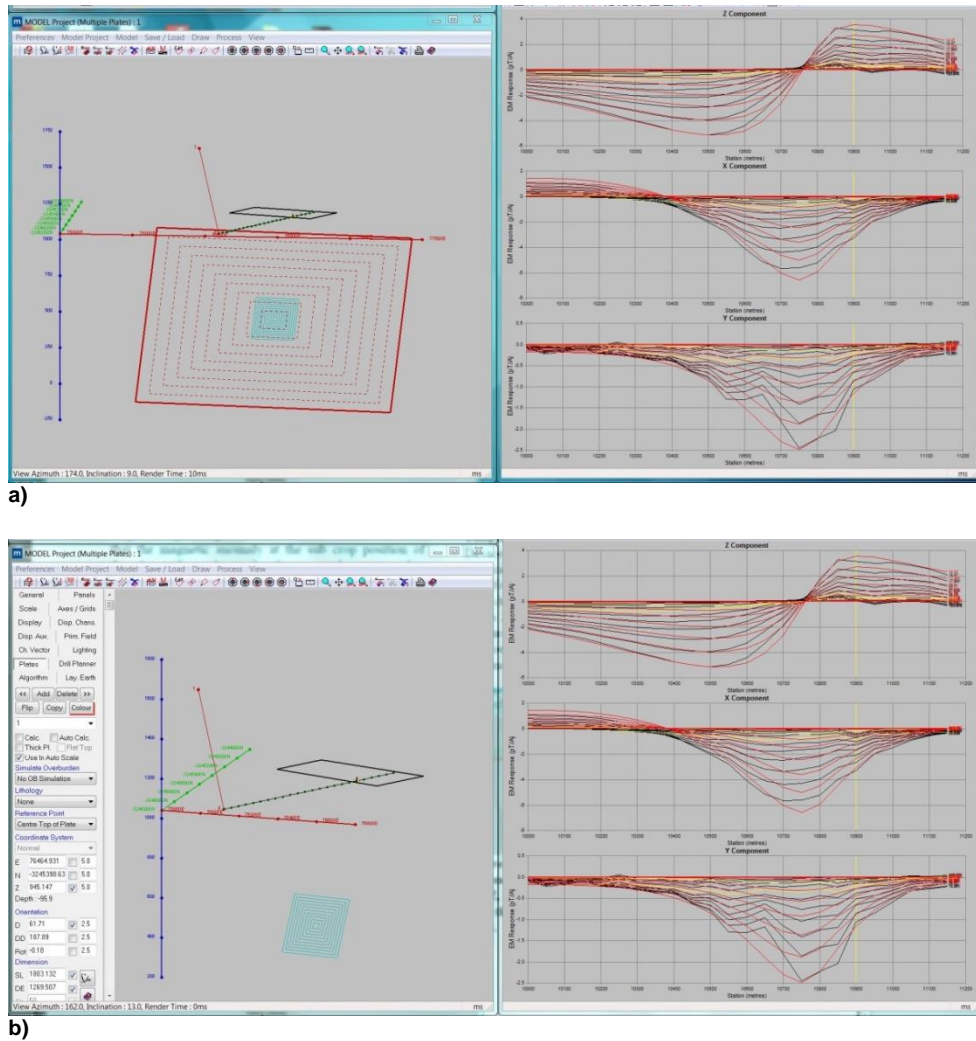
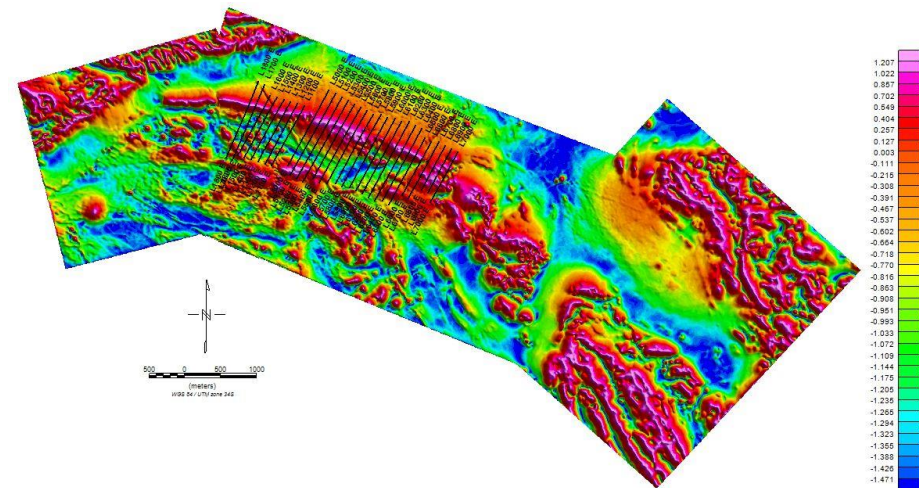


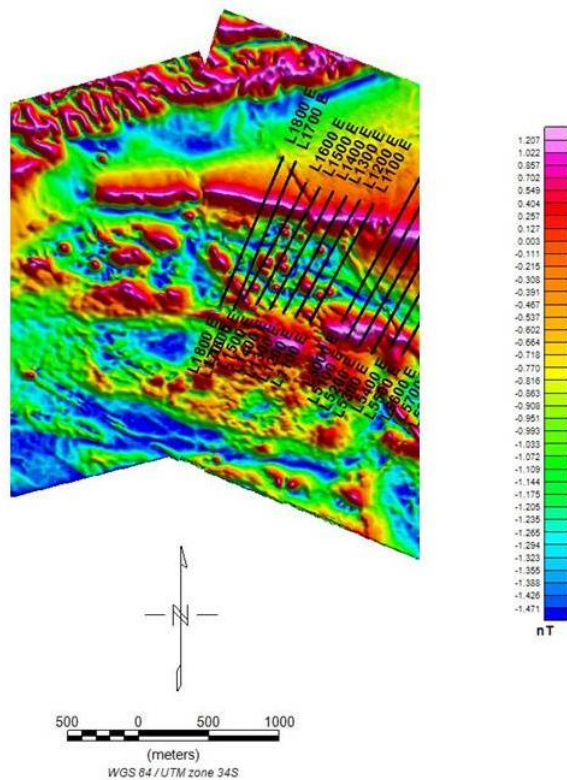
**Figure 9.25 – a)** Modelling results for line 1500 showing the large plate in red and the constructed 'resultant EM Plate' in blue. The 'resultant' EM plate has no effect on the modelling results **b)** Modelling results for line 1500 showing only the 'resultant EM plate'.

### 9.3.4 Modelling of Moving Loop EM Data

A strike length of about 2.7km was covered by moving loop EM surveying at a line spacing of 100m and 50m station spacing. However, only lines covering the study area will be considered. This is also the area covered by drilling. Data for lines 1400, 1500, 1600, 1700, and 1800 that were considered in this study were acquired using a Fluxgate sensor. Data for all the other lines shown in Figure 9.26 were acquired using an LT SQUID.



a)



b)

**Figure 9.26** – a) Surveyed lines of the moving loop mode relative to the Tilt Angle Derivative image of the high resolution aeromagnetic survey, b) modelled lines for this study showing the line numbers on Tilt Angle Derivative image.

Modelling of moving loop data was again carried out using Maxwell. The procedure for modelling the data is the same as that for fixed loop. This procedure has been explained before. The Maxwell configuration file for the survey was created using Table 9.3.

**Table 9.3 – Waveform parameters used for the Moving Loop survey**

Duty cycle	50%
Base Frequency	1Hz
On Time	250ms
Off Time	250ms
Turn On time	0.2ms
Turn Off time	0.2ms
Timing Mark	250.2ms
Transmitter Current	20A

Figure 9.27 show the EM results in Maxwell for line 1800 (indicated by a yellow cross) after creating the profile plots and the configuration file. On the left side is the plan view which depicts the surveyed lines and on the right, line 1800 time channel traces for the measured EM response for the **Z**, **X** and **Y** components in that order going down.

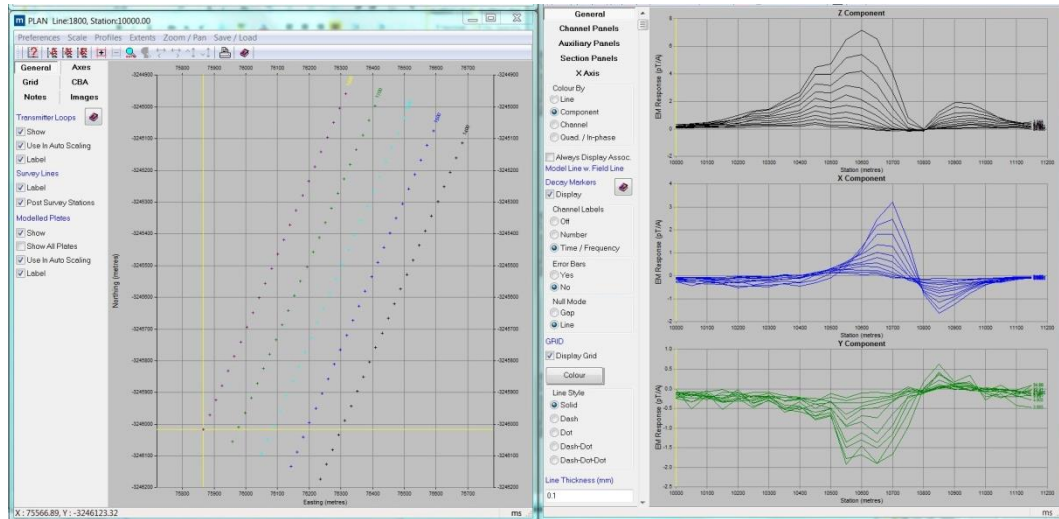


**Figure 9.27** - The moving loop data after importation into Maxwell. On the left side is the Plan view which shows the surveyed lines and on the right, the time channel traces for the measured EM response are shown for the Z, X and Y components in that order going down for line 1600 (indicated by a yellow cross).

Forward modelling was then carried out following the same procedure explained before for the fixed loop data. Plate parameters were adjusted until the model response mimicked the measured EM response as shown in Figure 9.28. The black traces depict the measured time channel EM response while the red traces show the calculated model response.



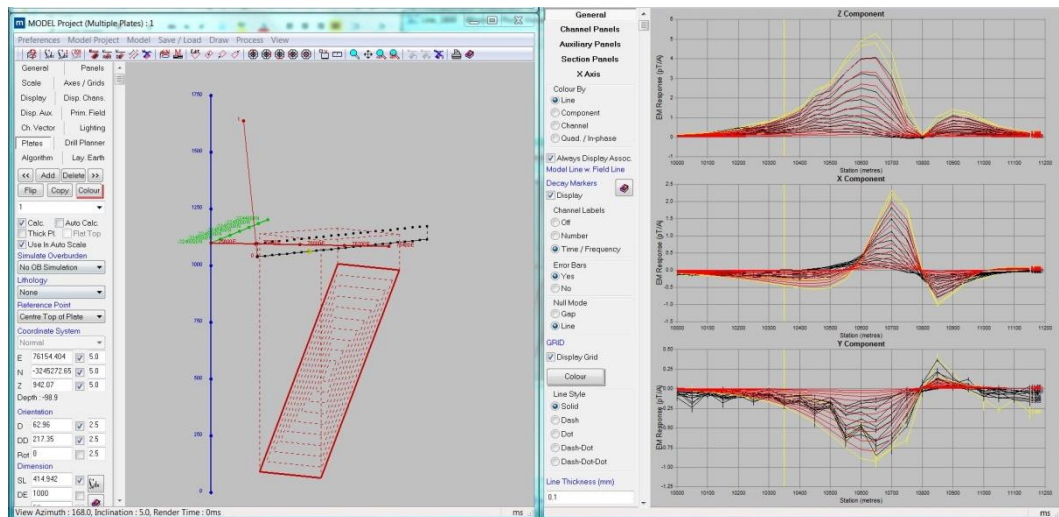


**Figure 9.28** – Modelling results for Line 1800. The left window shows the modelled EM plate steeply dipping to the south correlating with the mineralised ultramafic sill. The right window shows the measured EM response profiles in black and the modelled EM response in red for the three components Z, X and Y.

As for the fixed loop modelling, the size of the plate is defined by the strike length, which is the plate width along the strike direction, and depth extent, which is the plate height along the dipping side of the plate. The product, conductivity x thickness or conductance, was used to characterize the electrical property of the thin conductor. Table 9.4 below shows the plate parameters for the modelled lines.

**Table 9.4** – EM plate parameters for the modelled moving loop lines

Line Number	Strike (m)	Length	Depth (m)	Extent	Dip (Degrees)	Conductance (S)
1400	724.8		1368.2		69.3	55.73
1500	752		1954.1		69.01	88.9
1600	701.6		1974		63.4	93.69
1700	551.4		2126.2		56.47	114.9
1800	565.9		2008.6		56.9	94.04

Since the mineralised ultramafic sill which has elevated conductivity values has a large strike and depth extent so do the modelled EM plates. However, the conductance values which is a measure of the electrical property were generally very low for the moving loop data as compared to fixed loop indicating that this method mainly mapped the tremolite schist which is host to the disseminated style of mineralisation. This is due to a much smaller dipole moment and the harzburgite is only present at some depth.

Modelling results of the moving loop data shows a steeply dipping EM plate with a large strike and depth extent. However, no 'resultant EM plates' were constructed at the centre of the large EM plates for the moving loop since indications from the conductance value (less than 100S) are that mainly the disseminated mineralisation which is the tremolite schist was mapped by the method. This was attributed to the low dipole moment due to the small transmitter loop (200m x 200m). The other reason is also that the data were

collected using a fluxgate sensor which is not capable of measuring into the late decay times and thus greater depths compared to the SQUID.

#### 9.4 Modelling of DHEM Data

A total of 17 boreholes were drilled over the main study area. Out of the 17 drilled boreholes, 12 were selected for DHEM surveying. From the ground EM surveying carried out on the main target zone and the drilling results, information regarding the target and positioning of the fixed loop was available to ensure good coupling with the target. All the boreholes were surveyed using one large fixed transmitter loop (Figure 9.29a).

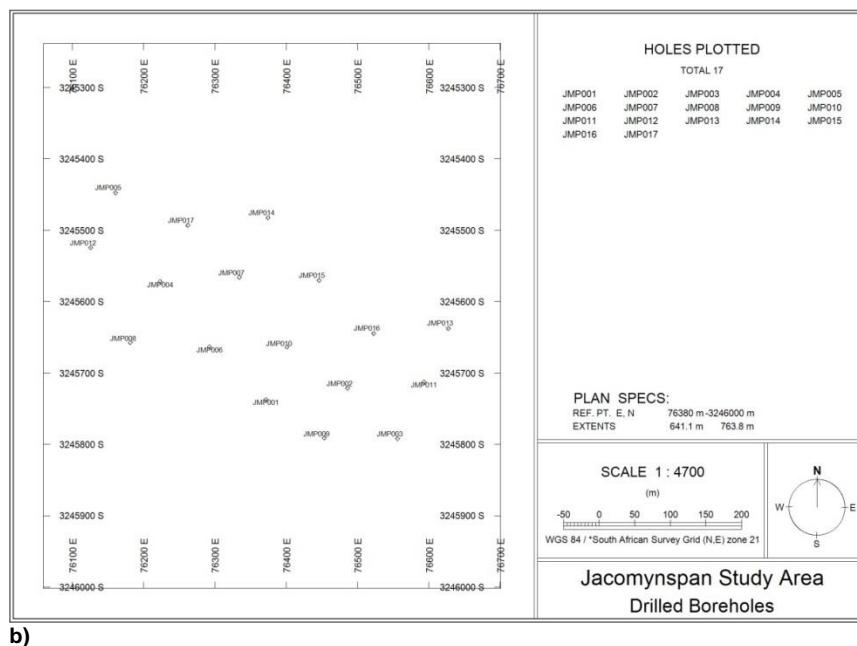
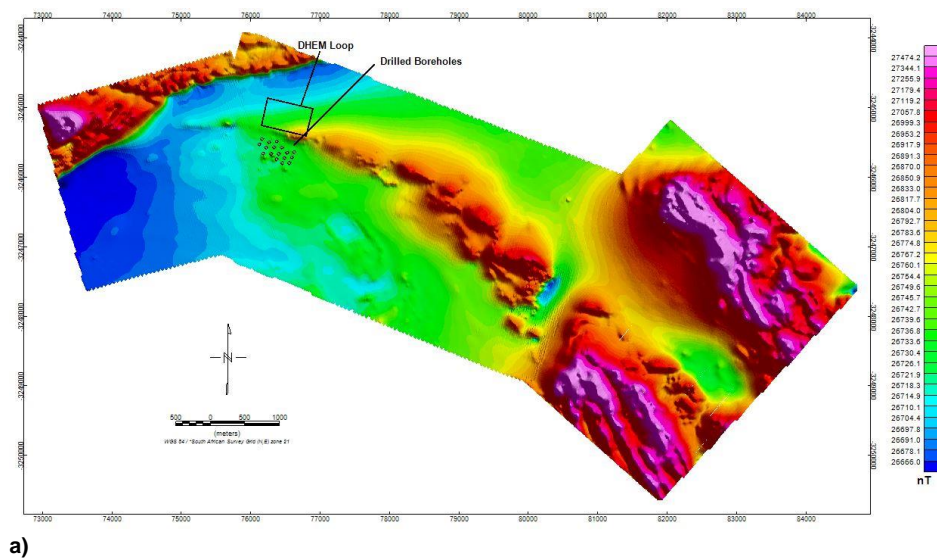


**Figure 9.29** – a) Collar positions of the drilled boreholes showing Transmitter position on TMI image of the aeromagnetic data, b) Plan of the position of the boreholes drilled within the study area showing the borehole names.

The DHEM data were modelled using Maxwell software. The procedure for modelling the data is almost the same as that for the fixed and moving loop data. The main difference is that DHEM modelling needs accurate downhole orientation survey data which were collected simultaneously with the EM data and integrated into the EM data.

A configuration file was created in Maxwell using the waveform parameters shown in Table 9.5.

**Table 9.5 – Waveform parameters used for DHEM survey**

Duty cycle	50%
Base Frequency	1Hz
On Time	250ms
Off Time	250ms
Turn On time	0.4ms
Turn Off time	0.4ms
Timing Mark	250.4ms
Transmitter Current	20A

For the DHEM data the measured components are designated by **A**, **U** and **V** instead of **X**, **Y** and **Z** (Figure 9.30). The transmitter loop position is shown as a yellow rectangle and the borehole trace in black in the plan view on the left hand side while the late time channel data are shown as traces for the 3 components on the right side of Figure 9.30.

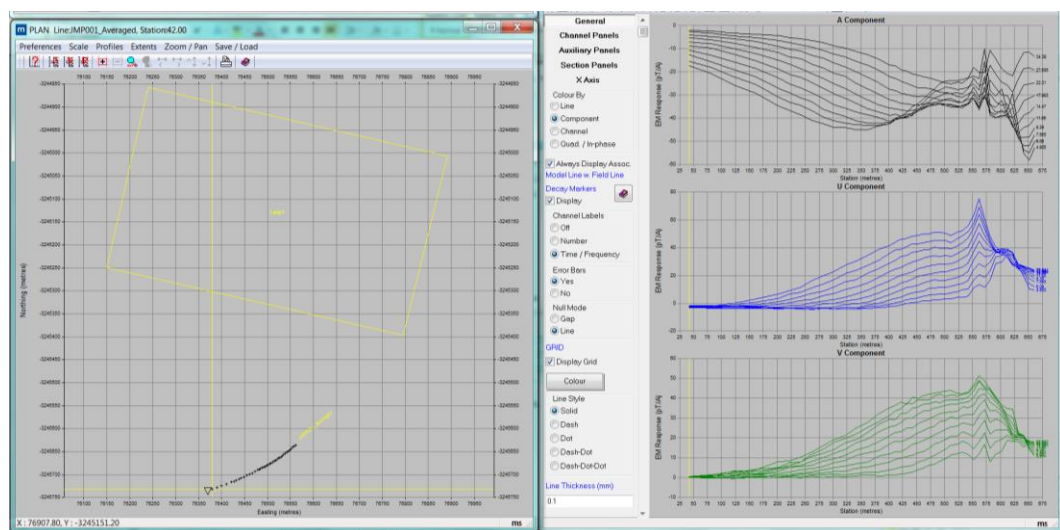


**Figure 9.30** - The DHEM data after importation into Maxwell showing the EM response profiles for the three components A, U, and V on the right and the borehole trace and fixed loop position (yellow triangle) on the left for borehole JMP001 located in the study area.

Each borehole was modelled individually. All the modelled boreholes intersected the poorly mineralised tremolite schist with only a few intersecting the well mineralised harzburgite which the modelling tries to resolve. Modelling results for borehole JMP001 are shown in Figure 9.31.

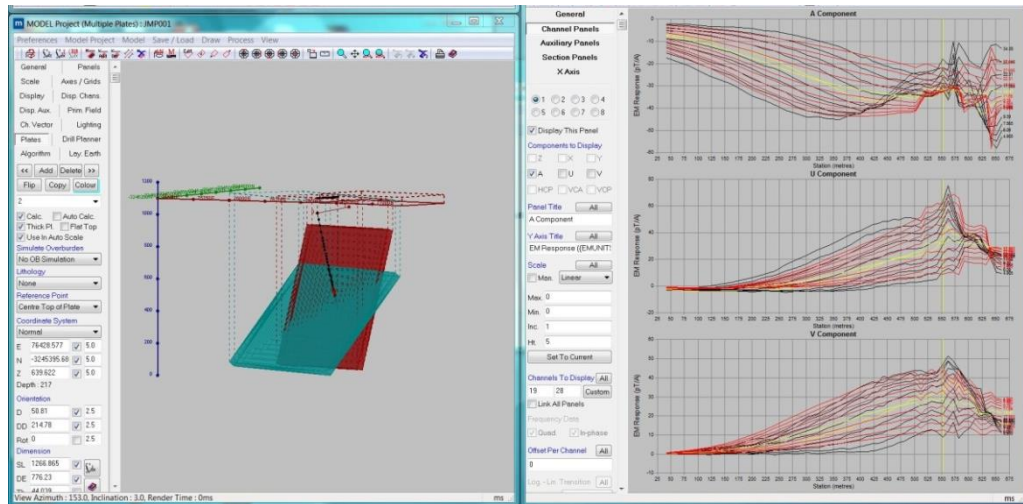


**Figure 9.31** – Modelled EM plates for JMP001 shown on the left. On the right the pane shows the measured EM response traces in black and the modelled EM response in red for the three components A, U and V.

Since the intersected tremolite schist is conductive and has a substantial strike and depth extent so do the modelled EM plates. Using thick plates to mimic the measured EM behaviour gave a better fit for all the deeper boreholes. The distinguishing physical parameter of these thicker plates is given in Siemens per meter and not their conductivity thickness product in Siemens. The modelling results for all the boreholes are shown in Table 9.6.

**Table 9.6** – EM plate parameters for modelling results for all the surveyed boreholes.

BHID	Strike Length (m)	Depth Extend (m)	Dip (Degrees)	Thickness (m)	Conductivity
JMP001	757.5	894.3	73.68	44.039	6.1 S/m
JMP002	629.5	777.4	47.5		159 S
JMP003	901.4	518.9	59.2	65.679	5.65 S/m
JMP004	976.9	564.2	69.1		212.53 S
JMP005	598.5	255.1	64.1		355.9 S
JMP006	704.9	575.6	67.4	55.206	2.9 S/m
JMP007	318.2	400	75.7		263.7 S
JMP009	1214.1	669.9	70.5	49.83	6.42 S/m
JMP012	885.8	502.1	72.8		159.95 S
JMP014	312	200	63.4		134.5 S
JMP016	498.4	745	47.5		112.8 S
JMP017	2015	611.8	70		141.5 S

Just as for the fixed loop EM modelling, again an assumption is made that at late decay times the currents would be focused in the centre of the large EM plate giving an indication of the most conductive part of the intrusion. In order to better constrain view the targets, smaller ‘Resultant EM plates’ of dimensions, 300x300m that coincide with the centre of the large EM plates where current will be focused at late decay times were constructed in Maxwell software (Figure 9.32). This was done only for EM plates with



large conductance values of 200S and above assumed to be indicating well mineralised harzburgite.

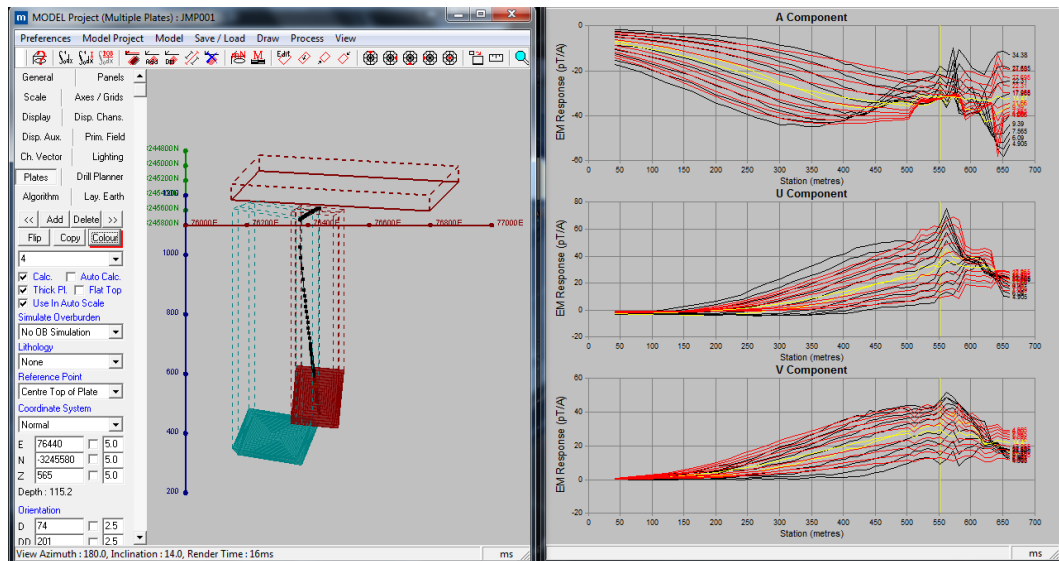


**Figure 9.32** - The constructed 'resultant' centre of plates for JMP001 is shown on the left. The right-hand window shows the measured EM response traces in black and the modelled EM response in red for the three components A, U and V.

It must again be noted that the constructed centre plate is just a dummy plate with no physical effect on the modelling results but simply gives an indication of where the currents will be concentrated at late decay times.

## 9.5 Modelling of the AMT data

From the AMT measurements undertaken a total of 21 lines as plotted in Figure 9.33 were modelled.

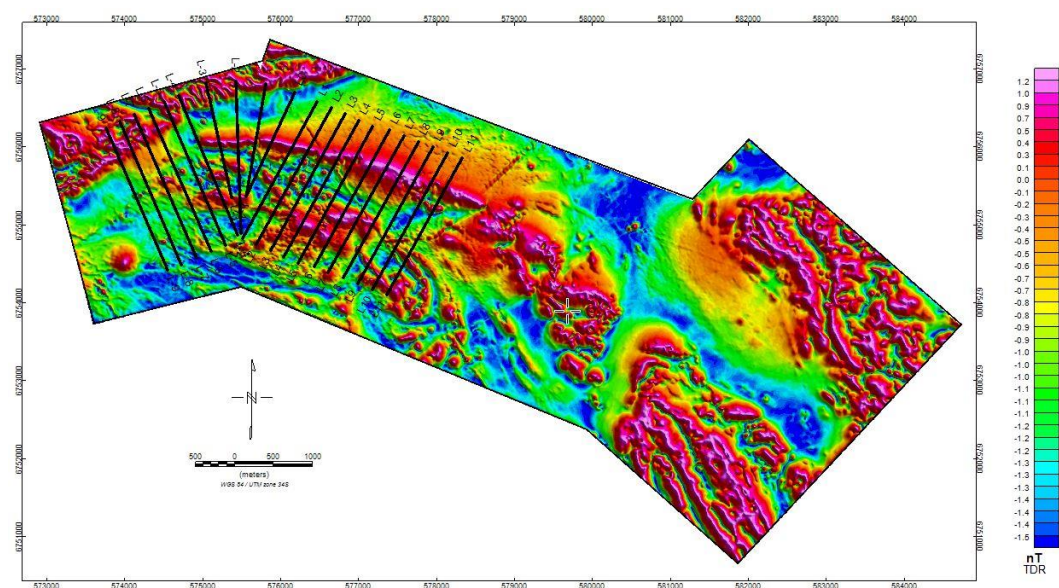


**Figure 9.33** – AMT surveyed lines shown on aeromagnetic TDR image.

Detailed images of conductivity structure at depth can be obtained by inverting AMT Cagniard Resistivity and Impedance Phase. 1-D and 2-D modelling programs were used to convert the measured results to profiles of resistivity versus depth. 1-D modelling is to determine a layered earth model for the measured AMT response at every measurement station where the number of layers, the thickness and resistivity of each layer is manipulated by a forward or inverse process to obtain a model response that mimics the measured values. In 2-D modelling the subsurface is discretized into squares on a distance-depth plot in log-log scale. This is because the model has to be inserted into a much larger resistive Earth that ends far in distance and depth for the area of interest to meet the boundary conditions as dictated by the theory and mathematical considerations. Smooth-model inversion mathematically “back-calculates” from the measured data a likely location, size and depth of the source or sources of resistivity changes. Zonge 2D inversion algorithms allow for various types of input model parameters and geometry constraints to yield the most reasonable model (Zonge, 2010). 2D inversion models have several advantages over 1D models in that the 2D inversion shows two dimensional shaped structures (for example, edges associated with contacts at depth).

#### 9.5.1 AMT Model Types

The technique that was used during the survey is vector AMT where both the **T<sub>m</sub>** (Transverse magnetic) and **T<sub>e</sub>** (Transverse electric) modes were measured. The **T<sub>m</sub>** and **T<sub>e</sub>** modes assume a 2D geology to be present where the profile crosses the geology at right angles and that the geology is of infinite strike. This of course is obviously never true in the real world but is often a reasonable assumption.

**T<sub>m</sub>** mode data tend to produce a result similar to a resistivity sounding as the response is dominated by the electric field. In a scalar **T<sub>m</sub>** mode survey with only a few **H<sub>y</sub>** measurements and many **E<sub>x</sub>** measurements, **H<sub>y</sub>** can be considered as a means of normalizing the **E<sub>x</sub>** amplitudes so that the result is very much like a resistivity survey. This mode is good for general structural mapping.

The **T<sub>e</sub>** mode tends to give a result that is more akin to an EM survey as it is dominated by the magnetic field **H<sub>x</sub>**. This mode is good if one is trying to map good conductors.

A series of models was therefore produced where the components are weighted differently and the best result has to be determined empirically by reference to the known geology and objectives.

#### 9.5.2 AMT Resistivity Depth Sections

Typically four resistivity depth section models were produced for each profile.

- **1D model:** In the 1D world, horizontal layers of infinite extent form the model. An average of the **T<sub>m</sub>** and **T<sub>e</sub>** components are used to smooth the result lightly to minimize the customary vertical stripeyness in the image. This model works well where the basic 1D assumption is approximately true. Usually the 1D model is used as a starting model for the other models described below.
- **Vector model:** This is a 2D model with equal weighting on the **T<sub>m</sub>** and **T<sub>e</sub>** components. Instinctively this should be the best model, but sometimes does not show any structures when the geology deviates a lot from the 2D geometry.
- **T<sub>m</sub> model:** Often the best model for mapping structure. But note that the **T<sub>m</sub>** response for a narrow steeply dipping conductor is small in amplitude.
- **T<sub>e</sub> model:** Often shows the best map of deep conductors.

Since the geology of the study area does not meet the basic assumption of the 1D world, Figure 9.34 provides an example of the three products derived for line 4 (which cuts across the study area) i.e. **T<sub>e</sub>**, **T<sub>m</sub>** and 2D models respectively. All three models clearly map the ultramafic intrusion and the plotted sections extend down to a depth of -500m below mean sea level i.e., more than 1500m in section depth extent.

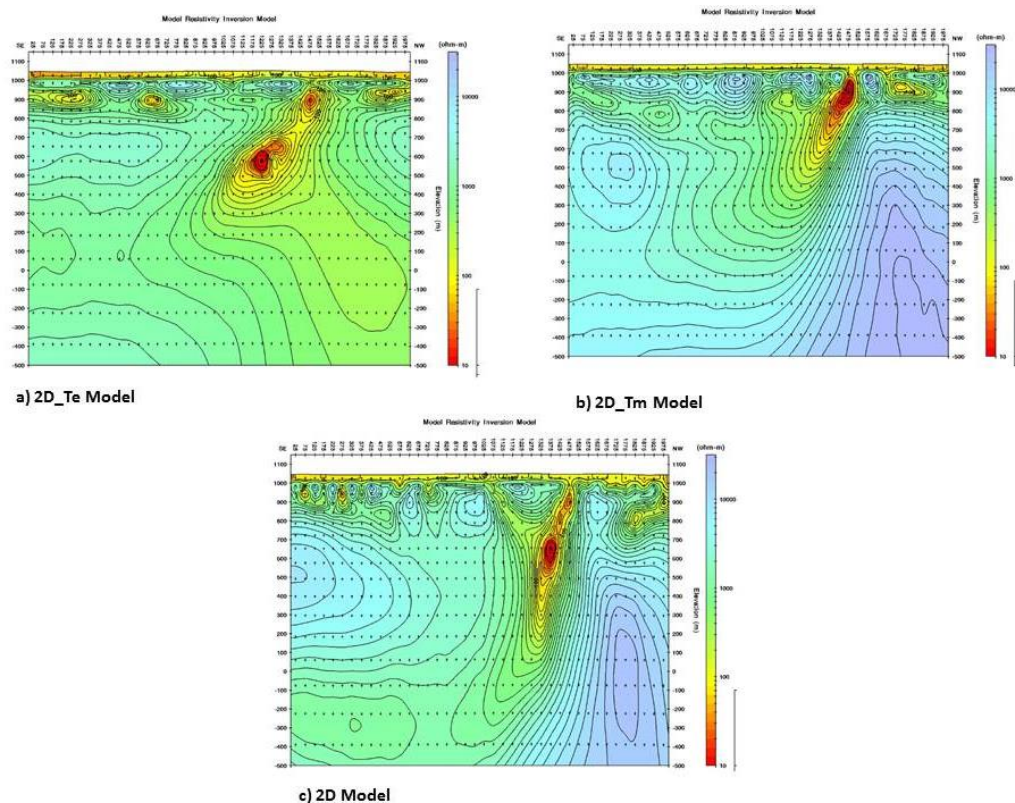


**Figure 9.34** – 2D Smooth-Model Inversion Sections for line 4 clearly mapping the intrusion, a) 2D **T<sub>e</sub>** Smooth-Model, b) 2D **T<sub>m</sub>** Smooth-Model, c) 2D Smooth-Model.

It is clear that the general appearances of the three models are the same, but there are significant differences in the finer detail. Since the **T<sub>e</sub>** model is good at mapping deep

conductors it is apparent in Figure 9.34a that there is a strong conductor which has been mapped at depth. The **Tm** model is good at mapping structure and the ultramafic sill was clearly mapped in Figure 9.34b. Figure 9.34c is a 2D model with equal weighting on the **Tm** and **Te** components and is usually the best model in terms of mapping both structure and conductors. The ultramafic intrusion has been mapped to great depths and also a deep conductor has been mapped.

### 9.5.3 3D-model Representation of AMT Models

Since no 3D modelling was carried out on the AMT data because the software is not yet readily available, a 3D-model representation of the 2D model was produced. This was possible because the survey was carried out as a grid at 200m apart. The resistivity data from each AMT line was imported into a single database and gridded in three dimensions using the Kriging algorithm of Geosoft. The 3D smooth-model representation of the 2D, **Tm** and **Te** models were produced as shown in Figure 9.35.

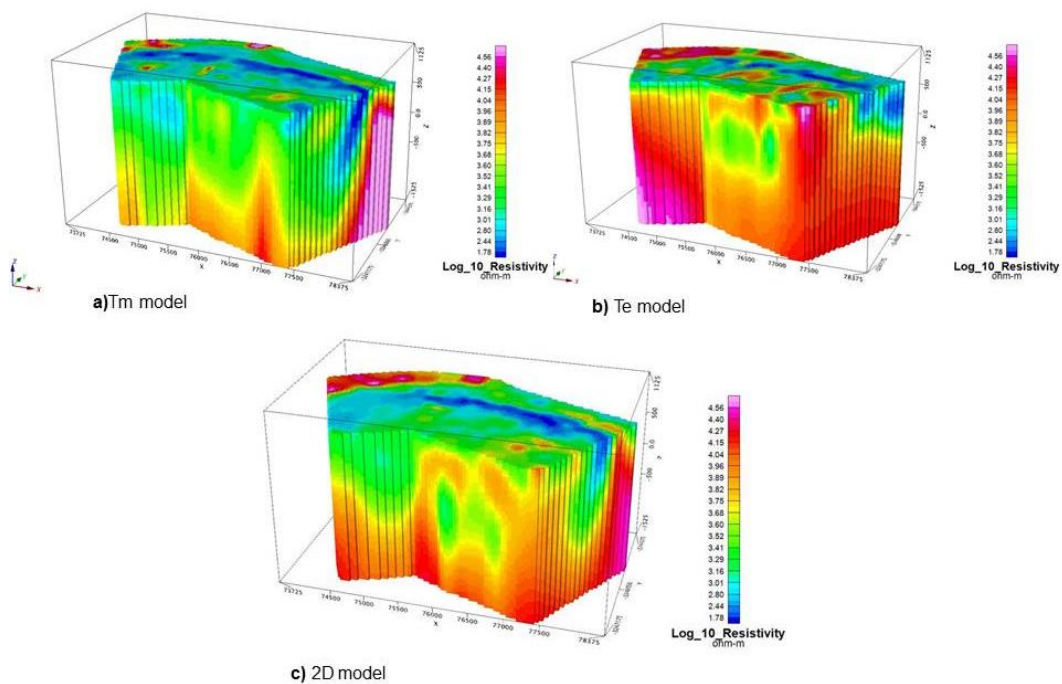


**Figure 9.35** – 3D Smooth-model representation of the 2D a) **Tm** model, b) **Te** model, c) 2D vector model.

3D iso-surfaces of different resistivities were also produced from the created voxel as shown in Figure 9.36. These derived 3D products can then be integrated with other datasets.

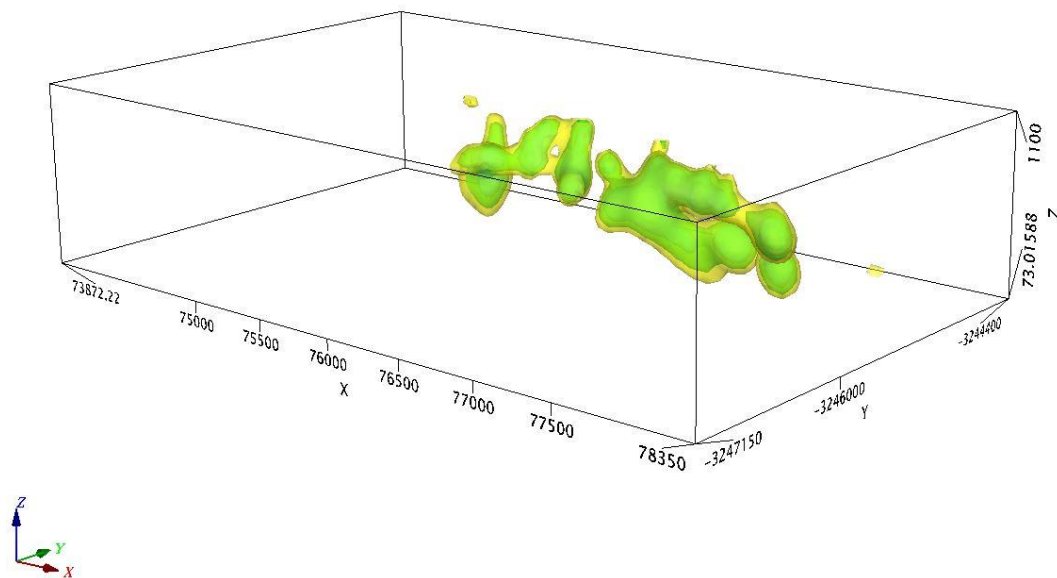


**Figure 9.36** – 3D iso-surfaces created from the Te voxel model. The iso-surfaces represent 25 and 50 ohm-m showing the most conductive part of the intrusion.

The iso-surfaces representing different resistivities in Figure 9.36 show the most conductive part of the intrusion. The derived 3D products can then be integrated with other models.

## 9.6 Summary of Geophysical Modelling

The three-dimensional model of the Jacomynspan mineralised ultramafic sill that was created in Micromine using drilling information was used as a starter model for all the modelling done in this study.

The high resolution aeromagnetic data were modelled using both Mag2dc and VOXI modelling software. A 3D model representation was created from the Mag2dc models using Stettler's Magmodintrap software. The mineralised ultramafic sill was clearly mapped in both 3D model representation and VOXI smooth model. However, the slightly magnetic material south of the sill was resolved by Mag2dc modelling but not with VOXI. VOXI's IRI Focus results showed a more compact and focused but deeper magnetic susceptibility distribution of the mineralised intrusion compared to the smooth model inversion.

Ground EM data for both the fixed loop and the moving loop modes were modelled using Maxwell EM modelling software. In both cases a large EM plate steeply dipping to the south with a large strike and depth extent was modelled in agreement with the starter model. An assumption was made that at late decay times, the currents would be focused in the centre of the large EM plate giving an indication of the most conductive part of the intrusion which was inferred to represent the well mineralised harzburgite. To better constrain the targets, smaller 'Resultant EM plates' of dimensions 300m x 300m that

coincide with the centre of the large EM plates (only with conductance above 100S) were constructed. This however was not done for the moving loop since the conductivity thicknesses were too low.

The same modelling procedure done for ground EM was also applied to DHEM data. A total of 12 out of 17 boreholes were modelled. Just like for the ground EM, the modelled plates had a large strike and depth extent. The same assumption as for the fixed loop EM modelling was made and 'Resultant EM plates' with the same dimensions as for fixed loop coinciding with the centre of the plate were created. This was done only for EM plates with conductance values of 200S and above.

A total of 21 lines of AMT data were modelled using Zonge software and Geosoft. The mineralised ultramafic sill was clearly mapped with the modelling. A 3D model representation was created by importing the resistivity data from each AMT line into a single database and gridded in 3D using the Kriging algorithm of Geosoft. 3D iso-surfaces of different resistivities were also produced from the created voxels. These can then be integrated with other datasets.



## CHAPTER 10: DATA INTEGRATION, INTERPRETATION AND DISCUSSION

The aim of this study was to take advantage of physical property contrasts (conductivity and magnetic susceptibility) to delineate and map the high grade harzburgite pods hosted within the conductive, poorly mineralised Jacomynspan ultramafic sill using the acquired geophysical and geological datasets. The final objective is to integrate the different geophysical models together with the geological model in order to come up with a final model of the well mineralised harzburgite pods to guide further drilling.

### 10.1 Micromine Geology Model of the Intrusion

A total of 17 boreholes were drilled by African Nickel over the main study area. Drilling results have shown that the Ni-Cu mineralisation at Jacomynspan project is hosted within a steeply dipping tabular, differentiated, sill of mafic to ultramafic composition intruded into country rocks of the Namaqualand Metamorphic complex. Using the drilling results, and that from historic drilling the geology model of the poorly mineralised tremolite schist (metamorphosed pyroxenite) as well as the high-grade well mineralised net textured harzburgite was created in Micromine software. The tremolite schist model (Figure 10.1) was used as a 'starter model' for all the modelling carried out in this study.

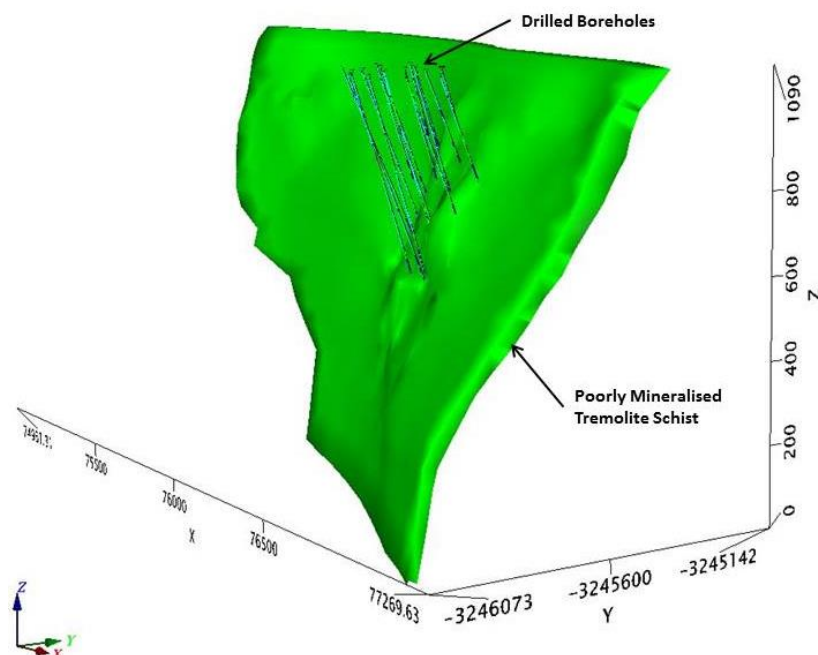


**Figure 10.1** - 3D view of the Micromine model (in green) showing the mineralised ultramafic intrusion (tremolite schist) steeply dipping to the south and the drilled boreholes.

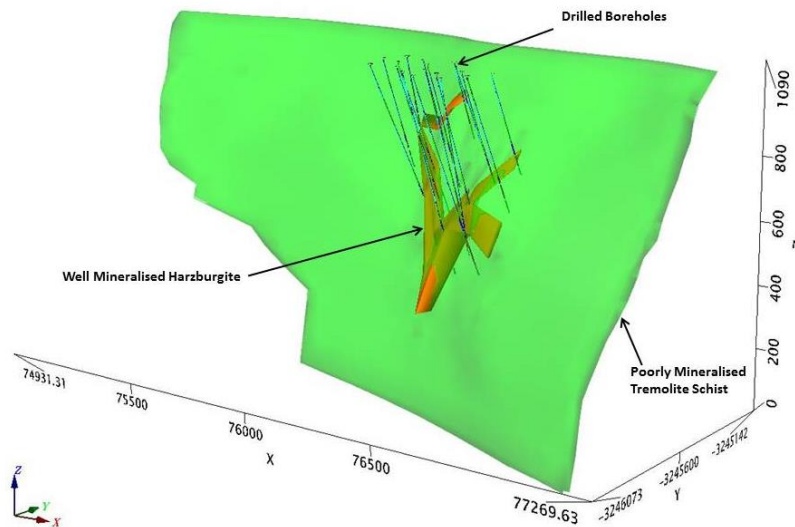


**Figure 10.2** - 3D view of the Micromine model showing the mineralised ultramafic intrusion (tremolite schist) in green steeply dipping to the south, the well mineralised net-textured harzburgite in orange and the drilled boreholes.

The well mineralised net-textured harzburgite is hosted within the poorly mineralised tremolite schist as can be seen in Figure 10.2.

## 10.2 Interpretation of the High Resolution Aeromagnetic Data

From the tilt angle derivative, the approximate perimeters and depth to the vertical edge of the magnetic bodies can be determined (Salem *et al.*, 2007) as was shown in Chapter 7 and inferred faults and other linear structures are also shown in Figure 10.3.

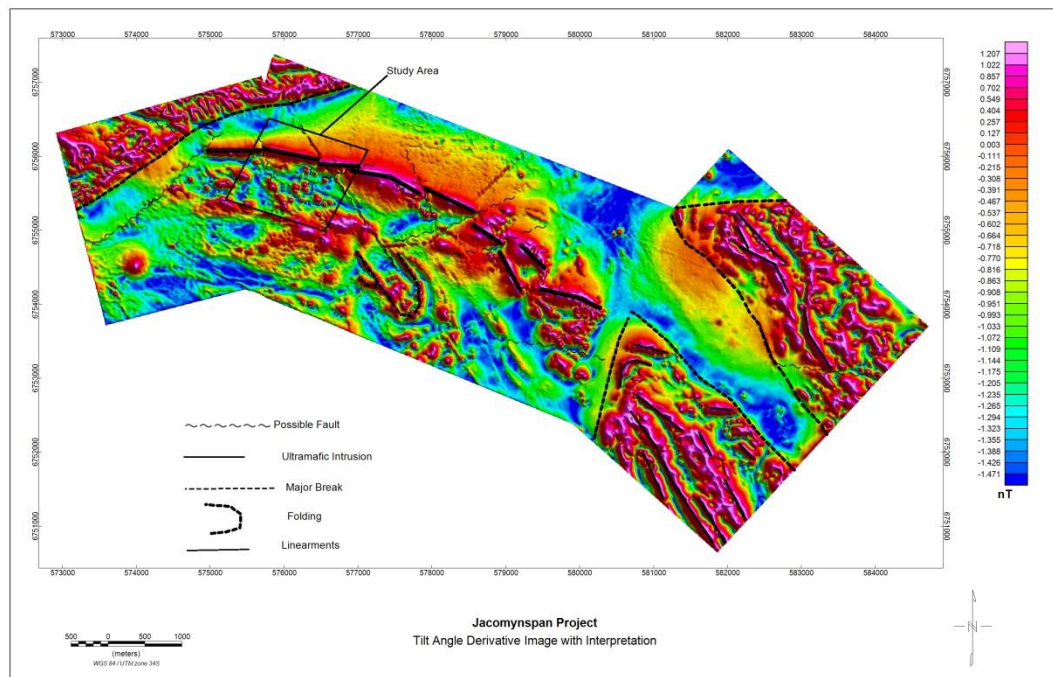


**Figure 10.3** - Xcalibur high resolution aeromagnetic data interpretation on a Tilt angle Derivative image for the study area.



The approximately 5km strike of the known Jacomynspan intrusion is clearly visible in the enhanced magnetic images especially the tilt angle derivative image (Figure 10.3). The magnetic anomaly due to the intrusion is terminated against major breaks in the magnetic image at both the eastern and western boundaries, where folded magnetic rocks occur. These folded magnetic rocks could be magnetite quartzite. The ultramafic intrusion appears to become progressively more faulted and folded and possibly duplicated towards the east.

### 10.3 Integrating Magnetic Models with the Geology Model

Models representing the magnetic geology were created from the magnetic data using Magmodintrp software and Geosoft's cloud based VOXI. In both instances, the 3D model adequately represented the Micromine generated model of the mineralised ultramafic sill without invoking remanent magnetic directions.

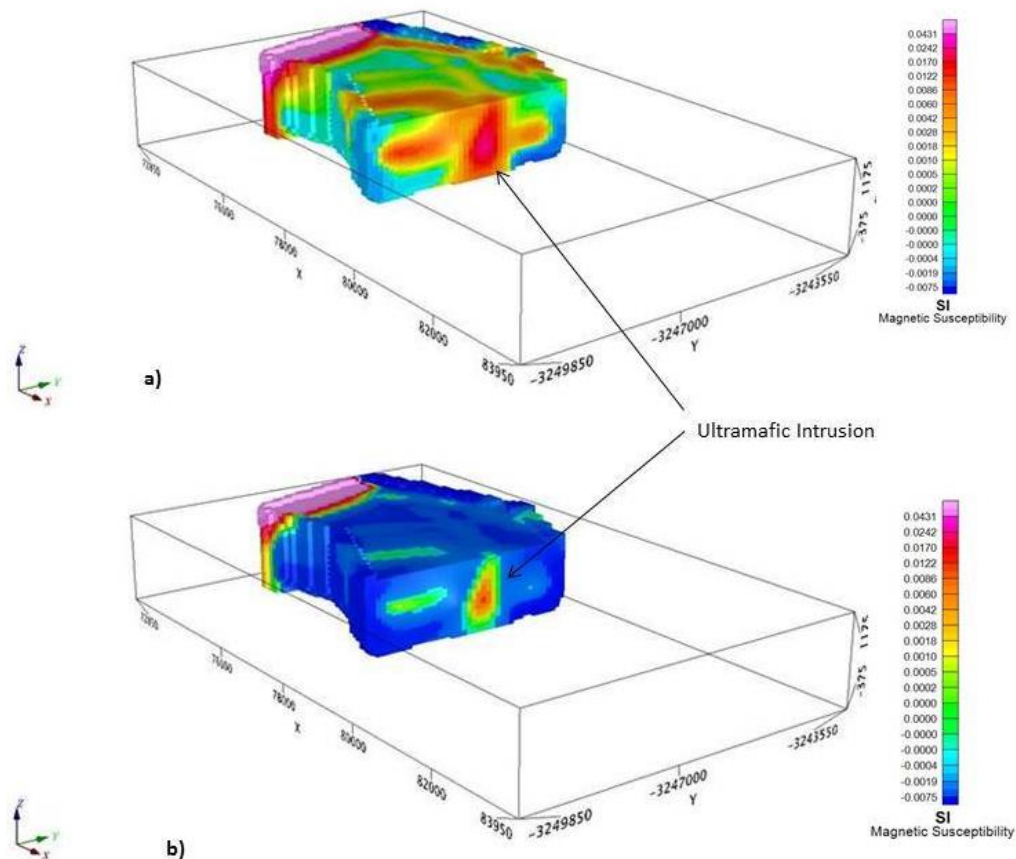


**Figure 10.4** – Final 3D model representation (Magmodintrp) of Jacomynspan clipped to the mineralised ultramafic sill of the study area. a) Smooth model showing the mineralised ultramafic sill, b) Smooth model with the colour tool applied to clearly map the mineralised ultramafic sill.

Integrating the 3D model representation with the Micromine geology model of the poorly mineralised tremolite schist shows that the intrusion has been clearly mapped as shown in Figure 10.5.

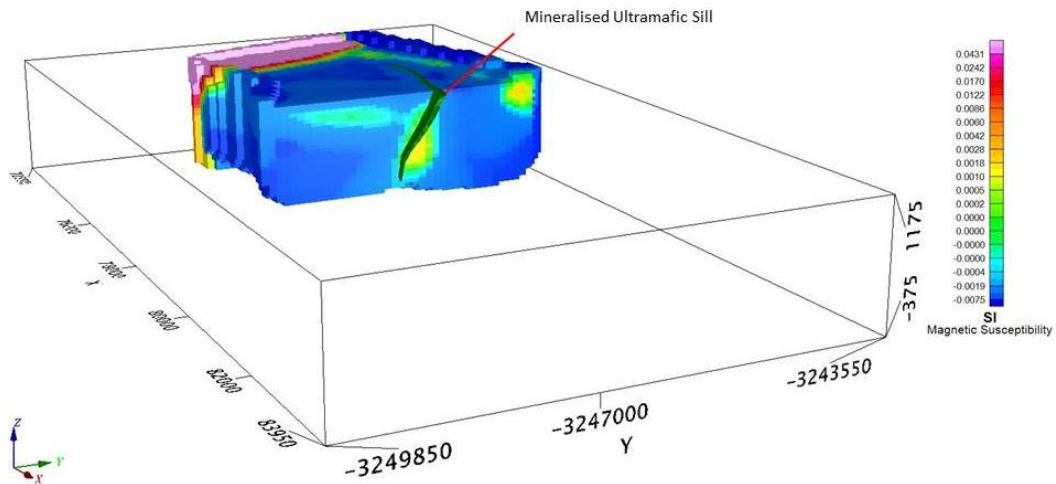


**Figure 10.5** – Integrating the 3D smooth model inversion results (Magmodintp) with the Micromine model of the mineralised ultramafic sill (green) there is a direct correlation.

Smooth-model inversion carried out using geosoft's VOXI software shown in Figure 10.6 places the magnetic model deeper, making it broader than in the previous result (Figure 10.5) but the dip is very similar as known from the drilling.

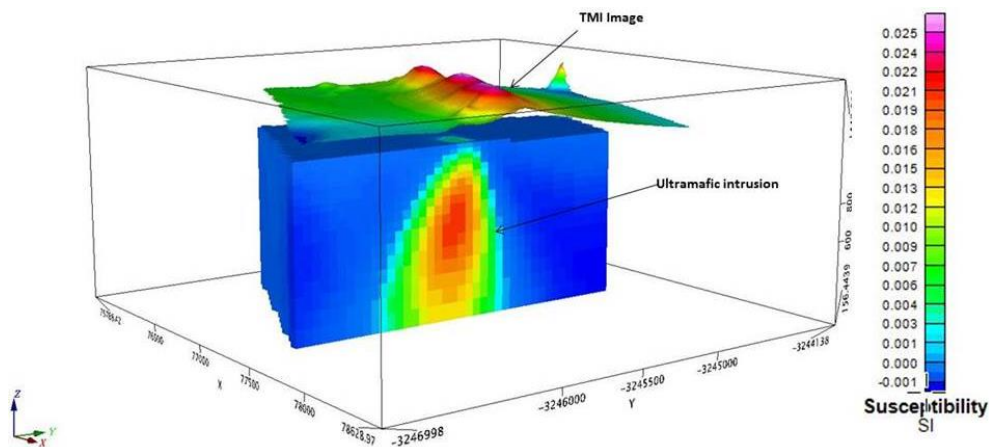


**Figure 10.6** – 3D unconstrained VOXI smooth model inversion results of the study area showing the mineralised Jacomynspan ultramafic intrusion with elevated magnetic susceptibility values.

Integrating the VOXI smooth model inversion results with the Micromine model of the mineralised ultramafic sill there is a direct correlation as can be seen in Figure 10.7. However the slightly magnetic material south of the sill which has been resolved by the Mag2dc inversion process does not appear on the VOXI inversion results.

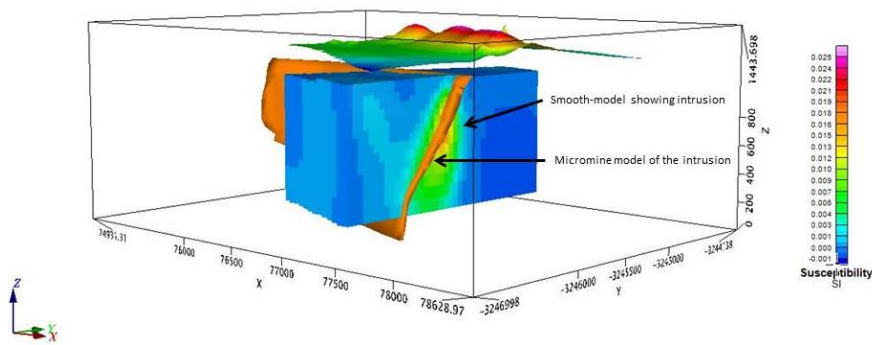


**Figure 10.7** – Integrating the 3D smooth model inversion results with the Micromine model of the mineralised ultramafic sill (orange) there is a direct correlation.

To map and delineate the well mineralised harzburgite the Micromine geology model of the harzburgite was used to create a geo-surface which was then used as a constraint during the VOXI constrained inversion process. The constrained inversion results are shown in Figure 10.8.

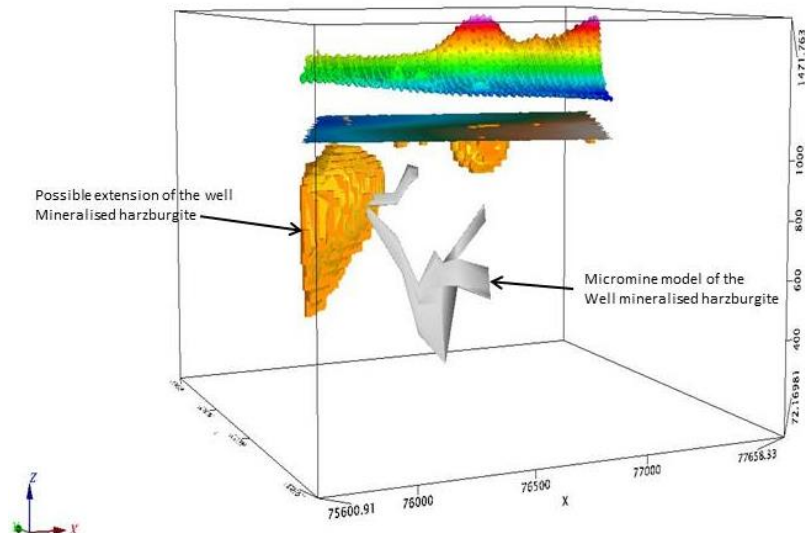


**Figure 10.8** – Constrained inversion results showing the possible extension of the well mineralised harzburgite.

The constrained inversion process results may suggest a possible extension of the well mineralised harzburgite to the western side of drilled area if an additional conductive body is also present.

#### 10.4 Interpretation of Ground EM Data

Modelling both moving loop and fixed loop modes produced EM plates with a large depth and strike extend. However, depth extends for the moving loop modelled EM plates were not as large as that for the fixed loop and so was the conductivity thickness because the transmitter loop size for the moving loop was only about 200m x 200m while that for the fixed loop was 600m x 300m, the latter giving a larger dipole moment, therefore 'looking' deeper. The other factor is that the fixed loop data were acquired using an LT SQUID

which has the capability of measuring at very late times. Only data for the fixed loop mode was used here for interpretation and integration. Modelling results for Line 1600 is shown in Figure 10.9.

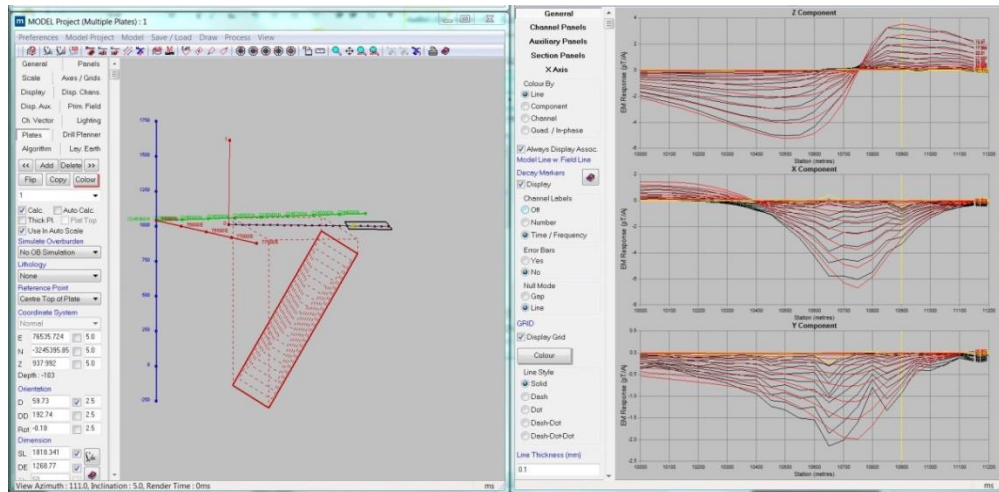


**Figure 10.9** – Modelling results for Line 1600 fixed loop mode. The left window shows the modelled EM plate steeply dipping to the south correlating with the mineralised ultramafic sill. The right window shows the measured EM response profiles in black and the modelled EM response in red for the three components Z, X and Y.

## 10.5 Integration of Modelled EM Plates with Geology Models

The DXF file of the Micromine geology model of the mineralised ultramafic sill was integrated with the modelled EM plates and there is a direct correlation as can be seen in Figure 10.10 with the EM plate suggesting that the sill extends deeper than the drilled depth.

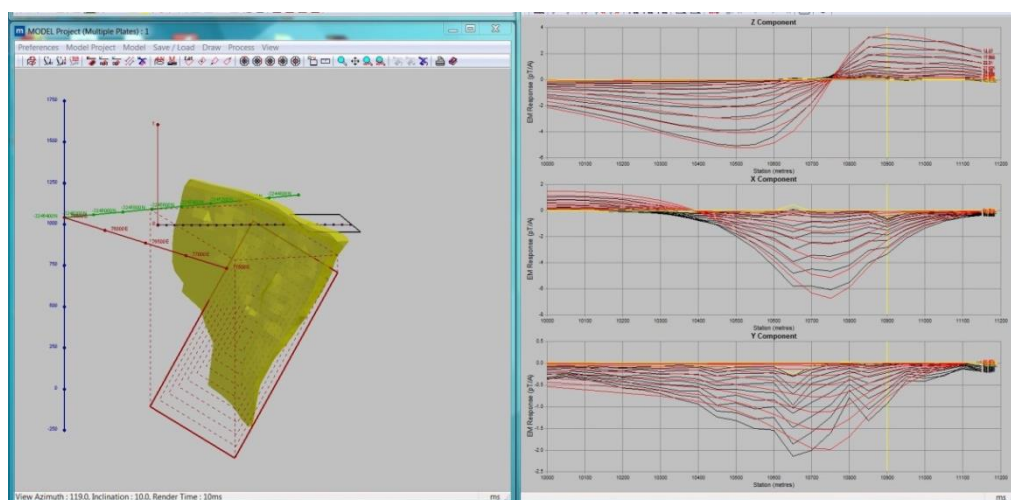


**Figure 10.10** – The modelled EM plate in red integrated with Micromine geology model of the mineralised ultramafic sill in yellow showing a direct correlation. The right window shows the measured EM response profiles in black and the modelled EM response in red for the three components Z, X and Y.

An assumption was made as explained before that at late decay times the currents would be focused in the centre of the large EM plate giving an indication of the most conductive

part of the intrusion. Therefore, in order to better constrain the targets, smaller 'Resultant' EM plates of dimensions, 300x300m that coincide with the centre of the large EM plate (with a conductance above 100S) where current will be focused at late decay times, were constructed in Maxwell software (Figure 10.11).

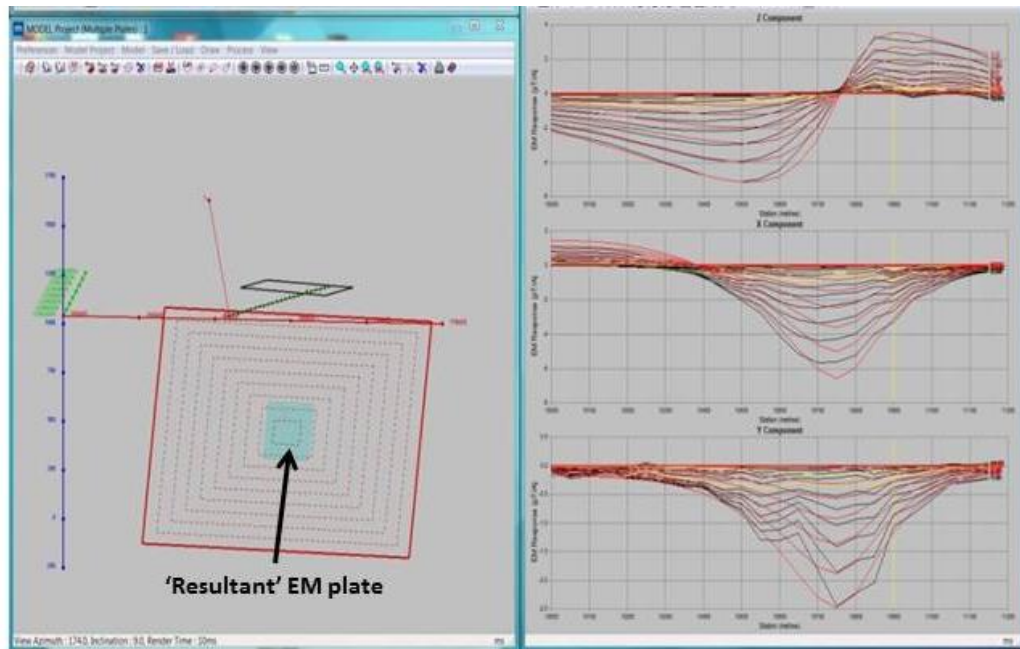


**Figure 10.11** – Modelling results for line 1500 showing the large plate in red and the constructed 'resultant' EM plate in blue. The 'resultant' EM plate has no effect on the modelling results. The right window shows the measured EM response profiles in black and the modelled EM response in red for the three components Z, X and Y.

Since the conductivity measurements taken on the drill core indicate the net-textured well mineralised harzburgite to be more conductive than the disseminated mineralised tremolite schist, the constructed centre of EM plates with conductivity thickness above 100 Siemens were interpreted as to give an indication of the location of the well mineralised harzburgite and massive sulphide stringers.

Integrating in Maxwell software the DXF file of the Micromine geology model of the well mineralised harzburgite with the constructed 'resultant' EM plates (Figure 10.12) gives an indication that the well mineralised harzburgite has been mapped and could be extending to the eastern side.



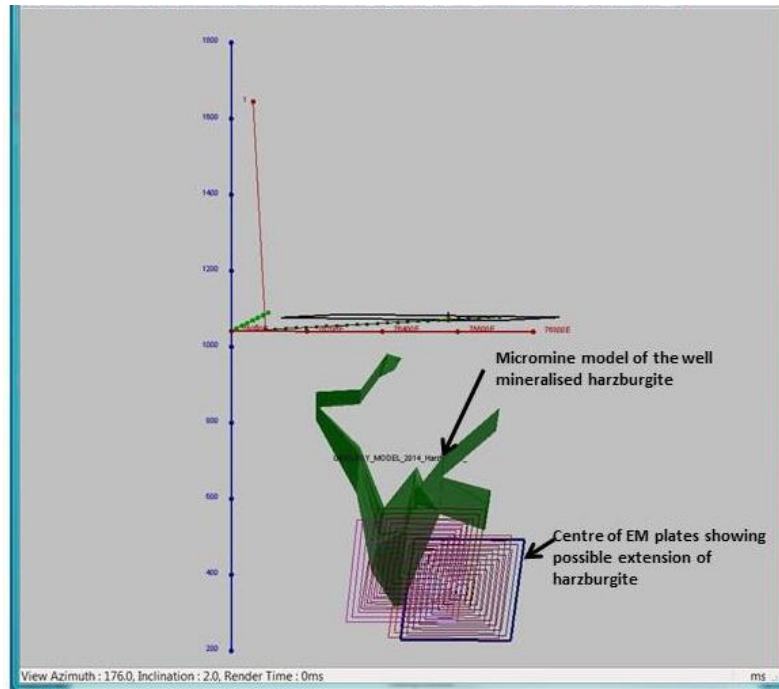


**Figure 10.12** – Integration in Maxwell the well mineralised harzburgite geology model (green) with the best fitting conductive centre plates that correlate with the harzburgite and shows that more conductive material could be extending to the east.

## 10.6 Integration of the Modelled DHEM Plates with Geology Models

Similar to surface TDEM, the modelled EM plates were of a very large strike and depth extent thus clearly representing the poorly mineralised ultramafic sill (Figure 10.13).

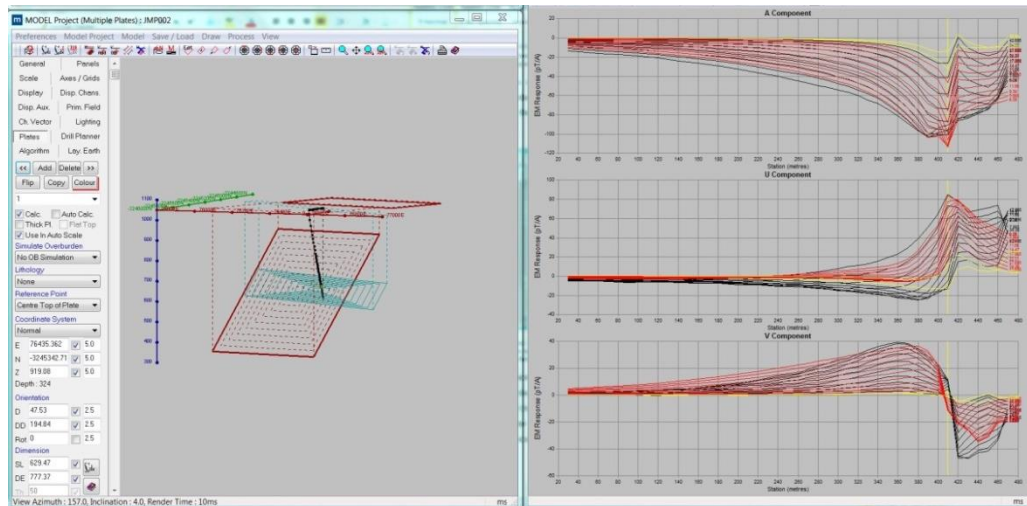


**Figure 10.13** – Modelling results for borehole JMP002 showing a large steeply dipping EM plate which map the mineralised ultramafic intrusion. The right hand window shows the measured EM response profiles in black and the modelled EM response in red for the three components A, U and V.

Upon integrating the modelled EM plate with the Micromine geology model of the Tremolite schist there is a direct correlation between the two in space (Figure 10.14).

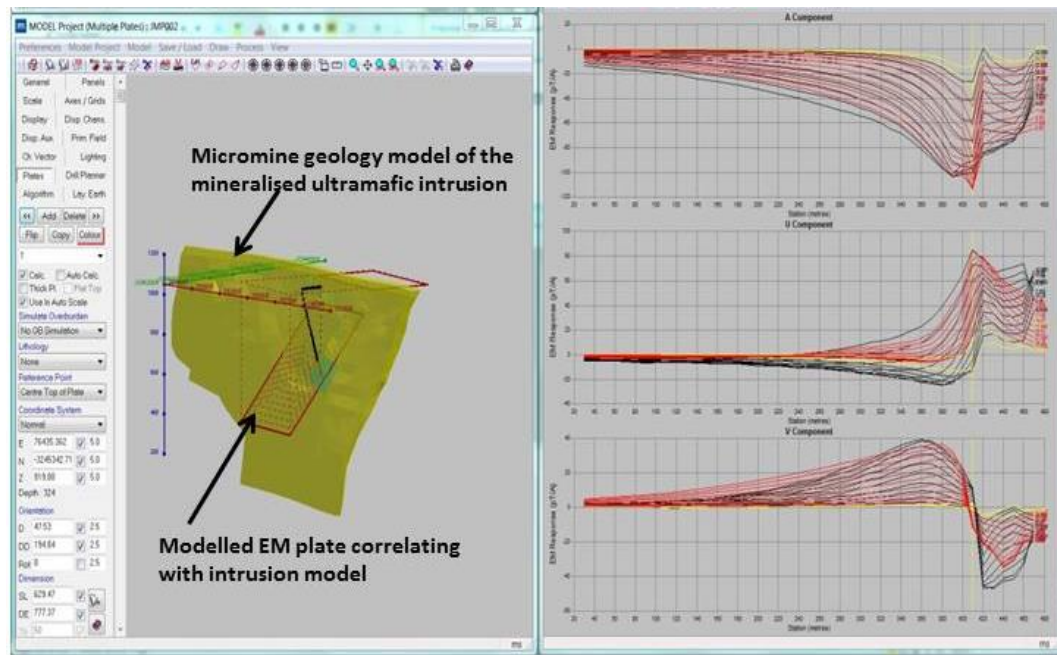


**Figure 10.14** – Modelling results for borehole JMP002 showing the modelled EM plate integrated with the Micromine geology model of the mineralised ultramafic intrusion. The right hand window shows the measured EM response profiles in black and the modelled EM response in red for the three components A, U and V.

Again an assumption is made that at late decay times, the currents would be focused in the centre of the large EM plate indicating the most conductive part of the intrusion. Smaller 'Resultant' EM plates of dimensions, 300x300m that coincide with the centre of the large EM plate where current will be focused at late decay times were constructed in Maxwell. This was done only for EM plates with large conductance values of 200S and above, assumed to be indicating well mineralised harzburgite. The known well mineralised net-textured harzburgite was clearly mapped by the 'Resultant' EM plates created in Maxwell as shown in Figure 10.15.

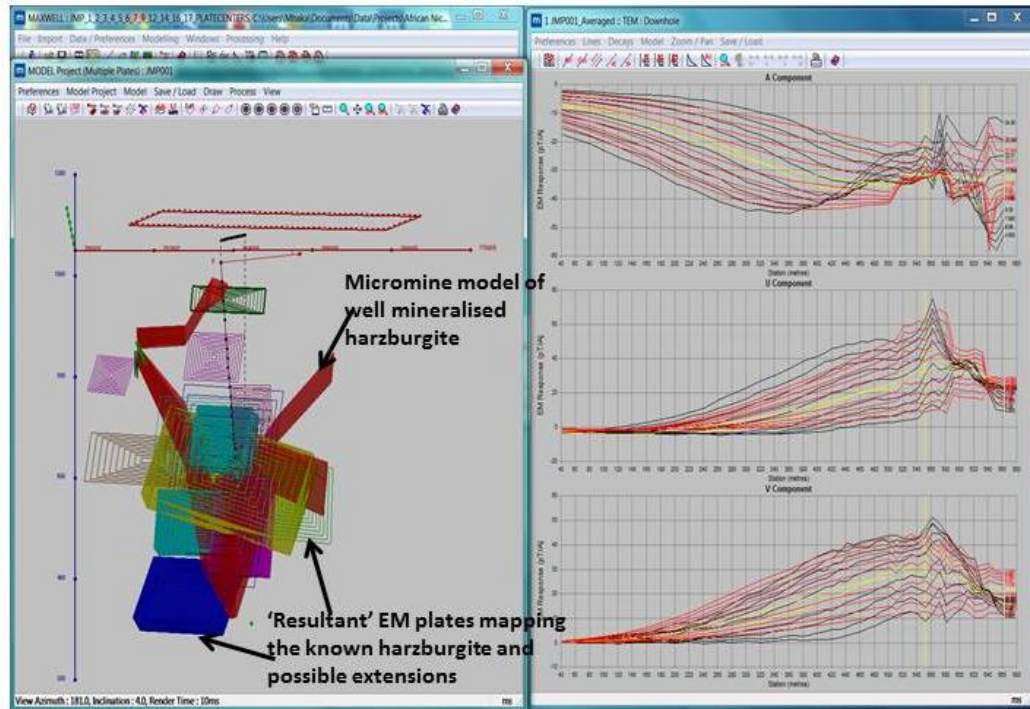


**Figure 10.15** - The Micromine geology model of the well mineralised harzburgite in red is integrated with the 'resultant' EM plates with conductivity thickness above 200 S. The right hand window shows the measured EM response profiles in black and the modelled EM response in red for the three components A, U and V.

These 'resultant' EM plates represent the centre of the modelled EM plates where current will be gathered in late decay times. The 'resultant' EM plates also map possible extension to the known harzburgite.

## 10.7 Interpretation of AMT Data

As already described four resistivity depth section representations of 'models' were created for each AMT line. For the 1D model the assumption of a layered earth is implicit i.e. layers are horizontal and of infinite extent. For the 2D model that has equal weighting on the  $T_m$  and  $T_e$  components, it is instinctively considered to be the best model, but is somewhat featureless when the geology deviates significantly from a 2D geometry. The  $T_m$  model is often the best model for mapping structure while the  $T_e$  model is usually the most effective product to map deep conductors. The  $T_e$  mode does not respond to flat conductors and the product can therefore be useful to penetrate through conductive overburden.

It can be seen that the 2D model shown in Figure 10.16 clearly maps the mineralised ultramafic intrusion as steeply dipping to the south. The 2D model was mainly used during interpretation together with the  $T_m$  and  $T_e$  models.



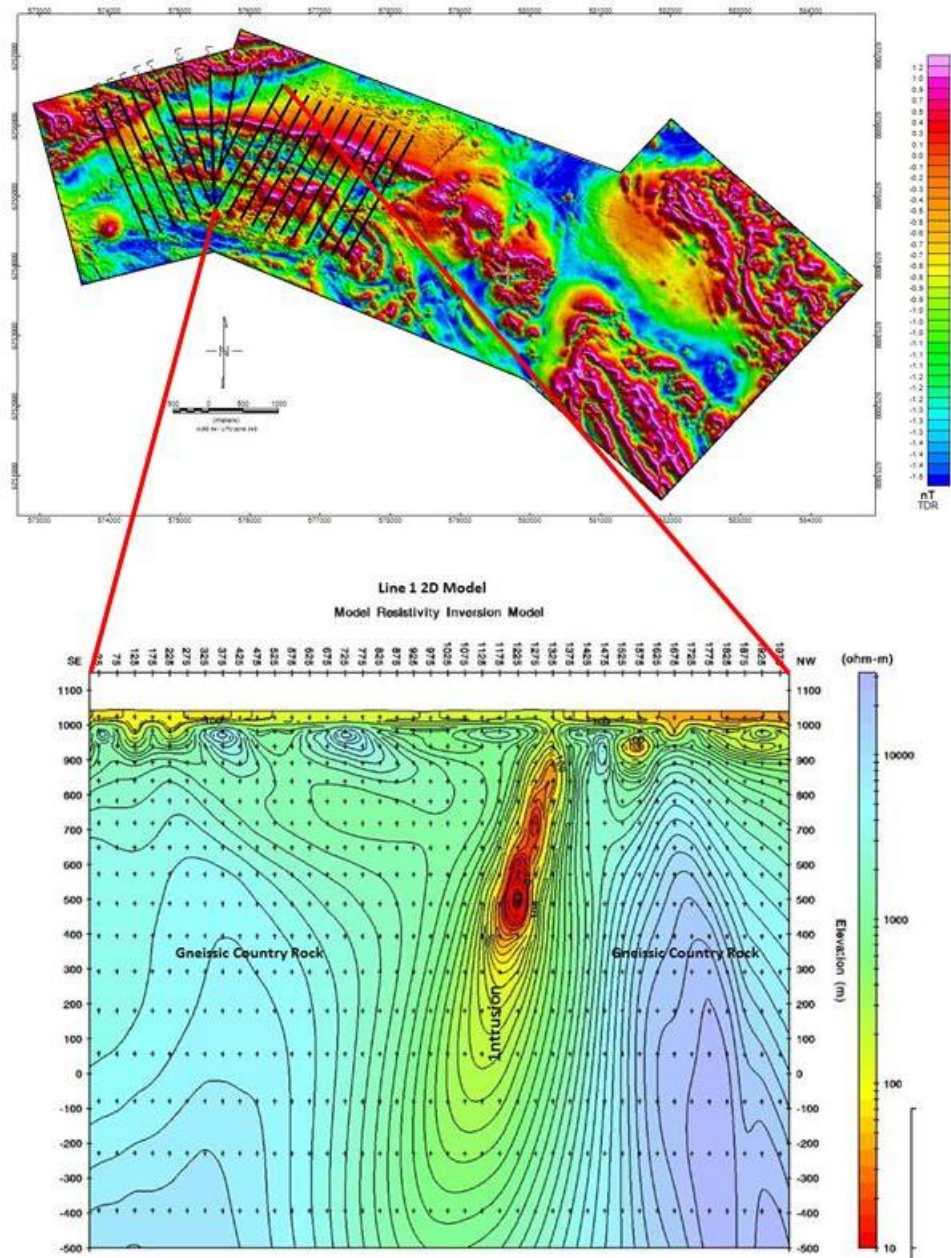


**Figure 10.16** – 2D Section model for Line 1 clearly maps the ultramafic intrusion shown by the high resolution aeromagnetic data. Top image illustrates the surveyed lines on the magnetic tilt angle derivative map.

The Jacomynspan ultramafic intrusion was clearly mapped on all the surveyed lines as can be seen on the four lines in Figure 10.17.

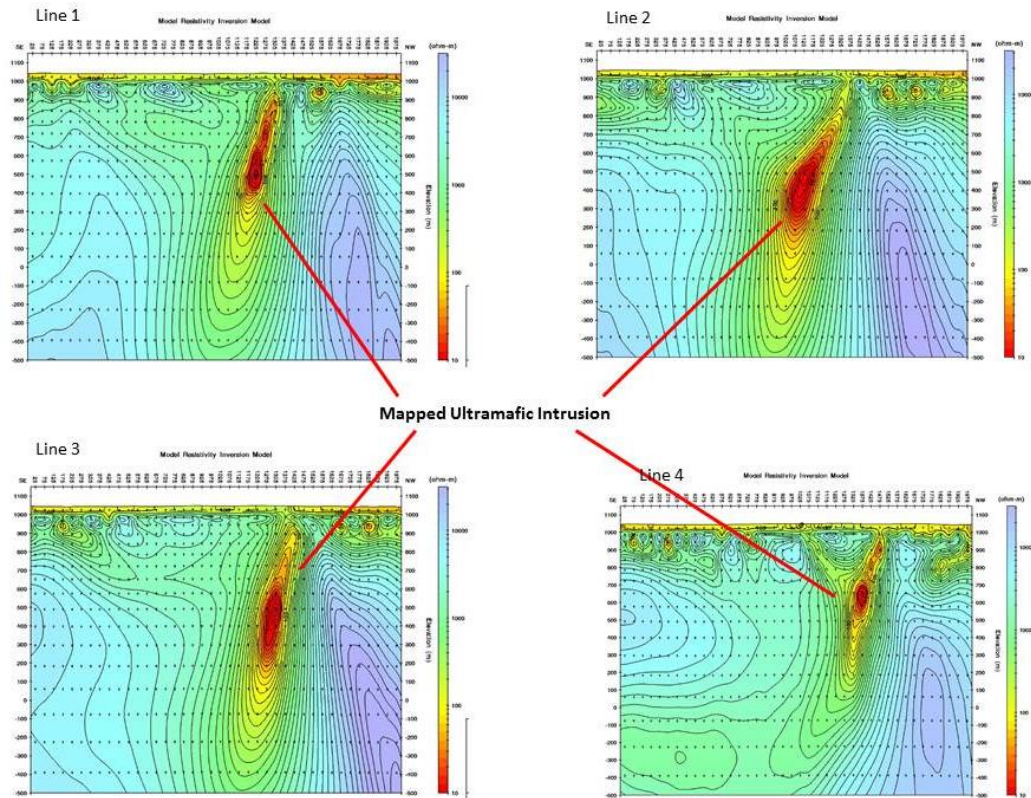


**Figure 10.17** – 2D models with equal weight to  $T_e$  and  $T_m$  mode for four lines covering the study area clearly map the steeply dipping mineralised ultramafic. Line 4 agrees with an earlier mag model carried out using Mag2dc.

The mineralised ultramafic intrusion was clearly mapped as steeply dipping to the south on all the four lines covering the study area.

### 10.8 Integrating AMT Data with Geology Models

The AMT data was not modelled in 3D, only 2D models were produced. A 3D model representation was then created by gridding the data in 3D (Figure 10.18) as explained before and a 3D iso-surface exported to compare with the drilling. This derived 3D product was imported into Geosoft along with all boreholes and the modelled EM plates.

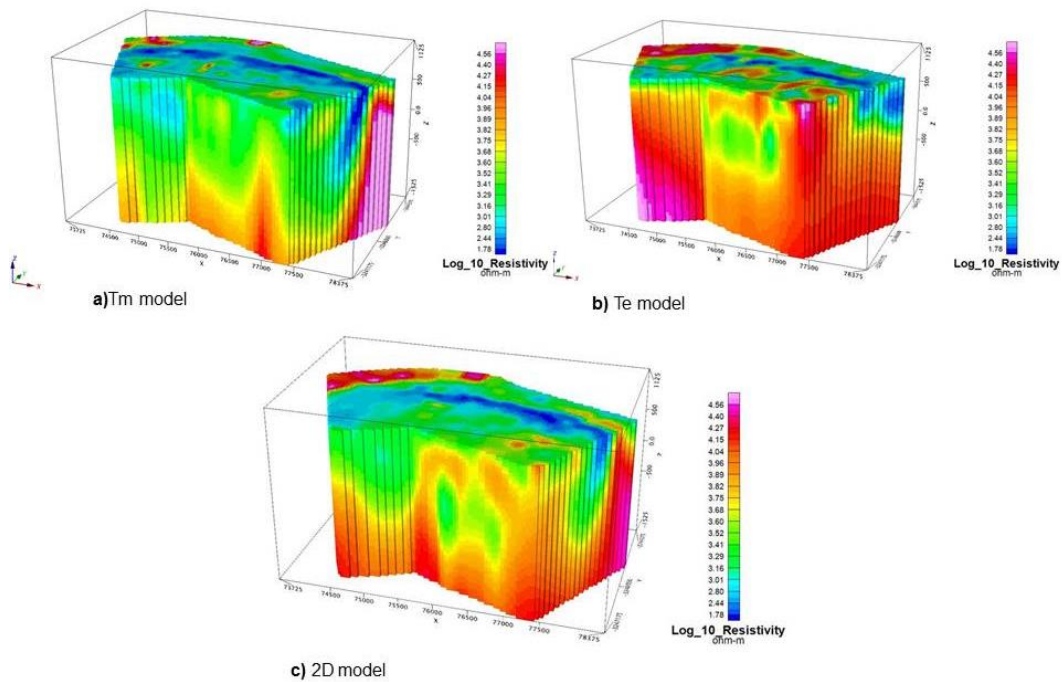


**Figure 10.18** - Smooth-model representation of the 2D a) Tm model, b) Te model, c) 2D vector model.

3D iso-surfaces were created from the 3D smooth-model representation and integrated with the Micromine geology model of the tremolite schist as shown in Figure 10.19 below.

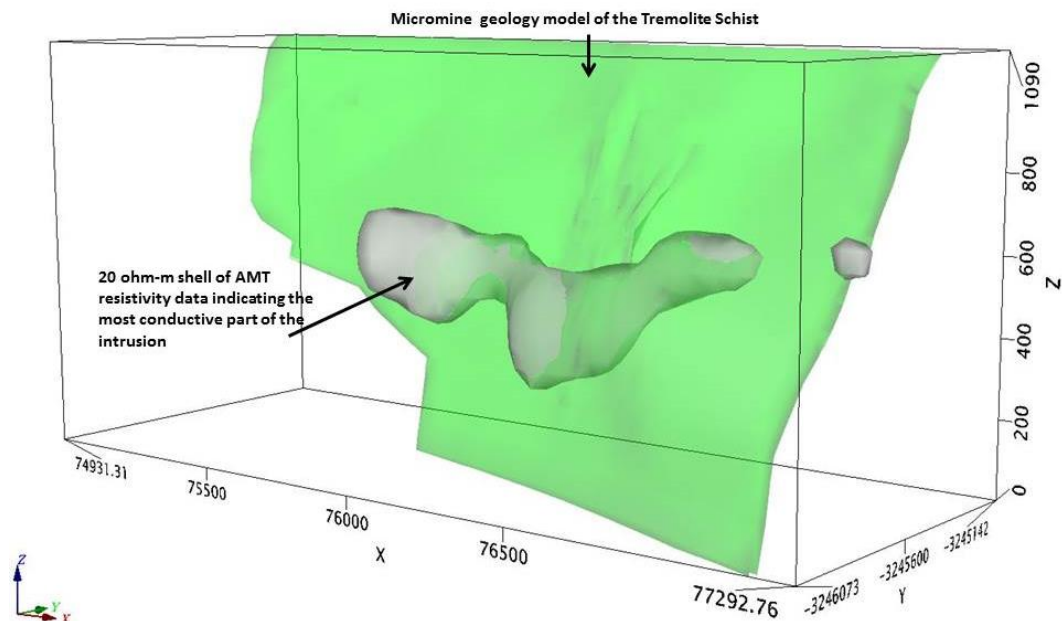


**Figure 10.19** – 3D representation of the 20 ohm-m iso-surfaces created from AMT resistivity data in grey integrated with the Micromine geology model of the tremolite schist in green.

The 20 ohm-m shell of the AMT resistivity data was also integrated with the Micromine geology model of the harzburgite as shown in Figure 10.20.



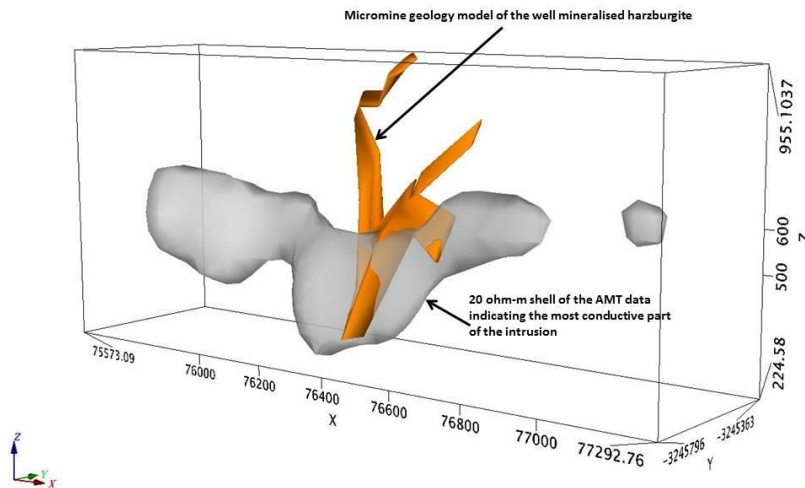


**Figure 10.20** – 3D representation of the 20 ohm-m iso-surface created from AMT resistivity data in grey integrated with the Micromine geology model of the well mineralised harzburgite in orange.

The AMT mapped the mineralised ultramafic sill but could not clearly map the well mineralised harzburgite as was expected.

## 10.9 Integrating different models

The models of the different datasets were integrated as shown in Figure 10.21.

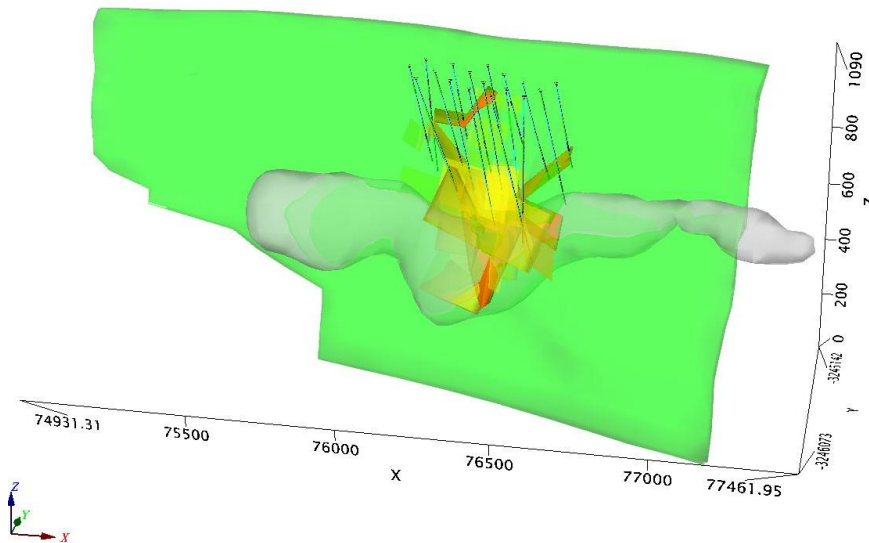


**Figure 10.21** – 3D representation of ultramafic sill (green), mineralised harzburgite (orange) AMT shell (grey), EM plates (yellow) and drillhole traces.

The 20ohm AMT shell (grey) managed to map the most conductive part of the intrusion (green) but could not clearly distinguish the well mineralised harzburgite (orange) which has elevated values of conductivity as expected. The DHEM modelled plates (yellow) managed to map the well mineralised harzburgite showing its possible extensions. The mapped possible extensions of the well mineralised harzburgite have not been drill tested as shown by the drillhole traces (dark blue).

## CHAPTER 11: CONCLUSIONS AND SUGGESTIONS FOR FURTHER WORK

Physical property studies (relative conductivity and magnetic susceptibility) carried out on Jacomynspan drill core by the author indicated that the country gneissic rocks are not conductive and neither are they magnetically susceptible. The well mineralized net-textured harzburgite has elevated values of both magnetic susceptibility and relative conductivity compared to the poorly mineralized tremolite schist which is hosting it. Laboratory Palaeomagnetic measurements carried out at the Council for Geoscience in Pretoria, bulk magnetic susceptibility and Natural Remanent Magnetism (NRM) on core specimens indicated that the deposit has no significant remanent magnetism. It is therefore unnecessary to take this into consideration during modelling.

The main objective of this research project was to establish a 3D model of the well mineralised harzburgite which is hosted within the Jacomynspan Ni-Cu mineralised mafic to ultramafic sill in order to guide further drilling. This model was developed by modelling available different geophysical datasets collected over the study area. The 3D geology model generated in Micromine from drilling results was used as a 'starter' model. Geophysical modelling was then carried out on all the available datasets in this study.

Since the Jacomynspan Ni-Cu sulphide deposit has a coincident magnetic and EM response, Cooper's Mag2dc, Stettler's Magmodintp and Geosoft's VOXI Earth Modelling software were used for modelling the high resolution aeromagnetic data. The mineralised ultramafic sill which has elevated values of magnetic susceptibility was clearly mapped in both the 3D model representation from Mag2dc modelling and VOXI's 3D unconstrained smooth model inversion for the study area. However the slightly magnetic material south of the sill resolved by the Mag2dc inversion process was not detected with the VOXI inversion process. VOXI's Iterative Reweighting Inversion (IRI) Focus was also applied to the study area in order to refine the smooth model inversion and emphasize a desirable model characteristic. The IRI Focus results showed a more compact and focused magnetic susceptibility distribution of the mineralised mafic to ultramafic intrusion. However, since the objective of this study was to map and delineate the well mineralised harzburgite, drilling constraints with wire-framing was used with VOXI inversion to validate the geologic interpretation deduced from drilling and to indicate where unrecognised additional mineralization may be located. The constrained inversion results suggested a possible extension (if a conductor exists) of the well mineralised harzburgite to the western extent of the mapped harzburgite. East of the study area the magnetic data set also indicates some potential.

The dominant physical property for the inductive EM methods used in this study is the electrical conductivity. Because of the huge physical contrast between the electrical

properties of the well mineralised harzburgite and the host rocks, EMIT's Maxwell Electromagnetic software was used in the modelling of all the ground EM data and Downhole Electromagnetics (DHEM) data. Since the mineralised Jacomynspan mafic to ultramafic intrusion is a steeply dipping sheet with a large strike and depth extent, so were the EM model plates. The modelled plates were very large with a strike extent of about 1.8km and a depth extent of 1.2 km dipping steeply to the south correlating very well with the Micromine geology model of the mineralised ultramafic sill. In order to better constrain the targets, an assumption was made that at late decay times the currents would be focused in the centre of the large EM plate giving an indication of the most conductive part of the intrusion. Smaller 'Resultant EM plates' of dimensions, 300x300m that coincide with the centre of the large EM plates (with a conductance above 100 Siemens) where current will be focused at late decay times were therefore constructed in Maxwell software. Since the physical property measurements (conductivity) taken on the drill core indicate that the net-textured well mineralised harzburgite is more conductive than the disseminated mineralised tremolite schist, the constructed centre of EM plates with conductivity thickness above 100 Siemens were interpreted to give an indication of the well mineralised net-textured harzburgite and massive sulphide stringers. Integrating in Maxwell software the DXF file of the Micromine geology model of the well mineralised harzburgite with the constructed 'resultant EM plates' gave an indication that the well mineralised harzburgite was mapped and could be extending both sides.

Inversion models of AMT Cagniard Resistivity and Impedance Phase data provided detailed images of the conductivity structure at depth. The mineralised ultramafic intrusion which has elevated values of conductivity compared to the country gneissic rocks was clearly mapped as steeply dipping to the south on all the four lines covering the study area. Since no 3D modelling was carried out on the AMT data because the software is not yet readily available, a 3D-model representation of the 2D,  $T_m$  and  $T_e$  models was produced. Iso-surfaces were created in Geosoft and mapped the most conductive part of the intrusion but could not clearly distinguish the well mineralised harzburgite.

Modelling of the available data has pointed towards possible extension of the well mineralised harzburgite with the DHEM modelled EM plates correlating very closely with the mapped well mineralised harzburgite. It is therefore suggested that further work involve drill testing of these possible extensions of the well mineralised harzburgite.

## APPENDIX A

### DETERMINATION OF KONIGSBERGER RATIOS

#### Difference between cgs and SI units

Remanent magnetization of rock ( $J_n$ ):

$$J_n = 1 \times 10^{-6} \text{ e.m.u./cm}^3 \quad \text{cgs}$$

$$= 1 \times 10^{-3} \text{ A/m} \quad \text{SI}$$

Magnetic susceptibility ( $k$ ):

$$K = 1 \times 10^{-6} \quad \text{cgs}$$

$$= 4\pi \times (1 \times 10^{-6}) \quad \text{SI}$$

Induced magnetization of Earth's field ( $H$ ):

$$H = 30\,000 \text{ Gamma} \quad \text{cgs}$$

$$= 0.3 \text{ Oersted}$$

$$H = (0.3 \times 1/4\pi) \times 10^3 \text{ A/m} \quad \text{SI}$$

$$= 23.87 \text{ A/m}$$

Koenigsberger Ratio ( $Q_n$ ):

$$Q_n = J_n/kH$$

$$= \frac{1 \times 10^{-6}}{(1 \times 10^{-6})(0.3)} \quad \frac{\text{e.m.u./cm}^3}{\text{Oersted}} \quad \text{cgs}$$

$$Q_n = \frac{1 \times 10^{-6}}{(4\pi \times 1 \times 10^{-6}) \left(0.3 \times \frac{1}{4\pi}\right) \times 10^3} \quad \text{SI}$$

## APPENDIX B

### MAGNETIC FIELD UNITS

**B** = Magnetic field Tesla ( $\text{NA}^{-1}\text{m}^{-1}$ )

**H** = Magnetising force: A/m

**M** = Magnetisation (magnetic moment per unit volume): A/m

**J** = Natural Remanent Magnetisation: A/m

$\mu_0$  = magnetic permeability of free space:  $4\pi \times 10^{-7}$  Wb/A.m (or H/m or  $\text{NA}^{-2}$ )

$k = \mathbf{M}/\mathbf{H}$  = magnetic susceptibility: dimensionless

$\mu_r = (1 + k)$  = relative permeability: dimensionless

$\mu = \mu_0 \mu_r$  magnetic permeability of a material (measure of the ability of a material to convey a magnetic flux): Wb/A.m

$Q = \mathbf{J}/k\mathbf{H}$  = Koenigsberger ratio : dimensionless

$$\mathbf{B} = \mu_0(\mathbf{H} + \mathbf{M}) = \mu_0(\mathbf{H} + k\mathbf{H}) = \mu_0(1 + k)\mathbf{H} = \mu_0\mu_r\mathbf{H} = \mu\mathbf{H}$$

$$\mathbf{B} = \mu_0(\mathbf{H} + \mathbf{M}) = \mu_0(\mathbf{M}/k = \mathbf{M}) = \mu_0(1 + 1/k)\mathbf{M}$$

### UNITS

$$\mathbf{B} = \mu_0(1 + k)\mathbf{H} = \left[ \frac{\text{Weber}}{\text{A.m}} \right] [\text{dimensionless}] \left[ \frac{\text{A}}{\text{m}} \right] = \left[ \frac{\text{weber}}{\text{m}^2} \right] = [\text{Tesla}]$$



## REFERENCES

- Attridge, R.L., 1986. The Jacomynspan Copper-Nickel Occurrence, Kenhardt District. Mineral Deposits of Southern Africa, **1**, 1539-1545.
- Austin, J., Clark, D., Schmidt, P., Hillan, D. and Foss, C., 2013. Magnetic anomalies to mines: Practical insights into myths, methods and mysteries in relating mineralisation and magnetisation. ASEG 2013 Remanence and Demagnetisation Forum.
- Austin, J.R. and Foss, C.A., 2014. The Paradox of scale: Reconciling magnetic anomalies with rock magnetic properties for cost-effective mineral exploration. Journal of Applied Geophysics, **104**, 121-133.
- Balch, S.J., 2007. Geophysics in Mineral Exploration: Fundamentals and Case Histories Ni-Cu Sulphide Deposits with examples from Voisey's Bay. Inco Technical Services Limited, Copper Cliff, Ontario.
- Bedrosian, P.A., 2007. MT+, Integrating Magnetotellurics to Determine Earth Structure, Physical State and Processes. Surv Geophys, **28**, 121 – 167.
- Blakely, R.J., 1995. Potential Theory in Gravity and Magnetic Applications. Cambridge University Press, Cambridge.
- Boelema, R., 1994. The Metallogeny of the Upington and Kenhardt Area, Northern Cape, MSc Thesis, Rhodes University, Grahamstown, 225 pp.
- Burns, C., 2012. Introduction of VOXI Earth Modelling technology. Geosoft.
- Butler, R.F., 1992. Paleomagnetism: Magnetic Domains to Geologic Terranes. Blackwell Science, Boston, 238pp.
- Cagniard, L., 1953. Basic theory of the magnetotelluric method of geophysical prospecting. Geophysics, **18**, 605 – 635.
- Carmichael, R.S., 1989. Physical Properties of Rocks and Minerals. CRC Press.
- Claerbout, J.F., 1976. Fundamentals of Geophysical data processing: with applications to Petroleum Prospecting. McGraw-Hill International Series, New York.
- Cooley, J.W. and Tukey, J.W., 1965. An algorithm for the machine calculation of complex Fourier series. Math. Comput., **19**, 297 – 301.
- Comber, S.J., 2008. Gravity modelling in the Western Bushveld Complex, South Africa, Using Integrated Geophysical data, MSc Dissertation, University of Witwatersrand, 216 pp.
- Combrinck, M. and Botha, W., 2010. Decay Characteristics of Airborne Time-Domain Electromagnetic Data: where to find the Constant (TAU). Presentation, Johannesburg, South Africa.
- Cooper, G.R.J., 2015. Available at [www.wits.ac.za](http://www.wits.ac.za). (2 June 2015).

- Cooper, G.R.J., 1997. Forward Modelling of Magnetic Data. Computers and Geosciences, **23**, No. 10 pp1125-1129.
- Cooper, G.R.J., 2004. Numerical Methods in Geophysics: Space Domain Filtering, Geophysics Honours Lecture Notes, University of Witwatersrand, 97 pp.
- Dean, W.C., 1958. Frequency analysis for gravity and magnetic interpretation. Geophysics, **23**, 97-127.
- d'Ecreville, I. and Kunetz, G., 1962. The effect of a fault on the Earth's Natural Electromagnetic field. Geophysics, **27**, 651-665.
- Dobrin, M.B. and Savit, C.H., 1988. Introduction to Geophysical Prospecting. McGraw-Hill International Editions, New York.
- Duncan, A., 2007. Available at [www.emit.iinet.net.au/](http://www.emit.iinet.net.au/) (10 July 2015).
- Dyck, A.V. and West, G.F., 1984. The role of simple computer models in interpretation of wide-band drill-hole Electromagnetic surveys in mineral exploration. Geophysics, **49**, 957-980.
- Eadie, T. and Staltari G., 1987. Introduction to Downhole Electromagnetic Methods. Exploration Geophysics, **18**, 247-254.
- Ellis, G.E., de Wet, B. and Macleod, I.N., 2012. Inversion of Magnetic Data from Remanent and Induced Sources. International Geophysical Conference and Exhibition.
- Emerson, D.W., Williams, P.K., Luitjens., 2001. The Conductivities of Komatiitic Nickel Ores at Kambalda W.A., ASEG Preview Magazine.
- EMIT, 2010. Available at [www.emit.iinet.net.au](http://www.emit.iinet.net.au) (20 October 2014).
- EMIT User Guide, 2015. Available at [www.electromag.com.au](http://www.electromag.com.au) (30 November 2014)
- Geometrics, 1995. G-856 Memory-Mag™ Proton Precession Magnetometer Operator's Manual, California, USA, 61 pp.
- Geosoft, 2013. Oasis Montaj, Standard Edition v8.1 Help Notes.
- Geosoft, 2013. Available at [www.geosoft.com](http://www.geosoft.com) (3 March 2014)
- Ghosh, G.K. and Dasgupta, R., 2013. Edge detection and depth estimation using 3D Euler deconvolution, Tilt angle derivative and TDX derivative using magnetic data of thrust fold belt area of Mizoram. SAGA 10<sup>th</sup> Biennial International Conference & Exposition, 70pp.
- Grant, F.S. and West, G.F., 1965. Interpretation theory in Applied Geophysics. McGrawHill, New York, 583pp.
- Heath, P., 2007. Analysis of potential field gradient tensor data: forward modelling, inversion and near-surface exploration, University of Adelaide, Adelaide, 206 pp.

- Hohmann, G.W. and Raiche, A.P., 1988. Inversion of controlled-source electromagnetic data. In: Nabighian MN (ed) Electromagnetic methods in applied geophysics. Soc. Of Expl. Geophys., **1**, 313-363.
- Irvine, R.J., 1987. Drillhole TEM surveys at Thalanga, Queensland. Exploration Geophysics, **18**, 285-293.
- Irving, E., 1964. Palaeomagnetism and its application to geological and geophysical problems. John Wiley & Sons, Inc., New York, 399 pp.
- Jessy Deep., 2010. Manual, 5pp
- Jones, A.G., 2002. Magnetotelluric Theory. MT Short Course, SEG, Johannesburg, South Africa.
- JR-6A User's Manual, 2004. Spinner Magnetometer JR-6A User's manual
- Kearey, P., Brooks, M. and Hill, I., 2002. An Introduction to Geophysical Exploration. Third Edition, Blackwell Science, London, 262 pp.
- Klinkert, P., Devkurran, N. and Polome, L., 2012. SPECTREM Survey of the African Nickel Limited – Jacomynspan North Area, Client Report, Johannesburg, South Africa.
- King, A., 2007. Review of Geophysical Technology for Ni-Cu-PGE deposits. Ore Deposits and Exploration Technology, **45**, 647-665.
- Kaufman, A.A., Keller, G.V., 1981. The magnetotelluric sounding method, methods in Geochemistry and Geophysics. Elsevier, Amsterdam, vol 15.
- Lamontagne, Y. and West, G.F., 1971. EM Response of a Rectangular thin plate. Geophysics, **36**, 1204 – 1222.
- Lelievre, P.G., 2003. Forward Modelling and Inversion of Geophysical Magnetic Data, MSc Thesis, University of British Columbia, 206 pp.
- Letts, S.A., 2007. The Palaeomagnetic Significance of the Bushveld Complex and Related 2 GA Magmatic Rocks in Ancient Continental Entities. PhD Thesis, University of Witwatersrand, 223 pp.
- Long, A. and Fischer, K., 2013. Geosoft VOXI Workshop 1. A practical guide to inversion.
- Macnae, J. and Staltari, G., 1987. Classification of Sign Changes in Borehole TEM Decays. Exploration Geophysics, **18**, 331-339.
- Mariita, N.O., 2007. The Magnetic Method. Short Course II on Surface Exploration for Geothermal Resources, 8 pp.
- McEnroe, S.A., Fabian, K., Robinson, P., Gaina, C. and Brown, L., 2009. Crustal Magnetism, Lamellar Magnetism and Rocks that Remember, *Elements*, **5**, 241-246.
- Milligan, P.R. and Gunn, P.J., 1997. Enhancement and presentation of airborne geophysical data. Journal of Australian Geology and Geophysics, **17**(2), 63-75.

- Nabighian, M.N., 1972. 'The analytic signal of two-dimensional magnetic bodies with polygonal cross-section: Its properties and use for automated anomaly interpretation'. *Geophysics* **37**, 507 – 517.
- Nabighian, M.N., 1979. Quasi-static transient response of a conducting half-space. An approximate representation, *Geophysics*, **44**, 1700-1705.
- Oldenburg, D.W. and Pratt, D.A., 2007. Geophysical Inversion for Mineral Exploration: a Decade of Progress in Theory and Practice. *The Leading Edge*, 61-95.
- Paasche, H., and Eberle, D., 2009. Rapid Integration of large airborne geophysical data suites using a fuzzy partitioning cluster algorithm: A tool for geological mapping and mineral exploration targeting. *Exploration Geophysics*, **40**, 277-287.
- Pilkington, M., 1997. 3-D magnetic imaging using conjugate gradients. *Geophysics*, **62**, 1132-1142.
- Pirttijarvi, M., 2003. Numerical Modelling and Inversion of Geophysical EM measurements using a thin plate model, PHD thesis, University of Oulu.
- Pratt, D.A., McKenzie, K.B. and White, A.S., 2012. The remote determination of magnetic remanence. 22<sup>nd</sup> International Geophysical Conference and Exhibition, 26-29 February Brisbane, Australia.
- Raiche, A.P., 1984. The effect of ramp function turnoff on the TEM response of a layered ground, *Expl. Geophys.*, **15**, 37-41.
- Roux, A.T., 1980. The magnetic Method. *Geophysical field manual for Technicians*, No. 1. South African Geophysical Association, Johannesburg, South Africa, 71pp.
- Salem, A., Williams, S., Fairhead, J.D., Ravat, D. and Smith, R., 2007. Tilt-depth method: A simple depth estimation method using first-order magnetic derivatives. *The Leading Edge*, 1502 – 1505.
- Southern Geophysical Exploration, 1995. *Transient Electromagnetic Field Manual (TDEM Profiling)*.
- Schmidt, P.W. and Lackie, M.A., 2013. Practical considerations: making measurements of susceptibility, remanence and Q in the field. ASEG 2013 Remanence and Demagnetisation Forum.
- Sharma, P., 1976. *Geophysical Methods in Geology*. Elsevier, Amsterdam
- Telford, W.M., Geldart, L.P. and Sherrif, R.E., 1990. *Applied Geophysics*. Cambridge University Press, New York, 770pp.
- Ushendibaba, M., du Plessis, S.J., Hornsey, R.A., Nonoise, N., 2013. The Geophysics of the Jacomynspan Project. Short paper of the SAGA 13<sup>th</sup> Biennial Conference and Exhibition, Kruger National Park, South Africa.
- World Wide Science., 2014. Available at [www.worldwidescience.org](http://www.worldwidescience.org) (14 September 2014)
- Zonge, 2010. Introduction to NSAMT available at [www.zonge.com](http://www.zonge.com). (9 July 2014)